



PhD Thesis

Morten Holm Christensen
Niels Bohr Institute

**Exotic Magnetic Orders and Their
Interplay with Superconductivity**

January 6, 2017

Supervisor:
Brian Møller Andersen, Niels Bohr Institute

This thesis has been submitted to the PhD School of The Faculty of Science,
University of Copenhagen

Abstract

The interplay between magnetism and superconductivity poses an interesting problem in the field of condensed matter physics. In this thesis we study the commensurate and incommensurate magnetic orders appearing in the iron-based superconductors and emphasise the importance of including the orbital content of the bands when determining the symmetry of the magnetic order parameter. We elucidate the appearance of six new incommensurate magnetic phases and argue that a number of these are prime candidates for exhibiting topologically protected edge modes. Within a simplified hybrid model we include a spin-orbit coupling and propose an explanation for the reorientation of magnetic moments observed in certain hole-doped compounds. The mechanism of spin-driven nematic order is reviewed and it is shown, using a band structure suitable for the iron-based superconductors, that the multi-orbital Hubbard model exhibits a spin-driven nematic instability. We then proceed to consider magnetic stripes in cuprate superconductors and review experimental results on $\text{La}_{2-x}\text{Ba}_x\text{CuO}_4$ which led to the proposal of pair-density-wave superconductivity in this material. A recent experiment reported the absence of a magnetic resonance peak in $\text{La}_{2-x}\text{Ba}_x\text{CuO}_4$ for $x = 0.095$ and motivated by this we employ a simple model to evaluate the magnetic resonance and show that pair-density-wave superconductivity indeed fails to produce a magnetic resonance. Finally we turn to the subject of topological superconductivity and the appearance of Majorana end modes. The concept of topologically non-trivial phases is introduced using the Kitaev chain and we describe how realistic physical systems can constitute an effective Kitaev chain. One such system is a chain of magnetic adatoms exhibiting spiral magnetic order deposited on a superconducting substrate. We study the physical mechanisms responsible for the formation of a stable spiral magnetic order along the chain and show that this spiral order is stable against the effects of selfconsistency and the addition of a direct exchange coupling between the adatoms.

Acknowledgements

I am eternally grateful to my advisor Brian M. Andersen without whom this thesis would not exist. These past few years have been both challenging and fun and this is in no small part due to him. I have also benefitted immensely from discussions with Maria Gastiasoro, Astrid Rømer, Shantanu Mukherjee, Andreas Kreisel, Daniel Scherer, Mike Schecter, Jens Paaske, Karsten Flensberg, Panagiotis Kotetes, Henrik Jacobsen, Ilya Eremin, Peter Hirschfeld, and Monica Kovacic.

I am also indebted to Michael Schütt, Marc Schulz, Peter Orth, Jian Kang, Xiaoyu Wang, Jiaming Zheng and Rafael Fernandes at the School of Physics and Astronomy at the University of Minnesota who contributed to making my six months there both educational and fun.

I also owe Panagiotis Kotetes and Henrik Jacobsen a debt of gratitude for their helpful comments concerning this thesis and for their heroic struggle to keep it free of typos.

Contents

Introduction	1
1 Magnetism in Iron-based Superconductors	5
1.1 Renormalisation Group Flow of Quartic Coefficients	9
1.2 Modeling the Iron-based Superconductors	11
1.2.1 Minimal models	12
1.2.2 Hybrid models	15
1.2.3 Multi-orbital models	17
1.3 Commensurate magnetic order	19
1.4 Incommensurate magnetic order	22
2 Spin reorientation driven by the interplay between spin-orbit coupling and Hund's rule coupling in iron pnictides	29
2.1 Introduction	30
2.2 Low-energy microscopic model	31
2.3 Anisotropic magnetic free energy	38
2.4 Tetragonal vs stripe magnetic order	43
2.5 Discussion and Conclusions	47
Appendices	49
2.A Expansion of tight-binding Hamiltonian for small \mathbf{k}	49
2.B Spin-orbit coupling in orbital basis	50
2.C Evaluation of Two-loop Diagrams	53
2.D Diagrams contributing to w	53
3 Spin-Driven Nematic Instability of the Multi-Orbital Hubbard Model: Application to Iron-Based Superconductors	55
3.1 Introduction	56
3.2 Orbitorally resolved nematic susceptibility	57
3.3 Results	59
3.4 Conclusions	63
Appendices	64
3.A Fourth order coefficients	64
3.B Nematic susceptibility	65
3.C Frequency dependence of the magnetic susceptibility	66
3.D Derivation of the ferro-orbital order susceptibility	67
4 Interplay of Magnetism and Superconductivity in Cuprate Superconductors	69
4.1 Magnetic Susceptibility in the Superconducting State	72
4.2 Magnetic Stripes in Cuprates	73

5	Magnetic fluctuations in pair density wave superconductors	75
5.1	Introduction	76
5.2	Model	77
5.3	Results	79
5.4	Conclusions	82
	Appendices	83
5.A	Transverse magnetic susceptibility with supercells	83
5.B	Selfconsistent determination of U	84
6	Topological Superconductivity and Majorana End Modes	87
6.1	Majorana Modes in the Kitaev chain	88
6.2	Magnetic Adatom Chains on Superconductors	91
6.3	Bound States induced by Magnetic Adatoms	92
7	Spiral magnetic order and topological superconductivity in a chain of magnetic adatoms on a two-dimensional superconductor	95
7.1	Introduction	96
7.2	Model	97
7.3	Weak exchange interactions	99
7.3.1	Exchange interactions along the (10) direction	100
7.3.2	Exchange interaction along the (11) direction	102
7.4	Magnetic adatom chain	103
7.4.1	Phase diagram	105
7.4.2	Topological phases	106
7.4.3	Effect of direct exchange interaction	108
7.5	Effects of selfconsistency	110
7.6	Conclusions	113
	Appendix	115
7.A	Effect of spin-orbit coupling	115
8	Concluding Remarks and Outlook	117
	Bibliography	119

Introduction

The discovery of superconductivity in 1911 is among the major scientific accomplishments of the 20th century and this exotic state of matter finds applications in all branches of condensed matter physics. The microscopic origin of superconductivity puzzled researchers for almost 50 years until Bardeen, Cooper and Schrieffer presented their theory in which Cooper pairs are formed by a phonon-mediated electron attraction [1]. With this the problem seemed to be solved, however when Bednorz and Müller surprisingly discovered superconductivity in the ceramic compound $\text{La}_{2-x}\text{Ba}_x\text{CuO}_4$ in 1986 [2] the field was revitalised. The subsequent period yielded a flood of new superconducting materials being discovered and over time it has become clear that the phonon-induced pairing is inadequate to describe this new family of superconductors [3]. At the time it was widely believed that magnetic phases were highly detrimental to superconductivity (cf. the Matthias rules [4]) however the parent compounds of the cuprates are antiferromagnets displaying characteristics consistent with Mott-insulators. In the Mott-insulating phase electrons are localised at individual sites due to strong electron-electron repulsion. The Coulomb repulsion therefore plays a significant role in these compounds and theoretical attempts to understand these materials have brought with them significant advances in the field of strongly correlated electrons. The strength of interactions along with an observed resistivity linear in temperature has fuelled speculation that cuprates are not described by the celebrated Landau-Fermi liquid theory and led to proposals of e.g. marginal Fermi liquids [5], fractionalised Fermi liquids [6], and resonating valence bond theory [7].

The addition of iron-based superconductors [8] (FeSC) to the family of materials exhibiting unconventional superconductivity added an additional layer of complexity to the problem. In contrast to the cuprates the parent compounds of these materials are metallic with a magnetic spin-density-wave (SDW) phase at lower temperatures [9]. A substantial number of orbitals contribute to the Fermi surface, which exhibits numerous electron and hole pockets, and multiorbital models are required to describe many of the observed phenomena [10,11]. These materials are believed to be moderately correlated though [12] and it is unclear whether Fermi liquid theory offers a good description. The interplay between orbitals and interactions opens up the possibility of some orbitals being more correlated than others and the quasiparticles associated with these orbitals are therefore less coherent. This has been explored in the context of orbitally selective Mott phases [13,14] and more recently in an effort to explain the peculiar gap structure of FeSe [15].

The structure of the superconducting order parameter provides an important piece of the puzzle regarding the origin of the electron pairing. Experiments on the cuprates

are consistent with a d -wave gap structure [16, 17], with nodes along the diagonal of the Brillouin zone. The sign-change allows for a pairing driven by repulsive interactions such as the one mediated by magnetic fluctuations. In the FeSC the situation is more complicated. The exact nature of the gap structure in these materials is still unclear and distinguishing between the two viable candidates is experimentally challenging. One candidate is the standard s -wave structure well-known from conventional superconductors (in FeSC called s^{++}), while the other is the more exotic s^\pm which features a sign change between electron and hole pockets [18–24]. s^{++} and s^\pm thus only differ by the sign of the order parameter on the electron pockets and phase-sensitive measurements are therefore required in order to discriminate between the two. This proves to be rather challenging since, in contrast to the case of a d -wave order parameter, the phase is unchanged by a 90° rotation. Recently however, a proposal based on the qualitative behaviour of certain quasiparticle interference data with temperature was put forth [25], which appears capable of distinguishing the s^{++} gap structure from the s^\pm [15]. The lack of a sign-change in the s^{++} case implies that the pairing in this case should be mediated by an effective attractive interaction, like the phonons for conventional superconductors [24]. On the other hand, the s^\pm scenario favours a magnetically mediated pairing due to the sign-change between parts of the Fermi surface [24]. Combining this with the proximity of the magnetic and superconducting phases in the phase diagrams for unconventional superconductors has made a magnetically mediated pairing a prime contender for the pairing glue in both cuprates and FeSC.

Motivated by these links between superconductivity and magnetism, in this thesis we focus on understanding the magnetic phases of both cuprates and FeSC. While a complete theoretical understanding is still lacking, the important role of magnetism is undeniable and elucidating the intricate relationship between magnetism and unconventional superconductivity remains one of the most important questions of contemporary condensed matter physics.

Superconductivity also has an important role to play in the quest for quantum computers. It allows for the formation of topologically protected states which are stable against quantum decoherence, a highly desirable property for quantum bits [26]. The existence of such topological boundary modes depends on the presence of certain anti-unitary symmetries and various proposals of how to achieve this experimentally have been put forth. Amongst the most popular ones is the so-called nanowire setup where a topological phase is obtained by tuning of an external magnetic field [27–30]. An alternative approach based on magnetic chains of adatoms is independent of any external parameters, relying instead on the magnetic order along the chain and thus actualising a self-organised topological phase [31]. This has both advantages and drawbacks. On the one hand, the independence of external tuning parameters allows for applications in the presence of magnetic fields required for other purposes, while on the other hand their absence implies that the system should be designed to lie in the topologically non-trivial region. This puts rather stringent constraints on the viable systems and requires a good understanding of the mechanisms relevant for the formation of a topologically non-trivial regime. To this end, in this thesis we consider a specific system where a topological phase is possible and outline the relevant

physical mechanisms responsible for the formation of the appropriate magnetic order.

In this thesis we investigate a number of rather distinct topics related to the interplay between magnetism and superconductivity in a variety of systems. We provide further details concerning the FeSC in Chapter 1. After introducing a number of key concepts we consider the various magnetic orders that arise in the FeSC. Using a renormalisation group approach we demonstrate the stability of the mean-field phase diagram. We consider in some detail the various band structures that are used in the description of the FeSC and highlight the importance of taking into account the orbital content of the bands when considering the magnetic order. In Chapter 2 we show how spin-orbit coupling affects the magnetic order and can explain a reorientation of the magnetic moments to lie out-of-plane, as observed in the magnetic tetragonal phase of some FeSC [32–35]. At last we extend the usual approach to spin-driven nematicity in Chapter 3 to include orbital content and demonstrate the existence of a spin-driven nematic instability in the multi-orbital Hubbard model using a bandstructure appropriate for the FeSC. In Chapter 4 we provide an overview of the cuprates and outline relevant theoretical and experimental results with a particular focus on the appearance of a so-called magnetic resonance. This plays an important role in the study of the interplay between magnetic and superconducting orders and serves as motivation for the work presented in Chapter 5. Motivated by a recent experimental result by Xu *et al.* [36] we here study the shape of the magnetic resonance in the presence of various magnetic and superconducting orders. In Chapter 6 we briefly consider the subject of Majorana modes and introduce a number of key concepts in the field of topological superconductivity using the Kitaev chain. This serves as motivation for the study presented in Chapter 7 in which we consider a magnetic chain of adatoms deposited on a two-dimensional superconductor. The mechanisms responsible for the formation of spiral magnetic order along the chain are described and we further discuss the influence of selfconsistency on our results. In Chapter 8 we present our conclusions and remark on future directions.

Chapter 1

Magnetism in Iron-based Superconductors

The first iron-based superconductor, LaOFeP, was synthesised in 2006 by Hideo Hosono and collaborators [8]. The arrival of a new family of unconventional superconductors was highly anticipated in the high- T_c community and the advent of the FeSC provided a testing ground for many of the theories that had been developed to describe the cuprates. The iron-based materials are similar in structure to the cuprates, i.e. they are quasi-2d with superconductivity having its origin in the Fe-pnictide or Fe-chalcogenide layers. Instead of the perovskite structure of the cuprates, the crystal structure of FeSC consists of two-dimensional layers of Fe atoms with pnictogens or chalcogens above or below in a staggered fashion, as shown in Fig. 1.1. Six electrons occupy the five Fe d -orbitals and while the tetragonal crystal environment leaves the xz and yz orbitals degenerate, the rest are split by the crystal field.

The nature of the superconducting order parameter in the FeSC is unclear, the main contenders are the sign-changing extended s -wave, s^\pm and standard s -wave, or s^{++} . The two order parameters only differ by a relative sign on the electron pockets of the Fermi surface, and deciding between them thus requires a phase sensitive measurement of the superconducting order parameter in the entire Brillouin zone. This is rather challenging although progress has been made recently with a recent theoretical proposal by Hirschfeld *et al.* [25] relying on the temperature dependence of certain quasiparticle interference data. This method was used in determining the relative sign of the electron and hole pockets in FeSe in favour of an s^\pm order parameter [15]. Theoretically, an s^\pm order parameter is obtainable from a pairing mediated by magnetic fluctuations [24]. An s^{++} order parameter on the other hand is constant in momentum space and does not arise from repulsive interactions [38].

The parent compounds for the iron-based superconductors are metals typically exhibiting an SDW magnetic stripe order. Such magnetic order is well-described both by localised and itinerant electrons and both are applied in the literature. In localised models the starting point is typically a $J_1 - J_2$ or $J_1 - J_2 - K$ effective spin-Hamiltonian [39, 40], where J_1 and J_2 are respectively the nearest neighbour and next-nearest neighbour ex-

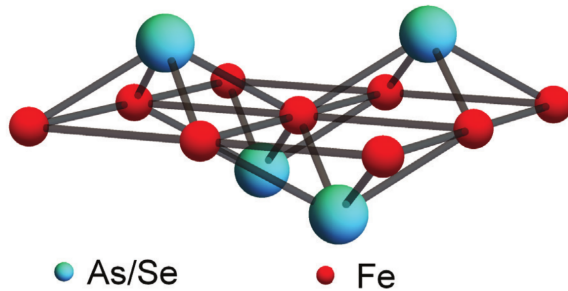


Figure 1.1: Structure of the Fe-pnictide or Fe-chalcogenide planes showing the puckering of the pnictogen (As) or chalcogen (Se) atoms in relation to the Fe-plane. Figure from Ref. [37].

change couplings, and in general these depend on the orbital content. K is a biquadratic nearest neighbour coupling controlling the relative spin orientation. Calculations of the spin-wave spectra using such models yield qualitative agreement with observations but require unphysical values for the exchange couplings [41]. The localised models also have issues describing magnetic states where the magnetic moment vanishes on some sites, as observed in $\text{Sr}_{1-x}\text{Na}_x\text{Fe}_2\text{As}_2$ [35].

The mass renormalisation factors of a number of FeSC have been evaluated within dynamical mean-field theory (DMFT) indicating that some compounds are more strongly correlated than others evidenced by their comparatively large mass renormalisation factors [12]. Itinerant models are thus more likely to be applicable to the compounds with smaller mass renormalisation factors, such as 1111 and 122, while the 11 materials should be approached with more caution, and are more likely described by a combination of itinerant and localised electrons. The multi-orbital nature of the FeSC furthermore implies that the various orbitals are correlated to different degrees [14]. Within a slave-spin approximation this leads to the formation of orbitally selective Mott phases in which some orbitals exhibit itinerant behaviour while others remain completely localised [13, 14, 42]. In this thesis we shall not make this distinction and we remain within the itinerant scenario throughout.

Within the itinerant scenario SDW magnetic order is a consequence of a nested Fermi surface with nesting vectors $(\pi, 0)/(0, \pi)$. Two distinct nesting vectors imply the existence of two magnetic order parameters, \mathbf{M}_1 and \mathbf{M}_2 , with ordering vectors $(\pi, 0)$ or $(0, \pi)$ and depending on the details of the band structure these order parameters will either compete or coexist. The dominant magnetic phase both experimentally and theoretically [19, 24] is the $(\pi, 0)/(0, \pi)$ magnetic stripe where the magnetic moments are oriented antiferromagnetically along one direction and ferromagnetically along the other (see inset in Fig. 1.2), although more recent observations find tetragonal magnetic phases in a number of hole-doped compounds [32–35]. The choice of either $(\pi, 0)$ or $(0, \pi)$ is associated with a breaking of a discrete \mathbb{Z}_2 symmetry resulting in a preemptive electronic-nematic order [43]¹. The origin of this symmetry breaking is challenging to determine as any breaking of rotational

¹Note that the term electronic-nematic usually refers to the breaking of a discrete rotational symmetry unlike nematic liquid crystals which break a continuous rotational symmetry.

symmetry implies a splitting of the xz/yz orbital degeneracy and an orthorhombic distortion. Conversely, due to linear couplings in the free energy, several mechanisms can be responsible for the breaking of rotational symmetry. The phonon-driven orthorhombic distortion can be the primary transition, with the spin- or charge-driven nematic and orbital order transitions being secondary. In contrast, both the splitting of the xz and yz orbitals, and the choice of magnetic ordering vector can be attributed to electronic degrees of freedom. Orbital (charge) fluctuations can drive an instability in the orbital occupations such that $\langle n_{xz} - n_{yz} \rangle \neq 0$, in the literature known as orbital order [44,45]. On the other hand, spin fluctuations are capable of breaking the \mathbb{Z}_2 symmetry by becoming anisotropic such that $\langle \mathbf{M}_1^2 - \mathbf{M}_2^2 \rangle \neq 0$ while still satisfying $\langle \mathbf{M}_1 \rangle = \langle \mathbf{M}_2 \rangle = 0$, i.e. there is no magnetic order and translational symmetry is unbroken [46,47].

The orthorhombic distortion is on the order of 1% [48], however measurements of the resistivity anisotropy in detwinned $\text{Ba}(\text{Co}_x\text{Fe}_{1-x})_2\text{As}_2$ crystals reveal a much larger difference between the resistivities along a and b directions, and find that the resistivity along the shorter b axis is greater [49]. While not direct evidence for an electronically driven mechanism, the large electronic response is certainly indicative of the importance of electrons in the formation of the symmetry-broken phase. Later measurements of the nematic susceptibility in $\text{Ba}(\text{Co}_x\text{Fe}_{1-x})_2\text{As}_2$ [50] indicate that this exhibits Curie-Weiss behaviour around the structural transition and provides more concrete evidence that the initial symmetry breaking is driven by electronic degrees of freedom.

The so-called spin-nematic scenario is in agreement with many experimental observations [24, 35, 51–53], however the presence of an orthorhombic phase in FeSe, a material without long-range magnetic order, has been interpreted in favour of the orbital scenario [54]. Moreover, observations on FeSe indicate that the orbital order $\langle n_{xz} - n_{yz} \rangle \neq 0$ has a non-trivial structure factor, and changes sign between hole and electron pockets [55]. Several scenarios explaining this apparent discrepancy between FeSe and other FeSC have been put forth. It has been shown that including nearest neighbour Coulomb interactions can account for the formation of a nematic phase in the absence of a magnetic state [56] and so can the smallness of the Fermi pockets [57]. We will return to the subject of spin-driven nematic order below and in Chapter 3.

A multitude of models have been applied to understand the iron-based superconductors, ranging from simple band models devoid of orbital structure to multiorbital models with a large number of hopping parameters. Before we delve into a description of these models however, we consider the formation of magnetic order in the iron-based superconductors. A natural starting point for the study of magnetic order is the Ginzburg-Landau expansion for the magnetic free energy. The free energy functional is entirely determined by the point group symmetries of the system; for the iron-based superconductors the relevant expression, up to fourth order, is

$$\begin{aligned} \mathcal{F}[\mathbf{M}_1, \mathbf{M}_2] = & \sum_q \left[U^{-1} - \chi_0(q) \right] \mathbf{M}(q)^2 \\ & + \frac{u}{2} \left(\mathbf{M}_1^2 + \mathbf{M}_2^2 \right)^2 - \frac{g}{2} \left(\mathbf{M}_1^2 - \mathbf{M}_2^2 \right)^2 + 2w \left(\mathbf{M}_1 \cdot \mathbf{M}_2 \right)^2 \end{aligned} \quad (1.1)$$

in the absence of spin-orbit coupling. The generalisation to a case including spin-orbit

coupling is considered in Chapter 2. In the quartic and higher-order terms we assume that the order parameters are momentum-independent and we will return to this assumption shortly. Hence we denote \mathbf{M}_1 as the magnetic order parameter with modulation along $\mathbf{Q}_1 = (\pi, 0)$ while \mathbf{M}_2 is modulated along $\mathbf{Q}_2 = (0, \pi)$. Generally, \mathbf{Q}_1 and \mathbf{Q}_2 are the values for which $\chi_0(\mathbf{Q}_{1,2}) = U^{-1}$. U is the local Hubbard repulsion and $\chi_0(q)$ is the bare magnetic susceptibility, where q is a four-vector $q = (\omega, \mathbf{q})$. Naive minimisation suggests that magnetic order occurs when the second order coefficient changes sign, and it would seem magnetic order can occur simply by lowering temperature until $\chi_0(\mathbf{q}, \omega = 0) = U^{-1}$. This, however, is an oversimplified conclusion since the effects of order parameter fluctuations have been neglected. Including these will suppress the transition temperature or, if the dimensionality of the system is too small, even prevent finite-temperature order entirely. This is the content of the Mermin-Wagner theorem, in one- or two-dimensional systems thermal fluctuations prevent the condensation of any order parameter whose finite expectation value breaks a continuous symmetry². Capturing the order parameter fluctuations requires the inclusion of higher-order contributions to the free energy. The fourth order coefficients govern the fluctuations of the order parameters and determine the symmetry of the magnetic order at the transition temperature and slightly below. As the magnetic order parameter increases, higher-order terms become important, ultimately resulting in an expression containing contributions at all orders in \mathbf{M} along with an infinite hierarchy of equations governing the feedback of fluctuations on the magnetic order. Here we will only include the lowest order corrections from the fluctuations as these are sufficient to describe both the complete suppression of magnetic order in two-dimensional systems and the occurrence of so-called preemptive orders which result from breaking a discrete symmetry (and are therefore allowed to order in two dimensions).

From the free energy it is evident that three different magnetic orders are possible depending on the signs and relative magnitude of g and w . Positive g generally favours a single- \mathbf{Q} phase where only \mathbf{M}_1 or \mathbf{M}_2 is non-zero. However, for sufficiently negative w such that $|w| > g$ coexistence of \mathbf{M}_1 and \mathbf{M}_2 is favoured, resulting in a state where $\mathbf{M}_1 \parallel \mathbf{M}_2$. If g is negative coexistence is also favoured and the sign of w decides the relative alignment of \mathbf{M}_1 and \mathbf{M}_2 with $\mathbf{M}_1 \perp \mathbf{M}_2$ for positive w . Here we follow standard conventions and denote the state with e.g. $\mathbf{M}_1 \neq 0$ and $\mathbf{M}_2 = 0$ (or vice versa) as a magnetic stripe (MS), for $\mathbf{M}_1 \parallel \mathbf{M}_2$ we use charge-spin-density-wave (CSDW) and designate $\mathbf{M}_1 \perp \mathbf{M}_2$ as the spin-vortex-crystal (SVC) phase. The phase diagram summarising the points above is depicted in Fig. 1.2.

Within a specific microscopic model the coefficients of the free energy can be evaluated and the magnetic ground state determined. The free energy will play a central part in our studies of the FeSC allowing us to study in detail the doping dependence of the magnetic order, see Sec. 1.3, but also the formation of a preemptive nematic order, see Chapter 3. Extensions of the above expression also permit us to study both the formation of incommensurate magnetic order (Sec. 1.4) and the effect of spin-orbit coupling on the orientation of the magnetic moments (Chapter 2). With the free energy playing such

²In one-dimensional systems zero-temperature quantum fluctuations ensure that the order parameter does not condense even at zero temperature.

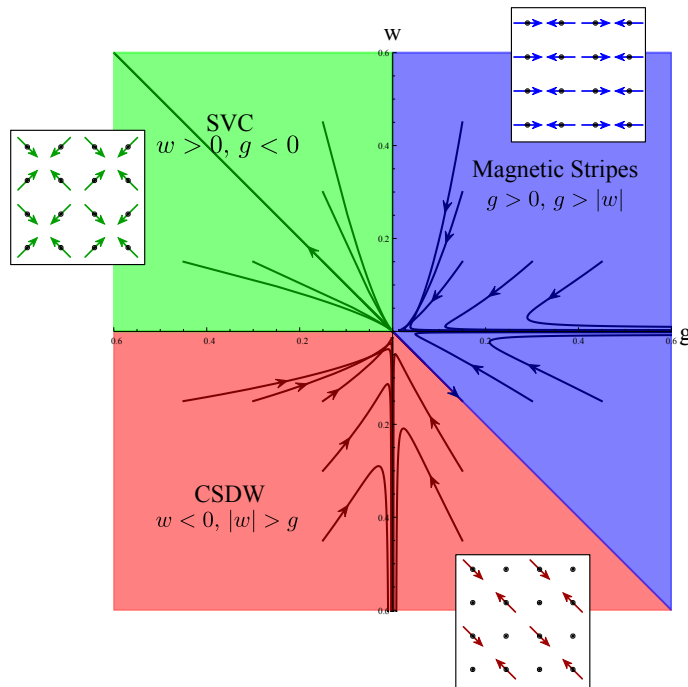


Figure 1.2: Mean-field phase diagram with flows of the quartic coefficients superimposed. The colours denote the various phases obtained from mean-field calculations while the arrows show the flow of the quartic coefficients under the renormalisation group (RG), described in Sec. 1.1. Note that the flows remain within their respective phases and the mean-field phase diagram is stable under the RG flow.

a prominent role we briefly consider the behaviour of the quartic coefficients under a renormalisation group flow to show that the mean-field phase diagram is stable against the fluctuations of the high-energy order parameter fluctuations.

1.1 Renormalisation Group Flow of Quartic Coefficients

In the expression for the free energy above, the quartic terms were assumed to be momentum-independent. Allowing for a momentum-dependence can lead to a renormalisation of the coefficients and the question is whether this renormalisation leaves the mean-field phase diagram unaltered. To answer this we perform a momentum-shell renormalisation group (RG) analysis which elucidates the effects of the high-energy order parameter fluctuations upon the low-energy sector that we typically study. We achieve this by assuming that the quartic interactions are local in space such that the quartic term in the free energy (in real space) reads

$$\mathcal{F}^{(4)}[\mathbf{M}_1, \mathbf{M}_2] = \frac{u}{2} \int_x (\mathbf{M}_1^2 + \mathbf{M}_2^2)^2 - \frac{g}{2} \int_x (\mathbf{M}_1^2 - \mathbf{M}_2^2)^2 + 2w \int_x (\mathbf{M}_1 \cdot \mathbf{M}_2)^2 \quad (1.2)$$

The local nature of the interactions implies that high-momentum fluctuations impact low-momentum ones and vice versa. To quantify this effect we write the free energy

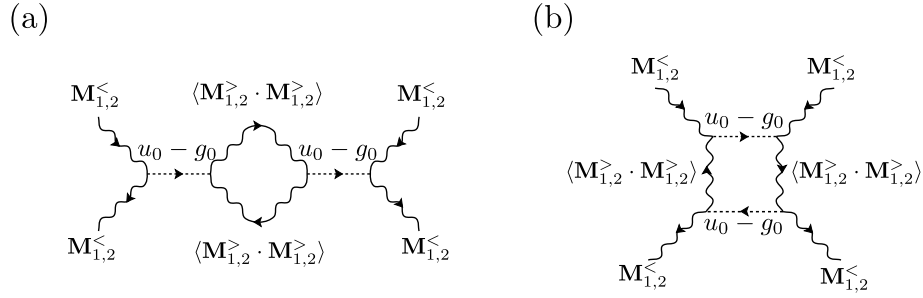


Figure 1.3: A subset of the diagrams contributing to the renormalisation of u , g and w . The diagrams shown here both contribute to u and g . The loop in (a) contributes an additional factor of N due to the sum over components of the magnetic order parameter.

in momentum-space and define

$$\mathbf{M}(\mathbf{k}) \equiv \begin{cases} \mathbf{M}^{<}(\mathbf{k}) & \text{for } 0 < \mathbf{k} < \Lambda/\ell \\ \mathbf{M}^{>}(\mathbf{k}) & \text{for } \Lambda/\ell < \mathbf{k} < \Lambda \end{cases} \quad (1.3)$$

where Λ is the UV-cutoff and $\ell > 1$ [58]. With these definitions we obtain the partition function

$$Z = \int \mathcal{D}[\mathbf{M}_1^{<}, \mathbf{M}_2^{<}] e^{-S^{<}} \langle e^{-S_{\text{int}}} \rangle \quad (1.4)$$

with S_{int} the action describing interactions between high- and low-momentum modes and $S^{<}$ ($S^{>}$) is the action describing the free low-momentum (high-momentum) modes. The presence of the high-momentum degrees of freedom alters the interactions between the low-momentum modes through a renormalization of the coupling constants, and integrating out the high-momentum modes results in equations describing the flow of the free energy coefficients towards a fixed point describing the low-energy physics. $\langle e^{S_{\text{int}}} \rangle$ is expressed in terms of a cumulative expansion up to second order i.e.

$$\langle e^{S_{\text{int}}} \rangle \approx e^{-\langle S_{\text{int}} \rangle + \frac{1}{2}(\langle S_{\text{int}}^2 \rangle - \langle S_{\text{int}} \rangle^2)}, \quad (1.5)$$

and the term of interest is $\langle S_{\text{int}}^2 \rangle$, which yields the one-loop renormalisation of four-point vertices by the high-momentum modes. A representative subset of the contributing diagram is depicted in Fig. 1.3. The RG flow equations are obtained by evaluating such diagrams, and we assume that we are at the quantum critical point implying that the dynamic critical exponent $z = 2$ and the effective dimensionality is thus $d_{\text{eff}} = 4$. In this case the wave-function does not renormalise and we can furthermore ignore the finite momentum transfer in the one-loop diagrams [59]. The resulting flow equations are

$$\frac{du}{dt} = -4(N+4)u^2 - 8wu - 8w^2 + 8ug - 8g^2, \quad (1.6)$$

$$\frac{dw}{dt} = -4(N+2)w^2 - 24wu - 8wg, \quad (1.7)$$

$$\frac{dg}{dt} = 4(N+2)g^2 + 8gw - 24gu, \quad (1.8)$$

1.2 Modeling the Iron-based Superconductors

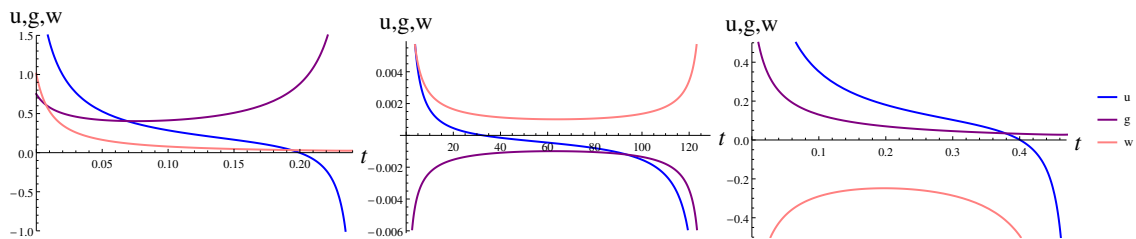


Figure 1.4: Flows of the quartic coefficients in the striped case (left), SVC case (middle) and CSDW case (right). In all three cases u flows to a negative value signalling that the magnetic transition is first order.

where $t \equiv \log \ell$ and N is the number of components of the magnetic order parameter which was left unspecified for completeness. Below we shall confine attention to the $N = 3$ case. These equations were studied for a specific set of initial conditions in Ref. [47] and more recently the influence of superconductivity was considered in Ref. [60].

We here consider the fixed points and trajectories of Eqs. (1.6)-(1.8). This is most easily achieved by defining $\tilde{u} \equiv u/g$ and $\tilde{w} \equiv w/g$ and consider the corresponding equations for \tilde{u} , \tilde{w} and g . This reveals the fixed points

$$\tilde{w} = 0 \quad \tilde{w} = -1 \quad \tilde{w}^{-1} = 0. \quad (1.9)$$

Note that these points correspond to fixed trajectories for the original coefficients. Analysing the stability of the various fixed points reveals that $\tilde{w} = 0$ is stable for $g > 0$ and unstable for $g < 0$. The fixed trajectory at $\tilde{w}^{-1} = 0$ is however unstable for $w > 0$ but stable for $w < 0$ while the trajectory $\tilde{w} = -1$ is unstable for $g > 0$ and stable for $g < 0$. To each stable fixed point we can associate a basin of attraction corresponding to a specific magnetic order. From the above analysis we find that the basin of attraction corresponding to the fixed trajectory $w/g = -1$ is thus given by $w > 0$ and $g < 0$, thus corresponding to the SVC phase. For the fixed trajectory at $g/w = 0$, the basin of attraction is given by $w > 0$ and $-w < g$, implying CSDW magnetic order. The basin of attraction belonging to the fixed trajectory at $w/g = 0$ is given by $g > 0$ and $g > -w$, yielding magnetic stripes. As the fixed lines bounding the various basins of attraction correspond exactly to the phase boundaries in the mean-field phase diagram, we see that the mean-field phase diagram remains stable under the RG flow. These conclusions are supported by the numerical solution of Eqs. (1.6)-(1.8) resulting in the flows depicted in Fig. 1.2. In general u flows to a negative value (Fig. 1.4) implying that the magnetic transition is first order.

With these simple facts established we now proceed to consider the various models used in describing the FeSC, ranging from simple band models to complicated multiorbital models.

1.2 Modeling the Iron-based Superconductors

The Fermi surface for most iron-based compounds consists of two hole pockets at the Γ point and two electron pockets at respectively the X and Y points, and, in e.g. LaFeAsO,

1.2 Modeling the Iron-based Superconductors

a hole pocket at the M point [61–63] (in the 1Fe/unit cell). Early studies approximated this Fermi surface by a three-band model where the two hole pockets at Γ are merged and the orbital content of the bands is ignored [64]. Cvetkovic and Vafeek [65] went beyond the simple band picture and used the orbitals with dominant weight at the high-symmetry points, Γ , X, and Y, as a starting point for a $\mathbf{k} \cdot \mathbf{p}$ -expansion. This results in a model with t_{2g} -orbital content and provides a controlled way of adding a spin-orbit coupling. In Chapter 2 we apply this model and show that a finite spin-orbit coupling can account for the reorientation of magnetic moments observed in the C_4 -phase of some hole-doped FeSC [32–35]. However, to more accurately describe the physics of the FeSC, more realistic models rely on tight-binding fits to density-functional-theory (DFT) calculations using five-band models [66,67]. Such calculations neglect the effects of correlations, although in most cases performing a suitable rescaling of the effective masses roughly reproduces the band structure as observed by e.g. angular-resolved photo emission spectroscopy (ARPES) [68]. An additional complication arises from the puckering of the pnictogen or chalcogen atoms, as seen in Fig. 1.1. This increases the size of the unit cell to include two Fe atoms. However, in the absence of spin-orbit coupling there is a glide-plane symmetry [65, 69] which relates the single Fe atom unit cell with an atom puckered above the plane, to one with an atom puckered below the plane, implying that a unit cell containing a single Fe atom is sufficient. Both 1Fe/unit cells and 2Fe/unit cells are applied in the literature, and throughout this thesis we will work in the 1Fe/unit cell. Below we briefly review the predictions and limitations of a number of common models for the FeSC. A succinct overview is given in Ref. [37].

1.2.1 Minimal models

A good starting point for the study of the iron-based superconductors is a three-band model with a single hole pocket at the Γ -point and electron pockets at the X- and Y-points. The Fermi surface for such a model is depicted in Fig. 1.5 and allows itinerant magnetism with wavevector $(\pi, 0)/(0, \pi)$ to form due to nesting between hole and electron pockets. Such models have been widely studied [47, 64, 70, 71] and the presentation here will be rather rudimentary and serves chiefly as motivation and context for introducing the more complicated multi-orbital models.

The bandstructure given by

$$\varepsilon_{\Gamma, \mathbf{k}} = \epsilon_0 - \frac{\mathbf{k}^2}{2m} - \mu \quad (1.10)$$

$$\varepsilon_{X, \mathbf{k}} = -\epsilon_0 + \frac{k_x^2}{2m_x} + \frac{k_y^2}{2m_y} - \mu \quad (1.11)$$

$$\varepsilon_{Y, \mathbf{k}} = -\epsilon_0 + \frac{k_x^2}{2m_y} + \frac{k_y^2}{2m_x} - \mu \quad (1.12)$$

enacts the Fermi surface exhibited in Fig. 1.5. Since these models are designed with the goal of capturing the Fermi surface, they are inapt at describing phenomena relying on the formation of finite-energy electron-hole pairs. On the other hand these models are very well suited to capture effects related to the topology of the Fermi surface, although

1.2 Modeling the Iron-based Superconductors

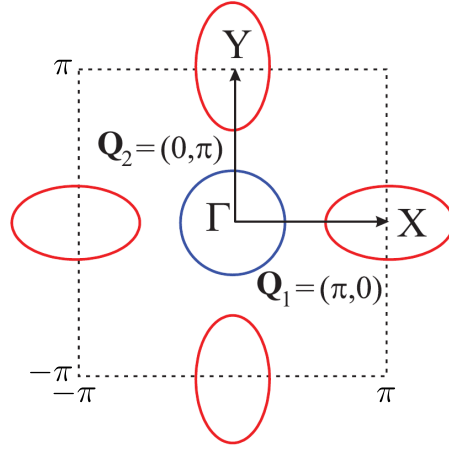


Figure 1.5: Fermi surface of the three-band model given in Eqs. 1.10–1.12. Magnetism is driven by nesting between the hole pocket at Γ and the electron pockets at X and Y. Figure from Ref. [47].

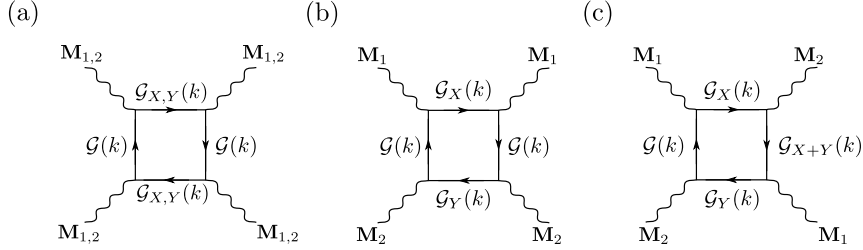


Figure 1.6: Illustration of the Feynman diagrams contributing to the quartic coefficients of the free energy. The diagrams in (a) and (b) contribute to both u and g while the diagram in (c) is equivalent to w . Note that the diagram in (c) is subleading since there is no pocket at the M point in the three-band model. Details can be found in Chapter 2.

the lack of orbital character can in some instances lead to wrong results, as we shall see below. Using the dispersion above we can evaluate the coefficients of the free energy and thus determine the symmetry of the magnetic order parameter. The quartic coefficients are determined by the diagrams shown in Fig. 1.6 and are straightforward to evaluate (see Ref. [47]):

$$u = \frac{1}{2} \int_k \mathcal{G}_\Gamma(k)^2 (\mathcal{G}_X(k) + \mathcal{G}_Y(k))^2 \quad (1.13)$$

$$g = \frac{1}{2} \int_k \mathcal{G}_\Gamma(k)^2 (\mathcal{G}_X(k) - \mathcal{G}_Y(k))^2 \quad (1.14)$$

$$w = 0. \quad (1.15)$$

Here $k = (\mathbf{k}, \omega_n)$ where ω_n is a fermionic Matsubara frequency, $\int_k = T \sum_n \int \frac{d^d k}{(2\pi)^d}$ and $\mathcal{G}_\Gamma(k)$ is the Green function with momentum near the Γ point:

$$\mathcal{G}_\Gamma(k) = \frac{1}{i\omega_n - \xi_\Gamma(\mathbf{k})}. \quad (1.16)$$

Note that w vanishes due to the lack of a pocket at the M point in this model as this implies that the propagator $\mathcal{G}_{X+Y}(k)$ is off-shell. Further details concerning this result

1.2 Modeling the Iron-based Superconductors

are given in Chapter 2. A positive g points to a stripe phase and as was shown in the preceding section, the mean-field phase diagram is stable under the RG flow. While u in general flows to negative values under the RG flow, the bare value of u is positive and the expansion of the free energy to quartic order is well-defined. Taking into account interactions between the pockets can lead to a different sign of g and give a non-zero value for w . We note however, that w in general turns out to be positive (see Ref. [47]) resulting in a tetragonal SVC phase if g is negative. This proves a problem for the model since the C_4 phases observed so far in experiments are CSDW, implying a negative w . In this case the missing orbital character of the Fermi surface offers an explanation since unrestricted Hartree-Fock calculations reproduce a CSDW phase [72] and, as is shown below, taking into account orbital content results in a negative w . The addition of disorder has also been shown to favour the CSDW phase [73].

The simplicity of the model allows us to go beyond mean-field theory and include fluctuations when considering the onset of magnetic order. To achieve this we start from the free energy Eq. 1.1 and introduce additional fields corresponding to the Gaussian (ψ) and nematic (ϕ) fluctuations [47]:

$$\psi = \mathbf{M}_1^2 + \mathbf{M}_2^2, \quad (1.17)$$

$$\phi = \mathbf{M}_1^2 - \mathbf{M}_2^2, \quad (1.18)$$

where we have assumed that $w = 0$ such that the corresponding fluctuation field can be neglected. Performing a Hubbard-Stratonovich decoupling in these two fields and applying the large- N approximation we can derive equations of motions for the remaining fields:

$$\frac{\psi}{u} = \int_q \frac{r_0 + \psi + q^2}{(r_0 + \psi + q^2)^2 - \phi^2}, \quad (1.19)$$

$$\frac{\phi}{g} = \int_q \frac{\phi}{(r_0 + \psi + q^2)^2 - \phi^2}, \quad (1.20)$$

where we ignored contributions from a finite Matsubara frequency. In these equations, r_0 is the distance from the quantum critical point, i.e. the quadratic coefficient for momentum independent order parameters and q is the momentum. These were solved in Ref. [47] where it was shown that the feedback of fluctuations upon the magnetic order suppresses the magnetic transition to zero temperature in 2d, in agreement with the Mermin-Wagner theorem. More interestingly, nematic order onsets at a finite temperature, even in 2d. Note that this is not prohibited by the Mermin-Wagner theorem, since nematic order is a consequence of the spontaneous breaking of a discrete symmetry (the critical dimension for discrete symmetries is $d_c = 1$). In 3d, magnetism sets in at a finite temperature and occurs simultaneously with a nematic transition. As the iron-based superconductors are layered materials, the experimentally relevant scenario is somewhere in between the 2d and 3d cases. In Ref. [47] both the $d = 2.5$ case and the case with an anisotropic dispersion were considered and the conclusions are qualitatively the same. As a function of u/g three separate regimes are found. For low u/g the magnetic and nematic transitions are simultaneous and first order, while for intermediate values the transitions split and the magnetic transition becomes second order. For higher values both transitions become second order. Further details can be found in Ref. [47].

1.2 Modeling the Iron-based Superconductors

If one is interested in establishing the appearance of a nematic phase, one can consider the nematic susceptibility [74]

$$\chi_{\text{nem}} = \frac{\int_q \chi_{\text{mag}}(q)^2}{1 - g \int_q \chi_{\text{mag}}(q)^2}, \quad (1.21)$$

where $\chi_{\text{mag}}(q)$ is the magnetic propagator

$$\chi_{\text{mag}}(q) = U^{-1} - \chi_0(q) \quad (1.22)$$

and U the spin-spin interaction. In the spin-nematic scenario the nematic susceptibility can be found from summing an infinite series of Aslamazov-Larkin diagrams [75] or equivalently by introducing a conjugate field to the nematic order parameter ϕ and taking functional derivatives [47], a method outlined in the appendix of Chapter 3 (for the multi-orbital case). In the work presented in Chapter 3 we consider the generalisation of nematic susceptibility to multi-orbital models and show that such models also exhibit preemptive nematic phases.

1.2.2 Hybrid models

Extending the band models above to include some orbital character results in so-called hybrid models. These models can be rigorously justified using group-theoretical arguments. Cvetkovic and Vafek [65] carried out a thorough analysis of the crystallographic space group $P4/nmm$ and its associated point group D_{4h} relevant for a large number of the iron-based compounds. In effect, the resulting Hamiltonian can be considered a result of a $\mathbf{k} \cdot \mathbf{p}$ -expansion and is thus valid in the vicinity of the high-symmetry points. At the Γ -point the xz and yz orbitals are degenerate and the $\mathbf{k} \cdot \mathbf{p}$ -expansion can be performed in a basis of these two orbitals. Similarly, at the X (Y) point the yz (xz) and xy orbitals are dominant and an appropriate low-energy basis can be constructed from these two orbitals. We thus find the Hamiltonian

$$H_0(\mathbf{k}) = \begin{pmatrix} h_Y(\mathbf{k}) & 0 & 0 \\ 0 & h_X(\mathbf{k}) & 0 \\ 0 & 0 & h_\Gamma(\mathbf{k}) \end{pmatrix} \quad (1.23)$$

written in the basis

$$\Psi_{\mathbf{k}} = \begin{pmatrix} \psi_{Y,\mathbf{k}} \\ \psi_{X,\mathbf{k}} \\ \psi_{\Gamma,\mathbf{k}} \end{pmatrix}. \quad (1.24)$$

1.2 Modeling the Iron-based Superconductors

Here

$$h_{\Gamma}(\mathbf{k}) = \begin{pmatrix} \epsilon_{\Gamma} + 2\frac{\mathbf{k}^2}{2m_{\Gamma}} + b(k_x^2 - k_y^2) & 4ck_xk_y \\ 4ck_xk_y & \epsilon_{\Gamma} + 2\frac{\mathbf{k}^2}{2m_{\Gamma}} - b(k_x^2 - k_y^2) \end{pmatrix} \otimes \sigma^0 \quad (1.25)$$

$$h_X(\mathbf{k} + \mathbf{Q}_1) = \begin{pmatrix} \epsilon_1 + 2\frac{\mathbf{k}^2}{2m_1} + a_1(k_x^2 - k_y^2) & -iv_X(\mathbf{k}) \\ iv_X(\mathbf{k}) & \epsilon_3 + 2\frac{\mathbf{k}^2}{2m_3} + a_3(k_x^2 - k_y^2) \end{pmatrix} \otimes \sigma^0 \quad (1.26)$$

$$h_Y(\mathbf{k} + \mathbf{Q}_2) = \begin{pmatrix} \epsilon_1 + 2\frac{\mathbf{k}^2}{2m_1} - a_1(k_x^2 - k_y^2) & -iv_Y(\mathbf{k}) \\ iv_Y(\mathbf{k}) & \epsilon_3 + 2\frac{\mathbf{k}^2}{2m_3} - a_3(k_x^2 - k_y^2) \end{pmatrix} \otimes \sigma^0 \quad (1.27)$$

with

$$v_X(\mathbf{k}) = 2vk_y + 2p_1k_y(k_y^2 + 3k_x^2) - 2p_2k_y(k_x^2 - k_y^2) \quad (1.28)$$

$$v_Y(\mathbf{k}) = -2vk_x - 2p_1k_x(k_x^2 + 3k_y^2) - 2p_2k_x(k_x^2 - k_y^2), \quad (1.29)$$

and the basis spinors of Eq. 1.24 are defined near the Γ , X and Y points respectively, such that e.g.

$$\psi_{X,\mathbf{k}+\mathbf{Q}_1} = \begin{pmatrix} c_{yz,\mathbf{k}+\mathbf{Q}_1\uparrow} \\ c_{xy,\mathbf{k}+\mathbf{Q}_1\uparrow} \\ c_{yz,\mathbf{k}+\mathbf{Q}_1\downarrow} \\ c_{xy,\mathbf{k}+\mathbf{Q}_1\downarrow} \end{pmatrix}. \quad (1.30)$$

In these expressions the constants are free parameters which can be chosen to best fit the results of DFT calculations. This Hamiltonian presented in the preceding equations is studied in detail in Chapter 2 where we seek to explain the reorientation of magnetic moments observed in the tetragonal magnetic phase in $\text{Ba}_{1-x}\text{Na}_x\text{Fe}_2\text{As}_2$ [51] and later in other 122 compounds [32–35]. An illustration of the Fermi surface for a specific choice of parameters based on Ref. [76] is presented in Fig. 2.2. The model above exhibits spin-rotational symmetry and to address the issue of reorientation the spin-rotational invariance should be broken. This is achieved by introducing a spin-orbit coupling, which was also considered by Cvetkovic and Vafeek in Ref. [65]. By taking into account the non-symmorphic nature of P4/nmm they extended the group-theoretical analysis to also account for a finite spin-orbit coupling. In the vicinity of the high-symmetry points, the leading terms in the spin-orbit Hamiltonian are \mathbf{k} -independent and due to the smallness of spin-flip hopping parameters compared to non-spin-flip hopping parameters we can neglect \mathbf{k} -dependent terms. Hence the resulting spin-orbit term is identical to the atomic spin-orbit coupling following from evaluating $\mathbf{L} \cdot \mathbf{S}$ in the basis of cubic harmonics:

$$\mathcal{H}_{\text{SOC}} = \sum_{\mathbf{k}} \Psi_{\mathbf{k}}^{\dagger} H_{\text{SOC}}(\mathbf{k}) \Psi_{\mathbf{k}}, \quad (1.31)$$

1.2 Modeling the Iron-based Superconductors

with

$$H_{\text{SOC}}(\mathbf{k}) = \begin{pmatrix} 0 & h_M^{\text{SOC}}(\mathbf{k}) & 0 \\ (h_M^{\text{SOC}}(\mathbf{k}))^\dagger & 0 & 0 \\ 0 & 0 & h_\Gamma^{\text{SOC}}(\mathbf{k}) \end{pmatrix} \quad (1.32)$$

$$h_\Gamma^{\text{SOC}}(\mathbf{k}) = \frac{1}{2}\lambda(\tau^y \otimes \sigma^z), \quad (1.33)$$

$$h_M^{\text{SOC}}(\mathbf{k}) = \frac{i}{2}\lambda(\tau^+ \otimes \sigma^x + \tau^- \otimes \sigma^y), \quad (1.34)$$

where λ is the spin-orbit coupling, $\tau^\pm = \frac{1}{2}(\tau^0 \pm \tau^z)$, and we have ignored the e_g orbitals. These results are derived in Appendix 2.A and 2.B where we carry out a $\mathbf{k} \cdot \mathbf{p}$ -expansion of a five-orbital model and show that, to third order in \mathbf{k} , the Hamiltonian around Γ , X and Y only includes xz , yz and xy and has a structure identical to the one provided above.

1.2.3 Multi-orbital models

While the above models have the advantage of being rather simple and even provide analytical answers in some cases, they rely on rather significant approximations. The minimal models tend to neglect the orbital character of the bands they describe, and while hybrid models remedy this to an extent, these are still based on $\mathbf{k} \cdot \mathbf{p}$ expansions around the high-symmetry points of the Brillouin zone. The last family of models we will consider goes beyond these approximations and include the orbital character of the entire bandstructure. These models are generally constructed from tight-binding fits to DFT calculations [66]. It has been shown that neither the two- nor three-orbital models [10, 11] correctly capture all the relevant low-energy physics [37]. The two-orbital models invariably break the glide-plane symmetry, i.e. a translation through $(\frac{a}{2}, \frac{a}{2})$ followed by a mirror reflection in the xy -plane [65]. Since the three t_{2g} -orbitals are dominant at the Fermi surface, one would believe that a three-orbital model containing xz , yz and xy would be able to describe the low-energy physics and here the issue is indeed a bit more subtle. The three-orbital models correctly reproduce the hole pockets at Γ and the electron pockets at X and Y, however, an additional hole pocket with xz/yz character is present at the M point, in addition to a hole pocket with xy character [37]. By changing the tight-binding parameters one can remove both pockets at M, which is also not desirable since some materials indeed exhibit an xy hole pocket at M. Taking into account the hybridisation between the t_{2g} and e_g orbitals removes the xz/yz hole pocket at M [57, 65, 77]. With the addition of the two e_g orbitals, $x^2 - y^2$ and z^2 , one is able to reproduce the experimental Fermi surfaces, however this comes at the cost of having rather complex five-orbital models referencing all the Fe d -orbitals. The five-orbital models can be constructed from tight-binding fits to DFT calculations and often involve several neighbour hoppings to achieve a good fit. Another complication arises from the fact that the crystallographic unit cell contains two Fe-atoms, due to the puckering of the pnictogens or chalcogens. Hence, fitting the result of DFT calculations typically requires 10 orbitals from which the five-orbital models are constructed by folding the 2Fe/unit cell to a 1Fe/unit cell. This subtlety plays a role if one wishes to include the effects of spin-orbit coupling, in which case one has to work

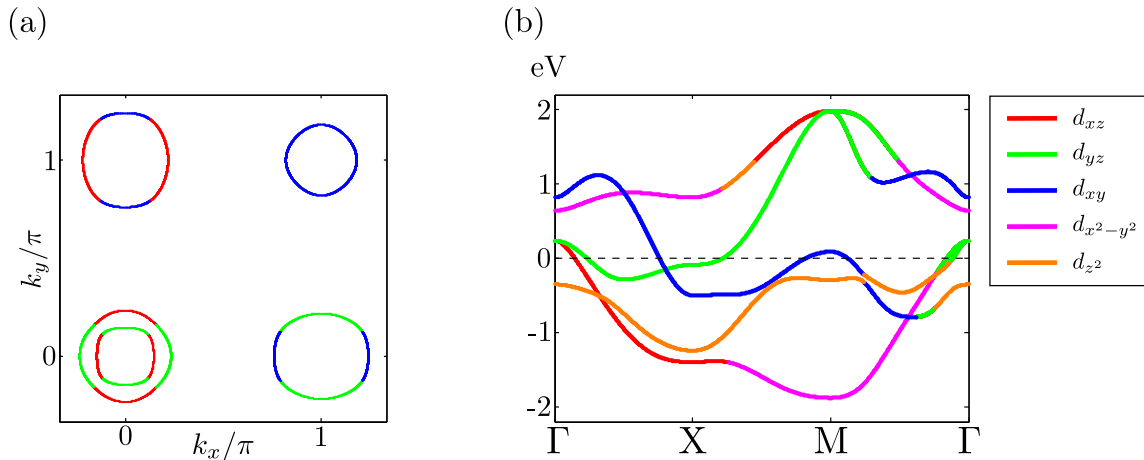


Figure 1.7: Fermi surface and bandstructure for the five-orbital model used in this thesis. The filling here is $\langle n \rangle = 6$. Like in the three-band case, magnetism is driven by the nesting between the hole pockets at Γ and the electron pockets at X and Y, although in this case the orbital content plays an important role, as we will see below.

with the full 10 orbital models. Since we will not seek to include spin-orbit effects in the multi-orbital models we shall not dwell further on this fact.

In orbital space we write the Hamiltonian as

$$\mathcal{H} = \sum_{\substack{\mathbf{k}\sigma \\ \mu\nu}} (\epsilon_{\mu\nu}(\mathbf{k}) - \mu\delta_{\mu\nu}) c_{\mathbf{k}\mu\sigma}^\dagger c_{\mathbf{k}\nu\sigma} + \mathcal{H}_{\text{int}}, \quad (1.35)$$

where the $\epsilon^{\mu\nu}(\mathbf{k})$ are the Fourier transforms of the input parameters from the fit to DFT calculations and \mathcal{H}_{int} describes the local interactions between electrons occupying different orbital and spin states:

$$\begin{aligned} \mathcal{H}_{\text{int}} = & U \sum_{\mu} n_{\mathbf{q}\mu\uparrow} n_{-\mathbf{q}\mu\downarrow} + U' \sum_{\mu < \nu} n_{\mathbf{q}\mu\sigma} n_{-\mathbf{q}\nu\sigma'} \\ & + \frac{J}{2} \sum_{\mu \neq \nu} c_{\mathbf{k}+\mathbf{q}\mu\sigma}^\dagger c_{\mathbf{k}\nu\sigma} c_{\mathbf{k}'-\mathbf{q}\nu\sigma'}^\dagger c_{\mathbf{k}'\mu\sigma'} + \frac{J'}{2} \sum_{\mu \neq \nu} c_{\mathbf{k}+\mathbf{q}\mu\sigma}^\dagger c_{\mathbf{k}'-\mathbf{q}\mu\bar{\sigma}}^\dagger c_{\mathbf{k}'\nu\bar{\sigma}} c_{\mathbf{k}\nu\sigma}. \end{aligned} \quad (1.36)$$

We will adopt the usual simplifying assumption that $U' = U - 2J$ and $J = J'$ although this relies on rotational invariance being unbroken and this is not strictly true in the presence of the crystal field caused by the nearby pnictogens or chalcogens. For the remainder of this work we shall adopt a specific multi-orbital tight-binding model by Ikeda *et al.* [61]. The Fermi surface for a filling of six electrons is shown in Fig. 1.7(a) and the bandstructure in Fig. 1.7(b).

The multi-orbital models with interactions provide a starting point for the study of both magnetic and superconducting instabilities. Within the fluctuation exchange approach one can obtain a superconducting pairing vertex and use e.g. the linearized gap equation or selfconsistent mean-field equations to determine the gap structure [72, 78], typically resulting in an order parameter with s^\pm symmetry. The occurrence of magnetism in multi-orbital systems has also been extensively studied within mean-field theory [72], capturing

1.3 Commensurate magnetic order

both the common magnetic stripe phase and the less common tetragonal magnetic phases as well as the low-energy excitations of these states [79]. At higher energies mean-field RPA tends to be less accurate and does not capture the spectral weight depletion found at higher frequencies by inelastic neutron scattering [80].

We here provide an alternative method of analysing the magnetic order, based on evaluating the coefficients of the free energy at the transition temperature. In the absence of orbital content the symmetry of the magnetic order parameter is determined by two numbers, g and w . When the magnetic order parameters acquire orbital content, so do the coefficients of the free energy, and the method outlined below takes this fact into account.

1.3 Commensurate magnetic order

In this part we study the occurrence of commensurate magnetism in the FeSC using an approach based on a minimisation of the free energy. This method, while only valid in the vicinity of a magnetic transition, has the advantage of being faster than more traditional selfconsistent mean-field studies, thus allowing for a more comprehensive study of the different parameter dependencies. To facilitate this, we adopt a parameterisation of the free energy slightly different from the one in Eq. 1.1. This is done in order to avoid the appearance of cross terms when generalising the free energy to orbital space and to ease comparison with the incommensurate case discussed in Sec. 1.4. Making the internal indices of the order parameters explicit we have

$$\begin{aligned}
\mathcal{F} &= \sum_{\mathbf{q}} \left((U^{-1})^{abcd} - \chi_0^{abcd}(\mathbf{q}) \right) \mathbf{M}^{ab}(\mathbf{q}) \mathbf{M}^{cd}(\mathbf{q}) \\
&+ \frac{1}{4} \left(\beta_1^{abcdefgh} \mathbf{M}_1^{ab} \cdot \mathbf{M}_1^{cd} \mathbf{M}_1^{ef} \cdot \mathbf{M}_1^{gh} + \beta_2^{abcdefgh} \mathbf{M}_2^{ab} \cdot \mathbf{M}_2^{cd} \mathbf{M}_2^{ef} \cdot \mathbf{M}_2^{gh} \right) \\
&+ \gamma^{abcdefgh} \mathbf{M}_1^{ab} \cdot \mathbf{M}_1^{cd} \mathbf{M}_2^{ef} \cdot \mathbf{M}_2^{gh} \\
&+ \omega^{abcdefgh} \mathbf{M}_1^{ab} \cdot \mathbf{M}_2^{cd} \mathbf{M}_1^{ef} \cdot \mathbf{M}_2^{gh}, \tag{1.37}
\end{aligned}$$

reflecting the fact that the order parameters have an orbital structure as well. Here U^{abcd} is a matrix comprised of the interaction parameters of the Hubbard-Hund interaction Hamiltonian (Eq. 1.36), whose exact form is provided in Eqs. (3.30)–(3.33) and $\chi_0^{abcd}(\mathbf{q})$ is the static bare spin-spin susceptibility

$$\chi_0^{abcd}(\mathbf{q}) = \sum_{nm\mathbf{k}} u_a^n(\mathbf{k} + \mathbf{q}) u_b^n(\mathbf{k} + \mathbf{q})^* u_c^m(\mathbf{k}) u_d^m(\mathbf{k})^* \frac{n_F(\xi_{\mathbf{k}}^m) - n_F(\xi_{\mathbf{k}+\mathbf{q}}^n)}{\xi_{\mathbf{k}+\mathbf{q}}^n - \xi_{\mathbf{k}}^m + i0^+}, \tag{1.38}$$

where the $u_a^n(\mathbf{k})$ are unitary matrices diagonalising the Hamiltonian in orbital space and $\xi^n(\mathbf{k})$ are the eigenenergies. Here we discuss a method to evaluate the quartic coefficients by writing the magnetic order parameters in terms of their irreducible representations and identifying which of these is the first to condense. This allows us to project the coefficients onto the appropriate irreducible representation. The decomposition in terms of irreducible representations also has the added benefit of providing an understanding of why specific orbital combinations appear together in the orbitally resolved magnetic order parameter.

The crystallographic space groups appropriate for the iron-based superconductors are either P4/nmm, for instance LaFeAsO, or I4/mmm, e.g. for BaFe₂As₂, and in both cases

1.3 Commensurate magnetic order

the relevant point group is D_{4h} . The absence of a spin-orbit coupling implies that the point group symmetries act separately on wavevector and orbital spaces, while spin space is inert. The relevant wavevectors are $\mathbf{Q}_X = (\pi, 0)$ and $\mathbf{Q}_Y = (0, \pi)$, which are located at the Brillouin zone boundary, such that $\mathbf{Q}_{X,Y} = -\mathbf{Q}_{X,Y}$. The relevant irreducible representations are A_{1g} , B_{1g} , A_{2g} and B_{2g} and at quadratic order A_{1g} and B_{1g} are degenerate, and so are A_{2g} and B_{2g} . This degeneracy is simply a manifestation of the inability of the quadratic term to distinguish between single- \mathbf{Q} and double- \mathbf{Q} states. The A_{1g}/B_{1g} correspond to a magnetic order parameter with the following orbital combinations having non-zero values (written in the basis $\{xz, yz, xy, x^2 - y^2, z^2\}$):

$$\mathbf{M}_{A_{1g}/B_{1g}} \sim \begin{pmatrix} M^{xz,xz} & & & & \\ & M^{yz,yz} & & & \\ & & M^{xy,xy} & & \\ & & & M^{x^2-y^2,x^2-y^2} & M^{x^2-y^2,z^2} \\ & & & M^{z^2,x^2-y^2} & M^{z^2,z^2} \end{pmatrix} \quad (1.39)$$

while for A_{2g}/B_{2g} the orbital composition is:

$$\mathbf{M}_{A_{2g}/B_{2g}} \sim \begin{pmatrix} & M^{xz,yz} & & & \\ M^{yz,xz} & & & & \\ & & & M^{xy,x^2-y^2} & M^{xy,z^2} \\ & & M^{x^2-y^2,xy} & & \\ & & M^{x^2-y^2,z^2} & & \end{pmatrix}. \quad (1.40)$$

As these different magnetic order parameters belong to different irreducible representations, they are mutually exclusive implying that certain orbital combinations never appear in tandem, at least not as a result of a transition from a paramagnetic phase.

As stated previously, our ultimate goal is to project the quartic coefficients onto the leading magnetic instability, which can be achieved in any representation. Hence, we write the magnetic order parameters as

$$\mathbf{M}_{1,2}^{ab} = \mathbf{M}_{1,2} v_{1,2}^{ab}, \quad (1.41)$$

where a, b label the internal structure of the order parameter in the chosen representation, e.g. orbital or irreducible, and this is determined entirely by the $v_{X,Y}^{ab}$. These, in turn, are found from the quadratic term in the free energy, which we refer to as the magnetic propagator, i.e.

$$\left(\chi_{\text{mag}}^{-1}(\mathbf{q})\right)^{abcd} = (U^{-1})^{abcd} - \chi_0^{abcd}(\mathbf{q}), \quad (1.42)$$

diagonalised at $\mathbf{q} = \mathbf{Q}_{X,Y}$. When written in terms of the irreducible representations A_{1g}, \dots, B_{2g} this quantity is block diagonal, i.e. there are no elements coupling different irreducible representations. The magnetic propagator is evaluated as a function of temperature until a magnetic transition, signified by the smallest eigenvalue crossing zero, occurs. Note that this is equivalent to a divergence of the leading eigenvalue of the RPA

1.3 Commensurate magnetic order

magnetic susceptibility. The eigenvalues of the magnetic propagator come in degenerate pairs when evaluated in the space of irreducible representations. This is a consequence of the aforementioned degeneracy between A_{1g}/B_{1g} and A_{2g}/B_{2g} at the quadratic level. Interestingly, for the parameters used here, the smallest pair of eigenvalues always originate from the A_{1g}/B_{1g} representations, with subleading eigenvalues also belonging to A_{1g}/B_{1g} . The condensation of the A_{1g}/B_{1g} representations is consistent with unrestricted Hartree-Fock methods, which find magnetic order parameters with the orbital structure given in Eq. 1.39 [72], with the only off-diagonal component being smaller than the diagonal components by an order of magnitude. Having established the orbital structure of the leading instability we can proceed to evaluate the quartic coefficients. The relevant Feynman diagrams are again the ones depicted in Fig. 1.6. In the present case however, evaluating the coefficients using a Hubbard-Stratonovich decoupling has a distinct advantage due to the presence of orbital indices. The quartic coefficients are rank-8 tensors in orbital space and to determine the symmetry of the magnetic order at the instability we project these onto the leading instability using the orbital content obtained from the diagonalisation of the magnetic propagator at the instability:

$$(\chi_{\text{mag}}^{-1})^{abcd}(\mathbf{Q}_{X,Y})v_{1,2}^{cd} = \lambda v_{1,2}^{ab}, \quad (1.43)$$

and we define

$$\beta_1^{abcdefgh}v_1^{ab}v_1^{cd}v_1^{ef}v_1^{gh} \equiv \beta, \quad (1.44)$$

$$\beta_2^{abcdefgh}v_2^{ab}v_2^{cd}v_2^{ef}v_2^{gh} \equiv \beta, \quad (1.45)$$

$$\gamma^{abcdefgh}v_1^{ab}v_1^{cd}v_2^{ef}v_2^{gh} \equiv \gamma, \quad (1.46)$$

$$\omega^{abcdefgh}v_1^{ab}v_2^{cd}v_1^{ef}v_2^{gh} \equiv \omega, \quad (1.47)$$

and we note that while the result of the contractions in Eq. 1.44 and 1.45 are identical by symmetry the orbitally resolved coefficients $\beta_1^{abcdefgh}$ and $\beta_2^{abcdefgh}$ are related by C_4 rotations since these act non-trivially on orbital space. With this method we can investigate the parameter dependence of the various coefficients and hence on the different symmetries attainable.

The starting Hamiltonian is the one provided in Eq. 1.35 and the interaction is decoupled in both the $\mathbf{q} = 0$ charge channel and the $\mathbf{q} = \mathbf{Q}_{X,Y}$ SDW channel. The SDW channel provides the starting point for the Hubbard-Stratonovich decoupling while the contribution from the charge channel is absorbed into an orbitally dependent shift of the chemical potential entering the quadratic term. We commence by making contact with known territory and consider the parameters $U = 0.85$ eV, $J = U/4$. These were investigated in detail in Ref. [72] and therefore provide a benchmark for our results. In Fig. 1.8(a) we show the doping-temperature phase diagram obtained from the quartic coefficients. The agreement with the phase diagram presented in Ref. [72] is encouraging except for the electron doped region which exhibits a CSDW region, contrary to the case in Ref. [72], where this region is characterised by an SVC phase. This apparent inconsistency is solved by focussing on the magnetic-paramagnetic boundary within unrestricted Hartree-Fock theory. This reveals a small CSDW region preempting the larger SVC region, thus confirming the results based

1.4 Incommensurate magnetic order

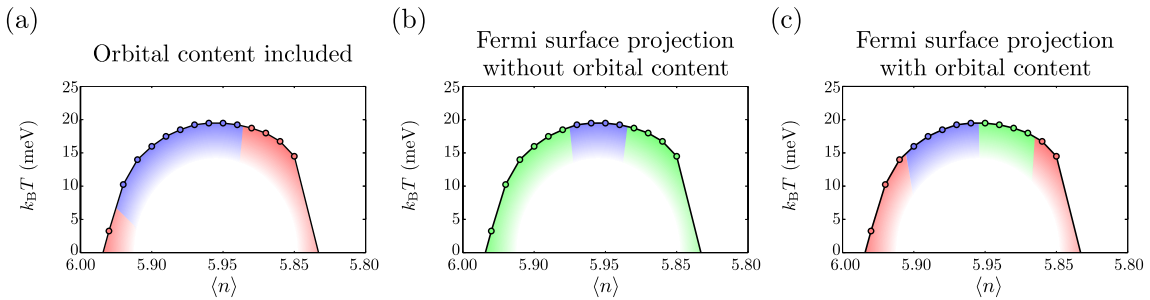


Figure 1.8: Phase diagrams for the bandstructure of Ref. [61] with $U = 0.85\text{eV}$ and $J = U/4$. The colour corresponds to the symmetry of the magnetic order parameter at the transition and is the same as the one in Fig. 1.2, red is the CSDW phase, blue is the magnetic stripe phase, and green is the SVC phase. As the free energy analysis with only quartic coefficients is only valid in the vicinity of the phase transition the bulk of the phase diagram is left blank.

on the free energy and providing an indication that the appearance of the SVC phase is a result of a secondary magnetic transition. Interestingly, a direct PM-SVC transition was not observed for any of the parameters considered, which is contrary to predictions based on a simpler three-band model discussed above, which predicts the dominant tetragonal phase to be the SVC phase. Indeed removing any effect of orbitals from our calculation by using e.g. $v^{ab} = \delta^{ab}$ we find a PM-SVC transition for a large doping range, as evidenced in Fig. 1.8(b). The absence of the CSDW phase in the generic three-band models is an indication that the orbital content of the Fermi surface plays an important role in deciding the symmetry of the magnetic phase. Finally, in an attempt to mimic the hybrid models, we consider the five-orbital model only in the vicinity of the Fermi surface (i.e. within 50 meV), implying that the contribution to the quartic coefficients originates from the high-symmetry points, Γ , X, Y, and M. The result is evidenced in Fig. 1.8(c) and the agreement with the case where no projection occurred is rather good.

Changing the interaction parameters alters the transition temperature and can change the symmetry of the leading instability although it seems to be a general trend that the SVC phase does not occur as a leading instability.

1.4 Incommensurate magnetic order

Part of the material presented in this section is available as a preprint by the author, Brian M. Andersen and Panagiotis Kotetes at arXiv:1612.07633.

Adding or removing electrons via doping changes the Fermi surface of the system. Within an itinerant scenario where magnetism is driven by Fermi surface nesting this can lead to a crossover from commensurate to incommensurate magnetism [81]. Incommensurate magnetic phases have been observed using neutron scattering [82–84] and more recently a new C_2 symmetric phase was observed in the incommensurate region of $\text{Ba}_{1-x}\text{Na}_x\text{Fe}_2\text{As}_2$ [60]. In addition to the incommensurate generalisations of the commensurate magnetic phases, the existence of two order parameters allow a number of new phases to appear [85], and

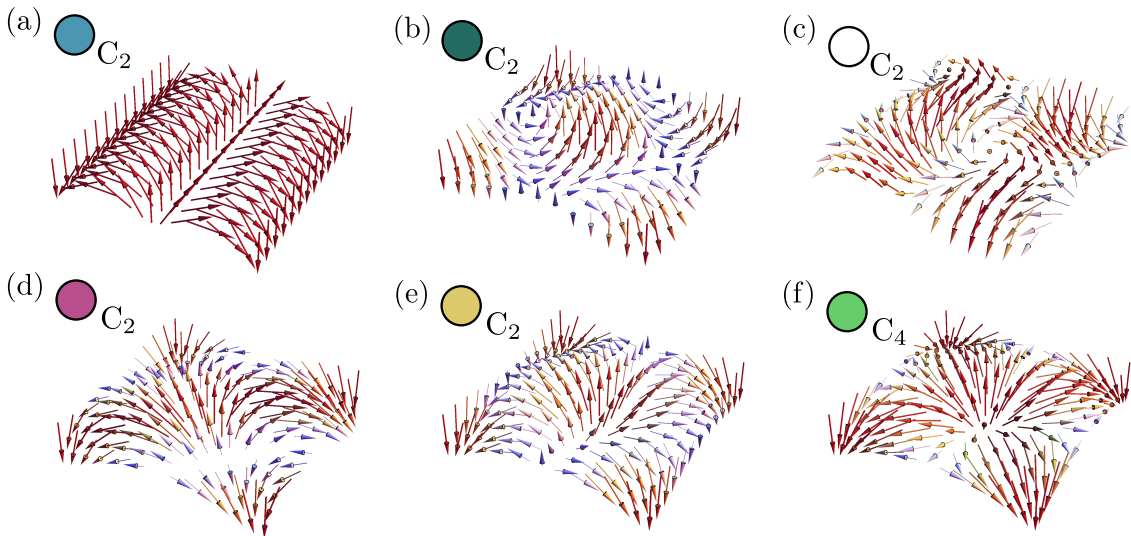


Figure 1.9: Illustration of the various new magnetic orders possible once magnetism becomes incommensurate. In (a)-(c) various magnetic spiral order parameters are shown. In (b)/(c) the spiral coexists with an in-/out-of-plane IC stripe. In (d) we present the C_2 -symmetric coplanar phase and in (e)/(f) the non-coplanar phase with C_2/C_4 symmetry.

as we show below, a number of these turn out to be non-coplanar. This is interesting in the context of realising intrinsic topological superconductivity which has been speculated to appear in a number of compounds such as Sr_2RuO_4 or $\text{Cu}_x\text{Bi}_2\text{Se}_3$ [86].

The case of incommensurate magnetism can be studied in a manner similar to the commensurate case. Incommensurability in this case refers to the wave vector peaking away from $(\pi, 0)$ or $(0, \pi)$. The expression for the free energy is slightly more complicated since the wave vectors are not at the Brillouin zone boundary implying that the magnetic order parameters are no longer necessarily real. Instead we have

$$\mathbf{M}_{\mathbf{Q}_1} = \mathbf{M}_{-\mathbf{Q}_1}^*, \quad (1.48)$$

and the invariance of the free energy functional under complex conjugation is not trivially ensured. The appropriate extension of the quartic term reads (here $\mathbf{M}_{\mathbf{Q}_1} \equiv \mathbf{M}_1$)

$$\begin{aligned} \mathcal{F}^{(4)} = & \frac{\tilde{\beta}}{2} (|\mathbf{M}_1|^2 + |\mathbf{M}_2|^2)^2 + \frac{\beta - \tilde{\beta}}{2} (|\mathbf{M}_1^2|^2 + |\mathbf{M}_2^2|^2) + (g - \tilde{\beta}) |\mathbf{M}_1|^2 |\mathbf{M}_2|^2 \\ & + \frac{\tilde{g}}{2} (|\mathbf{M}_1 \cdot \mathbf{M}_2|^2 + |\mathbf{M}_1 \cdot \mathbf{M}_2^*|^2), \end{aligned} \quad (1.49)$$

the quadratic term is unchanged compared to the commensurate case. One might expect the ground state configurations of the above free energy to simply be the incommensurate extensions of the MS, CSDW and SVC phases studied above. Indeed these are present in certain regions of the phase diagram, however, the incommensurability allows for the appearance of six additional phases, depicted in Fig. 1.9. Parameterising the order parameters as

$$\mathbf{M}_1 = M \cos \eta \hat{\mathbf{n}}_1, \quad (1.50)$$

$$\mathbf{M}_2 = M \sin \eta \hat{\mathbf{n}}_2, \quad (1.51)$$

1.4 Incommensurate magnetic order

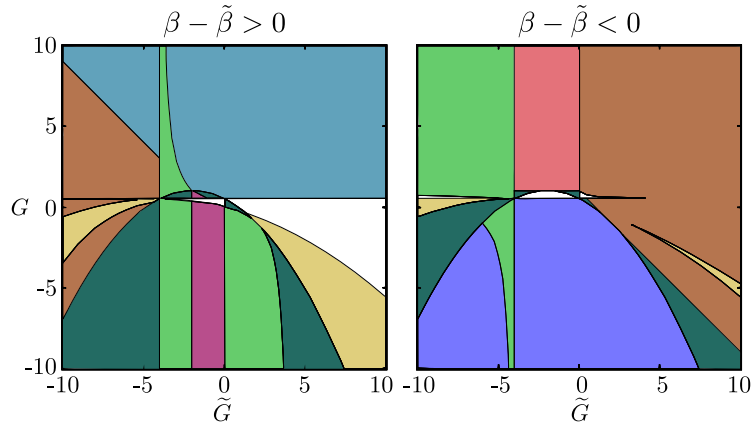


Figure 1.10: Phase diagrams resulting from a minimisation of the free energy in Eq. (1.49). Here the phases are: C_2 magnetic spiral (\bullet), C_2 IC stripe (\circ), C_4 collinear double- \mathbf{Q} (\blacklozenge), C_4 non-collinear double- \mathbf{Q} (\blacklozenge), C_2 magnetic spiral with in-plane (\parallel) IC stripe (\bullet), C_2 magnetic spiral with out-of-plane (\perp) IC stripe (\circ), C_2 coplanar (\bullet), C_4 non-coplanar (\bullet), and C_2 non-coplanar (\bullet). Note that the IC extensions of the original three phases ($\bullet, \bullet, \bullet$) are present, however they have yielded large regions of the phase diagrams to the new phases solely appearing in the IC regime.

and extremising the free energy functional with respect to η we find

$$\sin 2\eta = 0, \quad (1.52)$$

$$\cos 2\eta = \frac{|\hat{\mathbf{n}}_1|^2 - |\hat{\mathbf{n}}_2|^2}{2G + 2\tilde{G}P - (|\hat{\mathbf{n}}_1|^2 + |\hat{\mathbf{n}}_2|^2)}, \quad (1.53)$$

where we have introduced the coefficients

$$G \equiv \frac{g - \tilde{\beta}}{\beta - \tilde{\beta}}, \quad (1.54)$$

$$\tilde{G} \equiv \frac{\tilde{g}}{\beta - \tilde{\beta}}, \quad (1.55)$$

$$P \equiv \frac{|\hat{\mathbf{n}}_1 \cdot \hat{\mathbf{n}}_2|^2 + |\hat{\mathbf{n}}_1 \cdot \hat{\mathbf{n}}_2^*|^2}{2}. \quad (1.56)$$

The incommensurate extension of the standard phase diagram resulting from a full minimisation of the free energy functional is shown in Fig. 1.10. A significant number of the new double- \mathbf{Q} phases violate C_4 symmetry. Interestingly, a C_2 symmetric incommensurate magnetic phase distinct from an incommensurate stripe phase was recently observed in Na-doped $\text{Ba}_2\text{Fe}_2\text{As}_2$ [60] and it is conceivable that this phase corresponds to one of the new phases uncovered although further experimental studies are needed to conclude this with certainty.

The method outline in Sec. 1.3 can also be applied in the study of the incommensurate phases, although with a slight modification. Since $\mathbf{Q}_{1,2}$ are not at the Brillouin zone boundary, the equations for the quartic coefficients involve, in addition to \mathbf{k} and $\mathbf{k} + \mathbf{Q}_{1,2}$, also higher harmonics $\mathbf{k} + n\mathbf{Q}_{1,2}$ where n is an integer. Here we neglect these terms as the peaks associated with the higher harmonics are suppressed compared to the leading harmonic, as seen in Fig. 1.11. An incommensurate phase is found in the band structure

1.4 Incommensurate magnetic order

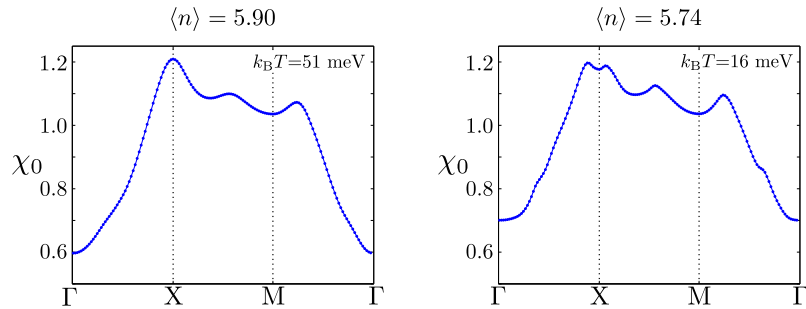


Figure 1.11: Plot of the bare physical susceptibility $\chi_0(\mathbf{q}) = \sum_{ab} \chi_0^{aabb}(\mathbf{q})$ for two different fillings using the band structure of Ref. [61]. We see that higher harmonics are suppressed compared to the dominant peak.

of Ref. [61] for $U = 0.95$ eV and $J = U/4$ at large hole doping for which $\langle n \rangle = 5.75$ if we neglect the orbitally-dependent adjustment of the chemical potential induced by the interactions as the system is doped³. The resulting phase diagram is shown in Fig. 1.12, depicting a large commensurate region and an incommensurate region on the hole doped side of the phase diagram. The C_4 non-coplanar magnetic order is given by the expression

$$\mathbf{M}(\mathbf{r}) = \begin{pmatrix} M \sin \lambda [\cos(Qx) + \cos(Qy)] \\ M \cos \lambda \sin(Qx) \\ M \cos \lambda \sin(Qy) \end{pmatrix}. \quad (1.57)$$

This magnetic texture has nodes at four points, $\mathbf{r} = (\pm\pi/Q, 0)$ and $\mathbf{r} = (0, \pm\pi/Q)$, and by application of an external magnetic field in the x -direction these four nodal points are gapped out and $|\mathbf{M}(\mathbf{r})| \neq 0$ everywhere. With this we can introduce a Chern number for the magnetic unit vector $\widehat{\mathbf{M}}(\mathbf{r}) = \mathbf{M}(\mathbf{r})/|\mathbf{M}(\mathbf{r})|$:

$$\mathcal{C} = \frac{1}{4\pi} \int d\mathbf{r} \widehat{\mathbf{M}}(\mathbf{r}) \cdot [\partial_x \widehat{\mathbf{M}}(\mathbf{r}) \times \partial_y \widehat{\mathbf{M}}(\mathbf{r})] \quad (1.58)$$

with $\mathcal{C} = \pm 1$ indicating a topologically non-trivial magnetic texture.

Attaining microscopic coexistence between spin-singlet superconductivity and C_2 or C_4 non-coplanar magnetic order paves the way for realising intrinsic topological superconductivity capable of hosting Majorana edge modes in the iron-based superconductors. While several of the other magnetic orders made possible by the incommensurate extension also allow for topological phases in one form or other, the C_2 and C_4 non-coplanar orders allow for a strong topological invariant whose existence only relies on the presence of the anti-unitary generalised charge-conjugation symmetry, as indicated in Table 6.1. This will be discussed further in Chapter 6 when we introduce the concept of symmetry

³At this point it is worth stressing that the band structure considered is rigid in the sense that the DFT calculations were only carried out at $\langle n \rangle = 6$. Since doping replaces one kind of element with another one should carry out new DFT-calculations taking into account this change. When doping the system in question we assume that the introduction of different elements does nothing to the band structure and only changes the filling. This is not entirely correct but whether the effect of different elements is best captured by including or omitting the orbitally-dependent shift of the chemical potential is not clear. Since the primary goal of the above study is to study an incommensurate phase we will not be concerned further with this subtlety.

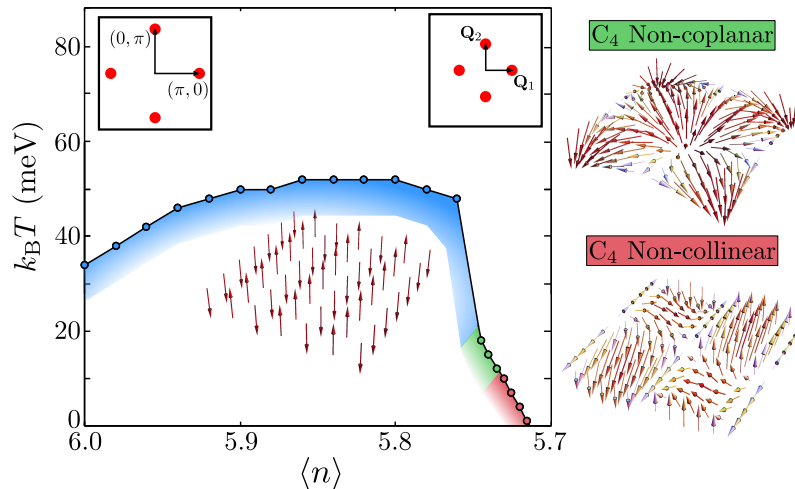


Figure 1.12: Magnetic transition temperature as a function of the filling, $\langle n \rangle$, for the band structure of Ref. [61] showing a dome similar to the ones depicted in Fig. 1.8. In the commensurate region the leading instability is the standard magnetic stripe. For $\langle n \rangle \approx 5.75$ we obtain the type of incommensurability investigated here, with $\mathbf{Q}_{1,2} = (\pi - \delta, 0)/(0, \pi - \delta)$. In the IC region, the dominant magnetic order is the C_4 non-coplanar phase (●) while the C_4 non-collinear phase (●) becomes stabilized for smaller filling. The insets show the evolution of the peaks in the RPA susceptibility as the system moves from the commensurate region with $\mathbf{Q}_{1,2} = (\pi, 0)/(0, \pi)$ to the IC with $\mathbf{Q}_{1,2} = (\pi - \delta, 0)/(0, \pi - \delta)$ and $\delta \approx \pi/10$.

classes. The topological invariant for this quantity is a Chern number, however, since we are dealing with a multi-orbital system, each band has its own Berry curvature and evaluating the Chern number is cumbersome. In the presence of an s^{++} superconducting order parameter Majorana cones are formed at points connected by the magnetic ordering vector $\mathbf{Q}_{1,2}$, as is shown in Fig. 1.13. In the vicinity of the Fermi surface we can instead consider the vector

$$\mathbf{g}(\mathbf{k}) = \begin{pmatrix} k_x \\ k_y \\ \Delta - M_{\text{eff}} \end{pmatrix}, \quad (1.59)$$

and define a topological invariant

$$\int d\mathbf{k} \hat{\mathbf{g}}(\mathbf{k}) \cdot [\partial_{k_x} \hat{\mathbf{g}}(\mathbf{k}) \times \partial_{k_y} \hat{\mathbf{g}}(\mathbf{k})]. \quad (1.60)$$

Note that this quantity is fractional since it involves only one gap closing in the Brillouin zone. The Nielsen-Ninomiya theorem [87] ensures that the gap closes at an even number of points in the Brillouin zone such that the sum of these numbers add up to an integer. Here M_{eff} is an effective order parameter decided by the value of the magnetic order parameter in the overlapping orbitals. In the present case the magnetic gap is due to an overlap between electron and hole parts of the Fermi surface. For Majorana cones to appear as shown in Fig. 1.13(b) the order parameter must have the same sign on electron and hole pockets, as shown in Fig. 1.13(c)-(e), while the configuration shown in Fig. 1.13(f) would not lead to a topologically non-trivial phase.

1.4 Incommensurate magnetic order

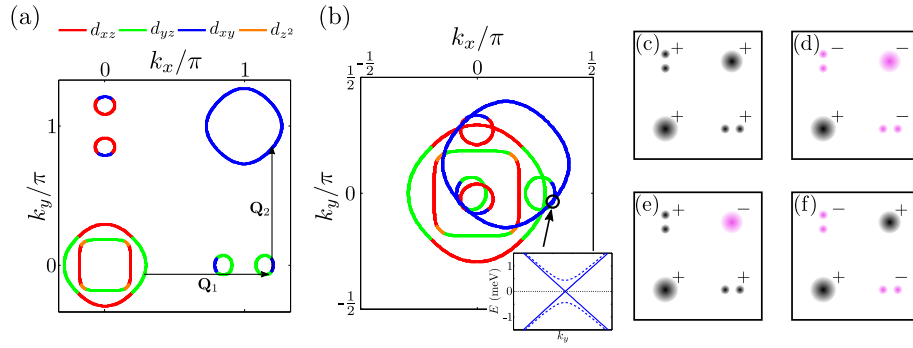


Figure 1.13: (a) Fermi surface for the filling exhibiting incommensurate magnetism. The main contributions to nesting along \mathbf{Q}_1 (\mathbf{Q}_2) arise in the xy and yz (xz) orbitals. (b) Fermi surface after folding once along both $\mathbf{Q}_{1,2}$. The inset shows the evolution of the energy dispersion when moving away from a nested point with direction along k_y , in the presence of magnetic order ($M = 20\text{meV}$ and $\lambda = \pi/5$) and two different values for the superconducting gap $\Delta = 10\text{meV}$ (dashed) and $\Delta = 5\text{meV}$ (full). In the latter we have chosen a SC gap value yielding a bulk Majorana cone associated with the occurrence of a topological phase transition. (c)-(f) Relative sign structure of the superconducting order parameter on the pockets, leading to topological (c)-(e) or trivial (f) phases.

In this chapter we have been introduced to the vast subject of magnetism in the FeSC. We reviewed various relevant models for the study of the FeSC and illustrated the importance of including the orbital character of the bands when determining the symmetry of the magnetic order parameter. Additionally, the concept of incommensurate magnetism was introduced in the context of the FeSC and we saw that such phases naturally arise in the phase diagram of a band structure suitable to describe the FeSC. Using the hybrid model introduced in Sec. 1.2.2 we investigate the role of a finite spin-orbit coupling in the FeSC in Chapter 2. Employing the multi-orbital model of Ref. [61] we show in Chapter 3 that the multi-orbital Hubbard model exhibits a spin-driven nematic instability akin to the one described in Sec. 1.2.1.

Chapter 2

Spin reorientation driven by the interplay between spin-orbit coupling and Hund's rule coupling in iron pnictides

*This chapter has been published by the author and Jian Kang, Brian M. Andersen, Ilya Eremin and Rafael M. Fernandes in Phys. Rev. B **92** 214509 (2015).*

Motivated by the observation of a tetragonal magnetic phase exhibiting a reorientation of the magnetic moments we study the effect of spin-orbit coupling on the magnetic order. To this effect we use the hybrid model introduced in Sec. 1.2.2. We show that the interplay between Hund's coupling and the spin-orbit coupling is responsible for a reorientation of the magnetic moments from in-plane to out-of-plane. A tetragonal phase with reoriented magnetic moments is found for a range of chemical potentials corresponding to hole-doped materials. The appendices contain a number of technical derivations including $\mathbf{k} \cdot \mathbf{p}$ expansion of a five-orbital model resulting in the hybrid model used, and a derivation of the spin-orbit term.

2.1 Introduction

In the iron pnictides, unconventional superconductivity appears in close proximity to a magnetic instability [18, 19, 22, 88]. As a result, much of the research into these compounds has been devoted to understanding the magnetic properties of these systems [9, 53, 89, 90]. Experimentally, the spin-density wave (SDW) magnetic order of most iron pnictides has orthorhombic (C_2) symmetry and corresponds to stripes of parallel spins modulated either along the \hat{x} direction (i.e. ordering vector $\mathbf{Q}_1 = (\pi, 0)$ and staggered magnetic order parameter \mathbf{M}_1) or along the \hat{y} direction (i.e. ordering vector $\mathbf{Q}_2 = (0, \pi)$ and staggered magnetic order parameter \mathbf{M}_2), in the coordinate system of the Fe square lattice [9, 90]. Theoretically, this state has been described by a variety of approaches, from purely localized Heisenberg spins [39, 44, 46, 91, 92] to itinerant nesting-based scenarios [47, 64, 70, 93–99] to hybrid models mixing local moments and itinerant carriers [45, 89, 100–103]. Common to nearly all these approaches is the assumption that the magnetic degrees of freedom have an underlying $O(3)$ spin-rotational symmetry. From a phenomenological perspective, this implies that the magnetic free energy F_{mag} depends only on the absolute value of the magnetic order parameters, i.e. $F_{\text{mag}}(M_1^2, M_2^2)$ [104].

Despite the success of these approaches in describing many magnetic properties of the iron pnictides – such as the onset of a preemptive nematic transition [24] and the appearance of a tetragonal magnetic ground state [95] – there are important features that remain largely unaddressed. In particular, the $O(3)$ rotational symmetry of a free spin does not hold for a magnetic moment in a crystal. Instead, the symmetries of the underlying lattice induce anisotropies in spin space that may be significant [105]. Indeed, in most iron pnictides, the magnetic moments are observed to point parallel to the modulation vector of the stripes, i.e. $\mathbf{M}_i \parallel \mathbf{Q}_i$ [9, 90]. Attesting the significance of this spin anisotropy, a sizable spin gap of the order of 10 meV is also found at low temperatures deep in the magnetically ordered state [106–109]. Interestingly, recent experiments in hole-doped iron pnictides have reported a spin reorientation near optimal doping, in which the direction of the magnetic moments flip from in-plane to out-of-plane [32–35]. Remarkably, this spin reorientation takes place in a region of the phase diagram in which the magnetic ground state changes from stripe/orthorhombic to tetragonal.

Therefore, elucidating the origins of these spin anisotropies and their impact on the normal state properties is paramount to advance our understanding of the iron pnictides. A natural candidate to account for these effects is the spin-orbit coupling (SOC) term $\lambda \mathbf{S} \cdot \mathbf{L}$ [65, 69, 110, 111], which converts the lattice anisotropies into anisotropies in spin space. Recent ARPES measurements of the SOC λ have reported values of the order of 20 meV [112], which is not far from the typical magnetic energy scale of the problem (as extracted for instance from optical conductivity measurements [113, 114]). To include the SOC term in theoretical models, it is necessary to account for the puckering of the As atoms along the FeAs plane, which effectively doubles the unit cell of the Fe-only square lattice. In this paper, instead of working with the cumbersome ten-band model relevant for the 2-Fe unit cell, we consider a simpler low-energy microscopic model that respects all the symmetries of the FeAs plane and focuses only on the states near the

2.2 Low-energy microscopic model

Fermi level. Such a model, which relies on the smallness of the Fermi surface pockets of the iron pnictides, was previously derived by Cvetkovic and Vafeek using rigorous group theoretical arguments [65]. Here, we show how the main ingredients of the model can be derived from a straightforward expansion of the usual five-orbital model for the pnictides. By computing microscopically the magnetic free energy in the paramagnetic state, we find the leading-order magnetic anisotropic terms:

$$\begin{aligned} \delta F &= \alpha_1 \left(M_{1,x}^2 + M_{2,y}^2 \right) \\ &\quad + \alpha_2 \left(M_{1,y}^2 + M_{2,x}^2 \right) \\ &\quad + \alpha_3 \left(M_{1,z}^2 + M_{2,z}^2 \right). \end{aligned} \quad (2.1)$$

The anisotropic coefficients α_i are proportional not only to the square of the SOC term, λ^2 , but also to the Hund's rule coupling J . Evaluation of the coefficients reveals that $\alpha_1 < \alpha_3, \alpha_2$ for most of the temperature-doping phase diagram, implying that the magnetic moments have a general tendency to lie in the plane. Interestingly, in the hole-doped side of the phase diagram, we find a small region in which $\alpha_3 < \alpha_1, \alpha_2$, indicating a spin reorientation from in-plane to out-of-plane. Both results are in qualitative agreement with the observations discussed above, providing evidence that the SOC term, with the aid of the Hund's rule coupling, is sufficient to account for the magnetic anisotropies of the iron pnictides. This conclusion contrasts with previous proposals that orbital and/or nematic order are necessary to explain the observed magnetic moment orientation [105].

For completeness, we also analyze the nature of the magnetic ground state across the phase diagram. We find a general tendency of electron-doped compounds to form an orthorhombic uniaxial (single- \mathbf{Q}) stripe state (i.e. either $\langle |\mathbf{M}_1| \rangle = 0$ or $\langle |\mathbf{M}_2| \rangle = 0$), whereas hole-doped compounds favor a tetragonal biaxial (double- \mathbf{Q}) magnetic state (i.e. $\langle |\mathbf{M}_1| \rangle = \langle |\mathbf{M}_2| \rangle$). Such an electron-hole asymmetry is also qualitatively consistent with experiments – and in particular with the recent observation that the spin reorientation takes place in a region of the phase diagram in which the magnetic ground state is tetragonal.

The paper is organized as follows: In section 2.2 we introduce the low-energy microscopic model with the SOC term and the electronic interactions. Section 2.3 is devoted to the analysis of the coefficients of the free energy responsible for the magnetic anisotropy within leading-order. In section 2.4 we refine the phase diagram by including fourth order contributions to the free energy that allow us to distinguish between stripe and tetragonal magnetic ground states. Concluding remarks are presented in section 2.5. Details of the calculations are included in four appendices.

2.2 Low-energy microscopic model

We start with a low-energy microscopic model that focuses only on the electronic states near the Fermi level, while respecting the symmetries of the FeAs plane. Such a model was originally derived in Ref. [65] using the symmetry properties of the non-symmorphic space group $P4/nmm$ of a single FeAs plane. Here, we present an alternative derivation

2.2 Low-energy microscopic model

based on the typical 5-orbital tight-binding model used for the iron pnictides [66]:

$$\mathcal{H}_0 = \sum_{\mathbf{k}\mu\nu\alpha} \varepsilon_{\mu\nu}(\mathbf{k}) c_{\mu,\mathbf{k}\alpha}^\dagger c_{\nu,\mathbf{k}\alpha} \quad (2.2)$$

where \mathbf{k} is the momentum, α is the spin, and μ, ν denote one of the five Fe orbitals, xz , yz , $x^2 - y^2$, xy , and $3z^2 - r^2$. The matrix $\varepsilon_{\mu\nu}(\mathbf{k})$ corresponds to the Fourier-transformed tight-binding dispersions involving up to fourth-nearest neighbor hoppings. Its explicit expression is given in Appendix A. Note that this Hamiltonian is based on the single-Fe square lattice (i.e. it refers to the “unfolded” Brillouin zone), and that the coordinate system is defined such that k_x and k_y are parallel to the nearest-neighbor Fe atoms directions. The actual crystallographic unit cell contains two Fe atoms due to the puckering of the As atoms, resulting in the so-called “folded” Brillouin zone, described by the coordinates K_x, K_y (see Fig. 2.1). Note that the two coordinate systems are related by:

$$\begin{aligned} K_x &= k_x + k_y \\ K_y &= -k_x + k_y \end{aligned} \quad (2.3)$$

where the momentum in the unfolded zone is measured in units of its inverse lattice constant $1/a$, whereas the momentum in the folded zone is measured in units of its inverse lattice constant $1/(\sqrt{2}a)$.

The key properties that allow us to derive a simpler low-energy model are the facts that the Fermi surface pockets are small and that the orbitals that mostly contribute to the Fermi surface are xz , yz , xy . In particular, the idea is to start at the high-symmetry points of the unfolded Brillouin zone (namely, $\Gamma = (0, 0)$, $X = (\pi, 0)$, and $Y = (0, \pi)$), where the band states are pure orbital states, and perform an expansion of the corresponding matrix elements $\varepsilon_{\mu\nu}(\mathbf{k})$ for small momentum. Note that, to focus on a general and analytically tractable model, we follow Ref. [65] and ignore the states near the (π, π) point of the unfolded Brillouin zone. While it is true that some iron pnictides display a hole-pocket with xy -orbital character centered at this point, this pocket is not usually present for all values of k_z , and is absent in many of the iron-based materials with a single FeAs plane per unit cell. Correspondingly we consider in this work the doping range in which this pocket lies below the Fermi level.

Consider first the Γ point; the two states closest to the Fermi level are the xz and yz orbitals, which form a degenerate doublet in the absence of SOC. Thus, for small \mathbf{k} , we define the spinor:

$$\psi_{\Gamma,\mathbf{k}} = \begin{pmatrix} c_{yz,\mathbf{k}\uparrow} \\ -c_{xz,\mathbf{k}\uparrow} \\ c_{yz,\mathbf{k}\downarrow} \\ -c_{xz,\mathbf{k}\downarrow} \end{pmatrix}. \quad (2.4)$$

Projecting $\varepsilon_{\mu\nu}(\mathbf{k})$ on this sub-space and expanding for small \mathbf{k} then yields the 4×4 Hamiltonian:

$$H_{0,\Gamma} = \sum_{\mathbf{k}} \psi_{\Gamma,\mathbf{k}}^\dagger h_{\Gamma}(\mathbf{k}) \psi_{\Gamma,\mathbf{k}} \quad (2.5)$$

2.2 Low-energy microscopic model

with

$$h_{\Gamma}(\mathbf{k}) = \begin{pmatrix} \epsilon_{\Gamma} + 2\frac{\mathbf{k}^2}{2m_{\Gamma}} + b(k_x^2 - k_y^2) & 4ck_x k_y \\ 4ck_x k_y & \epsilon_{\Gamma} + 2\frac{\mathbf{k}^2}{2m_{\Gamma}} - b(k_x^2 - k_y^2) \end{pmatrix} \otimes \sigma^0 \quad (2.6)$$

where σ^0 is a Pauli matrix acting on spin space. The coefficients ϵ_{Γ} , m_{Γ} , b , and c can be obtained directly from the tight-binding parameters (see Appendix A). Note, however, that as we move away from the high-symmetry points of the Brillouin zone, other orbitals start to contribute to the electronic states. Consequently, the coefficients of the expansion (as derived in Appendix 2.A) will be slightly renormalized by the hybridization with the orbitals not included in the expansion, although the form of the expansion remains invariant. To account for this issue, we can consider the coefficients to be free parameters that can be fit directly to the first-principle band dispersions.

Near the X point, the low-energy states correspond to the orbitals yz and xy . Defining the spinor:

$$\psi_{X,\mathbf{k}+\mathbf{Q}_1} = \begin{pmatrix} c_{yz,\mathbf{k}+\mathbf{Q}_1\uparrow} \\ c_{xy,\mathbf{k}+\mathbf{Q}_1\uparrow} \\ c_{yz,\mathbf{k}+\mathbf{Q}_1\downarrow} \\ c_{xy,\mathbf{k}+\mathbf{Q}_1\downarrow} \end{pmatrix}. \quad (2.7)$$

and expanding the projected $\varepsilon_{\mu\nu}(\mathbf{k})$ near $\mathbf{Q}_1 = (\pi, 0)$ yields:

$$H_{0,X} = \sum_{\mathbf{k}} \psi_{X,\mathbf{k}+\mathbf{Q}_1}^{\dagger} h_X(\mathbf{k} + \mathbf{Q}_1) \psi_{X,\mathbf{k}+\mathbf{Q}_1} \quad (2.8)$$

with

$$h_X(\mathbf{k} + \mathbf{Q}_1) = \begin{pmatrix} \epsilon_1 + 2\frac{\mathbf{k}^2}{2m_1} + a_1(k_x^2 - k_y^2) & -iv_X(\mathbf{k}) \\ iv_X(\mathbf{k}) & \epsilon_3 + 2\frac{\mathbf{k}^2}{2m_3} + a_3(k_x^2 - k_y^2) \end{pmatrix} \otimes \sigma^0 \quad (2.9)$$

and:

$$v_X(\mathbf{k}) = 2vk_y + 2p_1k_y(k_y^2 + 3k_x^2) - 2p_2k_y(k_x^2 - k_y^2). \quad (2.10)$$

Similarly, near the Y point, the low-energy states involve the orbitals xz and xy :

$$\psi_{Y,\mathbf{k}+\mathbf{Q}_2} = \begin{pmatrix} c_{xz,\mathbf{k}+\mathbf{Q}_2\uparrow} \\ c_{xy,\mathbf{k}+\mathbf{Q}_2\uparrow} \\ c_{xz,\mathbf{k}+\mathbf{Q}_2\downarrow} \\ c_{xy,\mathbf{k}+\mathbf{Q}_2\downarrow} \end{pmatrix}. \quad (2.11)$$

Projecting and expanding $\varepsilon_{\mu\nu}(\mathbf{k})$ near $\mathbf{Q}_2 = (0, \pi)$ gives:

$$H_{0,Y} = \sum_{\mathbf{k}} \psi_{Y,\mathbf{k}+\mathbf{Q}_2}^{\dagger} h_Y(\mathbf{k} + \mathbf{Q}_2) \psi_{Y,\mathbf{k}+\mathbf{Q}_2} \quad (2.12)$$

2.2 Low-energy microscopic model

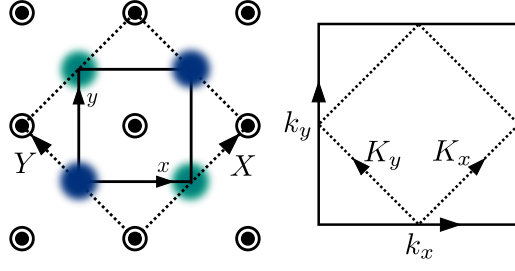


Figure 2.1: (Left) Illustration of the 2-Fe (dotted line) and 1-Fe (solid line) unit cells. The black dots denote iron atoms, while the pnictogens form two sublattices, one above the iron-plane (dark blue) and one below the iron-plane (light blue). (Right) Brillouin zones corresponding to the 1-Fe and 2-Fe unit cells. The dotted line is the “folded” Brillouin zone, corresponding to the 2-Fe unit cell, while the solid line is the “unfolded” Brillouin zone, corresponding to the 1-Fe unit cell.

with

$$h_Y(\mathbf{k} + \mathbf{Q}_2) = \begin{pmatrix} \epsilon_1 + 2\frac{\mathbf{k}^2}{2m_1} - a_1(k_x^2 - k_y^2) & -iv_Y(\mathbf{k}) \\ iv_Y(\mathbf{k}) & \epsilon_3 + 2\frac{\mathbf{k}^2}{2m_3} - a_3(k_x^2 - k_y^2) \end{pmatrix} \otimes \sigma^0 \quad (2.13)$$

and:

$$v_Y(\mathbf{k}) = -2vk_x - 2p_1k_x(k_x^2 + 3k_y^2) - 2p_2k_x(k_x^2 - k_y^2). \quad (2.14)$$

Having established the low-energy states in the unfolded Brillouin zone (i.e. the one referring to the 1-Fe unit cell), it is now straightforward to fold the states into the 2-Fe unit cell (see Fig. 2.1). Despite working in the folded Brillouin zone, described by the coordinates K_x, K_y , we will still make use of the coordinates k_x, k_y of the unfolded zone. From Eq. (2.3), we find that upon folding, both momenta $\mathbf{Q}_1 = (\pi, 0)$ and $\mathbf{Q}_2 = (0, \pi)$ are identified with the same momentum $\mathbf{Q}_M = (\pi, \pi)$. It is straightforward to show that the spinors X and Y now combine to form two new degenerate doublets at the $M = (\pi, \pi)$ point of the folded zone:

$$\psi_{M_1, \mathbf{k} + \mathbf{Q}_M} = \begin{pmatrix} c_{xz, \mathbf{k} + \mathbf{Q}_2 \uparrow} \\ c_{yz, \mathbf{k} + \mathbf{Q}_1 \uparrow} \\ c_{xz, \mathbf{k} + \mathbf{Q}_2 \downarrow} \\ c_{yz, \mathbf{k} + \mathbf{Q}_1 \downarrow} \end{pmatrix}; \quad \psi_{M_3, \mathbf{k} + \mathbf{Q}_M} = \begin{pmatrix} c_{xy, \mathbf{k} + \mathbf{Q}_2 \uparrow} \\ c_{xy, \mathbf{k} + \mathbf{Q}_1 \uparrow} \\ c_{xy, \mathbf{k} + \mathbf{Q}_2 \downarrow} \\ c_{xy, \mathbf{k} + \mathbf{Q}_1 \downarrow} \end{pmatrix} \quad (2.15)$$

Hereafter, we will consider the momentum of any spinor as measured relative to the high-symmetry points, as appropriate. Then, the non-interacting Hamiltonian becomes:

$$\mathcal{H}_0 = \sum_{\mathbf{k}} \Psi_{\mathbf{k}}^\dagger [H_0(\mathbf{k}) - \mu \mathbb{1}] \Psi_{\mathbf{k}}, \quad (2.16)$$

where we defined the enlarged spinor:

$$\Psi_{\mathbf{k}} = \begin{pmatrix} \psi_{Y, \mathbf{k}} \\ \psi_{X, \mathbf{k}} \\ \psi_{\Gamma, \mathbf{k}} \end{pmatrix} \quad (2.17)$$

2.2 Low-energy microscopic model

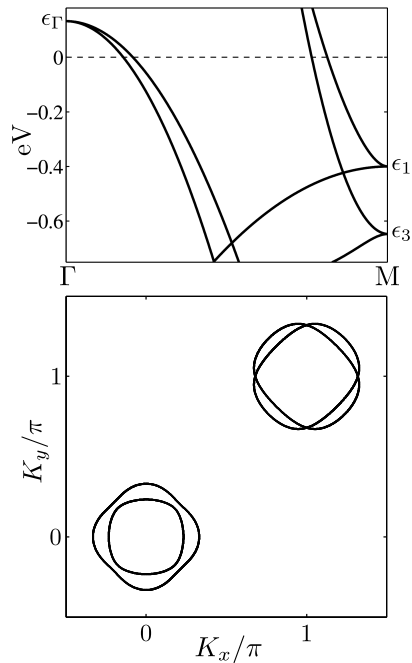


Figure 2.2: (upper panel) Cut of the low-energy band dispersion from the $\Gamma = (0, 0)$ to the $M = (\pi, \pi)$ point of the folded Brillouin zone with parameters fit to the tight-binding model of Ref. [76]. The corresponding Fermi surface is shown in the lower panel.

and the Hamiltonian matrix:

$$H_0(\mathbf{k}) = \begin{pmatrix} h_Y(\mathbf{k}) & 0 & 0 \\ 0 & h_X(\mathbf{k}) & 0 \\ 0 & 0 & h_\Gamma(\mathbf{k}) \end{pmatrix} \quad (2.18)$$

where μ is the chemical potential and $\mathbb{1}$ is the identity matrix. We note that this model has the same properties of the Hamiltonian derived by Cvetkovic and Vafeek in Ref. [65] combining a $\mathbf{k} \cdot \mathbf{p}$ expansion and the symmetry properties of the $P4/nmm$ space group (note, however, that the definition of the spinors X and Y are switched in Ref. [65] with respect to the notation adopted here). In the group-theory language, the spinor ψ_Γ belongs to the two-dimensional E_g representation of $P4/nmm$ near the Γ point, whereas ψ_{M_1} and ψ_{M_3} belong to the two-dimensional E_{M_1} and E_{M_3} representations of $P4/nmm$ near the M point. Hereafter, we will use for the coefficients of the Hamiltonian the parameters given by Table IX in Ref. [65]. Those were obtained by direct fitting of the band dispersions to first-principle calculations. The resulting band dispersions, as well as the Fermi surface, are shown in Fig. 2.2. Note also that this low-energy model is fundamentally different than two-orbital models that restrict the Hamiltonian to the subspace of the xz and yz orbitals. Our model, derived from the five-orbital tight-binding model as shown in Appendix A, not only obeys all the symmetries imposed by the $P4/nmm$ space group, but it also contains information about all the orbitals that contribute to the Fermi surface, including the xy orbital.

Besides the band dispersions, the non-interacting Hamiltonian must also contain the SOC term $\lambda \mathbf{S} \cdot \mathbf{L}$, with \mathbf{S} denoting the spin angular momentum operator and \mathbf{L} , the orbital

2.2 Low-energy microscopic model

angular momentum operator. Note that this atomic-like term preserves the Kramers degeneracy of each state. To proceed, we project this term from the $L = 2$ cubic harmonic basis to the orbital basis (see Appendix B for more details). At the Γ point, we obtain an admixture of the xz and yz orbitals:

$$\begin{aligned} \frac{\lambda}{2} \sum_{\mathbf{k}\alpha\beta} \left(i c_{yz,\mathbf{k}\alpha}^\dagger \sigma_{\alpha\beta}^z c_{xz,\mathbf{k}\beta} + \text{h.c.} \right) = \\ \frac{\lambda}{2} \sum_{\mathbf{k}} \psi_{\Gamma,\mathbf{k}}^\dagger (\tau^y \otimes \sigma^z) \psi_{\Gamma,\mathbf{k}} \end{aligned} \quad (2.19)$$

where, in the last step, we used the definition of the spinors. At the M point, we obtain the admixture of xz/yz and xy orbitals:

$$\begin{aligned} \frac{\lambda}{2} \sum_{\mathbf{k}\alpha\beta} \left(i c_{xz,\mathbf{k}\alpha}^\dagger \sigma_{\alpha\beta}^x c_{xy,\mathbf{k}\beta} + \text{h.c.} \right) = \\ \frac{\lambda}{2} \sum_{\mathbf{k}} \left[i \psi_{Y,\mathbf{k}+\mathbf{Q}_2}^\dagger (\tau^+ \otimes \sigma^x) \psi_{X,\mathbf{k}+\mathbf{Q}_1} + \text{h.c.} \right] \end{aligned} \quad (2.20)$$

as well as:

$$\begin{aligned} \frac{\lambda}{2} \sum_{\mathbf{k}\alpha\beta} \left(i c_{xy,\mathbf{k}\alpha}^\dagger \sigma_{\alpha\beta}^y c_{yz,\mathbf{k}\beta} + \text{h.c.} \right) = \\ \frac{\lambda}{2} \sum_{\mathbf{k}} \left[i \psi_{Y,\mathbf{k}+\mathbf{Q}_2}^\dagger (\tau^- \otimes \sigma^y) \psi_{X,\mathbf{k}+\mathbf{Q}_1} + \text{h.c.} \right] \end{aligned} \quad (2.21)$$

with $\tau^\pm = \frac{1}{2} (\tau^x \pm i\tau^y)$. Therefore, the SOC becomes:

$$\mathcal{H}_{\text{SOC}} = \sum_{\mathbf{k}} \Psi_{\mathbf{k}}^\dagger H_{\text{SOC}}(\mathbf{k}) \Psi_{\mathbf{k}}, \quad (2.22)$$

with:

$$H_{\text{SOC}}(\mathbf{k}) = \begin{pmatrix} 0 & h_M^{\text{SOC}}(\mathbf{k}) & 0 \\ (h_M^{\text{SOC}}(\mathbf{k}))^\dagger & 0 & 0 \\ 0 & 0 & h_\Gamma^{\text{SOC}}(\mathbf{k}) \end{pmatrix} \quad (2.23)$$

such that:

$$h_\Gamma^{\text{SOC}}(\mathbf{k}) = \frac{1}{2} \lambda (\tau^y \otimes \sigma^z), \quad (2.24)$$

$$h_M^{\text{SOC}}(\mathbf{k}) = \frac{i}{2} \lambda (\tau^+ \otimes \sigma^x + \tau^- \otimes \sigma^y), \quad (2.25)$$

in agreement with the group-theoretical arguments of Ref. [65].

The interacting part of this low-energy model is rather complex, involving 30 different possible biquadratic terms in the fermionic operators. Here, we will focus on the interactions coupling the Γ and the M points, since those are the ones that will be relevant for the calculation of the magnetic action in the next section. Defining $\tilde{\tau}^{1,3} \equiv \frac{1}{2} (\tau^0 \pm \tau^z)$, the interacting terms coupling the Γ and M points are written as (see Ref. [65]):

$$\begin{aligned}
\mathcal{H}_{\text{int}} = & \frac{1}{2} \sum_{\mathbf{k}\sigma} \left[v_{13} \left(\psi_{X\sigma}^\dagger(\mathbf{k}) \tau^- \psi_{\Gamma\sigma}(\mathbf{k}) + \text{h.c.} \right)^2 \right. \\
& + v_{13} \left(\psi_{Y\sigma}^\dagger(\mathbf{k}) \tilde{\tau}^3 \psi_{\Gamma\sigma}(\mathbf{k}) + \text{h.c.} \right)^2 \\
& + v_{15} \left(\psi_{X\sigma}^\dagger(\mathbf{k}) \tilde{\tau}^3 \psi_{\Gamma\sigma}(\mathbf{k}) + \text{h.c.} \right)^2 \\
& + v_{15} \left(\psi_{Y\sigma}^\dagger(\mathbf{k}) \tau^- \psi_{\Gamma\sigma}(\mathbf{k}) + \text{h.c.} \right)^2 \\
& + v_{17} \left(\psi_{X\sigma}^\dagger(\mathbf{k}) \tau^+ \psi_{\Gamma\sigma}(\mathbf{k}) + \text{h.c.} \right)^2 \\
& + v_{17} \left(\psi_{Y\sigma}^\dagger(\mathbf{k}) \tilde{\tau}^1 \psi_{\Gamma\sigma}(\mathbf{k}) + \text{h.c.} \right)^2 \\
& + v_{19} \left(\psi_{X\sigma}^\dagger(\mathbf{k}) \tilde{\tau}^1 \psi_{\Gamma\sigma}(\mathbf{k}) + \text{h.c.} \right)^2 \\
& \left. + v_{19} \left(\psi_{Y\sigma}^\dagger(\mathbf{k}) \tau^+ \psi_{\Gamma\sigma}(\mathbf{k}) + \text{h.c.} \right)^2 \right], \tag{2.26}
\end{aligned}$$

Note that all terms are diagonal in spin space. In terms of the more usual multi-orbital Hubbard model with onsite interactions, the first three coefficients originate from the Hund's rule coupling, $v_{13} = v_{15} = v_{17} = J$, while the last one arises from the intra-orbital Hubbard term, $v_{19} = U/2$ [65]. Here, we are not interested in which interactions will drive the SDW transition. Rather, we will assume a nearby SDW instability and compute how the interplay between these interactions and the SOC affect the magnetic action.

Finally, in order to be able to derive the magnetic action in the next sections, we need also to establish how the magnetic order parameters \mathbf{M}_1 and \mathbf{M}_2 , corresponding to $(\pi, 0)$ and $(0, \pi)$ order in the unfolded zone, couple to the low-energy electronic states. Here, we will consider only intra-orbital magnetism. Indeed, previous Hartree-Fock investigations of the five-orbital Hubbard model have shown that the dominant contributions to the magnetic instability arise from intra-orbital couplings [72, 115]. Therefore, the SDW vertices become:

$$\begin{aligned}
\mathcal{H}_{\text{SDW}} = & \mathbf{M}_1 \cdot \sum_{\mathbf{k}\alpha\beta} \left(c_{yz,\mathbf{k}\alpha}^\dagger \boldsymbol{\sigma}_{\alpha\beta} c_{yz,\mathbf{k}+\mathbf{Q}_1\beta} + \text{h.c.} \right) \\
& + \mathbf{M}_2 \cdot \sum_{\mathbf{k}\alpha\beta} \left(c_{xz,\mathbf{k}\alpha}^\dagger \boldsymbol{\sigma}_{\alpha\beta} c_{xz,\mathbf{k}+\mathbf{Q}_2\beta} + \text{h.c.} \right) \tag{2.27}
\end{aligned}$$

which, transformed to the spinor representation, yields:

$$\begin{aligned}
\mathcal{H}_{\text{SDW}} = & \mathbf{M}_1 \cdot \sum_{\mathbf{k}} \left[\psi_{\Gamma,\mathbf{k}}^\dagger \left(\tilde{\tau}^1 \otimes \boldsymbol{\sigma} \right) \psi_{X,\mathbf{k}+\mathbf{Q}_1} + \text{h.c.} \right] \\
& + \mathbf{M}_2 \cdot \sum_{\mathbf{k}} \left[\psi_{\Gamma,\mathbf{k}}^\dagger \left(-\tau^- \otimes \boldsymbol{\sigma} \right) \psi_{Y,\mathbf{k}+\mathbf{Q}_2} + \text{h.c.} \right] \tag{2.28}
\end{aligned}$$

Note that, in the language of Ref. [65], the SDW Hamiltonian transforms under the E_{M_4} two-dimensional irreducible representation of $P4/nmm$.

2.3 Anisotropic magnetic free energy

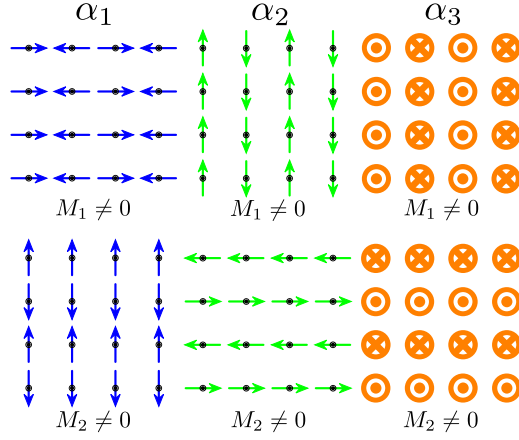


Figure 2.3: Sketch of the different uniaxial (i.e. stripe-like) magnetic configurations corresponding to the different anisotropic terms in the magnetic free energy (2.30) with coefficients α_1 , α_2 , and α_3 .

2.3 Anisotropic magnetic free energy

To understand the origin of the magnetic anisotropies, we first review the group theoretical arguments of Ref. [65]. In the absence of SOC, all the components of the magnetic order parameters belong to the same irreducible representation E_{M_4} , as shown above, and the free energy depends only on the invariant form $\mathbf{M}_1^2 + \mathbf{M}_2^2$. However, with the introduction of SOC, the spin and orbital degrees of freedom are no longer independent. Consequently, the components of \mathbf{M}_i must belong to different irreducible representations of $P4/nmm$, if one enforces the combination of the spin *and* orbital parts of the magnetic order parameter to still transform under E_{M_4} . As a result, the individual components of \mathbf{M}_1 and \mathbf{M}_2 transform according to the following two-dimensional irreducible representations [65]

$$E_{M_1} : \begin{pmatrix} M_{1,x} \\ M_{2,y} \end{pmatrix} \quad E_{M_2} : \begin{pmatrix} M_{1,y} \\ M_{2,x} \end{pmatrix} \quad E_{M_3} : \begin{pmatrix} M_{1,z} \\ M_{2,z} \end{pmatrix}. \quad (2.29)$$

Because these components belong to different irreducible representations, they will, in general, have different transition temperatures. Therefore, the free energy must acquire the leading-order anisotropic terms:

$$\begin{aligned} \delta F = & \alpha_1 (M_{1,x}^2 + M_{2,y}^2) \\ & + \alpha_2 (M_{1,y}^2 + M_{2,x}^2) \\ & + \alpha_3 (M_{1,z}^2 + M_{2,z}^2). \end{aligned} \quad (2.30)$$

The smallest α_i coefficient determines which type of magnetic order condenses first. In Fig. 2.3, we show separately the real-space spin configurations corresponding to the components of \mathbf{M}_1 and \mathbf{M}_2 associated with each coefficient α_i . Specifically, if $\alpha_1 < \alpha_2, \alpha_3$, then \mathbf{M}_i points parallel to the ordering vector \mathbf{Q}_i (of the unfolded zone); if $\alpha_2 < \alpha_1, \alpha_3$, \mathbf{M}_i still points in-plane, but perpendicular to the ordering vector \mathbf{Q}_i . Finally, if $\alpha_3 < \alpha_1, \alpha_2$, \mathbf{M}_i

2.3 Anisotropic magnetic free energy

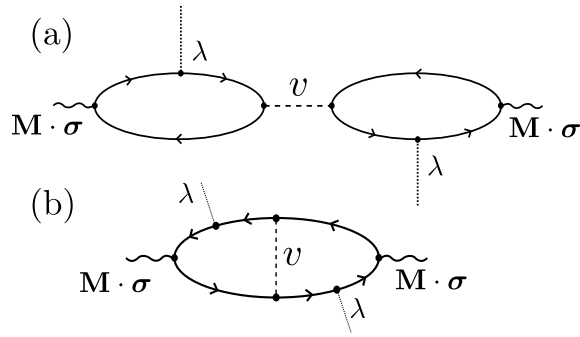


Figure 2.4: Schematic representation of the two distinct type of Feynman diagrams at $\mathcal{O}(v, \lambda^2)$: two-loop diagrams (a) and one-loop diagrams (b). Only the one-loop diagrams contribute to the anisotropic terms.

points out-of-plane. Note that this analysis does not reveal whether only either \mathbf{M}_1 or \mathbf{M}_2 condense, or if both condense simultaneously. To establish the actual ground state, it is necessary to go to higher order in the free energy. We will come back to this point in Section 2.4. Note that the spin-anisotropic terms preserve the tetragonal symmetry of the system.

Here, our goal is to evaluate microscopically the α_i coefficients using the model of the previous section. Within the non-interacting part of the model, we find that even the presence of spin-orbit coupling does not introduce magnetic anisotropies. The reason is that the model effectively has an enlarged $P4/nmm \otimes P4/nmm$ symmetry, since the states at Γ and the states at M are treated independently. Of course, the fact that these states are connected in realistic tight-binding models ensures that some level of spin-anisotropy will be introduced at the non-interacting level. Such an effect will be likely a high-energy effect, as it involves states away from the Fermi level [116]. Here, instead, we focus on the low-energy contributions to the spin anisotropy. Consequently, they must come from interactions – particularly, from the interaction terms that couple the states at Γ and at M , and therefore remove the enlarged $P4/nmm \otimes P4/nmm$ symmetry. These are precisely the terms listed in Eq. (2.26).

We proceed with a straightforward diagrammatic approach by dressing the non-interacting particle-hole bubble with the SOC term λ in Eq. (2.23) and with the interactions v_i in Eq. (2.26). The SDW vertices coupling the magnetic order parameters to the non-interacting Green’s functions are those derived in Eq. (2.28). Both λ and v_i are treated perturbatively to leading order. Because terms of the order $\mathcal{O}(\lambda)$ are forbidden by symmetry, we consider the diagrams of the orders $\mathcal{O}(\lambda^2)$ and $\mathcal{O}(v_i)$.

To order $\mathcal{O}(v_i)$, there are two distinct types of interaction-dressed diagrams, as depicted in Fig. 2.4. On top of that, to order $\mathcal{O}(\lambda^2)$, each of the two diagrams can be dressed by a pair of SOC legs in eight different ways. Because symmetry requirements forbid terms that couple directly \mathbf{M}_1 and \mathbf{M}_2 at the quadratic level, the pair of SOC legs must correspond to the same SOC term, i.e. either $h_{\Gamma}^{\text{SOC}}(\mathbf{k})$ or $h_M^{\text{SOC}}(\mathbf{k})$ in Eq. (2.23). Explicit calculation of the traces over the Pauli-matrices reveals also that the only combinations of SOC legs that yield anisotropic magnetic terms are those in which one SOC leg appears in the upper-

2.3 Anisotropic magnetic free energy

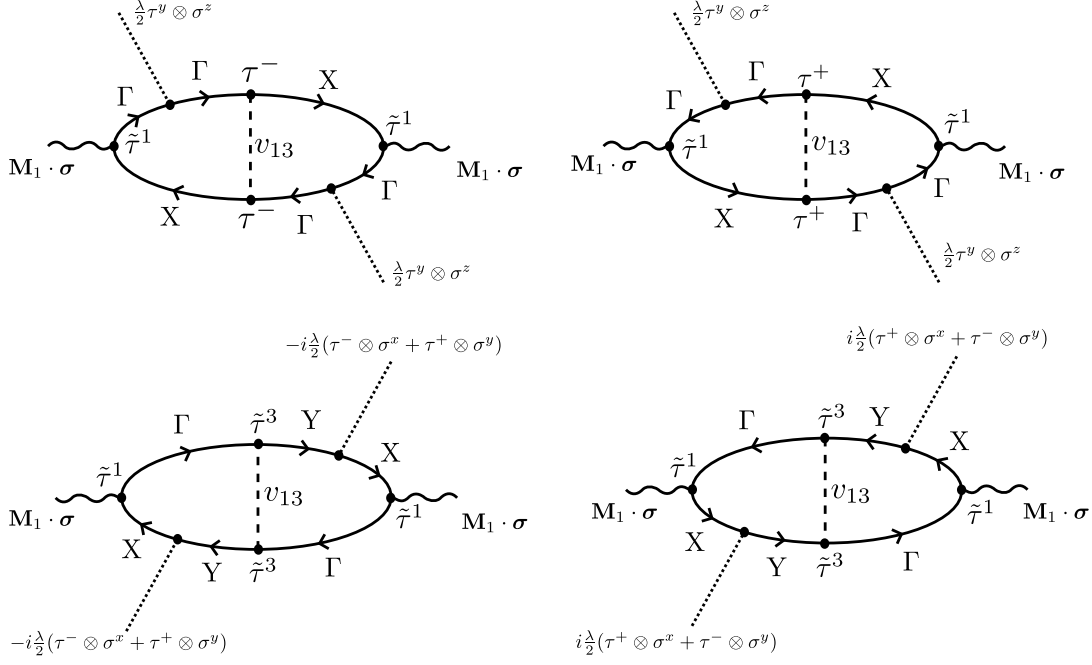


Figure 2.5: Illustration of distinct second-order one-loop diagrams in the case where the electron-electron interaction is given by v_{13} and the magnetic order parameter is \mathbf{M}_1 . Note that the electron-electron vertex depends on the direction of momentum, i.e. the upper left and upper right diagrams are not identical.

right (lower-right) part of the diagram and the other SOC leg appears in the lower-left (upper-left) part of the diagram.

We find that all two-loop diagrams (i.e. those represented in Fig. 2.4a) vanish, and therefore do not contribute to the magnetic anisotropy term (2.30). We show this explicitly in Appendix 2.C. Therefore, all that is left is to compute the one-loop diagram represented in Fig. 2.4b. The calculation is tedious but straightforward. To illustrate it, consider the interaction v_{13} . The one-loop diagrams contributing to the anisotropic terms $M_{1,\mu}^2$ are shown in Fig. 2.5. As mentioned above, there are two possible placements for the two SOC legs, in opposite sides of the loop. For each diagram, one has to also consider its hermitian-conjugate partner, since the interaction vertices and the SDW vertices are not adjoint operators. Furthermore, the diagrammatic rules derived for this problem impose an overall minus sign to each one-loop diagram, and enforce the trace over the Pauli matrices to be taken in the direction opposite to the arrows. Finally, to compute these traces, it is useful to employ the following Pauli matrix identity:

$$\text{tr} \left(\sigma^i \sigma^j \sigma^k \sigma^l \right) = 2 \left(\delta^{ij} \delta^{kl} - \delta^{ik} \delta^{jl} + \delta^{il} \delta^{jk} \right) \quad (2.31)$$

A straightforward evaluation of these four diagrams gives then three different anisotropic

2.3 Anisotropic magnetic free energy

terms for the magnetic free energy:

$$\begin{aligned}
\delta F &= - v_{13} \frac{\lambda^2}{2} \sum_{\substack{\mathbf{k}\mathbf{k}' \\ \omega_n\omega_{n'}}} \left[\text{tr} \left(\tilde{\tau}^1 G'_X \tau^- G'_\Gamma \tau^y G'_\Gamma \tilde{\tau}^1 G_X \tau^- G_\Gamma \tau^y G_\Gamma \right) \right. \\
&\quad + \left. \text{tr} \left(\tilde{\tau}^1 G'_\Gamma \tau^y G'_\Gamma \tau^+ G'_X \tilde{\tau}^1 G_\Gamma \tau^y G_\Gamma \tau^+ G_X \right) \right] \left(M_{1,z}^2 - M_{1,x}^2 - M_{1,y}^2 \right) \\
&\quad + v_{13} \frac{\lambda^2}{2} \sum_{\substack{\mathbf{k}\mathbf{k}' \\ \omega_n\omega_{n'}}} \left[\text{tr} \left(\tilde{\tau}^1 G'_X \tau^- G'_Y \tilde{\tau}^3 G'_\Gamma \tilde{\tau}^1 G_X \tau^- G_Y \tilde{\tau}^3 G_\Gamma \right) \right. \\
&\quad + \left. \text{tr} \left(\tilde{\tau}^1 G'_\Gamma \tilde{\tau}^3 G'_Y \tau^+ G'_X \tilde{\tau}^1 G_\Gamma \tilde{\tau}^3 G_Y \tau^+ G_X \right) \right] \left(M_{1,x}^2 - M_{1,y}^2 - M_{1,z}^2 \right) \\
&\quad + v_{13} \frac{\lambda^2}{2} \sum_{\substack{\mathbf{k}\mathbf{k}' \\ \omega_n\omega_{n'}}} \left[\text{tr} \left(\tilde{\tau}^1 G'_X \tau^+ G'_Y \tilde{\tau}^3 G'_\Gamma \tilde{\tau}^1 G_X \tau^+ G_Y \tilde{\tau}^3 G_\Gamma \right) \right. \\
&\quad + \left. \text{tr} \left(\tilde{\tau}^1 G'_\Gamma \tilde{\tau}^3 G'_Y \tau^- G'_X \tilde{\tau}^1 G_\Gamma \tilde{\tau}^3 G_Y \tau^- G_X \right) \right] \left(M_{1,y}^2 - M_{1,x}^2 - M_{1,z}^2 \right) \\
\delta F &= v_{13} \lambda^2 \left(\sum_{\mathbf{k}, \omega_n} [G_X]_{12} [G_Y]_{12} [G_\Gamma]_{21} \right)^2 \left(M_{1,x}^2 - M_{1,y}^2 - M_{1,z}^2 \right). \quad (2.32)
\end{aligned}$$

Here, the primed Green's functions are short-handed notations for $G'_i = G_i(\mathbf{k}', \omega'_n)$. The Green functions are given by

$$[G_A]_{ij} = \sum_m \frac{a_m^i(\mathbf{k})_A a_m^j(\mathbf{k})_A^*}{i\omega_n - (\epsilon_{A,m}(\mathbf{k}) - \mu)}, \quad (2.33)$$

where $\epsilon_{A,m}(\mathbf{k})$ are the eigenenergies of the matrix $h_A(\mathbf{k})$ and $a_m^i(\mathbf{k})_A$ is the unitary transformation between the spinor basis and the band basis. In Eq. (2.32), the coefficient of the term $(M_{1,z}^2 - M_{1,x}^2 - M_{1,y}^2)$ vanishes because of the antisymmetry of the $G_\Gamma \tau^y G_\Gamma$ matrix in spinor space, whereas the coefficient of $(M_{1,y}^2 - M_{1,x}^2 - M_{1,z}^2)$ vanishes because $[G_\Gamma]_{12}(\mathbf{k}) \propto k_x k_y$, causing the sum over momentum to vanish.

Note that while the upper diagrams shown in Fig. 2.5 introduce the anisotropy between the in-plane and out-of-plane components of the magnetic order parameter, the lower diagrams contribute to the anisotropy between $M_{1,x}$ and $M_{1,y}$. The reason for this is the character of the SOC in the effective model, which remains diagonal in the spin sector near the Γ -point due to xz - and yz -orbital characters of the electronic states. As a result, particle-hole excitations involving fermions from the Γ -point and from the X/Y -point do not allow for a spin-flip, which would be necessary to generate the anisotropy between $M_{1,x}$ and $M_{1,y}$. Only the inclusion of the particle-hole excitations between the two electron pockets, as described by the lower diagrams, generates the anisotropy between the x and y components of the magnetization.

Repeating the same calculation for \mathbf{M}_2 gives the same result, but with $M_{1,x} \rightarrow M_{2,y}$ and $M_{1,y} \rightarrow M_{2,x}$, as expected by symmetry. Therefore, we can recast this contribution to

2.3 Anisotropic magnetic free energy

the free energy in the form of Eq. (2.30) via differences in the anisotropic coefficients α :

$$\alpha_2^{(v_{13})} - \alpha_1^{(v_{13})} = -2v_{13}\lambda_M^2 \left(\sum_{\mathbf{k}, \omega_n} [G_X]_{12} [G_Y]_{12} [G_\Gamma]_{21} \right)^2 \quad (2.34)$$

$$\alpha_3^{(v_{13})} - \alpha_1^{(v_{13})} = 0. \quad (2.35)$$

The same procedure applied to the other interactions v_{15} , v_{17} , and v_{19} reveals that only the first two give rise to anisotropic terms. The final result for the anisotropic coefficients is:

$$\begin{aligned} \alpha_2 - \alpha_1 &= 2v_{15}\lambda^2 \left(\sum_{\mathbf{k}, \omega_n} [G_\Gamma]_{11} [G_X]_{11} [G_Y]_{22} \right)^2 \\ &\quad - 2v_{13}\lambda^2 \left(\sum_{\mathbf{k}, \omega_n} [G_\Gamma]_{21} [G_X]_{12} [G_Y]_{12} \right)^2, \end{aligned} \quad (2.36)$$

$$\begin{aligned} \alpha_3 - \alpha_1 &= 2v_{17}\lambda^2 \left(\sum_{\mathbf{k}, \omega_n} [G_\Gamma i\tau^y G_\Gamma]_{12} [G_X]_{11} \right)^2 \\ &\quad - 2v_{13}\lambda^2 \left(\sum_{\mathbf{k}, \omega_n} [G_\Gamma]_{21} [G_X]_{12} [G_Y]_{12} \right)^2. \end{aligned} \quad (2.37)$$

Mapping these interactions back to the more familiar multi-orbital Hubbard model, as done in Ref. [65], reveals that $v_{13} = v_{15} = v_{17} = J$, while the non-contributing term is $v_{19} = U/2$. Thus, our microscopic calculation reveals that the low-energy magnetic anisotropy arises from a combination of the SOC and of the Hund's rule coupling. This anisotropy is present in the paramagnetic tetragonal phase, and does not require orbital or nematic order.

It is now straightforward to determine which of the three terms in the free energy Eq. (2.30) dominates. For instance, if both $\alpha_2 - \alpha_1 > 0$ and $\alpha_3 - \alpha_1 > 0$, α_1 is the smallest of the three coefficients and the ordered components of the magnetic moments will be $M_{1,x}$ and/or $M_{2,y}$. By evaluating the expressions in Eqs. (2.36) and (2.37) numerically, using the parameters that give the band dispersions and Fermi surface of Fig. 2.2, we can establish an effective ‘‘doping-temperature phase diagram’’ for the dominant anisotropy term as function of different values of the chemical potential μ and of the magnetic transition temperature T . Because the phase boundaries of this phase diagram are given by the conditions $\alpha_2 = \alpha_1$ or $\alpha_3 = \alpha_1$, and because these coefficients are independent of U and have J as an overall pre-factor (see Eqs. (36) and (37)), the phase boundaries do not change by varying U and J . The phase diagram, shown in fig. 2.6, reveals that for most of the parameter space considered here, the α_1 term is the smallest one, implying that the magnetic moments point parallel to their ordering vectors \mathbf{Q}_i below the magnetic transition. There is a small range of parameters in which the moments lie in-plane, but perpendicular to their ordering vectors (i.e. α_2 is the smallest). Such a parameter regime is likely not relevant for the iron pnictides, since it would require an ‘‘undoped’’ composition (i.e. $\mu = 0$) to display a rather small magnetic transition temperature. Most interestingly, we find a robust region in which the moments point out-of-plane (i.e. α_3 is the smallest). This happens at any temperature, but always in the hole-doped side of the phase diagram

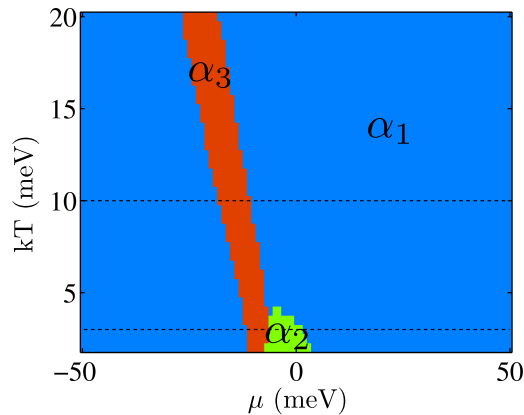


Figure 2.6: Doping-temperature phase diagram displaying the smallest magnetic anisotropy coefficient α . When α_1 is the smallest, the moments point in-plane and parallel to the ordering vectors; when α_2 is the smallest, the moments point in-plane but perpendicular to the ordering vectors; finally, when α_3 is the smallest, the moments point out-of-plane. The corresponding uniaxial configurations are shown in Fig. 2.3. Note that temperature here actually refers to the magnetic transition temperature, as our model approaches the onset of long-range magnetic order from the paramagnetic state.

($\mu < 0$). In Fig. 2.7, we plot a zoom of the behavior of $\alpha_2 - \alpha_1$ and $\alpha_3 - \alpha_1$ as function of the chemical potential for two fixed temperatures to illustrate the different regimes obtained. Note that, for most of the phase diagram, $(\alpha_2 - \alpha_1) \ll (\alpha_3 - \alpha_1)$, regardless of the value of $J\lambda^2$, which appears as an overall prefactor of all α_i terms. This implies that the spin anisotropy behaves effectively as an easy-plane anisotropy. The fact that α_3 becomes the smallest coefficient in a narrow region of the phase diagram can be attributed to the fact that the term $\sum_{\mathbf{k}, \omega_n} [G_{\Gamma} i \tau^y G_{\Gamma}]_{12} [G_X]_{11}$ in Eq. (2.37) changes sign from hole-doping to electron-doping. This behavior can be understood qualitatively by considering a hypothetical band structure in which all pockets are perfectly nested, $G_{\Gamma} = (i\omega_n + \varepsilon) \otimes \tau^0$ and $G_X = G_Y = (i\omega_n - \varepsilon) \otimes \tau^0$. A straightforward calculation reveals that the three-Green's function term above has different signs for $\mu > 0$ and $\mu < 0$, implying that it must vanish for a certain chemical potential value in the case of a realistic band structure.

Our results reveal not only an important asymmetry between electron- and hole-doping, but also agree qualitatively with experiments. In particular, neutron scattering measurements in hole- and electron-doped BaFe_2As_2 [32–35] find generally in-plane moments parallel to \mathbf{Q}_i in the magnetically-ordered state, except at a narrow hole-doping range in which the moments reorient and point out-of-the-plane.

2.4 Tetragonal vs stripe magnetic order

The previous section established the direction of the magnetic moments, but not the magnetic ground state. For instance, from the analysis of the second-order terms of the free energy, it is impossible to distinguish the cases in which either \mathbf{M}_1 or \mathbf{M}_2 condense (i.e. $\mathbf{M}_2 = 0$ or $\mathbf{M}_1 = 0$) from the case in which both condense simultaneously ($\mathbf{M}_1 = \mathbf{M}_2 \neq 0$). The former case gives the striped orthorhombic magnetic phases shown in Fig. 2.3, whereas

2.4 Tetragonal vs stripe magnetic order

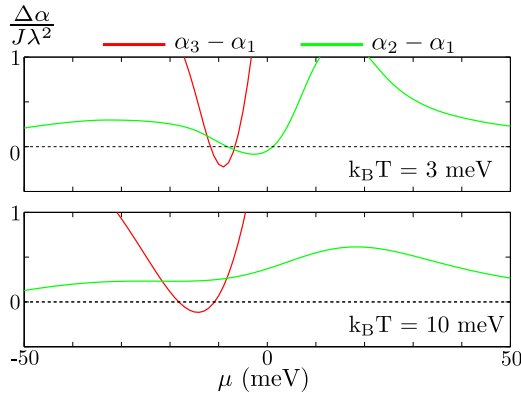


Figure 2.7: Plots showing the dependence of $\alpha_3 - \alpha_1$ (red curve) and $\alpha_2 - \alpha_1$ (green curve) for two distinct temperatures (see the dashed lines in Fig. 2.6) as function of the chemical potential.

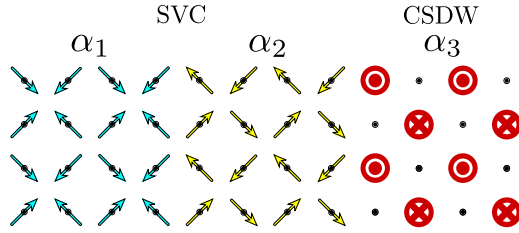


Figure 2.8: Sketch of the three possible biaxial tetragonal magnetic phases. Here SVC is the spin vortex crystal phase (with non-collinear magnetic moments) and CSDW is the charge-spin density wave phase (with non-uniform magnetic moments).

the latter case gives rise to a double- \mathbf{Q} (i.e. biaxial) magnetic state that preserves the tetragonal symmetry of the system. From the form of the anisotropic terms in the free energy (see Sec. 2.3), there are three different types of tetragonal magnetic ground states, as shown in Fig. 2.8. Two of them correspond to the so-called spin-vortex crystal phase (SVC), a non-collinear state in which $M_{1,x} = M_{2,y} \neq 0$ or $M_{1,y} = M_{2,x} \neq 0$, whereas the third one corresponds to the so-called charge-spin density-wave phase (CSDW) [117], a non-uniform state in which $M_{1,z} = M_{2,z} \neq 0$.

To determine whether the ground state corresponds to an orthorhombic uniaxial SDW (i.e. either $\mathbf{M}_1 \neq 0$ or $\mathbf{M}_2 \neq 0$) or to a tetragonal biaxial SDW (i.e. $\mathbf{M}_1 = \mathbf{M}_2 \neq 0$), we need to go to higher order in the free energy expansion. Symmetry requires the free energy to have the form (in the absence of SOC):

$$F^{(4)}(\mathbf{M}_1, \mathbf{M}_2) = \frac{u}{2} (\mathbf{M}_1^2 + \mathbf{M}_2^2)^2 - \frac{g}{2} (\mathbf{M}_1^2 - \mathbf{M}_2^2)^2 + 2w(\mathbf{M}_1 \cdot \mathbf{M}_2)^2. \quad (2.38)$$

Minimizing this expression shows that the tetragonal biaxial state is realized when $g < 0$ or $g < -w$, whereas the orthorhombic uniaxial state takes place when $g > 0$ and $g > -w$.

The same model was derived by different itinerant approaches for the magnetic instabilities of the iron pnictides, revealing different parameter regimes in which the uniaxial or the biaxial states are the ground states [64, 72, 79, 94, 95, 118, 119]. In this regard, the novelty of our approach relies on the relationship between these ground states and the

2.4 Tetragonal vs stripe magnetic order

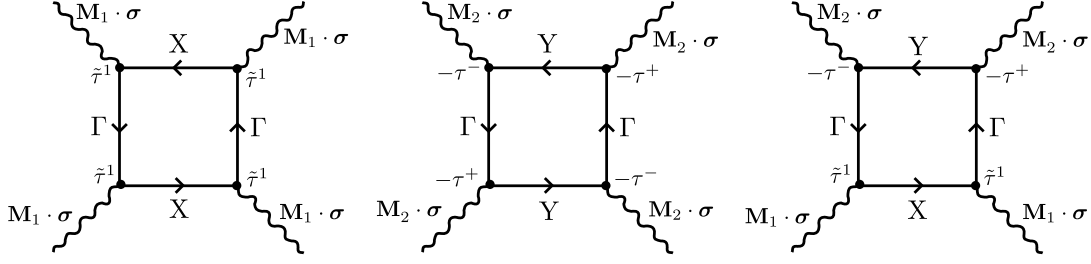


Figure 2.9: Illustration of the three distinct fourth order diagrams that contribute to $F^{(4)}$. Note that the right diagram has a symmetry factor of two, while the symmetry factor of the middle and left diagrams is one. One might expect there to be a fourth diagram with alternating \mathbf{M}_1 and \mathbf{M}_2 , however, the vertex coupling the SDW order parameter and the fermions forbids it (see Appendix 2.D for more details).

magnetic anisotropies, and also on the employment of a low-energy model that respects all symmetries of the FeAs plane, including the As puckering that enhances the size of the Fe unit cell. Because u and g are non-zero even for vanishing SOC and interactions, we compute only the contributions arising from the non-interacting part of the Hamiltonian. This is achieved either by standard diagrammatics or by explicitly integrating out the electronic degrees of freedom. We find:

$$\begin{aligned}
 F^{(4)} &= \mathbf{M}_1^4 \sum_{\mathbf{k}, \omega_n} \text{tr} \left(\tilde{\tau}^1 G_\Gamma \tilde{\tau}^1 G_X \tilde{\tau}^1 G_\Gamma \tilde{\tau}^1 G_X \right) + \mathbf{M}_2^4 \sum_{\mathbf{k}, \omega_n} \text{tr} \left(\tau^+ G_\Gamma \tau^- G_Y \tau^+ G_\Gamma \tau^- G_Y \right) \\
 &\quad + 2\mathbf{M}_1^2 \mathbf{M}_2^2 \sum_{\mathbf{k}, \omega_n} \text{tr} \left(\tau^+ G_\Gamma \tilde{\tau}^1 G_X \tilde{\tau}^1 G_\Gamma \tau^- G_Y \right) \\
 F^{(4)} &= \mathbf{M}_1^4 \sum_{\mathbf{k}, \omega_n} \left([G_\Gamma]_{11}^2 [G_X]_{11}^2 \right) + \mathbf{M}_2^4 \sum_{\mathbf{k}, \omega_n} \left([G_\Gamma]_{22}^2 [G_Y]_{11}^2 \right) \\
 &\quad + 2\mathbf{M}_1^2 \mathbf{M}_2^2 \sum_{\mathbf{k}, \omega_n} \left([G_\Gamma]_{12} [G_X]_{11} [G_Y]_{11} \right), \tag{2.39}
 \end{aligned}$$

with the corresponding diagrams shown in Fig. 2.9. Rewriting the free energy in the form (2.38), we can readily obtain u , g , and w :

$$u = \sum_{\mathbf{k}, \omega_n} \left([G_\Gamma]_{12}^2 [G_Y]_{11} [G_X]_{11} + [G_\Gamma]_{11}^2 [G_X]_{11}^2 \right) \tag{2.40}$$

$$g = \sum_{\mathbf{k}, \omega_n} \left([G_\Gamma]_{12}^2 [G_Y]_{11} [G_X]_{11} - [G_\Gamma]_{11}^2 [G_X]_{11}^2 \right) \tag{2.41}$$

$$w = 0. \tag{2.42}$$

One might expect the third diagram in Fig. 2.9 to result in a non-vanishing w , however, contraction of the Pauli matrices (see Eq. 2.31) reveals that the $\mathbf{M}_1 \cdot \mathbf{M}_2$ term cancels. More generally, $w = 0$ is a robust property of our model, a consequence of momentum conservation and the absence of a Fermi pocket at (π, π) (see Appendix 2.D). Including a hole-pocket at (π, π) or interactions will however lead to a non-zero contribution to w [79].

We can now compute numerically the value of g for the same ‘‘doping-temperature phase-diagram’’ studied in the previous section, see Fig. 2.6. The combined result, shown

2.4 Tetragonal vs stripe magnetic order

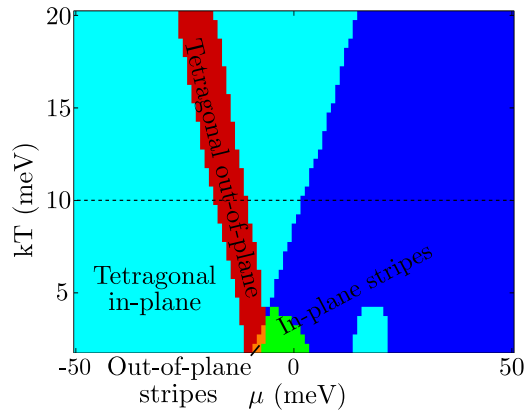


Figure 2.10: Doping-temperature phase diagram of the different types of magnetic ground state (stripes or tetragonal) and their corresponding spin orientation (in-plane or out-of-plane). The color-code corresponds to the magnetic configurations shown in Figs. 2.3 and 2.8. Note that temperature here actually refers to the magnetic transition temperature, as our model approaches the onset of long-range magnetic order from the paramagnetic state.

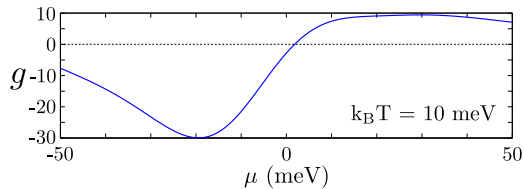


Figure 2.11: The quartic coefficient g as a function of the chemical potential μ for a constant temperature (see the dashed line in Fig. 2.10). When g is negative the system chooses a tetragonal biaxial magnetic phase whereas for positive g , the system selects an orthorhombic uniaxial stripe state.

in Fig. 2.10, accentuates the asymmetry between hole- and electron-doping discussed previously. In particular, while hole-doping tends to favor a tetragonal biaxial SDW state, electron-doping tends to favor an orthorhombic uniaxial SDW state. A cut with the behavior of g as function of μ for a fixed temperature is also shown in Fig. 2.11. To gain more insight into the behavior of g , we consider once again the hypothetical case of perfectly-nested bands, $G_\Gamma = (i\omega_n + \varepsilon)^{-1} \otimes \tau^0$ and $G_X = G_Y = (i\omega_n - \varepsilon)^{-1} \otimes \tau^0$. In this case, from the equations above, $g < 0$. Building on the results of Ref. [64], we expect that the sign of g will change once the two hole pockets become rather different in size, such that one of them becomes poorly nested with the electron pockets. Our calculations indicate that, for the general tight-binding model studied here, this is favored by hole doping rather than electron doping.

It is important to emphasize that these results should be understood as general trends as function of the chemical potential, rather than a full determination of the ground state for each specific value of μ . This is because, in contrast to the previous section, in which the lowest order contribution to the spin anisotropy arises solely from the SOC and the interactions, there are other potential contributions to g beyond the scope of the current work. Among these contributions, we highlight the sizable magneto-elastic coupling,

2.5 Discussion and Conclusions

which should extend the stripe phase to wider doping ranges [74, 120], and interaction corrections, which can also favor the uniaxial over the biaxial state [64, 79]. With this word of caution, we note that the tendency observed here that hole-doped compounds are more favorable to a tetragonal magnetic phase as compared to their electron-doped counterparts is in qualitative agreement with experiments, which observe a small region of tetragonal magnetism near the optimally-hole doped pnictides $\text{Ba}_{1-x}\text{Na}_x\text{Fe}_2\text{As}_2$ [51], $\text{Sr}_{1-x}\text{Na}_x\text{Fe}_2\text{As}_2$ [35], $\text{Ba}_{1-x}\text{K}_x\text{Fe}_2\text{As}_2$ [52, 121], and $\text{Ba}(\text{Fe}_{1-x}\text{Mn}_x)_2\text{As}_2$ [122].

Interestingly, in the first three compounds, neutron scattering has shown that the onset of a tetragonal magnetic state takes place in a region in which the magnetic moments reorient from in-plane to out-of-plane. Within our analysis, this can be attributed to the robust region in parameter space in which α_3 is the smallest anisotropic coefficient (see Fig. 2.10). More importantly, this anisotropic coefficient removes the degeneracy between the two types of tetragonal SDW phase – the SVC and the CSDW states (see Fig. 2.8) – by favoring the latter. This is expected to happen even if $w \neq 0$, since the latter is a quartic coefficient, whereas α_3 is a quadratic coefficient. Therefore, at least near the onset of the magnetic transition, it is the SOC and the Hund’s rule coupling that select the CSDW phase. Recently, Mössbauer [35] and μSR [123] experiments in $\text{Sr}_{1-x}\text{Na}_x\text{Fe}_2\text{As}_2$ and $\text{Ba}_{1-x}\text{K}_x\text{Fe}_2\text{As}_2$, respectively, have reported direct evidence that indeed the CSDW state is realized in the regime where the spin is reoriented and the magnetic long-range order preserves tetragonal symmetry.

2.5 Discussion and Conclusions

In summary, we have shown that within a low-energy model that respects the symmetries of the FeAs plane, magnetic anisotropy arises naturally from the combination of the spin-orbit coupling and the Hund’s rule coupling. The magnetic anisotropy consists of three terms (see Sec. 2.3). Although it cannot be mapped generally on an easy-axis or an easy-plane term, it effectively behaves as an easy-plane term for a large part of the parameter region studied here, since $(\alpha_2 - \alpha_1) \ll (\alpha_3 - \alpha_1)$. We found that, for most of the temperature-doping phase diagram, the spin anisotropy is such that the magnetic moments point in-plane and parallel to the direction of the ordering vector. For a small doping range in the hole-doped side, across all temperatures studied, the magnetic moments tend to reorient and point out-of-plane. These features are consistent with those observed experimentally, including the spin reorientation observed in the hole-doped pnictides $\text{Ba}_{1-x}\text{Na}_x\text{Fe}_2\text{As}_2$ [32], $\text{Sr}_{1-x}\text{Na}_x\text{Fe}_2\text{As}_2$ [35], $\text{Ba}_{1-x}\text{K}_x\text{Fe}_2\text{As}_2$ [34]. We also found a general tendency of tetragonal double- \mathbf{Q} magnetic order for the hole-doped side of the phase diagram, whereas the orthorhombic single- \mathbf{Q} stripe magnetic order is favored in the electron-doped side. Although this is in general agreement with the experimental observations in $\text{Ba}_{1-x}\text{Na}_x\text{Fe}_2\text{As}_2$ [51], $\text{Sr}_{1-x}\text{Na}_x\text{Fe}_2\text{As}_2$ [35], $\text{Ba}_{1-x}\text{K}_x\text{Fe}_2\text{As}_2$ [52], and $\text{Ba}(\text{Fe}_{1-x}\text{Mn}_x)_2\text{As}_2$ [122], our results seem to overestimate the size of the region in which the tetragonal magnetic state is stable. A possible reason for this discrepancy is that our model does not account for other factors that usually favor the stripe over the tetragonal magnetic state, such as the magneto-elastic coupling [74, 120] and the residual interactions

2.5 Discussion and Conclusions

not directly responsible for the SDW instability [64, 79]. Yet, our results provide a clear connection between the spin reorientation and the type of tetragonal magnetic state observed in the hole-doped iron pnictides – namely, the charge-spin density-wave state with a non-uniform magnetization [35, 123].

An important consequence of our results is that the spin anisotropy is not necessarily tied to the orbital order that is triggered across the nematic/structural transition [105]. Although it is plausible that such an orbital order affects the spin anisotropy, the latter exists already in the tetragonal paramagnetic state as a result of the symmetry properties of the FeAs plane. In this regard, it would be interesting to investigate how the spin anisotropies in the tetragonal-paramagnetic phase studied here are connected to the spin anisotropies in the low-temperature phase, after both magnetic and nematic orders are well established. Finally, our results open the important question of how this particular form of magnetic anisotropy impacts the normal state properties of the iron pnictides. In particular, the onset temperatures and the characters of the coupled nematic-magnetic transitions are expected to be strongly affected by any form of spin anisotropy [47, 105, 124].

Appendices

2.A Expansion of tight-binding Hamiltonian for small k

In this appendix we derive explicitly the non-interacting Hamiltonian H_0 introduced in sec. 2.2. As explained in that section, we need to project and expand the 5-orbital tight-binding dispersion $\varepsilon_{\mu\nu}(\mathbf{k})$, where $\mu, \nu = 1, \dots, 5$ are the orbital indices corresponding to xz , yz , $x^2 - y^2$, xy and $3z^2 - r^2$, respectively. The dispersions are given by [66]

$$\begin{aligned} \varepsilon_{11} = & \varepsilon_{xz/yz} + 2t_x^{11} \cos k_x + 2t_y^{11} \cos k_y + 4t_{xy}^{11} \cos k_x \cos k_y + 2t_{xx/yy}^{11} (\cos 2k_x - \cos 2k_y) \\ & + 4t_{xxy}^{11} \cos 2k_x \cos k_y + 4t_{xyy}^{11} \cos k_x \cos 2k_y + 4t_{xxyy}^{11} \cos 2k_x \cos 2k_y, \end{aligned} \quad (2.43)$$

$$\begin{aligned} \varepsilon_{22} = & \varepsilon_{xz/yz} + 2t_x^{22} \cos k_x + 2t_y^{22} \cos k_y + 4t_{xy}^{22} \cos k_x \cos k_y - 2t_{xx/yy}^{22} (\cos 2k_x - \cos 2k_y) \\ & + 4t_{xxy}^{22} \cos 2k_x \cos k_y + 4t_{xyy}^{22} \cos k_x \cos 2k_y + 4t_{xxyy}^{22} \cos 2k_x \cos 2k_y, \end{aligned} \quad (2.44)$$

$$\varepsilon_{33} = \varepsilon_{x^2-y^2} + 2t_{x/y}^{33} (\cos k_x + \cos k_y) + 4t_{xy}^{33} \cos k_x \cos k_y + 2t_{xx/yy}^{33} (\cos 2k_x + \cos 2k_y) \quad (2.45)$$

$$\begin{aligned} \varepsilon_{44} = & \varepsilon_{xy} + 2t_{x/y}^{44} (\cos k_x + \cos k_y) + t_{xy}^{44} \cos k_x \cos k_y + 2t_{xx/yy}^{44} (\cos 2k_x + \cos 2k_y) \\ & + 4t_{xxy/xyy}^{44} (\cos 2k_x \cos k_y + \cos k_x \cos 2k_y) + 4t_{xxyy}^{44} \cos 2k_x \cos 2k_y, \end{aligned} \quad (2.46)$$

$$\begin{aligned} \varepsilon_{55} = & \varepsilon_{z^2} + 2t_{x/y}^{55} (\cos k_x + \cos k_y) + 2t_{xx/yy}^{55} (\cos 2k_x \cos 2k_y) \\ & + 4t_{xxy/xyy}^{55} (\cos 2k_x \cos k_y + \cos k_x \cos 2k_y) + 4t_{xxyy}^{55} \cos 2k_x \cos 2k_y, \end{aligned} \quad (2.47)$$

$$\begin{aligned} \varepsilon_{12} = & 4t_{xy}^{12} \sin k_x \sin k_y + 4t_{xxy/xyy}^{12} (\sin 2k_x \sin k_y + \sin k_x \sin 2k_y) \\ & + 4t_{xxyy}^{12} \sin 2k_x \sin 2k_y, \end{aligned} \quad (2.48)$$

$$\varepsilon_{13} = i2t_y^{13} \sin k_y + i4t_{xy}^{13} \cos k_x \sin k_y - i4t_{xxy/xyy}^{13} (\cos k_x \sin 2k_y - \cos 2k_x \sin k_y) \quad (2.49)$$

$$\varepsilon_{14} = i2t_x^{14} \sin k_x - i4t_{xy}^{14} \sin k_x \cos k_y + i4t_{xxy}^{14} \sin 2k_x \cos k_y, \quad (2.50)$$

$$\varepsilon_{15} = i2t_y^{15} \sin k_y - i4t_{xy}^{15} \cos k_x \sin k_y - i4t_{xxyy}^{15} \cos 2k_x \sin 2k_y, \quad (2.51)$$

$$\varepsilon_{23} = i2t_x^{23} \sin k_x + i4t_{xy}^{23} \sin k_x \cos k_y - i4t_{xxy/xyy}^{23} (\sin 2k_x \cos k_y - \sin k_x \cos 2k_y) \quad (2.52)$$

$$\varepsilon_{24} = -i2t_y^{24} \sin k_y + i4t_{xy}^{24} \cos k_x \sin k_y - i4t_{xxyy}^{24} \cos k_x \sin 2k_y, \quad (2.53)$$

$$\varepsilon_{25} = -i2t_x^{25} \sin k_x + i4t_{xy}^{25} \sin k_x \cos k_y + i4t_{xxyy}^{25} \sin 2k_x \cos 2k_y, \quad (2.54)$$

$$\varepsilon_{34} = 4t_{xxy/xyy}^{34} (\sin k_x \sin 2k_y - \sin 2k_x \sin k_y), \quad (2.55)$$

$$\varepsilon_{35} = 2t_{x/y}^{35} (\cos k_x - \cos k_y) + 4t_{xxy/xyy}^{35} (\cos 2k_x \cos k_y - \cos k_x \cos 2k_y), \quad (2.56)$$

$$\varepsilon_{45} = 4t_{xy}^{45} \sin k_x \sin k_y + 4t_{xxyy}^{45} \sin 2k_x \sin 2k_y. \quad (2.57)$$

Here ε_i are the onsite energies associated with each orbital and $t_{ij}^{\mu\nu}$ are hopping parameters from orbital μ on site i to orbital ν on site j . The above expressions are accompanied by constraints on the coefficients $t_{ij}^{\mu\nu}$ due to tetragonal symmetry:

$$\begin{aligned} t_x^{11} &= t_y^{22} & t_y^{11} &= t_x^{22} & t_{xy}^{11} &= t_{xy}^{22} & t_{xx/yy}^{11} &= t_{xx/yy}^{22} \\ t_{xxy}^{11} &= t_{xyy}^{22} & t_{xxyy}^{11} &= t_{xxyy}^{22} & t_{xxyy}^{11} &= t_{xxyy}^{22} & t_y^{13} &= t_x^{23} \\ t_{xy}^{13} &= t_{xy}^{23} & t_{xxy/xyy}^{13} &= t_{xxy/xyy}^{23} & t_x^{14} &= t_y^{24} & t_{xy}^{14} &= t_{xy}^{24} \\ t_{xxy}^{14} &= t_{xxy}^{24} & t_y^{15} &= t_x^{25} & t_{xy}^{15} &= t_{xy}^{25} & t_{xxyy}^{15} &= t_{xxyy}^{25}. \end{aligned} \quad (2.58)$$

We are now in a position to expand the elements of $\varepsilon_{\mu\nu}(\mathbf{k})$ around the Γ , X and Y points. At the Γ point the orbitals xz and yz dominate, corresponding to the elements

2.B Spin-orbit coupling in orbital basis

ε_{11} , ε_{12} , ε_{21} and ε_{22} . Similarly, at the X (Y) point the dominant orbitals are yz (xz) and xy . To obtain these parts we expand ε_{22} (ε_{11}), ε_{24} (ε_{14}) and ε_{44} around $(k_x + \pi, k_y)$ ($(k_x, k_y + \pi)$):

$$h_\Gamma = \begin{pmatrix} C_1 + C_2(k_x^2 + k_y^2) + C_3(k_x^2 - k_y^2) & C_4 k_x k_y \\ C_4 k_x k_y & C_1 + C_2(k_x^2 + k_y^2) - C_3(k_x^2 - k_y^2) \end{pmatrix} \quad (2.59)$$

$$h_X = \begin{pmatrix} C_5 + C_6(k_x^2 + k_y^2) + C_7(k_x^2 - k_y^2) & -iv_X(\mathbf{k}) \\ iv_X(\mathbf{k}) & C_{11} + C_{12}(k_x^2 + k_y^2) + C_{13}(k_x^2 - k_y^2) \end{pmatrix} \quad (2.60)$$

$$h_Y = \begin{pmatrix} C_5 + C_6(k_x^2 + k_y^2) - C_7(k_x^2 - k_y^2) & -iv_Y(\mathbf{k}) \\ iv_Y(\mathbf{k}) & C_{11} + C_{12}(k_x^2 + k_y^2) - C_{13}(k_x^2 - k_y^2) \end{pmatrix}, \quad (2.61)$$

where

$$v_X(\mathbf{k}) = C_8 k_y + C_9 k_y (k_y^2 + 3k_x^2) - C_{10} k_y (k_x^2 - k_y^2) \quad (2.62)$$

$$v_Y(\mathbf{k}) = -C_8 k_x - C_9 k_x (k_x^2 + 3k_y^2) - C_{10} k_x (k_x^2 - k_y^2) \quad (2.63)$$

As a function of the tight-binding parameters, the constants C_1, \dots, C_{13} are

$$C_1 = \epsilon_\Gamma = \epsilon_{xz/yz} + 2(t_x^{11} + t_y^{11}) + 4(t_{xxy}^{11} + t_{xyy}^{11} + t_{xy}^{11} + t_{xxyy}^{11}) \quad (2.64)$$

$$C_2 = 2\frac{1}{2m_\Gamma} = -\frac{1}{2}(t_x^{11} + t_y^{11}) - 5(t_{xxy}^{11} + t_{xyy}^{11}) - 2t_{xy}^{11} - 8t_{xxyy}^{11} \quad (2.65)$$

$$C_3 = b = \frac{1}{2}(t_y^{11} - t_x^{11}) + 3(t_{xyy}^{11} - t_{xxy}^{11}) - 4t_{xx/yy}^{11} \quad (2.66)$$

$$C_4 = 4c = -4(t_{xy}^{12} + 4t_{xxyy}^{12} + 4t_{xxy/xyy}^{12}) \quad (2.67)$$

$$C_5 = \epsilon_1 = \epsilon_{xz/yz} + 2(t_x^{11} - t_y^{11}) - 4(t_{xxy}^{11} - t_{xyy}^{11} + 4t_{xy}^{11} - 4t_{xxyy}^{11}) \quad (2.68)$$

$$C_6 = 2\frac{1}{2m_1} = \frac{1}{2}(t_y^{11} - t_x^{11}) + 5(t_{xxy}^{11} - t_{xyy}^{11}) + 2t_{xy}^{11} - 8t_{xxyy}^{11} \quad (2.69)$$

$$C_7 = a_1 = \frac{1}{2}(t_x^{11} + t_y^{11}) - 3(t_{xxy}^{11} + t_{xyy}^{11}) + 4t_{xx/yy}^{11} \quad (2.70)$$

$$C_8 = 2v = 2(t_y^{14} + 2t_{xy}^{14} - 4t_{xxy}^{14}) \quad (2.71)$$

$$C_9 = 2p_1 = -\frac{1}{12}t_y^{24} - \frac{25}{6}t_{xy}^{24} + \frac{7}{3}t_{xxy}^{24} \quad (2.72)$$

$$C_{10} = 2p_2 = -\frac{1}{4}t_y^{24} + 3t_{xxy}^{24} \quad (2.73)$$

$$C_{11} = \epsilon_3 = \epsilon_{xy} + 4(-t_{xy}^{44} + t_{xx/yy}^{44} + t_{xxyy}^{44}) \quad (2.74)$$

$$C_{12} = 2\frac{1}{2m_3} = 2(t_{xy}^{44} - 2t_{xx/yy}^{44} - 4t_{xxyy}^{44}) \quad (2.75)$$

$$C_{13} = a_3 = t_{x/y}^{44} - 6t_{xxy/xyy}^{44}. \quad (2.76)$$

The overall minus sign in the coefficient C_4 arises due to the minus sign in the definition of the spinor in Eq. (2.4). The coefficients can be obtained either by using the relations above with the coefficients $t_{ij}^{\mu\nu}$ determined from tight-binding fits to DFT calculations, or by directly fitting the coefficients to DFT calculations.

2.B Spin-orbit coupling in orbital basis

Here we express the standard spin-orbit coupling term $\lambda \mathbf{S} \cdot \mathbf{L}$ in the orbital basis, which leads to Eqs. (2.19)-(2.21) of the main text. Denote the eigenstates of L_z by $|m\rangle$ where

2.B Spin-orbit coupling in orbital basis

$m = -L, \dots, L$. The spin-orbit Hamiltonian is then

$$H_{\text{SOC}} = \sum_{\substack{mn \\ \alpha\beta}} \langle m\alpha | \lambda \mathbf{S} \cdot \mathbf{L} | n\beta \rangle d_{m\alpha}^\dagger d_{n\beta}. \quad (2.77)$$

where $d_{m\alpha}^\dagger$ creates an electron with spin α and angular momentum projection m . Using the fact that $\mathbf{S} \cdot \mathbf{L} = L_z S_z + \frac{1}{2}(L^+ S^- + L^- S^+)$ and

$$S_z |n\alpha\rangle = \pm \frac{1}{2} |n\alpha\rangle, \quad S^\pm |n\alpha\rangle = \delta_{\alpha, \mp \frac{1}{2}} |n, \alpha \pm 1\rangle, \quad (2.78)$$

the Hamiltonian becomes

$$\begin{aligned} H_{\text{SOC}} &= \frac{\lambda}{2} \sum_{mn} \left[\langle m | L_z | n \rangle d_{m\uparrow}^\dagger d_{n\uparrow} - \langle m | L_z | n \rangle d_{m\downarrow}^\dagger d_{n\downarrow} \right. \\ &\quad \left. + \langle m | L^+ | n \rangle d_{m\downarrow}^\dagger d_{n\uparrow} + \langle m | L^- | n \rangle d_{m\uparrow}^\dagger d_{n\downarrow} \right] \\ &= \frac{\lambda}{2} \sum_{\substack{mn \\ \alpha\beta}} A_{mn}^{\alpha\beta} d_{m\alpha}^\dagger d_{n\beta}, \end{aligned} \quad (2.79)$$

with the matrix elements:

$$A_{mn}^{\uparrow\uparrow} = -A_{mn}^{\downarrow\downarrow} = \langle m | L_z | n \rangle = n \delta_{mn} \quad (2.80)$$

$$A_{mn}^{\downarrow\uparrow} = \sqrt{(L-n)(L+n+1)} \delta_{m, n+1} \quad (2.81)$$

$$A_{mn}^{\uparrow\downarrow} = \sqrt{(L+n)(L-n+1)} \delta_{m, n-1}. \quad (2.82)$$

We can transform the Hamiltonian in Eq. 2.79 to the basis spanned by the cubic harmonics (i.e. the orbital basis) using

$$d_{m\alpha} = \sum_{\mu} U_{m\mu} c_{\mu\alpha} \quad (2.83)$$

$$d_{m\alpha}^\dagger = \sum_{\mu} U_{m\mu}^* c_{\mu\alpha}^\dagger, \quad (2.84)$$

where $U_{m\mu} \equiv \langle m | \mu \rangle$ and $|\mu\rangle$ is the basis states in the space of cubic harmonics. The transformed Hamiltonian is

$$H_{\text{SOC}} = \frac{\lambda}{2} \sum_{\substack{\mu\nu \\ \alpha\beta}} \tilde{A}_{\mu\nu}^{\alpha\beta} c_{\mu\alpha}^\dagger c_{\nu\beta}, \quad (2.85)$$

with $\tilde{A}^{\alpha\beta} = U^\dagger A^{\alpha\beta} U$.

To proceed we specialize to the case $L = 2$, resulting in the well-known d -orbitals. The basis states are $\langle \mu | = \langle xz |, \langle yz |, \langle xy |, \langle x^2 - y^2 |, \langle z^2 |$ with

$$\langle xz | = \frac{1}{\sqrt{2}} (-\langle 1 | + \langle -1 |) \quad (2.86)$$

$$\langle yz | = \frac{i}{\sqrt{2}} (-\langle 1 | - \langle -1 |) \quad (2.87)$$

$$\langle xy | = \frac{i}{\sqrt{2}} (-\langle -2 | + \langle 2 |) \quad (2.88)$$

$$\langle x^2 - y^2 | = \frac{1}{\sqrt{2}} (\langle -2 | + \langle 2 |) \quad (2.89)$$

$$\langle z^2 | = \langle 0 |, \quad (2.90)$$

2.B Spin-orbit coupling in orbital basis

and U^\dagger can be read off as the coefficients of these equations. Thus, we find U to be

$$U = \frac{1}{\sqrt{2}} \begin{pmatrix} 0 & 0 & -i & 1 & 0 \\ -1 & i & 0 & 0 & 0 \\ 0 & 0 & 0 & 0 & \sqrt{2} \\ 1 & i & 0 & 0 & 0 \\ 0 & 0 & i & 1 & 0 \end{pmatrix}, \quad (2.91)$$

yielding the three independent \tilde{A} -matrices:

$$\tilde{A}^{\uparrow\uparrow} = \begin{pmatrix} 0 & -i & 0 & 0 & 0 \\ i & 0 & 0 & 0 & 0 \\ 0 & 0 & 0 & i2 & 0 \\ 0 & 0 & -i2 & 0 & 0 \\ 0 & 0 & 0 & 0 & 0 \end{pmatrix}, \quad (2.92)$$

$$\tilde{A}^{\uparrow\downarrow} = \begin{pmatrix} 0 & 0 & i & 1 & -\sqrt{3} \\ 0 & 0 & 1 & -i & -i\sqrt{3} \\ -i & -1 & 0 & 0 & 0 \\ -1 & i & 0 & 0 & 0 \\ \sqrt{3} & i\sqrt{3} & 0 & 0 & 0 \end{pmatrix}, \quad (2.93)$$

$$\tilde{A}^{\downarrow\downarrow} = \begin{pmatrix} 0 & 0 & i & -1 & \sqrt{3} \\ 0 & 0 & -1 & -i & -i\sqrt{3} \\ -i & 1 & 0 & 0 & 0 \\ 1 & i & 0 & 0 & 0 \\ -\sqrt{3} & i\sqrt{3} & 0 & 0 & 0 \end{pmatrix}. \quad (2.94)$$

Considering only the $|xz\rangle$, $|yz\rangle$ and $|xy\rangle$ orbitals, corresponding to the upper left 3×3 blocks in the above matrices results in the restricted matrix $\tilde{A}'_{\mu'\nu'}$:

$$\tilde{A}' = \begin{pmatrix} 0 & -i & 0 & 0 & 0 & i \\ i & 0 & 0 & 0 & 0 & -1 \\ 0 & 0 & 0 & -i & 1 & 0 \\ 0 & 0 & i & 0 & i & 0 \\ 0 & 0 & 1 & -i & 0 & 0 \\ -i & -1 & 0 & 0 & 0 & 0 \end{pmatrix}, \quad (2.95)$$

Decomposing it into spin and orbital parts gives:

$$\tilde{A}' = \begin{pmatrix} 0 & 0 & i \\ 0 & 0 & 0 \\ -i & 0 & 0 \end{pmatrix} \otimes \sigma^x + \begin{pmatrix} 0 & 0 & 0 \\ 0 & 0 & -i \\ 0 & i & 0 \end{pmatrix} \otimes \sigma^y + \begin{pmatrix} 0 & -i & 0 \\ i & 0 & 0 \\ 0 & 0 & 0 \end{pmatrix} \otimes \sigma^z. \quad (2.96)$$

Finally, applying this expression to the Hamiltonian (2.85) gives [65, 125]:

$$\frac{\lambda}{2} \sum_{\mu'\nu'} \tilde{A}'_{\mu'\nu'} c_{\mu'}^\dagger c_{\nu'} = i \frac{\lambda}{2} c_{xz,\alpha}^\dagger \sigma_{\alpha\beta}^x c_{xy,\beta} + i \frac{\lambda}{2} c_{xy,\alpha}^\dagger \sigma_{\alpha\beta}^y c_{yz,\beta} + i \frac{\lambda}{2} c_{yz,\alpha}^\dagger \sigma_{\alpha\beta}^z c_{xz,\beta} + \text{h.c.}, \quad (2.97)$$

which leads to Eqs. (2.19)–(2.21).

2.C Evaluation of Two-loop Diagrams

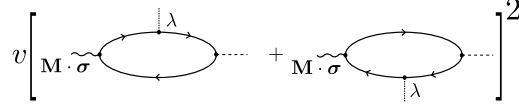


Figure 2.12: Illustration of the decomposition of a two-loop diagram into irreducible diagrams.

2.C Evaluation of Two-loop Diagrams

Diagrams of the two-loop type, as shown in Fig. 2.4a, can be split into irreducible diagrams. As a result, all two-loop diagrams for a given interaction can be obtained by squaring the sum of irreducible diagrams, as illustrated in Fig. 2.12. To illustrate the cancelation of the two diagrams in the sum, we choose the interaction v_{17} and the order parameter \mathbf{M}_1 . In this case, the sum in the brackets in Fig. 2.12 is, for the SOC leg related to the Γ spinor:

$$\begin{aligned} & \frac{\lambda}{2} \sum_{\mathbf{k},n} M_{1,i} \text{tr}[\sigma^z \sigma^i] \text{tr}[\tau^+ G_\Gamma \tau^y G_\Gamma \tilde{\tau}^1 G_X] + \frac{\lambda}{2} \sum_{\mathbf{k},n} M_{1,i} \text{tr}[\sigma^z \sigma^i] \text{tr}[\tau^- G_X \tilde{\tau}^1 G_\Gamma \tau^y G_\Gamma] \\ &= \lambda \sum_{\mathbf{k},n} M_{1,z} \left([G_\Gamma \tau^y G_\Gamma]_{21} [G_X]_{11} + [G_\Gamma \tau^y G_\Gamma]_{12} [G_X]_{11} \right), \end{aligned} \quad (2.98)$$

This term vanishes since $G_\Gamma \tau^y G_\Gamma$ is an antisymmetric matrix. For the contribution from the diagrams with the SOC leg related to the X/Y spinors, we find:

$$\begin{aligned} & -i\lambda \sum_{\mathbf{k},n} \left(M_{1,x} \text{tr} \left(\tilde{\tau}^1 G_Y \tau^- G_X \tilde{\tau}^1 G_\Gamma \right) + M_{1,y} \text{tr} \left(\tilde{\tau}^1 G_Y \tau^+ G_X \tilde{\tau}^1 G_\Gamma \right) \right) \\ &= -i\lambda \sum_{\mathbf{k},n} \left(M_{1,x} [G_Y]_{12} [G_X]_{11} [G_\Gamma]_{11} + M_{1,y} [G_Y]_{11} [G_X]_{21} [G_\Gamma]_{11} \right), \end{aligned} \quad (2.99)$$

which is also zero as the off-diagonal elements of the Green functions G_X and G_Y are odd functions of \mathbf{k} . Similar arguments apply in the case when the electron-electron interaction is given by either v_{13} , v_{15} or v_{19} and when the magnetic order parameter is \mathbf{M}_2 . Thus, all contributions from the two-loop diagrams vanish, and we are left with only the one-loop diagrams shown in Fig. 2.4b.

2.D Diagrams contributing to w

In this appendix we explain in more details the statement made in the main text concerning the vanishing of the quartic coefficient w in Eq. (2.38). Let us consider a generic diagram which would contribute to the coefficient w , as shown in Fig. 2.13. Note that we do not specify any vertices, i.e. the coupling between the electrons and the SDW order parameters do not necessarily arise from Eq. 2.28. Due to the Pauli matrix contraction, the diagram must have alternating \mathbf{M}_1 and \mathbf{M}_2 legs in order for it to contribute to w . Indeed, performing the trace over spin indices gives:

$$M_1^i M_2^j M_1^k M_2^l \text{tr} \left(\sigma^i \sigma^j \sigma^k \sigma^l \right). \quad (2.100)$$

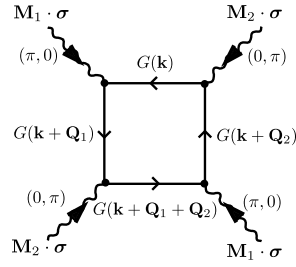


Figure 2.13: Illustration of a generic diagram contributing to the coefficient w . Here $\mathbf{Q}_1 = (\pi, 0)$ and $\mathbf{Q}_2 = (0, \pi)$. On the right diagram we have imposed momentum conservation at each vertex, resulting in the appearance of $G(\mathbf{k} + \mathbf{Q}_1 + \mathbf{Q}_2)$.

Using Eq. 2.31, we find:

$$2 (\mathbf{M}_1 \cdot \mathbf{M}_2)^2 - \mathbf{M}_1^2 \mathbf{M}_2^2, \quad (2.101)$$

thus resulting in a $(\mathbf{M}_1 \cdot \mathbf{M}_2)^2$ term. This contrasts to the third diagram in Fig. 2.9, which gives no contribution of the form $(\mathbf{M}_1 \cdot \mathbf{M}_2)^2$ after tracing over the Pauli matrices.

Let us now consider the internal lines of the diagram. Since \mathbf{M}_1 carries momentum $(\pi, 0)$ and \mathbf{M}_2 carries momentum $(0, \pi)$, the only way for momentum to be conserved is if one of the lines corresponds to a propagator with momentum $\mathbf{Q}_1 + \mathbf{Q}_2 = (\pi, \pi)$. However, in the absence of a Fermi pocket at $M = (\pi, \pi)$ (of the unfolded Brillouin zone), this will be an off-shell contribution. Thus, contributions to w must arise from the electronic states near $M = (\pi, \pi)$.

Chapter 3

Spin-Driven Nematic Instability of the Multi-Orbital Hubbard Model: Application to Iron-Based Superconductors

*This chapter has been published by the author and Jian Kang, Brian M. Andersen, and Rafael M. Fernandes in Phys. Rev. B **93** 085136 (2016).*

In this chapter we establish the existence of a nematic phase in the multi-orbital Hubbard model. This is done by generalising the result for the nematic susceptibility, introduced in Sec. 1.2.1, to orbital space. This requires the evaluation of the quartic coefficients of the free energy, and since there is no magnetic order, we cannot project these onto the leading instability, as done in Sec. 1.3 and Sec. 1.4. We therefore assume that the magnetic order parameters are diagonal in orbital space and as shown in Sec. 1.3 this is a well justified since the only non-zero off-diagonal element tends to be suppressed. Contrasting the nematic susceptibility with the ferro-orbital order susceptibility we show that the leading instability is a spin-driven nematic phase. Additionally we demonstrate that the inclusion of high-energy magnetic fluctuations can drive a nematic instability even in the absence of magnetic order.

3.1 Introduction

The elucidation of electronic Ising-nematic order [43] – the state in which electronic degrees of freedom spontaneously lower the point-group symmetry of the system – has become an important problem in unconventional superconductors [24, 126]. In both pnictides [49, 50, 127–130] and cuprates [131–133], the experimentally observed nematic order has been proposed to arise from the partial melting of an underlying spin density-wave (SDW) [39, 46, 47, 91] or charge density-wave (CDW) [134–136] stripe-order. This mechanism is based on robust symmetry considerations. Consider for concreteness the stripe SDW case: the ground state has an $O(3) \times Z_2$ degeneracy, with $O(3)$ denoting the direction of the magnetic order parameter in spin space, and Z_2 denoting the selection of the SDW ordering vector $\mathbf{Q}_X = (\pi, 0)$ or $\mathbf{Q}_Y = (0, \pi)$ (in the CDW case, the system has an $O(2) \times Z_2$ degeneracy). Fluctuations in layered systems suppress the continuous ($O(3)$ or $O(2)$) and the discrete (Z_2) symmetries differently, favoring an intermediate regime in which only the Z_2 symmetry is broken [47]. Because the Z_2 symmetry distinguishes between two ordering vectors related by a 90° rotation, its breaking implies a tetragonal-to-orthorhombic transition, and therefore nematic order.

Although this mechanism for spin-driven (or charge-driven) nematic order has been established in simplified low-energy models for pnictides [46, 47, 64, 91, 104] and cuprates [135, 136], it remains hotly debated whether more realistic microscopic models display nematic order as the leading electronic instability. For the cuprates, a sensible microscopic model is the single-band Hubbard model, whose phase diagram has been reported to display nematic correlations in the strong-coupling regime [137, 138]. For the pnictides, due to the $3d^6$ configuration of Fe and to the small crystal field splittings, a five-orbital Hubbard model, including Hund’s rule interactions, is a more appropriate starting point [139, 140]. Furthermore, because many pnictides display metallic behavior, a weak-coupling analysis of this intricate model can reveal important information about the underlying physics of these materials. Indeed, conventional RPA approaches have been employed to study the onset of SDW, CDW, and ferromagnetism. However, in contrast to these usual electronic instabilities, the standard RPA approach does not capture the nematic instability even qualitatively, as we show below, making it difficult to assess whether the realistic multi-orbital Hubbard model has a tendency towards nematic order.

In this paper, we extend the standard RPA approach and derive the nematic susceptibility of an arbitrary multi-orbital Hubbard model. The fluctuations included in this formalism arise solely from the non-interacting part of the Hamiltonian, such that interactions are treated at the same order as in the typical RPA method. We apply this formalism to the case of SDW-driven nematicity in iron pnictides, and establish that the leading instability of the five-orbital interacting model is a spin-driven nematic phase for a wide range of parameters. In general, we find that nematic order exists in a narrow T range above the magnetic transition line, in agreement with experiments in the pnictides [19–23]. However, magnetic fluctuations at higher energies can induce a sizable splitting between the two transitions, particularly in the regime where the SDW transition is suppressed to zero. We propose that this effect may be relevant to understanding the unusual nematic

phase of FeSe [141–145]. Previously, the investigation of the multi-orbital Hubbard model in Ref. [104] revealed the importance of the orbital content of the Fermi surface in the low-energy spin-nematic model of the pnictides. Here, we find from the orbitally-resolved nematic susceptibility that whereas the d_{xz} , d_{yz} , and d_{xy} orbitals contribute almost equally to the SDW instability, the d_{xy} orbital plays a stronger role in driving the nematic instability. Finally, we compare the nematic susceptibility with the RPA-derived ferro-orbital order susceptibility. Our work provides a promising route to search for nematicity in different compounds, as it is compatible with *ab initio* approaches and also with methods that include the effects of moderate interactions, such as LDA+DMFT [42, 146].

3.2 Orbitorally resolved nematic susceptibility

Our starting point is the multi-orbital Hubbard model with onsite interactions [72, 140]. The non-interacting part is given by $\mathcal{H}_0 = \sum_{\mu,\nu} (\epsilon_{\mu\nu}(\mathbf{k}) - \tilde{\epsilon}\delta_{\mu\nu}) c_{\mathbf{k}\mu\sigma}^\dagger c_{\mathbf{k}\nu\sigma}$, where $c_{\mathbf{k}\mu\sigma}^\dagger$ creates an electron with momentum \mathbf{k} and spin σ at orbital $\mu = 1, \dots, N_{\text{orb}}$ and the hopping parameters $\epsilon_{\mu\nu}(\mathbf{k})$ are determined from tight-binding fits to *ab initio* calculations (sums over spin and momentum indices are left implicit). The four onsite interaction terms correspond to the intra-orbital Hubbard term, $\mathcal{H}_U = U \sum_{\mu} n_{\mathbf{q}\mu\uparrow} n_{-\mathbf{q}\mu\downarrow}$, the inter-orbital Hubbard term, $\mathcal{H}_{U'} = U' \sum_{\mu < \nu} n_{\mathbf{q}\mu\sigma} n_{-\mathbf{q}\nu\sigma'}$, the Hund's rule coupling, $\mathcal{H}_J = J \sum_{\mu < \nu} c_{\mathbf{k}+\mathbf{q}\mu\sigma}^\dagger c_{\mathbf{k}\nu\sigma} c_{\mathbf{k}'-\mathbf{q}\nu\sigma'}^\dagger c_{\mathbf{k}'\mu\sigma'}$, and the pair-hopping term $\mathcal{H}_{J'} = J' \sum_{\mu < \nu} c_{\mathbf{k}+\mathbf{q}\mu\sigma}^\dagger c_{\mathbf{k}'-\mathbf{q}\mu\bar{\sigma}}^\dagger c_{\mathbf{k}'\nu\bar{\sigma}} c_{\mathbf{k}\nu\sigma}$. These coefficients are related by $U' = U - 2J$ and $J' = J$. Previous approaches considered the nematic susceptibility of a spin-fermion model [103]; here, we will focus on the Hubbard model within RPA. The mechanism in which nematic order arises from the partial melting of an SDW or a CDW requires fluctuations at two momenta related by 90° , in general $\mathbf{Q}_1 = (\frac{\pi}{n}, 0)$ and $\mathbf{Q}_2 = (0, \frac{\pi}{n})$, with integer n . Although our formalism can be extended in a straightforward way to arbitrary n , hereafter we focus on $n = 1$. To make contact with the pnictides, we consider the SDW channel. Performing a Hartree-Fock decoupling of \mathcal{H} in both the $\mathbf{q} = 0$ charge channel and the $\mathbf{q} = \mathbf{Q}_i$ SDW channel:

$$\mathcal{H}^{\text{MF}} = \sum_{\mathbf{k}} (\epsilon_{\mu\nu}(\mathbf{k}) - \tilde{\epsilon}_\nu \delta_{\mu\nu}) c_{\mathbf{k}\mu\sigma}^\dagger c_{\mathbf{k}\nu\sigma} - \frac{1}{2} \sum_{\mathbf{k}\mathbf{q}} \mathbf{M}_{\mathbf{q}\mu}^i \cdot c_{\mathbf{k}-\mathbf{q}+\mathbf{Q}_i\mu\sigma}^\dagger \boldsymbol{\sigma}_{\sigma\sigma'} c_{\mathbf{k}\mu\sigma'}, \quad (3.1)$$

where $\tilde{\epsilon}_\nu$ incorporates the changes in the mean-field densities and

$$\mathbf{M}_{\mathbf{q}\mu}^i = \frac{1}{2} \sum_{\mathbf{k}} U_\mu^\rho \langle c_{\mathbf{k}+\mathbf{q}+\mathbf{Q}_i\rho\sigma}^\dagger \boldsymbol{\sigma}_{\sigma\sigma'} c_{\mathbf{k}\rho\sigma'} \rangle \quad (3.2)$$

are the SDW order parameters with $i = X, Y$. The interaction matrix U_μ^ρ is $U_a^a = U$ and $U_{b \neq a}^a = J$. We consider only intra-orbital magnetism, since previous Hartree-Fock calculations revealed that in the ground state the intra-orbital SDW order parameters are the dominant ones [72]. In the standard RPA approach for the SDW instability, the electronic degrees of freedom are integrated out, yielding the quadratic magnetic free energy:

$$F_{\text{mag}}^{(2)}[\mathbf{M}_\mu^i] = \sum_{q,i=X,Y} \left[\chi_i^{\mu\nu}(q) \right]^{-1} \mathbf{M}_{q,\mu}^i \cdot \mathbf{M}_{-q,\nu}^i, \quad (3.3)$$

3.2 Orbitorally resolved nematic susceptibility

with the magnetic propagator $\chi_i^{\mu\nu}(q)$

$$\chi_i^{\mu\nu}(q) = \left[(U_\nu^\mu)^{-1} + \sum_k \mathcal{G}^{\nu\mu}(k) \mathcal{G}_i^{\mu\nu}(k+q) \right]^{-1}, \quad (3.4)$$

where $\mathcal{G}_i^{\mu\nu}(k) \equiv \mathcal{G}^{\mu\nu}(k + \mathbf{Q}_i)$ is the Green's function in orbital basis, $q = (\mathbf{q}, \Omega_n)$, $\sum_q = T/N_{\mathbf{q}} \sum_{\mathbf{q}} \sum_{\Omega_n}$, and $\Omega_n = 2n\pi T$ is the Matsubara frequency. The RPA magnetic susceptibility $\langle \mathbf{M}_{q,\mu}^i \cdot \mathbf{M}_{-q,\nu}^i \rangle$ is proportional to and diverges at the same temperature as the magnetic propagator $\chi_i^{\mu\nu}(q)$. Note that the tetragonal symmetry of the system implies that a peak of $\chi_i^{\mu\nu}(q)$ at $\mathbf{Q}_X = (\pi, 0)$ will be accompanied by an equal peak at $\mathbf{Q}_Y = (0, \pi)$. Therefore, at this order in perturbation theory, the system does not distinguish the case in which either \mathbf{Q}_X or \mathbf{Q}_Y is selected (single- \mathbf{Q} order) from the case in which both are selected (double- \mathbf{Q} order), i.e. the standard RPA approach is blind to nematicity. To remedy this problem, we go beyond the second-order expansion of the free energy and calculate the quartic-order terms:

$$\begin{aligned} F_{\text{mag}}^{(4)}[\mathbf{M}_\mu^X, \mathbf{M}_\mu^Y] &= \frac{1}{2} u^{\rho\nu\eta\mu} \left(\mathbf{M}_\rho^X \cdot \mathbf{M}_\nu^X + \mathbf{M}_\rho^Y \cdot \mathbf{M}_\nu^Y \right) \left(\mathbf{M}_\eta^X \cdot \mathbf{M}_\mu^X + \mathbf{M}_\eta^Y \cdot \mathbf{M}_\mu^Y \right) \\ &- \frac{1}{2} g^{\rho\nu\eta\mu} \left(\mathbf{M}_\rho^X \cdot \mathbf{M}_\nu^X - \mathbf{M}_\rho^Y \cdot \mathbf{M}_\nu^Y \right) \left(\mathbf{M}_\eta^X \cdot \mathbf{M}_\mu^X - \mathbf{M}_\eta^Y \cdot \mathbf{M}_\mu^Y \right) \\ &+ 2w^{\rho\nu\eta\mu} \left(\mathbf{M}_\rho^X \cdot \mathbf{M}_\nu^Y \right) \left(\mathbf{M}_\eta^X \cdot \mathbf{M}_\mu^Y \right), \end{aligned} \quad (3.5)$$

The quartic coefficients, whose expressions are shown explicitly in Appendix 3.A, depend only on the non-interacting Green's functions. Although interactions can also contribute to them, as shown in Refs. [79, 147], within the RPA approach these contributions are sub-leading and can be neglected. The most relevant coefficient for the nematic instability is $g^{\rho\nu\eta\mu}$, whose term distinguishes between single- \mathbf{Q} and double- \mathbf{Q} order. Specifically, a Hubbard-Stratonovich transformation of this term reveals the nematic order parameter $\langle \phi_{\mu\nu} \rangle \propto \langle \mathbf{M}_\mu^X \mathbf{M}_\nu^X \rangle - \langle \mathbf{M}_\mu^Y \mathbf{M}_\nu^Y \rangle$, a rank-2 tensor in orbital space that breaks the tetragonal symmetry of the system by making $X \neq Y$. The term with coefficient $u^{\rho\nu\eta\mu}$ is related to Gaussian magnetic fluctuations in both SDW channels, while the term with coefficient $w^{\rho\nu\eta\mu}$ mainly distinguishes between the two types of double- \mathbf{Q} order [79]. Eq. (3.5) is the multi-orbital generalization of the magnetic free energy previously obtained in effective low-energy models in the band basis, where the coefficient g becomes a scalar [47].

It is now possible to compute the static nematic susceptibility $\chi_{\text{nem}}^{\rho\nu\eta\mu} \propto \langle \phi_{\rho\nu} \phi_{\eta\mu} \rangle$ in the paramagnetic phase (see Appendix 3.B for details of the derivation):

$$\chi_{\text{nem}}^{\rho\nu\eta\mu} = \chi_{\text{nem},0}^{\eta\alpha\mu\beta} \left(\delta_{\rho\beta} \delta_{\nu\alpha} - g^{\rho\nu\gamma\delta} \chi_{\text{nem},0}^{\gamma\alpha\delta\beta} \right)^{-1}, \quad (3.6)$$

$$\chi_{\text{nem},0}^{\rho\nu\eta\mu} \equiv \frac{1}{2} \sum_{q,i=X,Y} \chi_i^{\rho\nu}(q) \chi_i^{\eta\mu}(-q). \quad (3.7)$$

The orbitally-resolved nematic susceptibility $\chi_{\text{nem}}^{\rho\nu\eta\mu}$ is a rank-4 tensor that generalizes the scalar nematic susceptibility derived previously for effective low-energy models [74, 148–150]. The impact of the magnetic fluctuations encoded in the coefficient $g^{\rho\nu\gamma\delta}$ is clear: if this term were absent, then the (bare) nematic susceptibility would be merely a higher-order convolution of the magnetic propagator, $\chi_{\text{nem},0}^{\rho\nu\eta\mu}$, and therefore diverge at the same

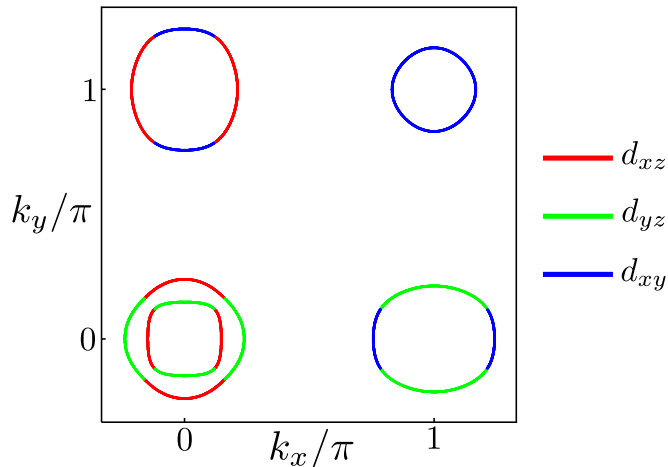


Figure 3.1: (Color online) Normal-state Fermi surface based on the parameters of Ikeda *et al.* [61]. The colors indicate the dominant orbital contribution.

T as the SDW susceptibility. To establish whether the nematic susceptibility diverges already in the paramagnetic phase, one needs to compute its leading eigenvalue $\lambda^{(n)}$ from $\chi_{\text{nem}}^{\rho\nu\eta\mu} \Phi_{\rho\nu}^{(n)} = \lambda^{(n)} \Phi_{\eta\mu}^{(n)}$, with $n = 1, \dots, N_{\text{orb}}^2$. The structure of the corresponding eigenmatrix $\Phi_{\eta\mu}^{(n)}$ reveals which orbitals promote the nematic instability, and which orbitals favor a double- \mathbf{Q} structure with no underlying nematicity. We note that in principle the Gaussian fluctuations associated with the term with coefficient $u^{\rho\nu\eta\mu}$ can also renormalize the magnetic propagator $\chi_i^{\rho\nu}$. However, because this effect merely renormalizes the SDW transition temperature, we do not include it hereafter.

3.3 Results

Equation (3.6) is the RPA-generalized nematic susceptibility, which can be compared on equal-footing with other RPA instabilities of a weakly-interacting system described by a multi-orbital Hubbard model. We apply this formalism to a five-orbital model for the iron-based superconductors and contrast the nematic susceptibility to the ferro-orbital RPA susceptibility. The hopping parameters are those from Ref. [61], whereas the interactions are set to $U = 0.95$ eV and $J = U/4$ [72]. Small changes in these parameters do not alter our main results. The Fermi surface for the occupation number $n = 6$ is presented in Fig. 3.1, consisting of three hole pockets at the center and the corner of the Brillouin zone, and two electron pockets at the borders of the Brillouin zone. that the d_{xy} hole pocket at (π, π) is not present in all materials, as it depends on the Fe-As distance [67, 151].

We evaluate Eqs. (3.4) and (3.6) numerically as functions of T for various values of the occupation number n . Consider first $n = 6$: in Fig. 3.2(a), we plot the T dependence of the largest eigenvalue of the static magnetic propagator $\chi_i^{\mu\nu}(0)$ as well as the largest eigenvalue of the *bare* nematic susceptibility $\chi_{\text{nem},0}^{\rho\nu\eta\mu}$. Despite having different T dependencies, both eigenvalues diverge at the same temperature T_{mag} , confirming our assertion that the standard RPA is blind to the nematic instability. In Fig. 3.2(b), we plot the largest

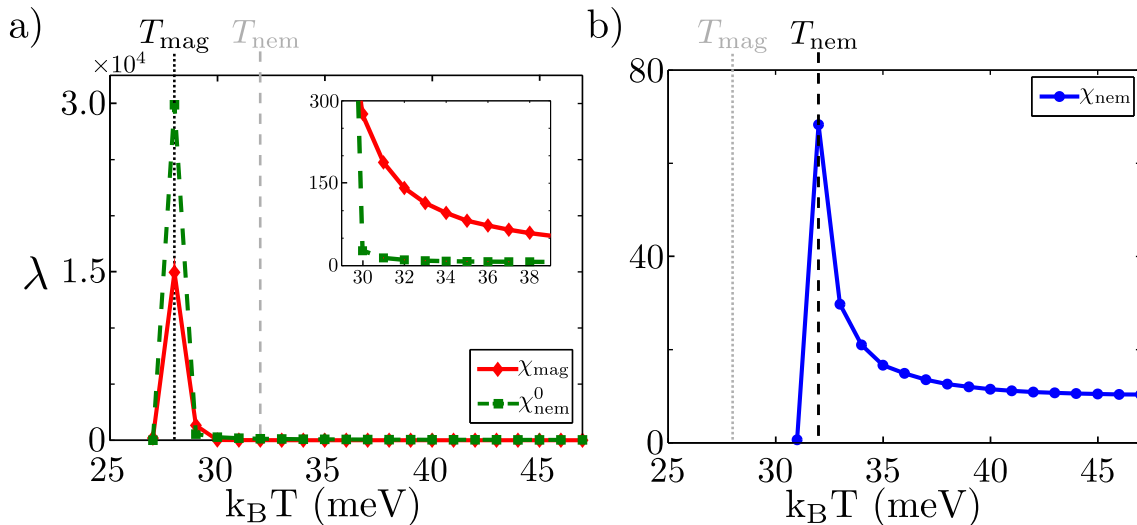


Figure 3.2: (Color online) The largest eigenvalues λ of (a) the bare nematic susceptibility $\chi_{\text{nem},0}^{\rho\nu\eta\mu}$, the $\mathbf{Q}_{X/Y}$ magnetic propagator χ_{mag} , and (b) the full nematic susceptibility $\chi_{\text{nem}}^{\rho\nu\eta\mu}$ as a function of T for the case $n = 6$. The inset in (a) shows the upturn of the magnetic susceptibility as it diverges.

eigenvalue of the *full* nematic susceptibility $\chi_{\text{nem}}^{\rho\nu\eta\mu}$, as given by Eq. (3.6). Clearly, the eigenvalue diverges at $T > T_{\text{mag}}$: this is exactly the nematic transition temperature T_{nem} .

Interestingly, our results reveal a relatively small splitting between T_{nem} and T_{mag} , with $T_{\text{nem}} \approx 1.14T_{\text{mag}}$, which resembles the small T -range in which a nematic-paramagnetic phase is observed experimentally in the iron pnictides [19–23]. We caution, however, that this value should be understood as an upper boundary for the splitting between the nematic and the actual magnetic transition, since \tilde{T}_{mag} calculated inside the nematic state is generally larger than T_{mag} calculated in the tetragonal state. Furthermore, the value for T_{mag} obtained via RPA overestimates the actual transition temperature due to the absence of Gaussian fluctuations, as discussed above.

While the largest eigenvalue $\lambda^{(n)}$ determines T_{nem} , the structure of the corresponding 5×5 eigen-matrix $\Phi_{\eta\mu}^{(n)}$ reveals the orbital-resolved nematic order parameter driving the transition, since $\Phi_{\eta\mu}^{(n)} \propto \langle \mathbf{M}_{\eta}^X \mathbf{M}_{\mu}^X \rangle - \langle \mathbf{M}_{\eta}^Y \mathbf{M}_{\mu}^Y \rangle$. In Fig. 3.3 we plot the normalized elements of the leading eigen-matrix $\Phi_{\eta\mu}^{(n)}$ for both the full and the bare nematic susceptibility – which, as shown above, contains information only about the magnetic instability. In both cases, the dominant processes involve the d_{xz} , d_{yz} , and d_{xy} orbitals.

There is however one important difference: the relative weight of the d_{xy} orbital is larger for $\chi_{\text{nem}}^{\rho\nu\eta\mu}$ than for $\chi_{\text{nem},0}^{\rho\nu\eta\mu}$, i.e. while the three orbitals seem to contribute equally to drive the magnetic instability, the d_{xy} orbital plays a more important role in driving the nematic instability. We interpret this in terms of the nesting properties of the orbital content of the Fermi surface in Fig. 3.1: while the d_{xy} hole-pocket at (π, π) can form a single- \mathbf{Q} SDW by combining with either the X or Y electron-pockets, since both have d_{xy} spectral weight, the two d_{xz}/d_{yz} hole-pockets at $(0, 0)$ can form a double- \mathbf{Q} SDW by combining with both the X and Y pockets, since they have d_{yz} and d_{xz} spectral weight, respectively.

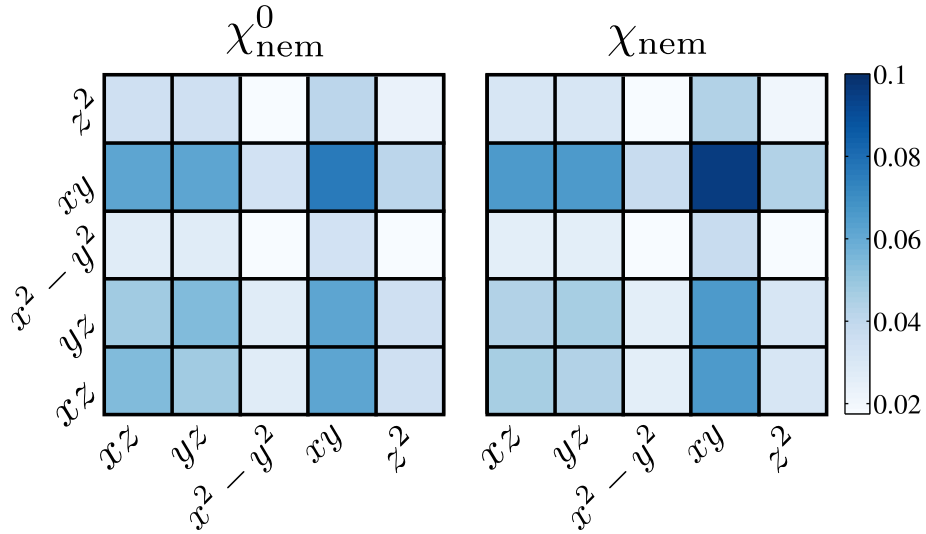


Figure 3.3: (Color online) Color plot of the normalized elements of the eigen-matrix $\Phi_{\eta\mu}^{(n)}$ corresponding to the leading eigenvalue of the bare (left) and of the full (right) nematic susceptibilities. The dominant contributions arise from the d_{xz} , d_{yz} , and d_{xy} orbital, with the d_{xy} being the most important for nematicity.

Having analyzed the $n = 6$ case, we present in Fig. 3.4(a) the complete (n, T) phase diagram for the magnetic and nematic transitions. We restrict our analysis to $n > 5.75$, since below this value we find incommensurate magnetic order. Accounting for the nematic transition in this regime requires changes in the formalism beyond the scope of this work. Note that, in contrast to experiments, T_{mag} is not peaked at $n = 6$. This is likely due to the absence of disorder effects introduced by doping, which are known to suppress T_{mag} [152, 153]. Most importantly, across the entire phase diagram the nematic transition line tracks closely the magnetic transition line, in agreement with the phase diagrams of the iron pnictides.

An important issue in obtaining this phase diagram is that, as shown in Eq. (3.7), the computation of the nematic susceptibility requires summing the magnetic fluctuations not only over the entire Brillouin zone, but also over energy (i.e. over Matsubara frequencies). Although the propagator $\chi_i^{\mu\nu}(\mathbf{q}, \Omega_n)$ is strongly peaked at $\Omega_n = 0$ (see Appendix 3.C), within RPA it saturates to a finite value for large energies [see Eq. (3.4)], requiring a frequency cutoff Ω_c . Near a finite- T magnetic transition, due to the very sharp peak in $\chi_i^{\mu\nu}(\mathbf{Q}_{X/Y}, \Omega_n)$, it is reasonable to take only the $\Omega_n = 0$ contribution – the low-energy magnetic fluctuations – resulting in the solid line of Fig. 3.4. However, near the region where $T_{\text{mag}} \rightarrow 0$, ignoring the high-energy magnetic fluctuations ($\Omega_n \neq 0$) is not justified. To address this problem, we introduce a cutoff $\Omega_c = 1$ eV, at which the propagator reaches values close to its saturation value, as shown in Appendix 3.C. The corresponding nematic transition line is shown as a dashed line in Fig. 3.4. Near the regime where the magnetic transition takes place at finite T , the only effect of the cutoff is to increase the nematic transition temperature, as expected. However, near the regime where $T_{\text{mag}} \rightarrow 0$, the nematic transition is stabilized even in the absence of long-range magnetic order. Although the precise value of T_{nem} depends on the cutoff value, the main result is that higher-energy

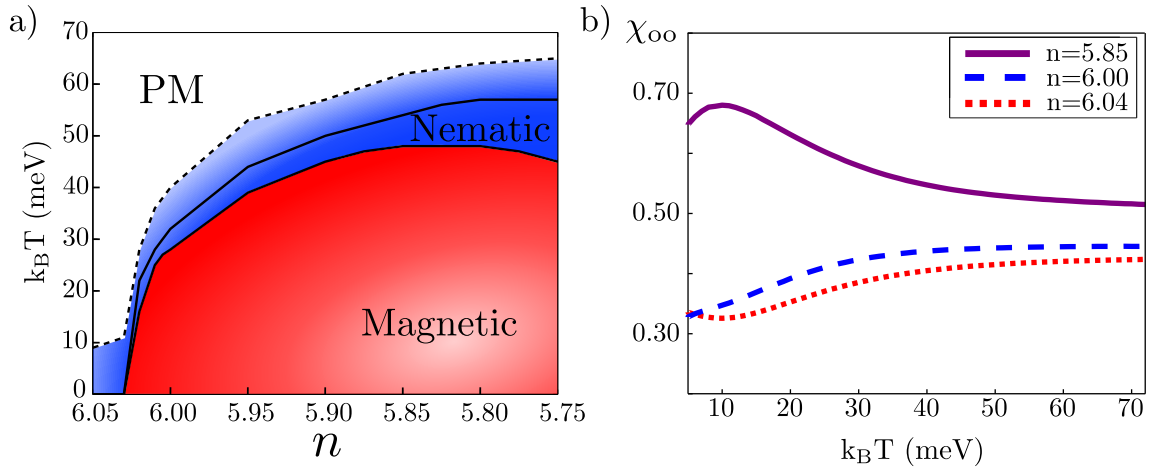


Figure 3.4: (Color online) **(a)** Occupation number-temperature (n, T) phase diagram for the bare magnetic and nematic phase transitions, evidencing the narrow region displaying nematic-paramagnetic order. The solid T_{nem} line takes into account only the contribution from low-energy ($\Omega_n = 0$) magnetic fluctuations, whereas the dashed line includes contributions from higher energies ($\Omega < \Omega_c = 1$ eV). For $n < 5.75$, an incommensurate magnetic order appears. **(b)** Ferro-orbital order susceptibility χ_{oo} a function of T for various values of the occupation number n . In contrast to the nematic susceptibility shown in Fig. 3.2, χ_{oo} is nearly featureless and T -independent at low energies.

magnetic fluctuations are essential to promote nematic order without magnetic order. In this regard, it is interesting to note that, in FeSe, the only parent material in which nematic order is observed in the absence of magnetic order, NMR measurements find no evidence for low-energy magnetic fluctuations [54, 154], whereas neutron scattering reports sizable fluctuations at modest energy values [155, 156].

A remaining question is whether or not the spin-driven nematic instability is the leading instability of the system. In particular, an ongoing debate [24, 44, 147, 157–159] concerning iron-based materials is whether ferro-orbital order, signaled by an unequal occupation of the d_{xz} and d_{yz} orbitals, $\Delta n \equiv n_{xz} - n_{yz} \neq 0$, could drive the nematic transition, instead of the spin-driven mechanism explored above. To investigate this issue, we calculate the $\mathbf{q} = 0$ static component of the RPA orbital order susceptibility, $\chi_{oo}(\mathbf{q}) = \langle \Delta n(\mathbf{q}) \Delta n(-\mathbf{q}) \rangle$ for the multi-orbital Hubbard model [145], of which a brief derivation is included in Appendix 3.D. As shown in Fig. 3.4(b), our results reveal a nearly T -independent χ_{oo} for the doping range and interactions investigated. This is not unexpected, since for reasonable values of U and J , there is no attraction in the RPA charge channel. Therefore, within RPA, ferro-orbital order is unable to drive the nematic instability. Of course, once the coupling to magnetic fluctuations is included, which requires going beyond RPA, χ_{oo} will diverge at the same T as χ_{nem} [104, 145, 160]. In this regard, by effectively decoupling these two channels, RPA provides an interesting route to investigate which instability is the leading one – at least for weak or moderate interactions.

3.4 Conclusions

In summary, we developed an appropriate extension of the RPA approach to obtain the orbital-resolved spin-driven nematic susceptibility of an arbitrary multi-orbital Hubbard model. Application to the case of iron-based superconductors reveals that the leading instability of the system is an interaction-driven nematic phase. The d_{xy} orbital plays a leading role in promoting the nematic instability, and higher-energy magnetic fluctuations are essential to stabilize nematic order in the absence of long-range magnetic order. Comparison with other RPA susceptibilities reveals that the nematic and magnetic transitions follow each other closely, and that the ferro-orbital susceptibility does not diverge on its own. More generally, our formalism can also be combined with first-principle approaches to search for other materials that may display electronic nematicity. Furthermore, because interactions appear only in the determination of the magnetic propagator, Eq. (3.4), this formalism can be combined with other approaches that specifically include moderate electronic interactions, such as DFT+U or LDA+DMFT [42, 146].

Appendices

3.A Fourth order coefficients

To derive the form of the free energy given in Eqs. (2) and (4) in the main text, we perform a Hubbard-Stratonovich (HS) decoupling thereby obtaining the electron-mediated interactions between the magnetic order parameters. Formally the HS decoupling relies on inserting unity in the partition function, where unity, in the present case, is given by

$$\begin{aligned} \mathbb{1} &= \int \mathcal{D}[\mathbf{M}_{\mu\nu}^X, \mathbf{M}_{\mu\nu}^Y] \\ &\exp \left[- \int_q \left(\mathbf{M}_{\mu\nu}^X(q) (U^{-1})_{\rho\lambda}^{\mu\nu} \mathbf{M}_{\rho\lambda}^X(-q) \right. \right. \\ &\quad \left. \left. + \mathbf{M}_{\mu\nu}^Y(q) (U^{-1})_{\rho\lambda}^{\mu\nu} \mathbf{M}_{\rho\lambda}^Y(-q) \right) \right], \end{aligned} \quad (3.8)$$

and $\int \mathcal{D}[\mathbf{M}_{\mu\nu}^X, \mathbf{M}_{\mu\nu}^Y]$ is chosen such that the path-integral evaluates to unity and $q = (\mathbf{q}, \Omega_n)$ (Ω_n being a bosonic Matsubara frequency). The electrons are then integrated out resulting in an effective action for the magnetic order

$$\begin{aligned} \mathcal{S}_{\text{eff}}[\mathbf{M}_{\mu\nu}^X, \mathbf{M}_{\mu\nu}^Y] &= \sum_i \int_q \mathbf{M}_{\mu\nu}^i(q) (U^{-1})_{\rho\lambda}^{\mu\nu} \mathbf{M}_{\rho\lambda}^i(-q) \\ &- \text{Tr} \ln \left[\mathbb{G}_{\mu\nu}^0(k)^{-1} - \mathcal{V}_{\mu\nu}(q) \right], \end{aligned} \quad (3.9)$$

where $i = X, Y$, μ and ν are orbital indices, $k = (\mathbf{k}, \omega_n)$, $\omega_n = (2n + 1) \pi T$ is the fermionic Matsubara frequency, and the trace is over all external indices (the spin indices have been suppressed, the Green's function is diagonal in spin). $\mathbb{G}_{\mu\nu}^0(k)$ is the matrix Green's function, obtained from the first term in Eq. (1) of the main text, and \mathcal{V} originates from the coupling between the magnetic order parameters and the electrons, the second term. In the basis

$$\Psi(\mathbf{k}) = \begin{pmatrix} \psi(\mathbf{k}) \\ \psi(\mathbf{k} + \mathbf{Q}_X) \\ \psi(\mathbf{k} + \mathbf{Q}_Y) \\ \psi(\mathbf{k} + \mathbf{Q}_X + \mathbf{Q}_Y) \end{pmatrix} \quad (3.10)$$

these are given by the matrices

$$\begin{aligned} \mathbb{G}_{\mu\nu}^0(k) &= \begin{pmatrix} \mathcal{G}_{\mu\nu}^0(k+q) & 0 & 0 & 0 \\ 0 & \mathcal{G}_{\mu\nu}^0(k+q+\mathbf{Q}_X) & 0 & 0 \\ 0 & 0 & \mathcal{G}_{\mu\nu}^0(k+q+\mathbf{Q}_Y) & 0 \\ 0 & 0 & 0 & \mathcal{G}_{\mu\nu}^0(k+q+\mathbf{Q}_X+\mathbf{Q}_Y) \end{pmatrix} \quad (3.11) \\ \mathcal{V}_{\mu\nu}(q) &= \begin{pmatrix} 0 & -\frac{1}{2} \mathbf{M}_{\mu\nu}^X(q) \cdot \boldsymbol{\sigma}_{\alpha\beta} & -\frac{1}{2} \mathbf{M}_{\mu\nu}^Y(q) \cdot \boldsymbol{\sigma}_{\alpha\beta} & 0 \\ -\frac{1}{2} \mathbf{M}_{\mu\nu}^X(q) \cdot \boldsymbol{\sigma}_{\alpha\beta} & 0 & 0 & -\frac{1}{2} \mathbf{M}_{\mu\nu}^Y(q) \cdot \boldsymbol{\sigma}_{\alpha\beta} \\ -\frac{1}{2} \mathbf{M}_{\mu\nu}^Y(q) \cdot \boldsymbol{\sigma}_{\alpha\beta} & 0 & 0 & -\frac{1}{2} \mathbf{M}_{\mu\nu}^X(q) \cdot \boldsymbol{\sigma}_{\alpha\beta} \\ 0 & -\frac{1}{2} \mathbf{M}_{\mu\nu}^Y(q) \cdot \boldsymbol{\sigma}_{\alpha\beta} & -\frac{1}{2} \mathbf{M}_{\mu\nu}^X(q) \cdot \boldsymbol{\sigma}_{\alpha\beta} & 0 \end{pmatrix} \quad (3.12) \end{aligned}$$

3.B Nematic susceptibility

where each element of the matrices should be understood as an $N_{\text{orb}} \times N_{\text{orb}}$ matrix in orbital space, with the Green function being

$$\mathcal{G}_{\mu\nu}^0(k) = \sum_m \frac{\langle \mu|m \rangle \langle m|\nu \rangle}{i\omega_n - \xi^m(\mathbf{k})}, \quad (3.13)$$

where m refers to band basis and μ, ν refer to orbital basis. Expanding the trace-log to fourth order in the magnetic order parameters and applying the Pauli matrix identity

$$\sigma_{\alpha\beta}^i \sigma_{\beta\delta}^j \sigma_{\delta\gamma}^k \sigma_{\gamma\alpha}^l = 2 \left(\delta^{ij} \delta^{kl} - \delta^{ik} \delta^{jl} + \delta^{il} \delta^{jk} \right) \quad (3.14)$$

yields the magnetic free energy as written in Eqs. (2) and (4) of the main text, with the fourth order coefficients

$$\begin{aligned} u^{\rho\nu\eta\mu} &= \frac{1}{16} \sum_k \left(2\mathcal{G}^{\mu\rho} \mathcal{G}_X^{\rho\nu} \mathcal{G}^{\nu\eta} \mathcal{G}_X^{\eta\mu} - \mathcal{G}^{\mu\rho} \mathcal{G}_X^{\rho\eta} \mathcal{G}^{\eta\nu} \mathcal{G}_X^{\nu\mu} + \mathcal{G}^{\mu\rho} \mathcal{G}_X^{\rho\nu} \mathcal{G}^{\nu\eta} \mathcal{G}_Y^{\eta\mu} \right. \\ &\quad \left. + \mathcal{G}^{\nu\rho} \mathcal{G}_X^{\rho\mu} \mathcal{G}_{X+Y}^{\mu\eta} \mathcal{G}_X^{\eta\nu} - \mathcal{G}^{\mu\rho} \mathcal{G}_X^{\rho\eta} \mathcal{G}_{X+Y}^{\eta\nu} \mathcal{G}_Y^{\nu\mu} \right) + (X \leftrightarrow Y), \end{aligned} \quad (3.15)$$

$$\begin{aligned} g^{\rho\nu\eta\mu} &= -\frac{1}{16} \sum_k \left(2\mathcal{G}^{\mu\rho} \mathcal{G}_X^{\rho\nu} \mathcal{G}^{\nu\eta} \mathcal{G}_X^{\eta\mu} - \mathcal{G}^{\mu\rho} \mathcal{G}_X^{\rho\eta} \mathcal{G}^{\eta\nu} \mathcal{G}_X^{\nu\mu} - \mathcal{G}^{\mu\rho} \mathcal{G}_X^{\rho\nu} \mathcal{G}^{\nu\eta} \mathcal{G}_Y^{\eta\mu} \right. \\ &\quad \left. - \mathcal{G}^{\nu\rho} \mathcal{G}_X^{\rho\mu} \mathcal{G}_{X+Y}^{\mu\eta} \mathcal{G}_X^{\eta\nu} + \mathcal{G}^{\mu\rho} \mathcal{G}_X^{\rho\eta} \mathcal{G}_{X+Y}^{\eta\nu} \mathcal{G}_Y^{\nu\mu} \right) + (X \leftrightarrow Y), \end{aligned} \quad (3.16)$$

$$\begin{aligned} w^{\rho\nu\eta\mu} &= \frac{1}{16} \sum_k \left(-2\mathcal{G}^{\mu\rho} \mathcal{G}_X^{\rho\eta} \mathcal{G}^{\eta\nu} \mathcal{G}_Y^{\nu\mu} + 2\mathcal{G}^{\nu\rho} \mathcal{G}_X^{\rho\eta} \mathcal{G}^{\eta\mu} \mathcal{G}_Y^{\mu\nu} - 2\mathcal{G}^{\eta\rho} \mathcal{G}_X^{\rho\mu} \mathcal{G}_{X+Y}^{\mu\nu} \mathcal{G}_X^{\nu\eta} + 2\mathcal{G}^{\eta\rho} \mathcal{G}_X^{\rho\nu} \mathcal{G}_{X+Y}^{\nu\mu} \mathcal{G}_X^{\mu\eta} \right. \\ &\quad \left. + \mathcal{G}^{\rho\mu} \mathcal{G}_Y^{\mu\eta} \mathcal{G}_{X+Y}^{\eta\nu} \mathcal{G}_X^{\nu\rho} + \mathcal{G}^{\rho\nu} \mathcal{G}_Y^{\nu\eta} \mathcal{G}_{X+Y}^{\eta\mu} \mathcal{G}_X^{\mu\rho} + \mathcal{G}^{\mu\rho} \mathcal{G}_X^{\rho\nu} \mathcal{G}_{X+Y}^{\nu\eta} \mathcal{G}_Y^{\eta\mu} + \mathcal{G}^{\nu\rho} \mathcal{G}_X^{\rho\mu} \mathcal{G}_{X+Y}^{\mu\eta} \mathcal{G}_Y^{\eta\nu} \right), \end{aligned} \quad (3.17)$$

where repeated orbital indices are not summed. Here all the Green functions are implicit functions of k and $\mathcal{G}_j^{\mu\nu}(k) = \mathcal{G}^{\mu\nu}(k + \mathbf{Q}_j)$ and $\sum_k = T/N_{\mathbf{k}} \sum_{\mathbf{k}} \sum_{\omega_n}$.

3.B Nematic susceptibility

Preparing for an additional HS-decoupling we introduce two bosonic fields $\psi_{\rho\nu}$ and $\phi_{\rho\nu}$ with the partition function

$$\mathcal{Z} = \int \mathcal{D}\phi \mathcal{D}\psi \exp \left[\frac{1}{2} (u^{\rho\nu\eta\mu})^{-1} \psi_{\rho\nu} \psi_{\eta\mu} - \frac{1}{2} (g^{\rho\nu\eta\mu})^{-1} \phi_{\rho\nu} \phi_{\eta\mu} \right], \quad (3.18)$$

with integration measures chosen appropriately such that $\mathcal{Z} = 1$. By performing the shifts

$$\psi_{\rho\nu} \rightarrow \psi_{\rho\nu} - u^{\rho\nu\eta\mu} \left(\mathbf{M}_\eta^X \cdot \mathbf{M}_\mu^X + \mathbf{M}_\eta^Y \cdot \mathbf{M}_\mu^Y \right), \quad (3.19)$$

$$\phi_{\rho\nu} \rightarrow \phi_{\rho\nu} + g^{\rho\nu\eta\mu} \left(\mathbf{M}_\eta^X \cdot \mathbf{M}_\mu^X - \mathbf{M}_\eta^Y \cdot \mathbf{M}_\mu^Y \right), \quad (3.20)$$

the terms quartic in \mathbf{M} cancel accordingly. Following the standard procedure we introduce a field $(h_{\rho\nu})$ conjugate to $\mathbf{M}_\rho^X \cdot \mathbf{M}_\nu^X - \mathbf{M}_\rho^Y \cdot \mathbf{M}_\nu^Y$ and define $\tilde{\phi}_{\rho\nu} = \phi_{\rho\nu} + h_{\rho\nu}$. The resulting action is then

$$\begin{aligned} \mathcal{S}[\mathbf{M}_\mu^i, \psi_{\mu\nu}, \phi_{\mu\nu}] &= \sum_{q, i=X, Y} \left(r_i^{\mu\nu}(q) + \psi_{\mu\nu} \right) \mathbf{M}_\mu^i \cdot \mathbf{M}_\nu^i - \frac{1}{2} (u^{\rho\nu\eta\mu})^{-1} \psi_{\rho\nu} \psi_{\eta\mu} \\ &\quad + \frac{1}{2} (g^{\rho\nu\eta\mu})^{-1} \left(\tilde{\phi}_{\rho\nu} - h_{\eta\mu} \right) \left(\tilde{\phi}_{\eta\mu} - h_{\rho\nu} \right) \\ &\quad - \tilde{\phi}_{\rho\nu} \left(\mathbf{M}_\rho^X \cdot \mathbf{M}_\nu^X - \mathbf{M}_\rho^Y \cdot \mathbf{M}_\nu^Y \right). \end{aligned} \quad (3.21)$$

3.C Frequency dependence of the magnetic susceptibility

Here $r_i^{\mu\nu}(q) = (U_\nu^\mu)^{-1} + \sum_k \mathcal{G}^{\nu\mu}(k) \mathcal{G}_i^{\mu\nu}(k+q)$ and $\mathcal{G}_i^{\mu\nu}(k) \equiv \mathcal{G}^{\mu\nu}(k + \mathbf{Q}_i)$. It is now straightforward to compute the nematic susceptibility:

$$\begin{aligned} \chi_{\text{nem}}^{\rho\nu\eta\mu} &= \lim_{h \rightarrow 0} \left(\frac{\delta^2 \ln \mathcal{Z}}{\delta h_{\rho\nu} \delta h_{\eta\mu}} \right) \\ &= \left(g^{\rho\nu\kappa} g^{\eta\mu\phi\lambda} \right)^{-1} \langle \phi_{\iota\kappa} \phi_{\phi\lambda} \rangle - (g^{\rho\nu\eta\mu})^{-1}, \end{aligned} \quad (3.22)$$

where we used the fact that $\langle \phi_{\rho\nu} \rangle = 0$ as we are above the nematic instability. To continue we note that

$$\frac{\delta^2 F}{\delta \phi_{\rho\nu} \delta \phi_{\eta\mu}} = \langle \phi_{\rho\nu} \phi_{\eta\mu} \rangle^{-1}, \quad (3.23)$$

where the free energy is

$$F = -T \ln \mathcal{Z}, \quad (3.24)$$

obtained by integrating out the magnetic degrees of freedom and taking the large N limit. We find the effective action

$$\begin{aligned} \mathcal{S}_{\text{eff}}[\psi_{\mu\nu}, \phi_{\mu\nu}] &= \frac{1}{2} (g^{\rho\nu\eta\mu})^{-1} \phi_{\rho\nu} \phi_{\eta\mu} + \frac{1}{2} \text{Tr} \ln \left[\chi_{\iota\kappa, Y}^{-1} \chi_{\kappa\lambda, X}^{-1} - \phi_{\iota\kappa} \phi_{\kappa\lambda} \right. \\ &\quad \left. + \chi_{\iota\kappa, Y}^{-1} \phi_{\kappa\lambda} - \phi_{\iota\kappa} \chi_{\kappa\lambda, X}^{-1} \right], \end{aligned} \quad (3.25)$$

where we have ignored the Gaussian fluctuations $\psi_{\rho\nu}$ and $(\chi_i^{\mu\nu}(q))^{-1} = r_i^{\mu\nu}(q)$. Finally

$$\langle \phi_{\rho\nu} \phi_{\eta\mu} \rangle^{-1} = (g^{\rho\nu\eta\mu})^{-1} - \frac{1}{2} \sum_{q, i=X, Y} \chi_{\rho\mu, i}(q) \chi_{\nu\eta, i}(-q) \quad (3.26)$$

and after some manipulations we arrive at the expression given in the text for the nematic susceptibility.

3.C Frequency dependence of the magnetic susceptibility

In this section we illustrate the frequency dependence of the magnetic propagator at various temperatures for representative filling factors of the (n, T) phase diagram (Fig. 4(a) of the main text). Because the magnetic propagator peaks at $(\pi, 0)/(0, \pi)$, we focus on \mathbf{Q}_X . For $n = 5.90$ as we approach the instability (at $k_B T = 45$ meV), the frequency dependence of the propagator $\sum_{\mu\nu} \chi_X^{\mu\nu}(\mathbf{Q}_X, \Omega_n)$ has the form shown in Fig. 3.5, where the bosonic Matsubara frequency is given by $\Omega_n = 2\pi n T$. The gray area denotes the region included in the cut-off $\Omega_c = 1$ eV, and the dotted line indicates $\sum_{\mu\nu} \chi_X^{\mu\nu}(\mathbf{Q}_X, \Omega_n \rightarrow \infty)$. The plots in Fig. 3.5 justify the statement made in the main text that near a finite-temperature magnetic transition, one can safely neglect the higher frequency contributions.

To illustrate the importance of including high frequency contributions in the case where magnetic order is absent, in Fig. 3.6 we also plot the frequency dependence of the magnetic propagator for $n = 6.04$. It is clear that the peak is broadened, implying that it is no longer justified to ignore the contributions originating from finite frequencies.

3.D Derivation of the ferro-orbital order susceptibility

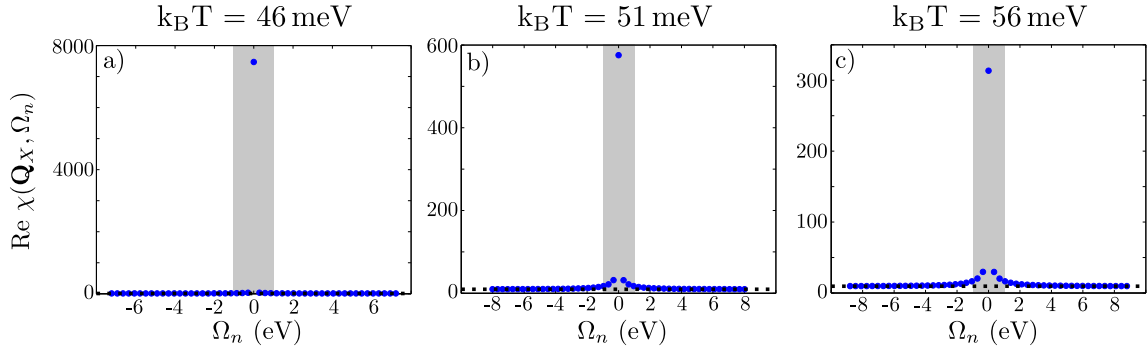


Figure 3.5: Frequency dependence of the magnetic propagator $\sum_{\mu\nu} \chi_X^{\mu\nu}(\mathbf{Q}_X, \Omega_n)$ for $n = 5.90$ at different temperatures. The parameters used are quoted in the main text. The magnetic instability takes place at $k_B T = 45$ meV. From (a) we see that the contribution to the bare nematic susceptibility comes mostly from the zero frequency part of the magnetic susceptibility.

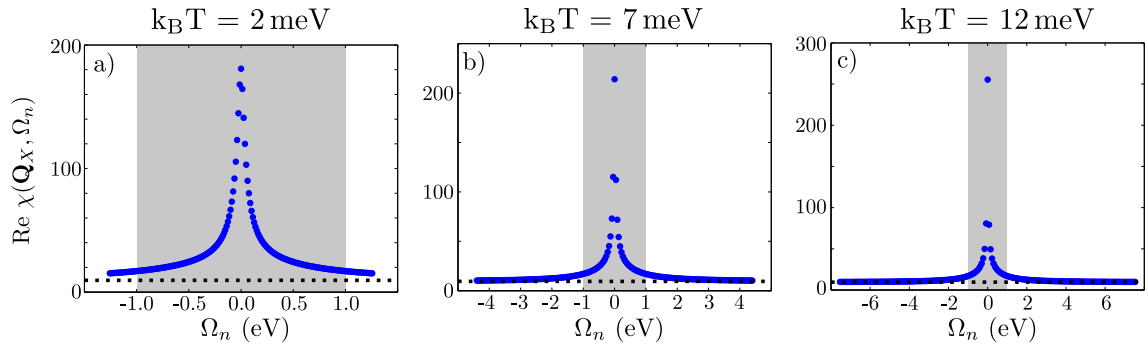


Figure 3.6: Frequency dependence of the magnetic propagator $\sum_{\mu\nu} \chi_X^{\mu\nu}(\mathbf{Q}_X, \Omega_n)$ for $n = 6.04$ at different temperatures. The parameters used are quoted in the main text. As is evident in (a), the peak broadens as zero temperature is approached. However, even at higher temperatures, shown in (b) and (c), finite Matsubara frequencies provide considerable contributions to the bare nematic susceptibility.

3.D Derivation of the ferro-orbital order susceptibility

Ferro-orbital order is characterized by the breaking of the degeneracy between the d_{xz} and d_{yz} orbitals. In the itinerant framework this is seen by an inequivalent occupation of the two orbitals, i.e. $n_{xz} \neq n_{yz}$. Defining $\Delta n(q) \equiv n_{xz}(q) - n_{yz}(q)$ as in the main text, the ferro-orbital susceptibility is given by $\langle \Delta n(q) \Delta n(-q) \rangle$. Using the definition of $\Delta n(q)$, we find that this is nothing but a linear combination of specific components of the charge susceptibility, $(\chi^c)_{\rho\lambda}^{\mu\nu}$. In the standard RPA approach, the full expression is [145, 160]

$$\begin{aligned} \chi_{oo} &= (\chi_{xz,xz}^c)_{\text{RPA}}^{xz,xz} + (\chi_{yz,yz}^c)_{\text{RPA}}^{yz,yz} \\ &- (\chi_{xz,yz}^c)_{\text{RPA}}^{xz,yz} - (\chi_{yz,xz}^c)_{\text{RPA}}^{yz,xz}, \end{aligned} \quad (3.27)$$

where the RPA charge susceptibility is given by the usual expression [140]

$$(\chi_{\text{RPA}}^c)_{\rho\lambda}^{\mu\nu} = \left([1 + \chi_0 U_c]^{-1} \right)_{\rho\gamma}^{\mu\delta} (\chi_0)_{\gamma\lambda}^{\delta\nu}, \quad (3.28)$$

3.D Derivation of the ferro-orbital order susceptibility

where χ_0 is the standard particle-hole bubble

$$(\chi_0(q))_{\rho\lambda}^{\mu\nu} = - \sum_k \mathcal{G}^{\mu\nu}(k) \mathcal{G}^{\rho\lambda}(k+q) \quad (3.29)$$

and U_c is the interaction matrix in the charge channel. The latter differs from the interaction in the SDW channel and is given by ($a \neq b$)

$$(U_c)_{aa}^{aa} = U, \quad (3.30)$$

$$(U_c)_{bb}^{aa} = 2U' - J = 2U - 5J, \quad (3.31)$$

$$(U_c)_{ab}^{ab} = 2J - U' = 4J - U, \quad (3.32)$$

$$(U_c)_{ab}^{ba} = J' = J. \quad (3.33)$$

We note that, due to the implicit summation over repeated indices in Eq. (3.28), all orbitals contribute to the RPA orbital order susceptibility. The static part of Eq. (3.27) at $\mathbf{q} = 0$ is the quantity plotted in Fig. 4(b) in the main text.

Chapter 4

Interplay of Magnetism and Superconductivity in Cuprate Superconductors

The discovery of superconductivity in a ceramic compound in 1986 [2] led to intense research into new superconducting materials. The first high-temperature superconductor, $\text{La}_{2-x}\text{Ba}_x\text{CuO}_4$, has a critical temperature of $T_c \sim 35$ K. Soon after the initial discovery, other ceramics such as $\text{YBa}_2\text{Cu}_3\text{O}_{6+x}$ and $\text{HgBa}_2\text{Ca}_2\text{Cu}_3\text{O}_{8+x}$, were also shown to be superconductors and within the first few years the record critical temperature was increased to above 100 K, making liquid nitrogen the coolant of choice. The parent compounds of these materials are antiferromagnetic Mott-insulators making the appearance of superconductivity highly unexpected. Furthermore, conventional wisdom at the time held that magnetism was detrimental for superconductivity [4]. Nonetheless, as the antiferromagnetic phase is suppressed with carrier doping, a superconducting dome emerges, and in some compounds a phase with coexisting superconductivity and magnetism even appears. These puzzling facts hinted at a mechanism substantially different from the celebrated phonon-mediated attraction between electrons underlying the formation of the superconducting state in conventional superconductors. With this, the field of unconventional superconductors was born and Bednorz and Müller were awarded the Nobel Prize in Physics in 1987 for their paradigm-changing discovery.

Cuprates are materials with a perovskite structure as shown in Fig. 4.1, and superconductivity emerges in the CuO_2 -layers. The oxygen octahedra are elongated along the direction perpendicular to the planes making the in-plane Cu-O bonds dominant and justifies considering the materials as quasi-2d. Considering for concreteness the parent compound La_2CuO_4 . Here the oxygen atoms are in the O^{2-} state while the lanthanum atoms are in the La^{3+} state. Thus, the copper atoms are in the Cu^{2+} state such that nine electrons are occupying the Cu d -orbitals. The octahedral environment breaks the rotational invariance and the degeneracy of the d -orbitals is lifted with the $d_{x^2-y^2}$ being the highest in energy, and the remaining hole occupies this state. Replacing lanthanum by barium or strontium reduces the number of electrons available and thus corresponds to

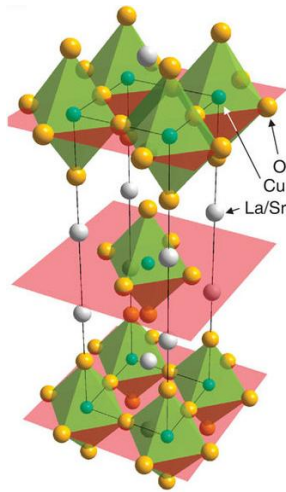


Figure 4.1: Unit cell of $\text{La}_{2-x}\text{Sr}_x\text{CuO}_4$ showing the perovskite structure and highlighting the CuO_2 . Figure from Ref. [161].

hole doping. Similarly, increasing the amount of interstitial oxygen in $\text{YBa}_2\text{Cu}_3\text{O}_{6+x}$ also adds additional holes to the system. A generic phase diagram for a cuprate superconductor is shown in Fig. 4.2. Electron doping generally leads to a lower critical temperature. Since the magnetic phases of interest to the study presented in Chapter 5 are found in the hole-doped regime the remaining discussion will focus on hole-doped cuprates.

A robust antiferromagnetic phase is formed due to the superexchange interactions between the copper and the oxygen atoms. With an odd number of electrons in a unit cell, one might naively expect these compounds to be metals. However, due to the presence of strong Coulomb interactions that serve to confine the electrons, the materials are charge-transfer insulators with a charge-transfer gap W smaller than the Coulomb repulsion. Upon slight hole-doping a pseudogap phase appears. In this phase, Fermi arcs centered on the Brillouin zone corners evolve signifying the fact that electrons moving parallel to the Cu-O bonds remain gapped, while electrons moving along the diagonal are unaffected. Due to the superconducting gap having nodes along the diagonal direction, the pseudogap has been interpreted as a signature of preformed electron pairs which display large phase fluctuations preventing the onset of actual superconducting order. However, this viewpoint is controversial and the origin of the pseudogap has also been attributed to phenomena not directly related to superconductivity, such as electronic stripes [162], loop-current order [163, 164], or d -density wave states [165].

A superconducting dome emerges as the antiferromagnetic order is suppressed by doping. The maximum value of T_c has been shown to depend on the number of CuO_2 layers in a unit cell, with more layers implying a higher value of T_c , up to a maximum of three, after which T_c decreases again [166]. As in the case of conventional superconductors, the onset of superconductivity is signified by the condensation of electrons into spin-singlet Cooper-pairs. In the case of cuprates however, the form-factor is of d -wave nature and the gap has nodes along the diagonal of the Brillouin zone [16, 17]. The origin of the pairing responsible for the condensation of electrons is still unclear, although the nodal d -wave

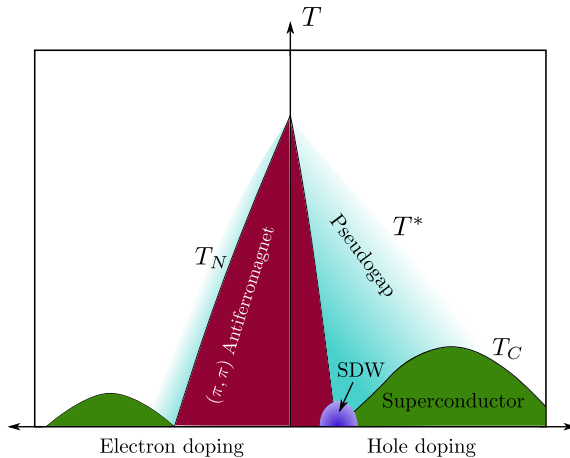


Figure 4.2: Schematic phase diagram of a cuprate superconductor. The transition to the pseudogap phase is here denoted by T^* . In Chapter 5 we consider the small blue SDW region where the magnetic and superconducting regions overlap.

gap is consistent with one mediated by magnetic fluctuations. This can be seen from the gap equation

$$\Delta_{\mathbf{k}} = -\frac{1}{2} \sum_{\mathbf{k}'} V_{\mathbf{k}\mathbf{k}'} \frac{\Delta_{\mathbf{k}'}}{\sqrt{|\xi_{\mathbf{k}}|^2 + |\Delta_{\mathbf{k}'}|^2}}, \quad (4.1)$$

where $V_{\mathbf{k}\mathbf{k}'} = V_{\mathbf{k}-\mathbf{k}'}$ for an effective (repulsive) electron interaction mediated by the magnetic fluctuations, and exhibits a peak in the vicinity of $\mathbf{k} - \mathbf{k}' = \mathbf{Q}$, where \mathbf{Q} is the magnetic ordering vector. In this case a solution to the gap equation can be found for $\Delta_{\mathbf{k}} = -\Delta_{\mathbf{k}+\mathbf{Q}}$, e.g. an order parameter with $d_{x^2-y^2}$ symmetry:

$$\Delta_{\mathbf{k}} = \frac{\Delta_0}{2} (\cos k_x a - \cos k_y a), \quad (4.2)$$

where a is the lattice constant. In real space this corresponds to a bond order parameter where the bonds along x have the opposite sign of the bonds along y .

At this point it is useful to consider a model capable of capturing at least some of the salient features described above. The first attempt at this came with a three-orbital model by Emery [167] and simultaneously by Varma *et al.* [168] using the hole states in the Cu $d_{x^2-y^2}$ orbital and the O p_x and p_y orbitals. The interaction part was made up of two on-site repulsion terms, for holes on the Cu or O sites, along with an additional nearest neighbour repulsion between holes on Cu and O sites. This model was refined and simplified by Zhang and Rice [169] who argued that a local singlet forms by hybridisation between a hole at the Cu site and a hole formed on each square of O atoms. The associated triplet state can be projected out due to the large energy difference between the singlet and the triplet [169]. The resulting Hamiltonian is the one-band $t - J$ -model, the well-known limit of the one-band Hubbard model in the case of large interactions U :

$$\mathcal{H} = - \sum_{ij} (t_{ij} - \mu \delta_{ij}) c_{i\sigma}^\dagger c_{j\sigma} + U \sum_i n_{i\uparrow} n_{i\downarrow}. \quad (4.3)$$

4.1 Magnetic Susceptibility in the Superconducting State

In this approximation the study of cuprate superconductors thus becomes the study of the two-dimensional single-band Hubbard model. It should be noted however, that the single-band approximation, while widely accepted, neglects the O p -orbitals completely and the validity of this approximation has been questioned by a number of authors [170–173]. Nevertheless, we will adopt a version of the single-band Hubbard model in Chapter 5.

4.1 Magnetic Susceptibility in the Superconducting State

The transverse magnetic susceptibility provides a useful probe of the magnetic fluctuations. Since this quantity is important for the considerations in Chapter 5 we here provide a few important results. The magnetic susceptibility is a measure of the spin-spin correlation and it is given by

$$\chi^{+-}(\mathbf{r}_i, \mathbf{r}_j, \tau) = \langle S^+(\mathbf{r}_i, \tau) S^-(\mathbf{r}_j, 0) \rangle, \quad (4.4)$$

where $S^+(\mathbf{r}_i, \tau)$ (S^-) creates (annihilates) a spin excitation at position \mathbf{r}_i and imaginary time τ . Evaluating the above expectation value using the random-phase-approximation (RPA) yields

$$\chi^{+-}(\mathbf{q}, \omega) = \frac{\chi_0^{+-}(\mathbf{q}, \omega)}{1 - U\chi_0^{+-}(\mathbf{q}, \omega)}, \quad (4.5)$$

where χ_0^{+-} is the bare susceptibility (in the superconducting state):

$$\begin{aligned} \chi_0^{+-}(\mathbf{q}, \omega) &= \frac{1}{\mathcal{V}} \sum_{\mathbf{k}} \frac{1}{4} \left(1 - \frac{\xi_{\mathbf{k}} \xi_{\mathbf{k}+\mathbf{q}} + \Delta_{\mathbf{k}} \Delta_{\mathbf{k}+\mathbf{q}}}{E_{\mathbf{k}} E_{\mathbf{k}+\mathbf{q}}} + \frac{\xi_{\mathbf{k}}}{E_{\mathbf{k}}} - \frac{\xi_{\mathbf{k}+\mathbf{q}}}{E_{\mathbf{k}+\mathbf{q}}} \right) \frac{1 - n_{\text{F}}(E_{\mathbf{k}}) - n_{\text{F}}(E_{\mathbf{k}+\mathbf{q}})}{\omega + E_{\mathbf{k}} + E_{\mathbf{k}+\mathbf{q}} + i0^+} \\ &\quad + \frac{1}{4} \left(1 - \frac{\xi_{\mathbf{k}} \xi_{\mathbf{k}+\mathbf{q}} + \Delta_{\mathbf{k}} \Delta_{\mathbf{k}+\mathbf{q}}}{E_{\mathbf{k}} E_{\mathbf{k}+\mathbf{q}}} - \frac{\xi_{\mathbf{k}}}{E_{\mathbf{k}}} + \frac{\xi_{\mathbf{k}+\mathbf{q}}}{E_{\mathbf{k}+\mathbf{q}}} \right) \frac{n_{\text{F}}(E_{\mathbf{k}}) + n_{\text{F}}(E_{\mathbf{k}+\mathbf{q}}) - 1}{\omega - E_{\mathbf{k}} - E_{\mathbf{k}+\mathbf{q}} + i0^+} \\ &\quad + \frac{1}{2} \left(1 + \frac{\xi_{\mathbf{k}} \xi_{\mathbf{k}+\mathbf{q}} + \Delta_{\mathbf{k}} \Delta_{\mathbf{k}+\mathbf{q}}}{E_{\mathbf{k}} E_{\mathbf{k}+\mathbf{q}}} \right) \frac{n_{\text{F}}(E_{\mathbf{k}}) - n_{\text{F}}(E_{\mathbf{k}+\mathbf{q}})}{\omega - E_{\mathbf{k}} + E_{\mathbf{k}+\mathbf{q}} + i0^+}, \end{aligned} \quad (4.6)$$

written in momentum and frequency space with \mathcal{V} being the volume of the system and $E_{\mathbf{k}}^2 = \xi_{\mathbf{k}}^2 + \Delta_{\mathbf{k}}^2$. The infinitesimal $i0^+$ originates from an analytical continuation from Matsubara frequency, $i\omega_n \rightarrow \omega + i0^+$. The imaginary part

$$\text{Im}\chi^{+-}(\mathbf{q}, \omega) = \frac{\text{Im}\chi_0^{+-}(\mathbf{q}, \omega)}{\left(1 - U\text{Re}\chi_0^{+-}(\mathbf{q}, \omega)\right)^2 + \left(U\text{Im}\chi_0^{+-}(\mathbf{q}, \omega)\right)^2} \quad (4.7)$$

contains information concerning the dynamics of the spin excitations and exhibits very distinct behaviour in the superconducting state. For non-zero $\text{Im}\chi_0^{+-}(\mathbf{q}, \omega)$ this becomes a Lorentzian with a peak at $1 - U\text{Re}\chi_0^{+-}(\mathbf{q}, \omega)$. However, the imaginary part of the bare susceptibility is (considering only Fermi surface scattering for simplicity)

$$\text{Im}\chi_0^{+-}(\mathbf{q}, \omega) = \frac{1}{\mathcal{V}} \sum_{\mathbf{k}} \frac{1}{4} \left(1 - \frac{\Delta_{\mathbf{k}} \Delta_{\mathbf{k}+\mathbf{q}}}{|\Delta_{\mathbf{k}}| |\Delta_{\mathbf{k}+\mathbf{q}}|} \right) \delta(\omega - |\Delta_{\mathbf{k}}| - |\Delta_{\mathbf{k}+\mathbf{q}}|) \quad (4.8)$$

which is non-zero only for $\omega > \Delta_{\mathbf{k}} + \Delta_{\mathbf{k}+\mathbf{q}}$ and if the gap changes sign between \mathbf{k} and $\mathbf{k} + \mathbf{q}$. For d -wave superconductivity with nodes along the diagonal of the Brillouin zone

as in Eq. 4.2, this implies the opening of a spin-gap in the superconducting state for frequencies $\omega < 2\Delta_0$ and the formation of a resonance peak at approximately $\omega = 2\Delta_0$, due to transfer of spectral weight. The appearance of the resonance peak has become a hallmark of unconventional superconductivity, appearing in both cuprates, heavy-fermion compounds and iron-based superconductors [174]. While a resonance is indicative of a sign-changing order parameter, an alternative explanation attributes the appearance of a peak in certain FeSC to dissipationless quasiparticles and suggesting that an s^{++} order parameter is not inconsistent with the observed magnetic resonances in FeSC [175].

4.2 Magnetic Stripes in Cuprates

In Chapter 5 we will focus on the crossover region between magnetism and superconductivity for a particular cuprate superconductor, $\text{La}_{2-x}\text{Ba}_x\text{CuO}_4$ (LBCO). Upon hole-doping the magnetic order in this compound changes from a simple (π, π) antiferromagnet to a striped antiferromagnetic phase in which the magnetic order is modulated along one direction in a manner dependent on the doping, while the other direction remains antiferromagnetic [176]. Evidence for the existence of static stripe order was first obtained from neutron scattering experiments on $\text{La}_{1.6-x}\text{Nd}_{0.4}\text{Sr}_x\text{CuO}_4$ [177] and later it was also observed in various other derivatives of La_2CuO_4 , including LBCO at $x = 0.125$ [178, 179]. The periodicity of the magnetic stripes depends on the doping such that the magnetic wavevector is $\mathbf{Q} \approx \pi(1 \pm 2x, 1)$ [180]. In addition to the modulation of the magnetic order there is a modulation of the charge order with twice the periodicity. This is manifested as areas containing a surplus of carriers, so-called rivers of charge, divided by areas of localised moments as shown in Fig. 4.3. The neighbouring CuO_2 -layer exhibits similar behaviour, only the stripes are along the orthogonal direction. In the next-nearest neighbour layer, the charge rivers have shifted in an effort to minimise the Coulomb repulsion, such that they are above the magnetic stripes of the first layer as indicated in Fig. 4.3.

The stripe phases originally attracted attention as an effort to explain an observed anomalous suppression of the critical temperature around $x = 0.125$ in LBCO [181, 182]. Using transport and magnetization measurements, Li *et al.* [183] showed that while the resistivity in the in-plane direction vanishes around 40 K, the Meissner effect is absent and bulk superconductivity does not occur until 4 K. Bulk superconductivity typically occurs as a consequence of 2D superconductivity due to the inter-layer Josephson coupling. The large disparity between the 2D superconducting temperature and the onset of bulk superconductivity was therefore interpreted as a vanishing of the Josephson coupling. Berg *et al.* [184] proposed a superconducting order parameter which coexists with the magnetic stripes but exhibits a phase difference across the intervening charge stripes, a so-called pair-density-wave (PDW) state [184, 194] (see Fig. 5.1(a) for an illustration). The orthogonal orientation of adjacent planes along with this phase difference imply that the Josephson couplings between a plane and its three nearest neighbours vanish by symmetry [184, 185]. Note that the PDW state also exhibits d -wave symmetry. This can be seen from the bond order parameter in real space, where the value on bonds in the x -direction is opposite that of bonds in the y -direction (compare Figs. 5.1(a) and 5.1(b)). Observing

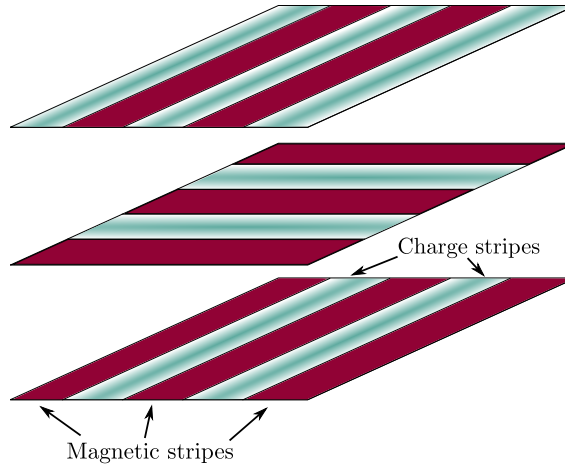


Figure 4.3: Schematic illustration of the intertwined charge and magnetic stripes occurring in LBCO around $x \sim 1/8$. Each plane denotes a CuO_2 -layer with stripes running in the direction indicated. The stripes are shifted by one quarter of a period in next-nearest neighbour planes so as to minimise the Coulomb interactions.

such an order parameter experimentally is rather challenging although progress in this direction came recently with STM experiments using a superconducting tip, and signs of a PDW state was reported [186]. In 2014 Xu *et al.* [36] used inelastic neutron scattering to measure the dynamic susceptibility of LBCO at $x = 0.095$, and found that a magnetic resonance does not form as the material becomes superconducting. As mentioned above, the absence of a resonance peak is highly unexpected and is in stark contrast to results for numerous other materials all exhibiting a resonance at roughly $2\Delta_0$ [174]. The authors conjectured that this discrepancy was due to the existence of a PDW state. To investigate whether this is consistent with theory we calculated the dynamic susceptibility with a PDW superconducting order parameter, both in the absence of any magnetic order and for the case when a PDW state coexists with a magnetic stripe. We find that in both cases a magnetic resonance is absent for PDW superconductivity thus agreeing with the experimental results.

Chapter 5

Magnetic fluctuations in pair density wave superconductors

*This chapter has been published by the author and Henrik Jacobsen, Thomas A. Maier, and Brian M. Andersen in Phys. Rev. Lett. **116** 167001 (2016).*

In an effort to establish the potential existence of a PDW phase in cuprate superconductors we compute the dynamic magnetic susceptibility for a number of different magnetic and superconducting orders. As argued in Chapter 4 the magnetic resonance is a useful probe for the existence of a sign-changing order parameter. Here we illustrate the appearance of a spin-gap and a magnetic resonance for standard d -wave superconductivity and show that neither appears in the case of PDW order. As PDW order is conjectured to arise in connection with the magnetic striped state in LBCO we additionally compute the resonance in the coexistence phase for which the presence of Goldstone modes precludes the opening of a spin-gap, however the resonance is still absent for PDW superconductivity coexisting with magnetism. This implies that the absence of a magnetic resonance reported in by Xu *et al.* in Ref. [36] is consistent with a PDW phase.

5.1 Introduction

Superconductivity can have significant effects on the structure of the spin fluctuations. This includes, for example, the opening of a spin-gap at low energies and the appearance of a magnetic neutron resonance when the gap exhibits sign changes along the Fermi surface as in cuprates and iron-based materials [187]. Similarly, the structure of the magnetic fluctuations can have important consequences for the superconducting state, even possibly its mere existence [188]. Thus, spin fluctuations and unconventional superconductivity are intimately linked, and the question of exactly how they are connected and what this tells us about the pairing mechanism [187] remains a challenging and relevant problem in the field of high-temperature superconductivity.

The pseudogap regime of the underdoped cuprates is highly susceptible to spin and charge order. Unidirectionally (striped) modulated spin and charge order was first discovered near a hole doping of $x = 1/8$ in $\text{La}_{1.6-x}\text{Nd}_{0.4}\text{Sr}_x\text{CuO}_4$ [176], and subsequently in other cuprates also exhibiting low-temperature tetragonal crystal structure, including $\text{La}_{2-x}\text{Ba}_x\text{CuO}_4$ [178, 182, 189, 190]. However, stripe correlations appear to be present in many other cuprates, and the universal hour-glass spin excitation spectrum observed in inelastic neutron scattering experiments has been explained within stripe models [126, 191, 192]. On the other hand, calculations based on purely itinerant models that include d -wave superconductivity but no static stripe order also find a neutron resonance with an hour-glass dispersion [193]. At present, a detailed quantitative description of the spin dynamics of the cuprates, and its evolution from antiferromagnetic spin waves in the parent compounds to itinerant paramagnons with a clear spin-gap and a neutron resonance in the overdoped regime, remains an unsettled problem. Hence it is important to study the intermediate doping regime where prominent stripe correlations coexist with superconducting order.

An experimental study of the transport properties of striped $\text{La}_{1.875}\text{Ba}_{0.125}\text{CuO}_4$ [183] reported 2D superconductivity coexisting with stripe order at temperatures above the 3D superconducting transition temperature. This was taken as evidence for an anti-phase ordering of the superconducting order parameter between the CuO_2 layers, which suppresses the inter-layer Josephson coupling required for 3D superconductivity. The existence of pair density wave (PDW) order, in which striped charge, magnetic and superconducting orders are intertwined with unusual sign changes of the superconducting phase [194, 195], has been proposed as a possible explanation of these findings [184, 185]. In the PDW state, the superconducting order parameter has a finite Cooper pair momentum with periodicity equal to that of the magnetic stripe order as illustrated in Fig. 5.1(a) [162]. This is to be contrasted with a more ordinary modulated d -wave superconductor (dSC), in which the superconducting order parameter is in-phase across the stripe domains, and modulated in amplitude with the same periodicity as the charge stripes, i.e. half the wave length of the PDW state as shown in Fig. 5.1(b).

The possibility of a PDW state was investigated within microscopic models, and numerical studies of the t - J model generally find that this state is energetically competitive with other more ordinary modulated superconducting states [196–199]. Similar conclusions were

5.2 Model

reached within an extended version of BCS theory above a critical pairing strength [200], while subsequent Hartree-Fock studies focused on the single-particle electronic properties of phases of combined PDW order and AFM stripes [201, 202]. More recently, finite momentum superconducting PDW order has resurfaced in theoretical studies of the charge density wave (CDW) order detected in underdoped cuprates [136, 203, 204]. The existence of an entangled CDW/PDW phase was found and analyzed both in the context of an emergent SU(2) symmetry of the fermionic hot-spot model [204, 205], and in the spin-fermion model close to the onset of antiferromagnetism [206, 207].

Experimentally, a recent neutron scattering study of the low-energy spin response in stripe ordered $\text{La}_{1.905}\text{Ba}_{0.095}\text{CuO}_4$ [36] found a number of remarkable results that were taken as evidence for a PDW state: (1) gapless spin excitations coexisting with superconductivity, and (2) the absence of a neutron resonance in the superconducting state. These results are highly unusual since both a spin-gap and a neutron resonance are expected in unconventional superconductors like the cuprates [187].

Motivated by the experimental findings of Ref. [36], we perform a theoretical study of the fingerprints of a putative PDW state on the inelastic neutron scattering spectrum. We focus on the consequences of the PDW state rather than its microscopic origin. We find that the PDW state in the *absence* of magnetic and charge order exhibits neither a spin-gap nor a neutron resonance, contrary to the standard dSC phase. For the state where PDW superconductivity coexists with striped magnetic order, we find qualitatively similar results. In particular, the neutron scattering spectrum in this coexistence phase is almost identical to that of the normal state. In the standard dSC phase, on the other hand, we show that the neutron resonance is robust to coexisting stripe order. These findings support a scenario where the absence of a spin-gap and a magnetic resonance in underdoped $\text{La}_{1.905}\text{Ba}_{0.095}\text{CuO}_4$ [36] is explained by the existence of a PDW condensate.

5.2 Model

The stripe phase coexisting with superconductivity is studied within a phenomenological mean-field one-band Hubbard model

$$\begin{aligned} \mathcal{H}^{\text{MF}} = & - \sum_{ij\sigma} (t_{ij} + \mu\delta_{ij}) c_{i\sigma}^\dagger c_{j\sigma} + U \sum_{i\sigma} \langle n_{i\bar{\sigma}} \rangle n_{i\sigma} \\ & - \sum_{\langle ij \rangle} \left[\Delta_{ji} c_{i\uparrow}^\dagger c_{j\downarrow}^\dagger + \text{H.c.} \right], \end{aligned} \quad (5.1)$$

with $U > 0$. For the hopping integrals t_{ij} , we include NN $t = 1$ (setting the unit of energy) and NNN couplings $t' = -0.3$. The details of the bandstructure are not important for the results discussed below. The associated Fermi surface of the tight-binding model is depicted in Fig. 5.1(c). The Hamiltonian (5.1) and its generalizations have been used previously to study the stripe phase of the cuprates [208–211], including the electronic properties of the PDW phase [201, 202], but an analysis of the spin response in the PDW phase has not previously been addressed theoretically.

Here we use an 8×2 supercell to study the effects of stripe and PDW order on the magnetic excitation spectrum. The periodicity of the magnetic (charge) stripe order is

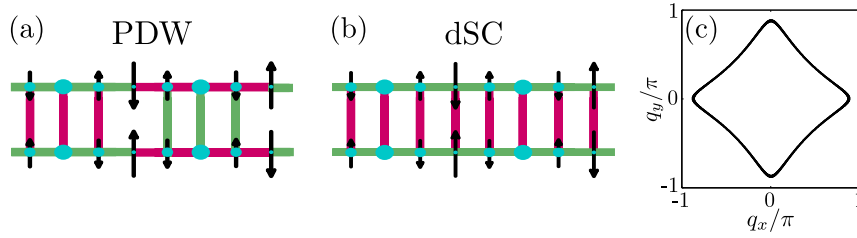


Figure 5.1: (Color online) (a)-(b) Illustration of the unit cells with charge and spin order, and either PDW (a) or dSC (b) superconducting order. The arrows denote the magnetization, the diameter of the circles the hole density, and the colors on the bonds indicate the sign of the superconducting order parameter, green is positive and magenta is negative. (c) Normal state Fermi surface with a doping of 12.5%.

therefore restricted to 8 (4) lattice sites along \hat{x} and 2 (1) sites along \hat{y} . This restriction limits the possible solutions and a selfconsistent iterative procedure in general only obtains a saddle point in the free energy landscape. The actual minimum is often located at a different periodicity which is inaccessible due to the restriction to 8×2 periodic unit cells. In such cases the Goldstone modes either remain gapped or the spin-wave branches cross zero energy before reaching the ordering vector [212]. To study the spin response in the presence of 8×2 periodic stripes we therefore adopt an alternative approach: we impose a density modulation $\langle n_{i\sigma} \rangle$, corresponding to site-ordered magnetic and charge stripes, and a superconducting order parameter, $|\Delta_{ij}| = 0.05$, corresponding to either dSC or PDW order, as shown in Fig. 5.1(a)-(b). For each chosen configuration, we subsequently adjust the bare interaction U such that Goldstone's theorem is satisfied, i.e. such that the denominator of the real part of the RPA susceptibility exhibits a zero eigenvalue at $q_x = \pi \pm \frac{\pi}{4}$ (see Appendix 5.B for further details). This procedure guarantees a stable energy minimum in the energy landscape of 8×2 periodic stripes, and has the benefit of allowing us to study PDW-, dSC-, and non-superconducting solutions within the same region of parameter space and the same assumed density modulations. This allows us to single out the effects of just the PDW order on the spin susceptibility.

We apply a supercell formalism, where the total $N \times N$ (here $N = 96$) system consists of supercells of size 8×2 . The dynamical spin susceptibility $\chi^{+-}(\mathbf{q}, \omega) = \chi^{+-}(\mathbf{q}, i\omega_n \rightarrow \omega + i\delta)$ that determines the neutron scattering intensity may be obtained from

$$\chi^{+-}(\mathbf{q}, i\omega_n) = \sum_{\mathbf{r}_i, \mathbf{r}_j} e^{-i\mathbf{q}(\mathbf{r}_i - \mathbf{r}_j)} \chi^{+-}(\mathbf{r}_i, \mathbf{r}_j, i\omega_n), \quad (5.2)$$

which contains terms originating from both the intra- and inter-supercell structure. Here $\mathbf{r}_i = \mathbf{R}_i + i$ where \mathbf{R}_i yields the supercell containing site \mathbf{r}_i and i gives the site of \mathbf{r}_i in that supercell. The site dependent susceptibility is obtained from

$$\chi^{+-}(\mathbf{r}_i, \mathbf{r}_j, i\omega_n) = \int_0^\beta d\tau e^{i\omega_n \tau} \langle S^+(\mathbf{r}_i, \tau) S^-(\mathbf{r}_j, 0) \rangle,$$

where $S^+(\mathbf{r}_i, \tau) = c_{\mathbf{r}_i\uparrow}^\dagger(\tau) c_{\mathbf{r}_i\downarrow}(\tau)$ is the spin raising operator at position \mathbf{r}_i at (imaginary) time τ and $S^-(\mathbf{r}_i, \tau)$ the corresponding spin lowering operator. The bare susceptibility takes the standard form, consisting of contributions from both normal and anomalous

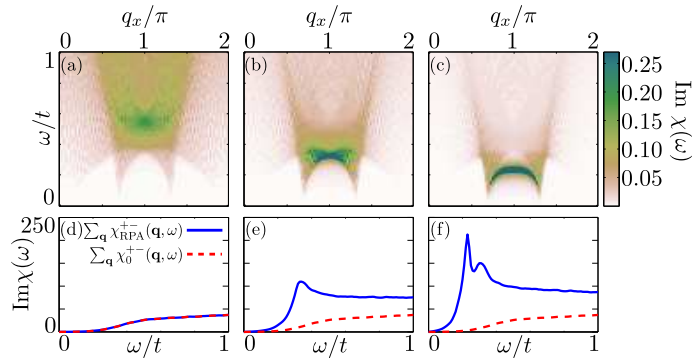


Figure 5.2: (Color online) (a)-(c) Imaginary part of the spin susceptibility $\text{Im}\chi^{+-}(\mathbf{q}, \omega)$ with only dSC order. Here we have set $q_y = \pi$ and plot $\text{Im}\chi^{+-}(q_x, \pi, \omega)$ versus q_x/π and ω/t with (a) $U = 0$, (b) $U/t = 1.8$, and (c) $U/t = 2.2$. For clarity the intensity of the first two cases has been rescaled. (d)-(e) show the imaginary part of the \mathbf{q} -integrated bare (red dashed) and RPA (blue solid lines) susceptibilities.

Green functions as detailed in Appendix 5.A. At the RPA level, the site-dependent susceptibility is given by

$$\begin{aligned} \chi^{+-}(\mathbf{r}_i, \mathbf{r}_j, \omega) &= \chi_0^{+-}(\mathbf{r}_i, \mathbf{r}_j, \omega) \\ &+ U \sum_{\mathbf{r}_l} \chi_0^{+-}(\mathbf{r}_i, \mathbf{r}_l, \omega) \chi^{+-}(\mathbf{r}_l, \mathbf{r}_j, \omega), \end{aligned} \quad (5.3)$$

where $\chi_0^{+-}(\mathbf{r}_i, \mathbf{r}_j, \omega)$ is the bare susceptibility calculated with respect to the mean-field Hamiltonian in Eq. (5.1).

5.3 Results

In order to disentangle the effects of superconductivity on the spin response from those of the striped magnetic order, we start by considering systems with either only dSC or only PDW order, i.e. without coexisting charge and magnetic order. In Fig. 5.2 we show the imaginary part of the RPA susceptibility for the dSC phase at $q_y = \pi$. As evident from the results for the bare susceptibility χ_0 (red dashed curve) in Fig. 5.2(c)-(d), one clearly sees the opening of a spin-gap below 2Δ (at $U = 0$). At finite U a resonance peak, which shifts to lower energies as U increases, appears at energies slightly below the bare spin-gap as seen more clearly from Fig. 5.2(e)-(f), as expected for a superconducting gap that changes sign under translation of $\mathbf{Q} = (\pi, \pi)$ [187, 193].

The corresponding results for the case with only PDW order are plotted in Fig. 5.3, and seen to be in stark contrast to the phase with only dSC order (Fig. 5.2). In the PDW phase, although the system is superconducting, a spin-gap is clearly absent. Without a spin-gap, quasiparticle damping is not suppressed which further implies that a magnetic resonance should be absent, consistent with the RPA results displayed in Fig. 5.3. As seen, the spectral weight is rather structureless and distributed over a wider range in both frequency and momentum. A comparison of the PDW phase with the normal (non-ordered) case, shown in Fig. 5.3(d-f) by the dotted black lines, reveals that the spin response of the normal state and the PDW state are in fact remarkably similar.

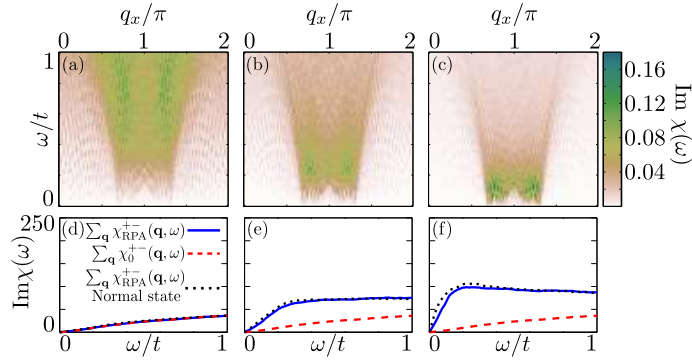


Figure 5.3: (Color online) (a)-(c) Imaginary part of the spin susceptibility $\text{Im}\chi^{+-}(\mathbf{q}, \omega)$ versus q_x/π and ω/t for a system with only PDW order for the same values of U as in Fig. 5.2. (d)-(f) Imaginary part of the \mathbf{q} -integrated susceptibilities corresponding to (a)-(c). The black dashed lines show the integrated RPA susceptibility in the normal state.

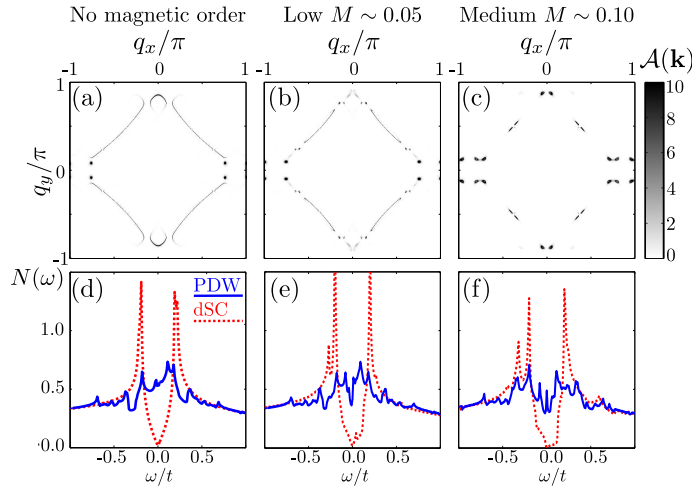


Figure 5.4: (Color online) (a)-(c) The spectral function $\mathcal{A}(\mathbf{k}, \omega = 0)$ for a system with PDW order and increasing magnitude of the site-averaged magnetic moment. (d)-(f) Comparison of the DOS for the PDW and dSC phases for the same parameters corresponding to panels (a)-(c).

One may understand the absence of a spin-gap in the PDW state from the zero frequency single-particle spectral weight $\mathcal{A}(\mathbf{k}, \omega = 0)$ and the associated density of states (DOS) displayed in Fig. 5.4(a) and 5.4(d). The dSC phase (not shown) exhibits the usual gap structure, with gap nodes along the $|k_x| = |k_y|$ lines in $\mathcal{A}(\mathbf{k})$. In contrast, the PDW phase exhibits states on large parts of the Fermi surface [Fig. 5.4(a)] and the DOS clearly does not exhibit a suppression of states near the Fermi level [202]. The low-energy states in the PDW state are caused by the mismatch of the real-space pairing bonds seen in Fig. 5.1(a), which are known to produce low-energy Andreev-like zero-energy states [213].

We now turn to the full coexistence phase with 8×2 -periodic magnetic and charge stripes as well as PDW or dSC orders present. Combining superconductivity with magnetic and charge order leads to a reconstruction of the Fermi surface, evidenced in Fig. 5.4(b,c).

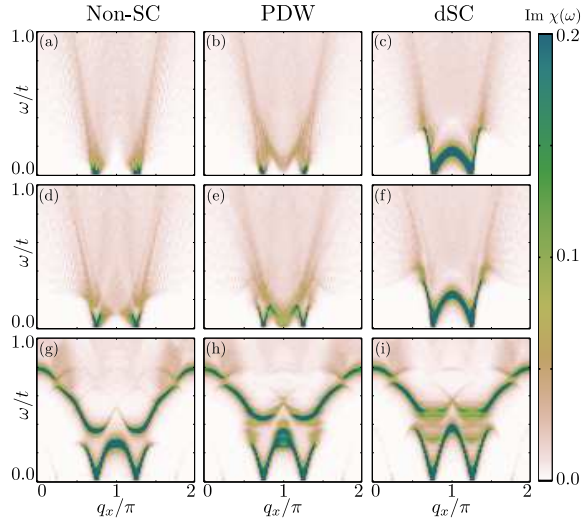


Figure 5.5: (Color online) Imaginary part of the spin susceptibility $\text{Im}\chi^{+-}(\mathbf{q}, \omega)$ in the presence of stripe charge and magnetic order without superconductivity (left column), and with superconductivity (middle and rightmost columns), for increasing magnetic order; (a)-(c) show the case where the site-averaged magnetic moment $M \sim 0.05$, (d)-(f) corresponds to $M \sim 0.1$, and (h)-(i) has $M \sim 0.4$.

The effect of a finite (weak) magnetization on the DOS is relatively minor, as seen in Fig. 5.4(e)-(f). The system with a PDW does not exhibit a full gap, even at $\omega = 0$, while the gap present in the dSC case is only altered quantitatively by the addition of magnetism. Similar conclusions hold for the spectral function: the PDW state still exhibits states on large parts of the Fermi surface, while only states along the nodal lines are present in the dSC phase.

Proceeding to study the spin-wave spectrum of the coexistence phase, we first note that the presence of Goldstone modes necessarily excludes the opening of a spin-gap. This is clearly seen in Fig. 5.5, where we show the imaginary part of the susceptibility $\chi^{+-}(\mathbf{q}, \omega)$ versus q_x with $q_y = \pi$ for an increasing magnitude of the site-averaged magnetic moment. The Goldstone modes are seen by the high intensity peaks at $\omega = 0$ for $q_x = \pi \pm \pi/4$ for all the cases shown. In Fig. 5.5, panels (a)-(c) corresponds to a site-averaged magnetic moment of $M \sim 0.05$, panels (d)-(f) has $M \sim 0.1$ ¹, and panels (g)-(i) has $M \sim 0.4$ (see Appendix 5.B for the exact order parameters used). In the dSC phase, there is still a resonance indicated by the region of high intensity at $q_x = \pi$ visible as the region of high intensity bridging the two spin wave branches as seen most clearly in Figs. 5.5(c,f). This is in stark contrast to the PDW case [Figs. 5.5(b,e)] where this coherent excitation is completely washed out, similar to the case shown in Fig. 5.3 without charge and spin order. For larger magnetic moments the magnetic excitations approach the standard spin-wave branches of the stripe phase [214–216], but a significantly broadened dispersion at the resonance point ($q_x = \pi$) is seen to remain present in the PDW phase compared to the dSC phase, as seen by comparison of Fig. 5.5(h)-(i).

¹In the two cases in Figs. 5.5(a)–(c) and Figs. 5.5(d)–(f), a slightly different value of $t' = -0.22$ was used to facilitate the satisfaction of Goldstone’s theorem.

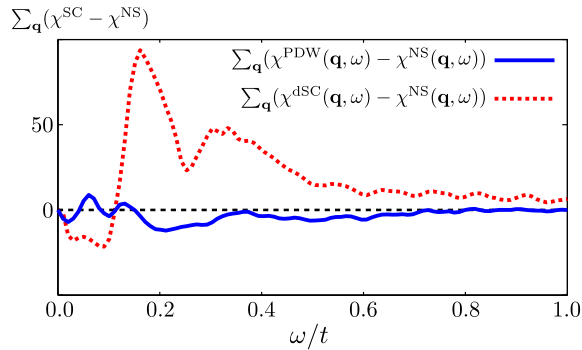


Figure 5.6: (Color online) Comparison of the integrated neutron resonance for the PDW and dSC cases. The blue curve shows the difference between the PDW and the non-superconducting case, while the red curve shows the difference between the dSC case and the non-superconducting case. The dSC shows clear signs of a resonance, which is absent for the PDW case.

To illustrate this more clearly, we show in Fig. 5.6 the difference in the \mathbf{q} -integrated spin susceptibility between the superconducting and normal state for both the PDW (solid blue) and dSC orders (dotted red). These results are for the case where the site-averaged magnetic moment $M \sim 0.1$ [cases (d)-(f) in Fig. 5.5]. As seen, the dSC phase exhibits a clear resonance around $w/t \sim 0.18$, while the PDW phase is structureless. In fact, the PDW case has an almost identical spin response to the normal state, a result that is in good agreement with the experimental data measured on LBCO at $x = 0.095$ by Xu *et al* [36].

5.4 Conclusions

To summarize, we have studied the distinct signatures of a PDW state with intertwined striped spin, charge, and anti-phase superconducting bond order on the dynamic spin susceptibility. We find that in the PDW state both a spin-gap and a neutron resonance are absent, in contrast to the coexistence phase with standard in-phase d -wave superconductivity where the neutron resonance is preserved. This absence of the usual fingerprint of a sign-changing superconducting gap in the PDW state can be traced back to its gapless single-particle excitation spectrum. These results are in agreement with recent neutron scattering results on $x = 0.095$ LBCO [36], where neither a spin-gap nor a resonance were observed below the superconducting critical temperature.

Appendices

5.A Transverse magnetic susceptibility with supercells

Here we provide the details of the derivation of the transverse susceptibility in real-space on a superconducting ground state. The bare transverse susceptibility is

$$\chi_0^{+-}(\mathbf{r}_i, \mathbf{r}_j, \tau) = \left\langle T_\tau S^+(\mathbf{r}_i, \tau) S^-(\mathbf{r}_j, 0) \right\rangle_0, \quad (5.4)$$

where $S^+(\mathbf{r}_i, \tau)$ [$S^-(\mathbf{r}_i, \tau)$] is the spin creation [annihilation] operator at position \mathbf{r}_i at (imaginary) time τ ,

$$S^+(\mathbf{r}_i, \tau) = c_{\mathbf{r}_i\uparrow}^\dagger(\tau) c_{\mathbf{r}_i\downarrow}(\tau). \quad (5.5)$$

Applying the Bogoliubov-de Gennes (BdG) transformation

$$c_{i\sigma} = \sum_{n\mathbf{k}} \left(u_{n\mathbf{k}\sigma}(i) \gamma_{n\mathbf{k}\sigma} + v_{n\mathbf{k}\sigma}^*(i) \gamma_{n\mathbf{k}\bar{\sigma}} \right) e^{-i\mathbf{k}\cdot\mathbf{R}_i}, \quad (5.6)$$

where the momentum \mathbf{k} is contained in the reduced Brillouin zone of the superlattice, and using the fact that

$$\chi_0^{+-}(\mathbf{r}_i, \mathbf{r}_j, \omega) = \frac{1}{\beta} \int_0^\beta d\tau e^{i\omega_n\tau} \chi_0^{+-}(\mathbf{r}_i, \mathbf{r}_j, \tau) \quad (5.7)$$

results in the expression

$$\chi_0^{+-}(\mathbf{r}_i, \mathbf{r}_j, \omega) = \sum_{\mathbf{k}\mathbf{k}'} f_{\mathbf{k}\mathbf{k}'}^0(i, j) e^{-i(\mathbf{k}-\mathbf{k}')\cdot(\mathbf{R}_i-\mathbf{R}_j)}, \quad (5.8)$$

where $f_{\mathbf{k}\mathbf{k}'}^0(i, j)$ is the following real space matrix (after analytical continuation, $\omega_n \rightarrow \omega + i\eta$)

$$f_{\mathbf{k}\mathbf{k}'}^0(i, j) = \frac{-1}{N_s^2} \sum_{nm} \left[v_{n\mathbf{k}\downarrow}(j) u_{n\mathbf{k}\uparrow}^*(i) v_{m\mathbf{k}'\downarrow}^*(i) u_{m\mathbf{k}'\uparrow}(j) - u_{n\mathbf{k}\uparrow}(j) u_{n\mathbf{k}\uparrow}^*(i) v_{m\mathbf{k}'\downarrow}^*(i) v_{m\mathbf{k}'\downarrow}(j) \right] \times \frac{n_F(E_{n\mathbf{k}\uparrow}) + n_F(E_{m\mathbf{k}'\uparrow}) - 1}{\omega - E_{n\mathbf{k}\uparrow} - E_{m\mathbf{k}'\uparrow} + i\eta} \quad (5.9)$$

with $N_s = N_{sx}N_{sy}$ is the number of supercells, and i and j denote sites within one supercell and η is an artificial broadening. The real-space Dyson equation yields

$$\chi_{\text{RPA}}^{+-}(\mathbf{r}_i, \mathbf{r}_j, \omega) = \chi_0^{+-}(\mathbf{r}_i, \mathbf{r}_j, \omega) + \sum_{\mathbf{r}_a} \chi_0^{+-}(\mathbf{r}_i, \mathbf{r}_a, \omega) U \chi_{\text{RPA}}^{+-}(\mathbf{r}_a, \mathbf{r}_j, \omega), \quad (5.10)$$

and since the dependence of the supercell vector \mathbf{R} should be the same for the bare and RPA expressions, this expression can be used to derive an expression for f^{RPA} :

$$\sum_{\mathbf{k}} f_{\mathbf{k}\mathbf{k}+\mathbf{p}}^{\text{RPA}} = \left[\mathbb{1} - U N_s \sum_{\mathbf{k}'} f_{\mathbf{k}'\mathbf{k}'+\mathbf{p}}^0 \right]^{-1} \sum_{\mathbf{k}} f_{\mathbf{k}\mathbf{k}+\mathbf{p}}^0, \quad (5.11)$$

note that this is really just the standard RPA expression in momentum space, but the ‘‘susceptibilities’’ now have matrix structure. Application of Eq. (5.8) for the RPA case results in

$$\chi_{\text{RPA}}^{+-}(\mathbf{r}_i, \mathbf{r}_j, \omega) = \sum_{\mathbf{k}\mathbf{k}'} f_{\mathbf{k}\mathbf{k}'}^{\text{RPA}}(i, j) e^{-i(\mathbf{k}-\mathbf{k}')\cdot(\mathbf{R}_i-\mathbf{R}_j)}. \quad (5.12)$$

To make contact with the cross section as measured by neutrons we take advantage of the fact that neutrons are not a local probe and in the Fourier transform to momentum space we average over sites, as indicated in Eq. (5) in the main text.

5.B Selfconsistent determination of U

When solving for self-consistent striped solutions, an assumption about the periodicity of the stripes has to be made. Hence, for a set of input parameters, the periodicity of the ground state might differ from the input periodicity, implying that the solution given from solving the self-consistent equations is not necessarily the ground state of the system.

In the present case we are interested in stripes with a certain periodicity (8×2) and varying magnetization and since we are interested in the dynamics of the spin-waves, ensuring that they remain gapless is critical. The regular iterative selfconsistent approach typically results in saddle points in the free energy due to the enforced periodicity, and we therefore adopt an approach focused on enforcing gapless Goldstone modes. In practice this means that we choose a modulation of the electron densities corresponding to an 8×2 -periodic state and adjust U such that the smallest eigenvalue of

$$\mathbb{1} - UN_s \text{Re} \left[\sum_{\mathbf{k}} f_{\mathbf{k}\mathbf{k}+\mathbf{q}}^0(\mathbf{i}, \mathbf{j}, U) \right], \quad (5.13)$$

the real part of the denominator of the RPA susceptibility, is zero. The gapless excitations should appear at $\mathbf{q} = (\pi \pm \frac{\pi}{4}, \pi)$ as the underlying state exhibits 8×2 -periodicity, and μ is adjusted to ensure that this is the case. Here we included U as a dependent in f^0 to remind the reader that f^0 also changes as a function of U , as is seen from the mean-field Hamiltonian.

This procedure allows us to vary the size of the magnetic moments and the type of superconducting order independently, while remaining in the same parameter regime and simultaneously satisfying Goldstone's theorem. In practice this is carried out by choosing a certain density modulation, i.e. the values of $\langle n_{i\sigma} \rangle$, and solving Eq. (5.13) for either no SC order, dSC or PDW order. The chosen density modulations are based on selfconsistent solutions for a given U and superconducting is imposed on top, without accounting for feedback effects. The values obtained for U and μ by finding the zero eigenvalues of Eq. (5.13) will therefore depend slightly on which type of superconducting order (if any) was assumed. Below the exact densities for the three cases (a) $M \sim 0.05$ (Tab. 5.1), (b) $M \sim 0.10$ (Tab. 5.2) and (c) $M \sim 0.4$ (Tab. 5.3) are provided, along with the various values of U and μ following from this procedure. Note that for cases (a) and (b) a slightly different value of $t' = -0.22$ was used in order for Eq. 5.13 to yield a zero eigenvalue.

Case (a)

Case (b)

Case (c)

5.B Selfconsistent determination of U

0.4070	0.4372	0.4680	0.3948	0.4680	0.4372	0.4070	0.4808
0.4680	0.4372	0.4070	0.4808	0.4070	0.4372	0.4680	0.3948

0.4680	0.4372	0.4070	0.4808	0.4070	0.4372	0.4680	0.3948
0.4070	0.4372	0.4680	0.3948	0.4680	0.4372	0.4070	0.4808

	non-SC	dSC	PDW
U	1.9467	2.2303	1.9074
μ	-0.1	0.131	-0.1

Table 5.1: (top) $\langle n_{i\uparrow} \rangle$, (middle) $\langle n_{i\downarrow} \rangle$ for the 8×2 sites in the supercell, and (bottom) parameters resulting in a zero eigenvalue solution of Eq. 5.13 for the various choices of superconducting orders.

0.3650	0.4300	0.5100	0.3250	0.5100	0.4300	0.3650	0.5650
0.5100	0.4300	0.3650	0.5650	0.3650	0.4300	0.5100	0.3250

0.5100	0.4300	0.3650	0.5650	0.3650	0.4300	0.5100	0.3250
0.3650	0.4300	0.5100	0.3250	0.5100	0.4300	0.3650	0.5650

	non-SC	dSC	PDW
U	2.1519	2.3564	2.1
μ	0.02	0.15	0.02

Table 5.2: (top) $\langle n_{i\uparrow} \rangle$, (middle) $\langle n_{i\downarrow} \rangle$ for the 8×2 sites in the supercell, and (bottom) parameters resulting in a zero eigenvalue solution of Eq. 5.13 for the various choices of superconducting orders.

0.2200	0.4400	0.6600	0.1800	0.6600	0.4400	0.2200	0.7200
0.6600	0.4400	0.2200	0.7200	0.2200	0.4400	0.6600	0.1800

0.6600	0.4400	0.2200	0.7200	0.2200	0.4400	0.6600	0.1800
0.2200	0.4400	0.6600	0.1800	0.6600	0.4400	0.2200	0.7200

	non-SC	dSC	PDW
U	3.16	3.3097	3.2235
μ	0.25	0.25	0.25

Table 5.3: (top) $\langle n_{i\uparrow} \rangle$, (middle) $\langle n_{i\downarrow} \rangle$ for the 8×2 sites in the supercell, and (bottom) parameters resulting in a zero eigenvalue solution of Eq. 5.13 for the various choices of superconducting orders.

Chapter 6

Topological Superconductivity and Majorana End Modes

The prospect of performing quantum computations - the coherent manipulation and read-out of quantum bits of information - has stimulated intense research in recent years. Ordinary bits can take one of two values, 0 or 1, while quantum bits, or *qubits*, can be in a superposition of two states $|0\rangle$ and $|1\rangle$. Prior to any measurement the quantum bit therefore samples all accessible states while a classical bit is confined to a single value. Such behaviour provides distinct advantages and quantum algorithms to factorise large numbers, search databases or solve systems of linear equations have already been shown to yield significant advantages over their classical counterparts [26, 217]. Amongst the problems currently faced by researchers striving to achieve quantum computation is the relatively short coherence time of the states comprising the qubits. A decoherence time of the order of milliseconds is desirable in order to perform most logical operations, and this is only realised in ideal scenarios. A possible way to circumvent such decoherence is to employ topologically protected qubits [218]. These are comprised of anyons obeying non-Abelian exchange statistics. One option to achieve this is to use zero-energy Majorana modes. The non-Abelian exchange statistics allow for logic gates to be constructed by braiding of the Majorana modes, and since the logic gate relies on the topological properties of the braid, it is in principle decoherence free if the braiding is performed adiabatically.

Majorana particles first appeared in 1937 as real solutions to the Dirac equation [219]. This implies that Majorana particles are their own anti-particles, meaning that creating and annihilating particles are essentially equivalent, hence $\gamma_E^\dagger = \gamma_{-E}$. Whether any elementary particles are Majorana particles are still debated in the particle physics community [220, 221], however it was realised recently that Majorana modes could exist as quasiparticle excitations of certain condensed matter systems [222–224]. By virtue of the above, Majorana quasiparticles must be equal superpositions of particles and holes, thus making superconductors a natural place to look for such quasiparticle excitations. This also implies that a particle or a hole can be seen as two Majorana modes locally bound together, and one would naively conclude that neighbouring Majorana modes always hybridise to form particles or holes, thus making sole Majorana modes unobservable.

6.1 Majorana Modes in the Kitaev chain

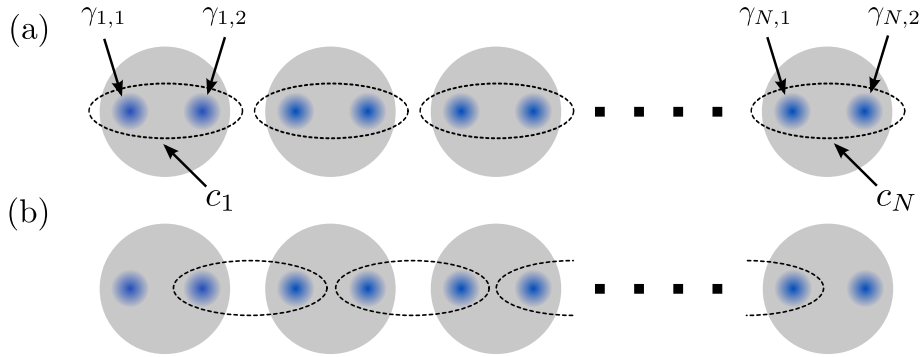


Figure 6.1: Sketch of the two distinct ways the Majorana modes at each site can pair up in a one-dimensional system. In (a) the modes pair up at each site and a topologically trivial phase results. In (b) Majorana modes from different sites are paired up resulting in a topologically non-trivial phase with localised modes at either end.

However, considering for simplicity finite one-dimensional systems there are two distinct ways of pairing up the Majorana modes, as emphasised in Fig. 6.1. Classifying the cases in which the Majorana modes pair up such that a localised mode is left at each end was achieved by Kitaev using a simple model outlined below. The great insight came with realising that the appearance of localised modes at the ends is a topological property of the system and not tied to the details of any microscopic model [218, 224–229]. A topological classification of the model in question is therefore sufficient to determine whether localised edge modes will appear in some region of parameter space. As a simple example of these concepts we consider the Kitaev chain [224], which can be mapped to the system considered in Chapter 7 and is considered topologically equivalent. Exactly what is meant by topologically equivalent will be made clear below when we discuss symmetry classes.

6.1 Majorana Modes in the Kitaev chain

In this section we describe the celebrated Kitaev chain and how this can lead to localised Majorana end modes. We review two ways to achieve an effective Kitaev chain in realistic physical systems and present various experimental results showing indications of Majorana modes being present. We then proceed to motivate the study presented in Chapter 7. In this work we consider a chain of magnetic adatoms deposited on a two-dimensional superconducting substrate and elucidate the mechanism responsible for the formation of spiral magnetic order leading to self-organised topological superconductivity. The work presented in Chapter 7 thus contributes to understanding how Majorana modes are realised in self-organised systems. Specifically, the focus is on the interplay between the Yu-Shiba-Rusinov (YSR) bound states due to the adatoms and the formation of magnetic order in the absence of external tuning parameters.

The simplest model hosting topological states in the form of Majorana modes is the Kitaev chain [224]. This is a one-dimensional lattice model of spinless fermions with p -wave superconducting pairing, a sketch of which is shown in Fig. 6.1. Kitaev showed that for a chemical potential smaller than the bandwidth, one could achieve a system supporting

6.1 Majorana Modes in the Kitaev chain

localised end modes. The Hamiltonian in question is

$$\mathcal{H} = -\mu \sum_{i=1}^N n_i - \sum_{i=1}^{N-1} \left(t c_i^\dagger c_{i+1} + \Delta c_i c_{i+1} + \text{h.c.} \right), \quad (6.1)$$

where N is the number of sites in the chain and n_i is the number operator $c_i^\dagger c_i$ at site i . Since only one spin-species is included superconductivity is odd under inversion symmetry. Transforming to the Majorana representation [230]

$$\begin{aligned} \gamma_{i,1} &= c_i^\dagger + c_i, \\ \gamma_{i,2} &= i \left(c_i^\dagger - c_i \right), \end{aligned} \quad (6.2)$$

we obtain the Hamiltonian in the Majorana representation

$$\begin{aligned} \mathcal{H} &= -i \frac{\mu}{2} \sum_{i=1}^N \gamma_{i,1} \gamma_{i,2} - i \frac{t}{2} \sum_{i=1}^{N-1} (\gamma_{i+1,1} \gamma_{i,2} - \gamma_{i+1,2} \gamma_{i,1}) \\ &+ i \frac{\Delta}{2} \sum_{i=1}^{N-1} (\gamma_{i+1,2} \gamma_{i,1} + \gamma_{i+1,1} \gamma_{i,2}) \end{aligned} \quad (6.3)$$

note the presence of the i which implies that the Hamiltonian matrix is antisymmetric. Following Kitaev [224], two distinct cases are identified corresponding to either the presence or absence of localised edge modes. By taking $t = \Delta = 0$ we recover the topologically trivial case in which no localised edge modes are present

$$\mathcal{H} = -i \frac{\mu}{2} \sum_{i=1}^N \gamma_{i,1} \gamma_{i,2}, \quad (6.4)$$

i.e. the Majorana operators at each site pair up. The topologically non-trivial case is found from taking $\mu = 0$ and e.g. $t = \Delta$ for which

$$\mathcal{H} = -it \sum_{i=1}^{N-1} \gamma_{i+1,1} \gamma_{i,2}, \quad (6.5)$$

where Majorana operators on consecutive sites are paired up. Note that neither $\gamma_{1,1}$ nor $\gamma_{N,2}$ enter the Hamiltonian, and that these are sitting at opposite ends of the wire (see Fig. 6.1). This constitutes the sought after edge mode, which, in the limit of an infinite wire is localised at each end and has zero energy.

The two phases uncovered are topologically distinct, implying that one cannot be recovered from the other without closing the bulk energy gap. A more thorough analysis reveals that the system is in the topologically trivial phase, i.e. localised Majorana modes are absent, when $2|t| < \mu$. For $2|t| > \mu$ the system is topologically non-trivial and hosts localised Majorana edge modes. In this more general case the end modes attain a finite energy resulting from a weak hybridisation between either end. This is evidenced in an exponential decay of the Majorana modes into the interior of the wire, with a decay length inversely proportional to the energy of the mode. It turns out that the existence of boundary modes can be determined from an analysis of the translationally invariant (bulk)

6.1 Majorana Modes in the Kitaev chain

Class	Θ	Ξ	Π	1	2	3	4	5	6	7	8
BDI	1	1	1	\mathbb{Z}	0	0	0	\mathbb{Z}	0	\mathbb{Z}_2	\mathbb{Z}_2
D	0	1	0	\mathbb{Z}_2	\mathbb{Z}	0	0	0	\mathbb{Z}	0	\mathbb{Z}_2
DIII	-1	1	1	\mathbb{Z}_2	\mathbb{Z}_2	\mathbb{Z}	0	0	0	\mathbb{Z}	0

Table 6.1: Table of the symmetry classes relevant for the discussion of Majorana boundary modes. The symmetries present are classified by ± 1 depending on whether $\Theta^2 = \pm 1$, $\Xi^2 = \pm 1$. If the symmetry is absent it is denoted by a 0. The \mathbb{Z} or \mathbb{Z}_2 denotes the type of topological invariants in the cases where one can be defined. Note that the table is periodic with period 8 with respect to dimensionality. Table is adapted from Ref. [229].

Hamiltonian. This is a massive simplification since it removes the need to diagonalise the system in real space to determine whether Majorana boundary modes are present. The topological invariants used to determine the presence of boundary modes are part of a grander classification scheme based on the action of the (generalised) charge-conjugation (Ξ) and time-reversal (Θ) anti-unitary operators on the Hamiltonian [231, 232]. A third symmetry can be defined, which is the unitary chiral symmetry Π and for systems in which both charge-conjugation and time-reversal symmetry are present this is given by $\Pi = \Xi\Theta$. Under this scheme, Hamiltonians are divided into ten symmetry classes each with an associated topological invariant. In Table 6.1 we show the symmetry classes relevant for the study of Majorana boundary modes, i.e. the three cases for which $\Xi^2 = 1$. While the topological invariant can change by closing and reopening the gap, the symmetry class is based on the discrete symmetries of the system and is thus unaffected. Hence, physical systems exhibiting Majorana edge modes in one dimension can be found by looking for systems in the same symmetry class as the Kitaev chain, which is BDI [233–235]. In the discussion of incommensurate magnetic order in the FeSC we encountered a system in symmetry class D. The boundary modes in the non-trivial phase of this two-dimensional system are so-called chiral edge modes. This was discussed in Sec. 1.4.

The topological invariant associated with class BDI in one dimension is a winding number, however this is not so easily accessible using numerical methods as it relies on evaluating derivatives of eigenstates. This can be numerically unstable in the sense that it is sensitive to finite-size effects, unless very large grids are used. In the work presented in Chapter 7, instead of the winding number we use the Majorana number to discern the topological phases from the trivial ones. The Majorana number is defined by

$$\mathcal{M} = \text{sign} \left\{ \text{Pf} [\mathcal{A}(0)] \text{Pf} [\mathcal{A}(\pi)] \right\}, \quad (6.6)$$

where $\mathcal{A}(k)$ is the Hamiltonian matrix written in the Majorana representation. Here $\mathcal{M} = 1$ indicates a trivial phase while $\mathcal{M} = -1$ indicates a non-trivial phase. The Majorana number has the advantage of being easily accessible with numerics, however it is a \mathbb{Z}_2 invariant and not a \mathbb{Z} invariant. This means that it is only capable of distinguishing an odd number of Majorana modes from an even one. For the work presented in Chapter 7 we supplemented the evaluation of the \mathbb{Z}_2 invariant with real space calculations to check that the $\mathcal{M} = 1$ cases did not harbour an even number of Majorana modes.

One model that fulfills the requirement of being in the same symmetry class as the Kitaev chain is the so-called nanowire setup, consisting of a one-dimensional wire with strong spin-orbit coupling proximity-coupled to an s -wave superconductor and subjected to a magnetic field. This was suggested as a possible experimental realisation of the Kitaev chain in 2010 [27–29]. Signatures of Majorana modes were first reported for this system by Mourik *et al.* [236] and more recently the exponential localisation of the Majorana modes was elucidated in Ref. [237].

6.2 Magnetic Adatom Chains on Superconductors

Here and in Chapter 7 we focus on an alternative method by which an effective Kitaev chain is constructed by deposition of a chain of magnetic adatoms on the surface of an s -wave superconducting substrate, thus inducing Yu-Shiba-Rusinov (YSR) bound states within the superconducting gap [238]. A chain consisting of such magnetic adatoms was recently studied experimentally in Ref. [239] using Fe-atoms deposited on a Pb substrate and observations consistent with the presence of localised Majorana end modes were reported. If the electrons experience a spatially varying local exchange field the superconducting pairing acquires a p -wave component and the system is in symmetry class BDI. An *effective* spatial variation can be accomplished in two ways, either through spin-orbit coupling in the substrate combined with a ferromagnetic or antiferromagnetic alignment of the adatoms, or if the ground state configuration of the magnetic adatoms exhibits a spiral structure. In fact, for one-dimensional substrates the two ways are identical, simply related by a gauge transformation. Going beyond one-dimensional substrates the relation between the two is no longer exact, however it can still be applied in the limit of weak spin-orbit coupling, as we show in Sec. 7.A. In the experiment of Ref. [239] the magnetic moments were oriented ferromagnetically although the presence of a spin-orbit coupling on the surface of Pb ensured that the system was in class BDI. For the majority of the work presented in Chapter 7 we assume that the spin-orbit coupling vanishes.

In the absence of any spin-orbit coupling in the system the magnetic order along the chain therefore presents a crucial ingredient to the formation of a topologically non-trivial state. In Chapter 7 we study the mechanisms underlying the formation of spiral magnetic order for a chain deposited on a two-dimensional substrate. Interactions between adatoms are mediated by the electrons via so-called indirect exchange. The most well-known example of such exchange, the Ruderman-Kittel-Kasuya-Yosida (RKKY) interaction [240–242], is a consequence of the polarizability of the electron gas; a single magnetic adatom polarizes the spin of the surrounding electrons in a position dependent manner. In a normal metal, this favours either alignment or anti-alignment of neighbouring electronic spins, depending on their distance from the adatom. In a superconductor, the RKKY interaction is supplemented by a weaker, albeit longer-ranged, component originating from the Cooper pairs in the superconductor. The presence of spin-singlet superconductivity implies that electrons of opposite spin can lower their energy by forming pairs, resulting in a purely antiferromagnetic contribution to the indirect exchange interactions. For quadratic dispersions and to lowest order in the adatom strength J , the exchange coupling between

6.3 Bound States induced by Magnetic Adatoms

adatoms in two dimensions is thus

$$J(r) = J^2 e^{-\frac{2r}{\xi}} \left[-\frac{v_F}{2\pi r^2} \sin(2k_F r) + \frac{\Delta}{r} \sin^2(k_F r + \pi/4) \right], \quad (6.7)$$

where the first term is the standard RKKY interaction and the second is the purely antiferromagnetic contribution. Here k_F (v_F) is the Fermi momentum (velocity) and ξ is the coherence length of the superconductor. Constructing a chain of magnetic adatoms introduces additional complexity as each adatom hosts a YSR bound state which hybridize with the neighbouring YSR states thus forming a YSR band in the superconducting gap. The origin of the magnetic order along the adatom chain thus depends on the YSR band. Prior to the YSR band crossing the Fermi energy, the system is in the trivial regime. In this case superconductivity destabilises a ferromagnetic arrangement and results in a spiral since the system tries to balance out the ferromagnetic contribution from the first with the antiferromagnetic contribution from the second term in Eq. 6.7. On the other hand, an antiferromagnetic alignment of the spins is stable against superconductivity since both terms in Eq. 6.7 have the same sign. As the YSR band crosses the Fermi level and the hybridisation between neighbouring YSR states causes the effective spin model underlying Eq. 6.7 to break down. After the YSR band-crossing the system is in the topologically non-trivial regime provided the chain exhibits spiral magnetic order. In this case, a ferromagnetic chain is also unstable to the formation of spiral order since this leads to the opening of a gap in the YSR band resulting in a net energy gain for the system [243].

6.3 Bound States induced by Magnetic Adatoms

Evidently the YSR bound states play an important role in the formation of magnetic order, and we therefore provide some further details. For illustrative purposes we confine attention to a single magnetic adatom located at the origin. In terms of Nambu-Gor'kov Green functions we can write the Dyson equation in real space as [244]

$$\mathcal{G}_{ij} = \mathcal{G}_{ij}^{(0)} + \mathcal{G}_{i0} \mathcal{H}_0^{\text{imp}} \mathcal{G}_{0j}^{(0)}, \quad (6.8)$$

where we note that the bare Green function $\mathcal{G}_{ij}^{(0)}$ is translationally invariant and $\mathcal{H}_0^{\text{imp}}$ is the Hamiltonian matrix for a magnetic adatom at the origin written in Nambu space, $(c_{i\uparrow} \ c_{i\downarrow}^\dagger)^T$:

$$\mathcal{H}_0^{\text{imp}} = \begin{pmatrix} V(0) & 0 \\ 0 & V(0) \end{pmatrix}. \quad (6.9)$$

An exact solution to Eq. 6.8 is given by

$$\mathcal{G}_{ij} = \mathcal{G}_{ij}^{(0)} + \mathcal{G}_{i0}^{(0)} \left(\mathbb{1} - \mathcal{H}_0^{\text{imp}} \mathcal{G}_{00}^{(0)} \right)^{-1} \mathcal{H}_0^{\text{imp}} \mathcal{G}_{0j}^{(0)}, \quad (6.10)$$

which provides a powerful way of studying the effect of a single adatom in a superconductor and can even be extended to arrays of adatoms [243]. The effect of the adatom is captured

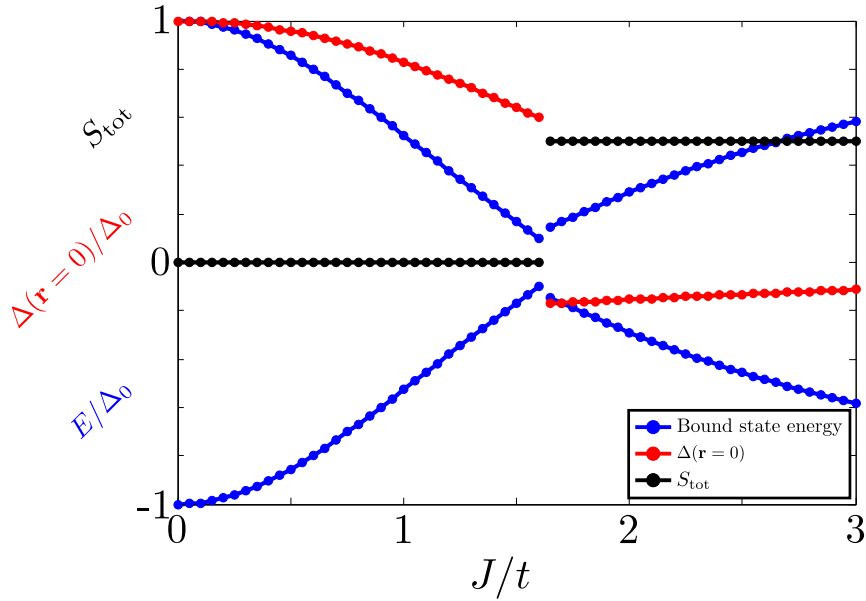


Figure 6.2: Plot showing the behaviour of the energy of the bound state energy (blue), the local order parameter (red) and the total spin of the system (black) as a function of adatom strength (J) divided by the nearest neighbour hopping (t). Selfconsistency implies a discontinuous jump in these quantities clearly visible at $J/t \approx 1.5$. The magnitude of the jump was shown to depend on the coherence length in Ref. [245], such that a longer coherence length implies a smaller jump.

by the so-called \mathcal{T} -matrix:

$$\mathcal{T}_0 = \left(\mathbb{1} - \mathcal{H}_0^{\text{imp}} \mathcal{G}_{00}^{(0)} \right)^{-1} \mathcal{H}_0^{\text{imp}}. \quad (6.11)$$

The bare Green function exhibits no poles for $|\omega| < |\Delta|$ and the occurrence of bound states within the gap is due to the poles of the \mathcal{T} -matrix for $|\omega| < |\Delta|$. Thus we look for solutions to the equation

$$\text{Det} \left(\mathbb{1} - \mathcal{H}_0^{\text{imp}} \mathcal{G}_{00}^{(0)}(\omega_B) \right) = 0 \quad (6.12)$$

with $|\omega_B| < |\Delta|$ and find

$$\omega_B = \pm \Delta \frac{1 - (V(0)\pi N(0))^2}{1 + (V(0)\pi N(0))^2}. \quad (6.13)$$

Note that no bound states are induced due to non-magnetic adatoms. This is because the interaction matrix for a non-magnetic adatom is given by

$$\mathcal{H}_0^{\text{imp}} = \begin{pmatrix} V(0) & 0 \\ 0 & -V(0) \end{pmatrix} \quad (6.14)$$

in Nambu space, and the associated \mathcal{T} -matrix has no in-gap poles.

The \mathcal{T} -matrix provides an efficient way of studying single adatoms. However, in an interacting system this approach is not exact and neglects the feedback from the adatom on

6.3 Bound States induced by Magnetic Adatoms

the electron-density and pair-potential. This can be ratified by employing Green functions dressed by Hartree and Fock self-energies evaluated in the presence of an adatom, which makes a closed-form solution difficult to obtain. Another strategy is to solve for the density and pair-potential in a selfconsistent manner, which is the approach we shall adopt below. In the remainder of this chapter we neglect local electron-electron interactions and restrict attention to an attractive nearest-neighbour interaction which stabilises s -wave superconductivity. The effects of selfconsistently including the feedback from the adatom on the s -wave pair-potential have been thoroughly studied elsewhere [245–247] and here we simply summarize these effects. A magnetic adatom leads to a suppression of the local pair-potential, and for increasing adatom strength, results in a π phase-shift of the local superconducting order parameter. Secondly, the energy of the bound state as function of adatom strength is modified and exhibits a jump from positive to negative energy at the critical adatom strength where also the local order parameter changes sign. These effects are summarised in Fig. 6.2, which also depicts the first order transition from an $S = 0$ to an $S = \frac{1}{2}$ state first discussed by Sakurai [248]. One of the questions addressed in the work presented in Chapter 7 is whether these effects play a role for the magnetic ground state of a chain of adatoms.

Chapter 7

Spiral magnetic order and topological superconductivity in a chain of magnetic adatoms on a two-dimensional superconductor

*This chapter has been published by the author and Michael Schechter, Karsten Flensberg, Brian M. Andersen, and Jens Paaske in Phys. Rev. B **94** 144509 (2016).*

In this chapter we elucidate the nature of magnetic order appearing in one-dimensional magnetic adatom chains deposited on two-dimensional superconducting substrates. If the chain exhibits spiral magnetic order or if there is spin-orbit coupling in the substrate the symmetry class is BDI and the models can exhibit topologically nontrivial phases. Indications of Majorana end modes were observed in such a system by Nadj-Perge *et al.* [239] although for a ferromagnetic chain with spin-orbit coupling in the substrate. Here we show that a topologically nontrivial phase arises in the subgap YSR states. This phase is stabilised by the presence of spiral magnetic order along the chain due to the competition between a short-range ferromagnetic component and a long-range antiferromagnetic component in the exchange interactions. We find that the exchange interactions along the diagonal directions exhibit behaviour similar to the one-dimensional case when close to half filling. In addition we show the stability of the topological phase diagram to the effects of selfconsistency and weak spin-orbit coupling and illustrate the effect of adding a direct ferromagnetic exchange interaction between adatoms. For a wide range of interaction strengths we find this to enlarge the topologically nontrivial region by aiding in the formation of a spiral magnetic state.

7.1 Introduction

The study of magnetic order in adatomic chains deposited on superconducting substrates has recently attracted widespread attention due to the ability of these systems to host Majorana bound states [31, 235, 239, 243, 249–263]. The local moments of the adatoms induce Yu-Shiba-Rusinov (YSR) bound states within the superconducting gap [238, 264–268], thus constituting an effective Kitaev chain [224] with long-range hopping and pairing amplitudes [252]. A topologically non-trivial phase is possible with the addition of a further crucial ingredient, namely an effective spatial variation of the local exchange field experienced by the electrons along the chain [252]. This can be achieved either by spin-orbit coupling (SOC) within the superconductor [235, 239, 249, 259], or without SOC if the moments order into a magnetic spiral [31, 243, 255–257, 260–263] (see also [30, 269–271]). In the latter case, spiral order is driven by electron-mediated indirect exchange interactions that in turn support topological superconductivity and give rise to the notion of self-organization.

The development of magnetic order in an adatom chain due to electron-induced exchange interactions has been studied analytically for both one- and three-dimensional superconductors [243, 255–257, 262, 263, 272]. In one-dimensional (1D) conductors, adatom spiral order has been shown to arise from the RKKY interaction [240–242] due to the singular behavior of the susceptibility at $2k_F$ [255–257, 263]. Effects beyond the RKKY approximation were recently considered and also support the formation of spiral order away from points of commensurability, and for weak adatom-electron exchange coupling [262, 272]. The three-dimensional (3D) case was studied in Ref. [243] where it was found that spiral order indeed forms due to indirect exchange interactions, however, the mechanism is distinct from the 1D case since there is no $2k_F$ peak in the adatom susceptibility [258]. In 3D spiral order arises from the interplay between the shorter-ranged RKKY exchange, and the longer-ranged antiferromagnetic exchange due to singlet superconductivity [243].

In two-dimensional (2D) systems the existence of self-organized topological phases was established numerically for finite systems [260], but the mechanism and conditions under which spiral magnetic order forms are not yet fully understood. In addition, single YSR states were recently imaged in the layered superconductor 2H-NbSe_2 [273], which demonstrates how the effectively reduced dimensionality enhances the spatial extent of the YSR states. This is expected to lead to a larger YSR pairing hybridization, and thus to a relatively larger gap protecting the topological superconducting phase.

In this paper we bridge the gap between the previous 2D numerical and 3D analytical calculations by providing comprehensive studies of the magnetic adatom and electronic ground states in a two-dimensional tight-binding model. We map out the magnetic phase diagram as a function of exchange coupling and electron chemical potential by minimizing the electron free energy within a classical spiral ansatz for the adatom chain. We find that the indirect exchange interactions generally follow behavior similar to 3D studies, favoring collinear order of the adatom chain in the normal state, while destabilizing ferromagnetism to spiral formation in the presence of superconductivity. This gives rise to a broad region of the phase diagram where the set of subgap YSR states exists in a topologically nontrivial

superconducting phase with Majorana bound states. The exchange interaction along the diagonal (11) direction is distinct near half filling due to Fermi surface nesting. As a result, the effective dimensionality of the substrate is reduced, and the magnetic order along the chain exhibits $2k_F$ spiral order known from 1D systems. Furthermore, we ascertain the effects of a direct exchange interaction between adatoms, finding that even a substantial direct exchange term can promote spiral order in the chain. This is contrary to 3D systems, where a spiral state in general only occurs when the direct exchange interaction is smaller than the indirect exchange.

Lastly, we elucidate the differences between performing the calculations selfconsistently and non-selfconsistently for the local pairing potential. The two cases are found to be qualitatively the same, i.e., suppression of the local pairing potential near the adatom chain leads only to minor modifications of the magnetic order and subgap states. This modification is interpreted in terms of a lowering of the effective chemical potential for the subgap YSR states induced by the suppression of the local pairing potential.

The paper is organized as follows: In Section 7.2 we introduce the model and methods. In Section 7.3 we study the indirect exchange interactions between two adatom spins mediated by the electron gas, and determine the dependence on chemical potential and exchange coupling both along (10) and (11) directions. We proceed to consider chains of magnetic adatoms in Sec. 7.4. We present magnetic and topological phase diagrams for different values of the superconducting order parameter in the plane of exchange coupling and chemical potential. These indicate that spiral order on a chain along (10) is formed by a mechanism similar to the 3D case. In this section we also contrast the behavior of chains along (10) and (11), and reveal substantial differences that arise due to the anisotropic Fermi surface. Additionally, we discuss the effects of a ferromagnetic direct exchange between the adatoms. In Sec. 7.5 we perform a detailed comparison between selfconsistent and non-selfconsistent approaches, and find that the two approaches yield qualitatively similar results. We discuss the influence of substrate spin-orbit coupling in the Appendix. Conclusions and outlook are presented in Sec. 7.6.

7.2 Model

To model the 2D superconducting substrate we use a tight-binding model with an on-site attractive interaction V to stabilize superconductivity. The magnetic adatom potentials are assumed to be local and are arranged into a chain along either the (10) or (11) directions, depicted in Fig. 7.1(a). The Hamiltonian is

$$\mathcal{H} = \mathcal{H}_0 + \mathcal{H}_{\text{SC}} + \mathcal{H}_{\text{imp}}, \quad (7.1)$$

$$\mathcal{H}_0 = -t \sum_{\langle ij \rangle} c_{i\alpha}^\dagger c_{j\alpha} - \mu \sum_{i\alpha} c_{i\alpha}^\dagger c_{i\alpha}, \quad (7.2)$$

$$\mathcal{H}_{\text{SC}} = -V \sum_i c_{i\uparrow}^\dagger c_{i\downarrow}^\dagger c_{i\downarrow} c_{i\uparrow}, \quad (7.3)$$

$$\mathcal{H}_{\text{imp}} = J_{\text{imp}} \sum_{\substack{i \in \mathcal{I} \\ \alpha\beta}} \mathbf{S}_i \cdot c_{i\alpha}^\dagger \boldsymbol{\sigma}_{\alpha\beta} c_{i\beta}, \quad (7.4)$$

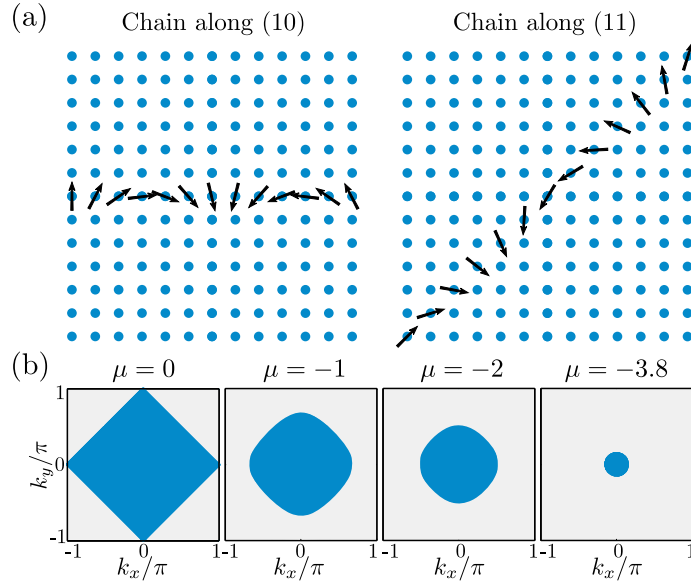


Figure 7.1: (a) Schematic illustration of the system under consideration. In this paper we consider both the (10)-direction and the (11)-direction, for respectively 120×71 , and 81×81 systems. (b) Fermi surface of the model in Eq. (7.2) for various values of the chemical potential.

where $c_{i\alpha}^\dagger, c_{i\alpha}$ are fermionic creation/annihilation operators with spin α and coordinate i , μ is the chemical potential, \mathcal{I} is the set of adatom locations, $\langle \rangle$ signifies that the summation is taken over nearest-neighbors, and $\boldsymbol{\sigma}$ is the vector of Pauli matrices. We choose $t = 1$ as the unit of energy and the lattice constant $a = 1$ as the unit of length. The adatom spin is denoted by $\mathbf{S} = S\hat{\mathbf{n}}$ where $\hat{\mathbf{n}}$ is a unit vector in the direction of the spin and S is the length. Throughout the paper we work in the large spin (classical) approximation, $S \rightarrow \infty$, $J_{\text{imp}} \rightarrow 0$ with the product $J \equiv J_{\text{imp}}S = \text{const}$. A mean-field decoupling in the Cooper channel is performed on the superconducting term Eq. (7.3) resulting in

$$\mathcal{H}_{\text{SC}}^{\text{MF}} = - \sum_i \left[\Delta_i c_{i\uparrow}^\dagger c_{i\downarrow}^\dagger + \text{h.c.} - \frac{|\Delta_i|^2}{V} \right], \quad (7.5)$$

where the superconducting order parameter is obtained *via* the selfconsistency equation

$$\Delta_i = V \langle c_{i\downarrow} c_{i\uparrow} \rangle. \quad (7.6)$$

The Fermi surfaces (with $V = J = 0$) for various representative values of the chemical potential are shown in Fig. 7.1(b). The dispersion inherits the point group symmetries of the square lattice, and a circular Fermi surface with quadratic dispersion is only achieved near the bottom of the band. We note that the tight-binding model has a finite band-width $W = 8t$ and is particle-hole symmetric around $\mu = 0$, implying that our results do not depend on the sign of μ . For purposes of determining both indirect exchange interactions and the magnetic order of the adatoms, we consider the thermodynamic potential Ω at zero temperature

$$\Omega = \langle \mathcal{H} \rangle. \quad (7.7)$$

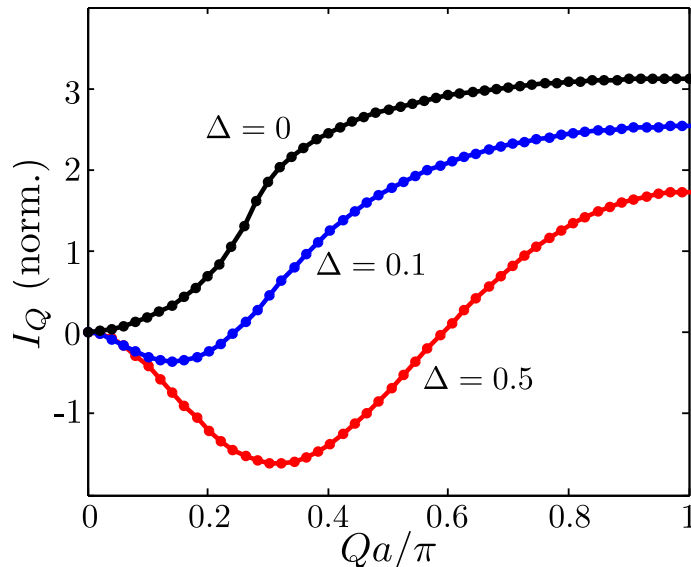


Figure 7.2: (Color online) The function I_Q in Eq. (7.8) calculated from Eq. (7.1) to leading order in J at $\mu = -3.8$ and for different values of Δ . The two adatoms are arranged along the (10) direction with lattice spacing $a_{\text{ad}} = a$. In the normal state ($\Delta = 0$), the magnetic ground state of the adatom chain is a ferromagnet ($q = 0$). The presence of superconductivity leads to a spiral magnetic ground state ($q \neq 0$) of the adatom chain. Here we assume a homogeneous pairing potential $\Delta_i = \Delta$. The effects of the selfconsistency condition, Eq. (7.6), are addressed in Sec. 7.5.

Below we study $\Omega\{\hat{\mathbf{n}}_i\}$ for different adatom configurations $\hat{\mathbf{n}}_i$ and determine the magnetic ground state for a chain of adatoms by minimizing Ω . To obtain an iterative selfconsistent solution to the Hamiltonian (7.1) we solve Eq. (7.6) for a given V and Δ_i and iterate until the difference between consecutive solutions is $< 10^{-3}$ at each site. This procedure includes the feedback of the adatoms on the superconducting order parameter and suppresses it in the proximity of the chain, as depicted in Fig. 7.11 below. This leads to the well-known π -phase shift of the superconducting order parameter at the adatom site [245, 247, 266]. As will be made clear in Sec. 7.5 this effect has no qualitative impact on the magnetic order along the chain, or the subgap YSR states. In Secs. 7.3 and 7.4 we therefore simplify the calculations and use the non-selfconsistent approximation.

7.3 Weak exchange interactions

To understand the magnetic phases of the adatom chain, we first consider the case where the adatom spacing a_{ad} is larger than the inverse Fermi wavevector, $k_F a_{\text{ad}} \gg 1$, and the exchange coupling to electrons is weak. The indirect exchange coupling between adatoms can then be computed perturbatively in J , resulting in an effective Heisenberg model for the adatoms given by

$$\mathcal{H}_{\text{Heis}} = \sum_{i,j} I_{(i-j)} \mathbf{S}_i \cdot \mathbf{S}_j = \sum_Q I_Q |\mathbf{S}_Q|^2, \quad (7.8)$$

7.3 Weak exchange interactions

where the second equality is written in the momentum representation for an infinite ring. For a chemical potential near the band bottom, the leading order in J indirect exchange coupling between adatoms separated by distance r is ($\hbar = 1$)

$$I_r \propto J^2 e^{-\frac{2r}{\xi}} \left[-\frac{v_F}{2\pi r^2} \sin(2k_F r) + \frac{\Delta}{r} \sin^2(k_F r + \pi/4) \right], \quad (7.9)$$

where v_F is the Fermi velocity and $\xi = v_F/\Delta$ is the coherence length of the superconductor. The first term in the square brackets of Eq. (7.9) is the well-known Rudermann-Kittel-Kasuya-Yosida (RKKY) interaction [240–242] mediated by a 2D electron gas [258, 274]. The second term is purely antiferromagnetic and arises from singlet superconducting correlations that disfavor the pair-breaking effect of a polarized exchange field [275–277]. The magnetic ground state \mathbf{S}_q can be determined to second order in J by finding the minimum Fourier component of the exchange interaction I_Q , see Fig. 7.2. Here we label a generic magnetic wavevector by Q , and denote the configuration minimizing the thermodynamic potential by q .

7.3.1 Exchange interactions along the (10) direction

In the normal state ($\Delta = 0$) the magnetic ground state calculated from Eq. (7.9) is a ferromagnet ($q = 0$) in the range $n < k_F a_{\text{ad}}/\pi < n + 1/2$ with integer n and an antiferromagnet ($q = \pi/a$) otherwise. In the presence of superconductivity the antiferromagnet is stable, while the ferromagnet becomes unstable to the formation of a spiral with finite $q \neq 0$. Indeed, for $\Delta \neq 0$, $\xi^{-1} \ll Q \ll \pi/a_{\text{ad}}$ the exchange interaction scales like $I_Q \propto \cot(k_F a_{\text{ad}}) v_F Q^2/k_F - \Delta \ln(Q a_{\text{ad}})/(k_F a_{\text{ad}})$, so that the ground state wavevector is shifted from zero to $q \propto \sqrt{\Delta}$.

This magnetic instability is akin to the Anderson-Suhl transition in 2D and 3D spin lattices [275, 276, 278] and results from two competing ordering mechanisms having different strengths and effective ranges: ferromagnetism from the RKKY exchange and antiferromagnetism due to superconductivity. The development of spiral order due to the presence of superconductivity is illustrated in Fig. 7.2. The spiral formation of a 1D spin chain on a 3D superconductor was recently demonstrated in Ref. [243], where the wavevector scales as $q \propto \Delta$ in contrast to $q \propto \sqrt{\Delta}$ found above. One can easily generalize this result to a superconductor/adatom lattice of arbitrary dimensions to find $q \propto \Delta^{1/(3-D^*)}$, where $0 \leq D^* \leq 2$ is the codimension of the adatom lattice in the s -wave superconductor (the case of nodal d -wave superconductors requires a separate analysis [275]). The famous Anderson-Suhl scaling $q \propto \Delta^{1/3}$ [278] is obtained only when the adatom lattice and superconductor have the same dimension, $D^* = 0$. This indicates that for the adatom chain, the influence of superconductivity on the magnetic order is substantially enhanced for a 2D substrate as compared to a 3D substrate.

We illustrate the dependence of q on Δ in Fig. 7.3, calculated for the model of Eq. (7.1) to leading order in J , for a dense set of adatoms along the (10) direction ($a_{\text{ad}} = a$). The black lines illustrate the proposed square-root behavior of $q(\Delta)$. The dependence of q on μ can be traced back to Eq. (7.9). For μ close to half filling we have $1/2 < k_F a_{\text{ad}}/\pi < 1$ and the resulting state is antiferromagnetic. For $\mu = -2$, we find $k_F a_{\text{ad}}/\pi = 1/2$ and there is a

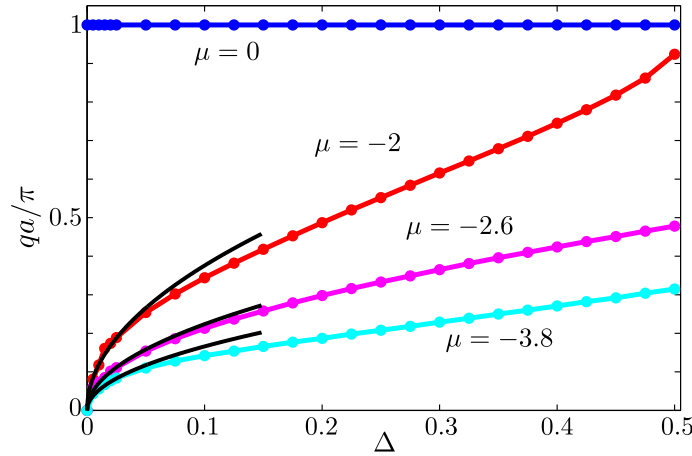


Figure 7.3: (Color online) Ground state wavevector q of an adatom chain along the (10) direction ($a_{\text{ad}} = a$) calculated from Eq. (7.1) to leading order in J as a function of Δ for different values of μ . The data points for $qa/\pi \lesssim 0.2$, $\Delta \lesssim 0.05$ are well-fit by the form $q \propto \sqrt{\Delta}$ (black lines), as predicted from the analysis of Eq. (7.9).

first order transition from an antiferromagnetic to a ferromagnetic (spiral) configuration in the normal (superconducting) state. Minimizing Eq. (7.9) as a function of q yields $q \propto \sqrt{\Delta}$ with a constant of proportionality that increases as $\mu = -2$ is approached, consistent with Fig. 7.3.

Higher order terms in J represent multiple-scattering processes which, in particular, lead to the formation of localized subgap YSR states around each adatom with energy $\varepsilon(J)$ [238, 264–266, 277] (e.g. for a parabolic band and delta-function magnetic potential one finds $\varepsilon = \pm \Delta \frac{1 - (\pi J \nu_F / 2)^2}{1 + (\pi J \nu_F / 2)^2}$ where ν_F is the normal-state density of states at the Fermi level). Heuristically, one can understand the role the YSR states play in modifying the adatom magnetic order by appealing to the general results found for the case of a 3D substrate [243]. In particular, it was shown that the overlap of the YSR states can reinforce the spiral formation, due to the renormalization of the antiferromagnetic exchange term that arises from superconductivity [277]. Essentially, the hybridization of a pair of YSR states with a Cooper pair in the substrate leads to an enhancement of the second term in Eq. (7.9), which amounts to replacing the prefactor Δ by $\Delta^2/|\varepsilon|$. As a result, the wavevector increases as $q \sim \sqrt{\Delta(\Delta/|\varepsilon|)}$ and is thus enhanced by the factor $\sqrt{\Delta/|\varepsilon|} > 1$. In the limit of a large substrate coherence length $\xi \gg a_{\text{ad}}$, this scaling of q is applicable for $|\varepsilon| > \Delta/\sqrt{k_F a_{\text{ad}}}$; for smaller values of $|\varepsilon|$ the YSR band (of width $\propto \Delta/\sqrt{k_F a_{\text{ad}}}$) crosses the Fermi level where ferromagnetic YSR double exchange occurs and favors a smaller value of q [243]. The double exchange mechanism, discussed more in Sec. 7.4, is controlled by the kinetic energy of the YSR band and is not captured by the effective Heisenberg model Eq. (7.8).

We thus find that the spiral wavevector exhibits a small peak as a function of ε (or J) near the topological superconducting transition of the order $q_{\text{max}} \sim (k_F a_{\text{ad}})^{1/4} q(J \rightarrow 0)$, i.e. there is a weak relative enhancement of q proportional to $(k_F a_{\text{ad}})^{1/4}$ compared to q in the small J limit. Consequently, for a 2D substrate, q depends very weakly on small to moderate exchange couplings, and only deviates substantially from the $q(J \rightarrow 0)$

value when the YSR band crosses the Fermi level and activates the ferromagnetic double exchange. Thus, in contrast to the case of a 3D substrate (where the dependence of q on ε , J is much stronger [243]), for a 2D substrate the magnetic order of the adatom chain at the topological transition can be understood rather well simply by studying the adatom magnetic susceptibility for weak exchange coupling, as shown in Figs. 7.2, 7.3. For chains along the (10) direction this conclusion is consistent with the numerical data presented in Sec. 7.4 even for the case $k_F a_{\text{ad}} < 1$, and for chemical potentials away from the band bottom (cf. Figs. 7.5 and 7.7).

7.3.2 Exchange interaction along the (11) direction

Along the (11)-direction the exchange interaction behaves quite differently when the substrate is near half-filling, $\mu = 0$. This is because the Fermi surface contains segments along the diagonals with very little curvature in the (k_x, k_y) -plane as well as segments along the axes with large curvature, see Fig. 7.1. This implies that the Fermi surface is nested and the electron Green function has spectral weight focused along the (11) and (-11) directions in real space [274] and thus displays effectively 1D behavior along the adatom chain. As a result, one expects the adatom chain to exhibit a $2k_F$ singularity in susceptibility, leading to $q = 2k_F$ spiral order even in the *absence* of superconductivity [255–257, 272]. Here k_F is defined as the Fermi momentum along the chain direction (i.e., for a (11) chain, k_F is taken along the diagonal $k_x = k_y$). The $q = 2k_F$ spiral order, based on perturbation theory, should be valid away from points of commensurability between $2k_F$ and π/a_{ad} [272]. For small $|\mu|$ (where $2k_F a_{\text{ad}} \approx 2\pi$), this implies that perturbation theory is valid for $J \ll |\mu|$ (where $q \approx 2k_F$), while for $J \gtrsim |\mu|$ we expect the system to lock into the commensurate ferromagnetic state [272]. This is consistent with the numerical data presented in Sec. 7.4 for the adatom chain where the magnetic order is determined by minimizing the total energy, Eq. (7.1), for large J and $|\mu|$ (cf. Fig. 7.7).

We now verify the $q = 2k_F$ behavior that exists for small J by computing q from Eq. (7.1) to leading order in J with adatoms placed along the (11)-direction, i.e. $a_{\text{ad}} = \sqrt{2}a$. In Fig. 7.4 the evolution of q and $2k_F$ as a function of chemical potential is plotted and confirms the $q = 2k_F$ behavior near $\mu = 0$. The deviation of q from $2k_F$ is expected as $|\mu|$ increases since the Fermi surface becomes more isotropic. Below a critical value of the chemical potential, $|\mu| \approx 1.5$ a transition to an antiferromagnetic state occurs. We cannot determine within our resolution whether this transition is first or second order, as indicated by the error bars in Fig. 7.4. As $|\mu|$ is increased further a second transition occurs to a spiral state that exists in the interval $2.6 \lesssim |\mu| \lesssim 3.1$, before finally transitioning into a ferromagnet for larger $|\mu|$. According to Eq. (7.9) there should be a transition between ferromagnetic and antiferromagnetic phases when $k_F a_{\text{ad}} = \pi/2$ (corresponding to the integer $n = 0$ above), or $|\mu| = 2\sqrt{2} \approx 2.8$. This is roughly consistent with Fig. 7.4, except that the first order antiferromagnet to ferromagnet transition at $|\mu| \approx 2.8$ is broadened into a narrow region of spiral order. Similar to the (10) direction, we find that antiferromagnetic order is stable against superconductivity, while ferromagnetic order is unstable to spiral formation with $q \propto \sqrt{\Delta}$. This is to be expected since ferromagnetic order in Fig. 7.4

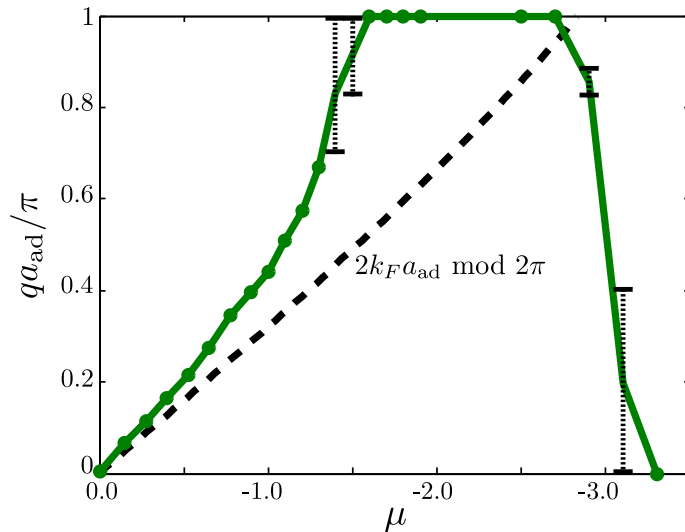


Figure 7.4: (Color online) Ground state wavevector q (green curve) of an adatom chain along the (11) direction calculated from Eq. (7.1) to leading order in J as a function of μ for $\Delta = 0$. The black dashed line is $2k_F a_{\text{ad}}$, where k_F is defined as the Fermi momentum along the (11) direction ($k_x = k_y$). The black dotted lines represent error bars inferred from the region of $\Omega(Q)$ which is essentially flat and therefore does not allow a reliable determination of the minimum.

occurs when the Fermi surface is approximately isotropic.

7.4 Magnetic adatom chain

As a chain of impurities is formed, the YSR subgap states localized at the impurities hybridize and a band develops inside the superconducting gap. To account for the effects of this band, we go beyond the two-spin exchange approximation considered above, and numerically calculate from the total electronic energy, Eq. (7.7), the preferred magnetic order for a chain of magnetic adatoms within a coplanar variational ansatz

$$\mathbf{S}_i = S \left(\cos(Qx_i), \sin(Qx_i), 0 \right) \quad (7.10)$$

parametrized by the wavevector of the chain $Q = \frac{2\pi}{Na}$, where N is an integer divisor of the number of adatom impurities. The choice of spin rotation axis as in Eq. (7.10) can be made without loss of generality in the absence of SOC. Including the SOC shifts the value of q but does not affect the topological phase boundaries, see Appendix 7.A. Along the (10) direction we let the chain extend over the entire length (120 sites) of the system, and we impose periodic boundary conditions, as indicated in the left panel of Fig. 7.1(a). A system width of 71 sites along the (01) direction is used. For chains along (11) we employ a 71×71 system and place adatoms along the $x = y$ line. Periodic boundary conditions are imposed in this case as well, but contrary to the (10) case we carry out all calculations in real space, making them more demanding.

To facilitate efficient computations, we follow Ref. [260] and perform a local spin-

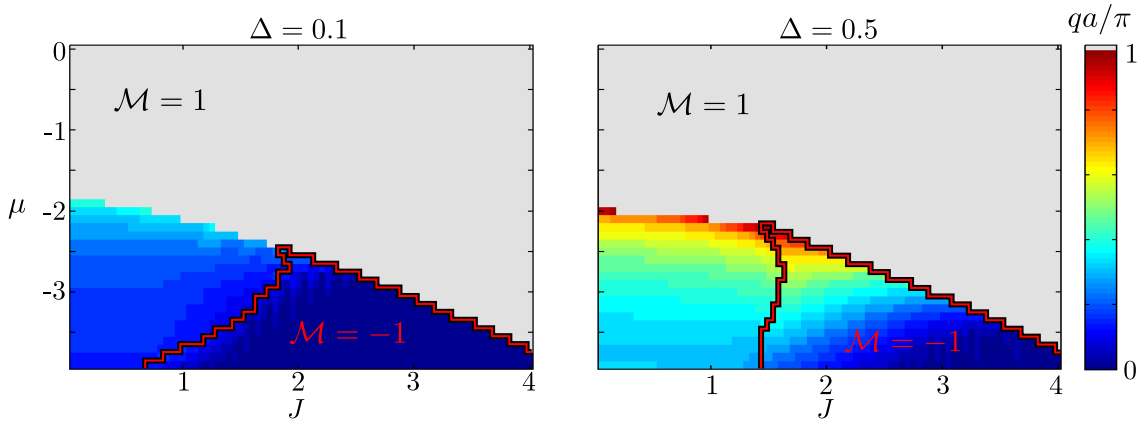


Figure 7.5: (Color online) Phase diagram for a chain along (10) with $\Delta = 0.1$ (left) and $\Delta = 0.5$ (right), and $N_x \times N_y = 120 \times 71$. Grey (blue) denotes an antiferromagnetic (ferromagnetic) state. The red lines denote the border between domains of Majorana number $\mathcal{M} = 1$ (trivial) and $\mathcal{M} = -1$ (non-trivial). For low fillings and small J the behaviour depicted is consistent with the expectation that superconductivity aids in the formation of a spiral phase. The transition between spiral and antiferromagnetic phases is first order.

rotation,

$$c_{i\sigma} \rightarrow \tilde{c}_{i\sigma} = e^{i\frac{\sigma}{2}qx_i} c_{i\sigma}, \quad (7.11)$$

which leaves \mathcal{H}_{SC} invariant and transforms \mathcal{H}_0 and \mathcal{H}_{imp} to

$$\tilde{\mathcal{H}}_0 = - \sum_{\substack{\langle ij \rangle \\ \alpha}} \tilde{t}_{ij,\alpha} \tilde{c}_{i\alpha}^\dagger \tilde{c}_{j\alpha} - \mu \sum_{i\sigma} \tilde{c}_{i\alpha}^\dagger \tilde{c}_{i\alpha}, \quad (7.12)$$

$$\tilde{\mathcal{H}}_{\text{imp}} = J_{\text{imp}} S \sum_{\substack{i \in \mathcal{I} \\ \alpha\beta}} \tilde{c}_{i\alpha}^\dagger \sigma_{\alpha\beta}^x \tilde{c}_{i\beta}. \quad (7.13)$$

In the rotated basis the spin chain is a ferromagnet polarized along \hat{x} , while the hopping amplitude becomes spin- and wavevector-dependent

$$t \rightarrow \tilde{t}_{ij,\sigma} = t e^{-i\frac{\sigma}{2}q(x_i - x_j)}, \quad (7.14)$$

where $x_i - x_j = \pm 1$ in units of the lattice constant. This transformation renders the Hamiltonian translationally invariant along the x -axis, and allows one to partially diagonalize the Hamiltonian using the Fourier transform

$$\tilde{c}_{i\alpha} = \sum_{k_x} e^{ik_x x_i} \tilde{c}_{k_x \alpha}(y_i), \quad (7.15)$$

with $k_x \in [-\pi/a, \pi/a[$. This reduces the time needed to obtain the full spectrum by a factor of $\sim N_x^2$. In the following, we evaluate the free energy of the system for 31 values of $q \in [0, \pi/a]$, which now enter exclusively via the hopping amplitudes $\tilde{t}_{ij,\sigma}$.

7.4.1 Phase diagram

Here we consider the evolution of the magnetic order of the chain with changing chemical potential, adatom potential strength and superconducting order parameter. As is shown in Sec. 7.5, including the feedback from the impurities on the local pairing potential in a selfconsistent manner does not significantly alter the magnetic or topological phases. Selfconsistency is therefore neglected in the remainder of this section. This also implies neglecting the other effect of selfconsistency, namely an overall suppression of the superconducting order parameter with changing chemical potential due to a reduction of the number of states available for pairing. The magnitude of the order parameter can thus be varied independently of the chemical potential. In Fig. 7.5 we show phase diagrams corresponding to $\Delta = 0.1$ and $\Delta = 0.5$, which reveal behavior consistent with the general trends found in Ref. [243] when the Fermi surface is approximately isotropic, as discussed in Sec. 7.3.

In particular, the analysis of Sec. 7.3 predicts the magnetic order to be antiferromagnetic for $k_F a_{\text{ad}} > \pi/2$, where k_F is the Fermi momentum along the chain direction. This translates to antiferromagnetic order for $0 < |\mu| \lesssim 2$ and spiral order for $|\mu| \gtrsim 2$, which for small J agrees well with the phase diagrams in Fig. 7.5 determined by minimizing $\Omega(Q)$. The superconductivity induced antiferromagnetic contribution to the exchange interaction, which is proportional to Δ [see Eq. (7.9)], slightly shifts the boundary between antiferromagnetic and spiral phases, thus accounting for the small difference between the $\Delta = 0.1$ and $\Delta = 0.5$ cases in Fig. 7.5. For $J \ll 1$ and a (10) chain, the magnetic order weakly depends on J (see Figs. 7.5 and 7.7), however, as J is increased the YSR band eventually crosses the Fermi level. As mentioned in Sec. 7.3, this activates the ferromagnetic YSR double exchange mechanism [243] and leads to a decrease in the wavevector q with increasing J . This behavior is shown in the last column of Fig. 7.7.

The transition to an antiferromagnetic state at larger J occurs in the absence of superconductivity. It is also reflected in the two-spin exchange coupling, indicating that it is not a multi-spin effect. Therefore, one could capture this effect by mapping the evolution of q as a function of μ and J including higher-order corrections in J to the two-spin exchange interaction, Eq. (7.9). In our model, the decrease of the antiferromagnetic phase boundary line occurs already at quartic order in J , but whether this particular behavior is generic remains an open problem.

As discussed in Sec. 7.3.2, there can be substantial differences between forming the adatom chain along the (10) and (11) crystallographic directions. In addition to a modification of the adatom spacing, the (11) direction also nests the Fermi surface near half-filling and this leads to the possibility of spiral order in the absence of superconductivity. In Fig. 7.6 we plot q for $\Delta = 0.1$ and $\Delta = 0.5$ for a chain along (11). Behavior distinct from the (10) direction is evident in particular for $|\mu| \lesssim 2$ where the Fermi surface nesting is the most prominent. For $|\mu| \approx 3$ the spiral phase appears and yields to an antiferromagnetic phase as J is increased. At this point the Fermi surface is nearly isotropic and the system exhibits behavior similar to the (10) direction with a slightly larger adatom spacing compared to the case considered above. To highlight the differences between (10)

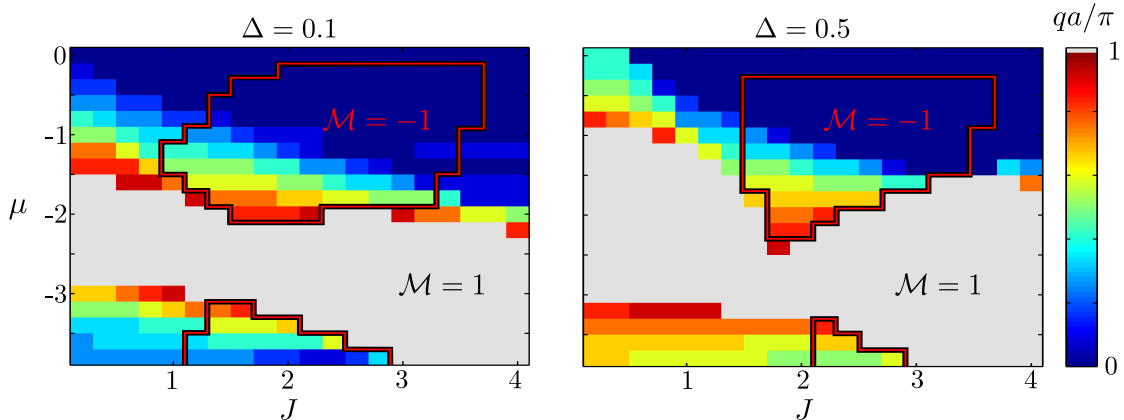


Figure 7.6: Phase diagrams for a chain along (11) with $\Delta = 0.1$ (left) and $\Delta = 0.5$ (right). Here $N_x \times N_y = 48 \times 48$. For $|\mu| \lesssim 2$ the behavior is found to match expectations from 1D, where a spiral yields to a ferromagnet when $J \sim |\mu|$. 2D behavior is recovered for $|\mu| \gtrsim 2$, although recall that the adatom spacing is modified. The red lines denote the border between domains of Majorana number $\mathcal{M} = 1$ (trivial) and $\mathcal{M} = -1$ (non-trivial). The resolution is different from Fig. 7.5 as the determination of q is substantially more demanding in real space.

and (11) we plot q in both cases as a function of J for cuts at fixed values of μ in Fig. 7.7. For $\mu = -1$, $\Delta = 0.1$, where Fermi surface nesting is still active, one finds the wavevector for $J \rightarrow 0$ in Fig. 7.7 to differ only slightly from the value $qa_{\text{ad}}/\pi \approx 0.45$ shown in Fig. 7.4 (the discrepancy is due to finite $\Delta = 0.1$ in the case of the former). As J is increased, however, q rapidly decreases until $J \approx 2$, beyond which it saturates. This is consistent with the result of Ref. [262, 272] for a 1D substrate that predicts a second order transition from a spiral into a ferromagnetic state at a critical value of J proportional to the deviation from commensurability. For a chain along the (11) direction this would occur for $J \sim |\mu|$, which appears to be consistent with Fig. 7.6 and Fig. 7.7. Contrary to a chain along (10), the ferromagnetic state along (11) for $\mu = 0$ is more robust towards the addition of superconductivity. We found a ferromagnetic ground state for systems up to 100×100 . This suggests that if spiral order occurs for larger systems, the value of qa is smaller than $\pi/50$.

7.4.2 Topological phases

By evaluating the Majorana number we can distinguish phases of trivial and non-trivial topology. The Majorana number is defined as [224]

$$\mathcal{M} = \text{sign}(\text{Pf}[\mathcal{A}(0)]\text{Pf}[\mathcal{A}(\pi)]) , \quad (7.16)$$

where $\tilde{H}(k) = \frac{i}{4}\mathcal{A}(k)$ is the Hamiltonian in the Majorana representation and Pf denotes the Pfaffian. In Fig. 7.5 regions with negative Majorana number, denoting the non-trivial phase, are bounded by red lines. We remind the reader that this is not a sufficient condition for the phase to support localized Majorana modes, as there should also be a quasiparticle gap, i.e. the Majorana modes should be separated from the bulk YSR spectrum by an

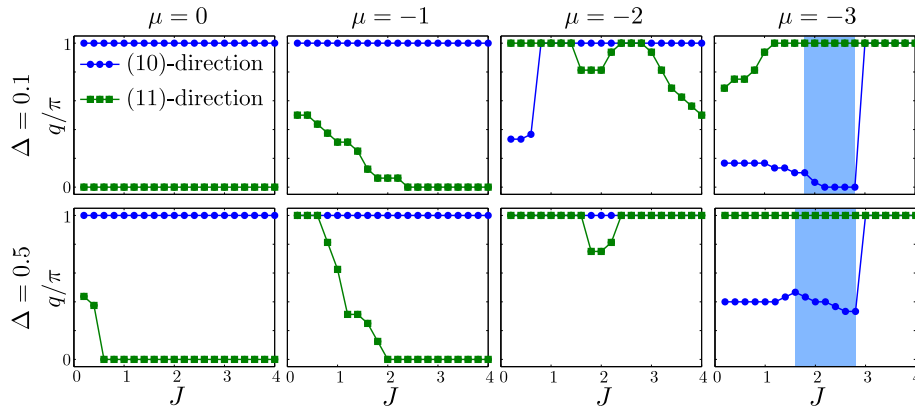


Figure 7.7: (Color online) Comparison of the ground state wavevector q of an adatom chain along the (10) (blue) and (11) (green) directions. Data for the (10) chain correspond to cuts at fixed μ through the phase diagrams in Fig. 7.5. The light-blue shaded regions indicate the topologically non-trivial phase for the (10) direction, as well as the onset of YSR double exchange. Data for the (11) chain are consistent with the concept that the substrate behaves effectively as a 1D superconductor near $\mu = 0$ (cf. Fig. 7.4 and the discussion in Sec. 7.3.2).

energy gap. The topological gap depends sensitively on the magnetic order of the adatom chain [252]. As q decreases and the magnetic order approaches ferromagnetism, the topological gap decreases and is strictly zero for $q = 0$. This is because singlet Cooper pairs in the substrate cannot tunnel into a spin-polarized YSR chain. We generally find that the presence of strictly ferromagnetic, $q = 0$, configurations in Fig. 7.5 appear to be a consequence of finite size effects, which quantize the value of q under periodic boundary conditions. We have confirmed that with increasing system size (to $N_x \times N_y = 240 \times 101$) the ferromagnetic phase for a (10) chain indeed becomes a weak spiral.

In Fig. 7.8(a) we plot the electron energy spectrum as a function of J for $\mu = -2.6$, $\Delta = 0.5$, showing the energy gap closing and reopening across the topological transition. Within the non-trivial phase there exists a pair of states near zero energy, which indicate the presence of Majorana bound states weakly hybridized due to the finite extent of the chain. A first order transition to the antiferromagnetic phase occurs at larger J (indicated by the grey region) and coincides with the abrupt termination of the zero energy state, see Fig. 7.8(a). This differs substantially from the case when the topological gap closes due to the formation of a ferromagnetic state, see Fig. 7.8(b). We note that the closing of the topological gap for $J \gtrsim 2$ in Fig. 7.8(b) reflects the decrease of q with J in Fig. 7.5.

The remaining subgap states seen in Fig. 7.8 in the antiferromagnetic phase can be understood in terms of an effective two-channel p -wave superconductor, where each channel supports a Majorana bound state at each end of the chain. The hard-wall boundary condition hybridizes these states to create a single localized fermionic state at each end of the chain [252].

The (11)-direction also exhibits Majorana bound states, albeit for different parameter values, consistent with the fact that the chain is parallel to the nesting wavevector and has a larger lattice spacing. Thus, the topologically non-trivial region already occurs for μ

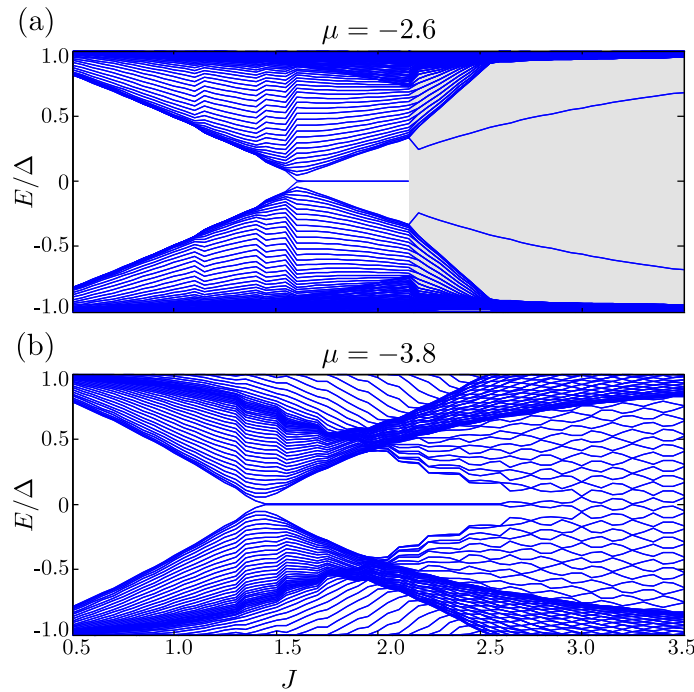


Figure 7.8: (Color online) Electron energy spectrum as a function of J for a (10) chain and two values of μ (here $\Delta = 0.5$). (a) The topological phase terminates at large J due to a first order magnetic transition into an antiferromagnetic state, indicated by the grey region. Two fermionic subgap states persist in the antiferromagnetic region and are localized to the chain boundaries. (b) The Majorana modes delocalize and hybridize when the topological gap closes as a result of ferromagnetic order $q = 0$, however ferromagnetic order appears to be a finite size effect.

close to half filling (but not for $\mu = 0$), and for $J \approx 1$. In Fig. 7.9 the bound states along the two different directions are illustrated.

7.4.3 Effect of direct exchange interaction

Motivated by the close proximity of the adatoms, we briefly remark on the consequences of having an additional direct, nearest neighbor ferromagnetic exchange interaction between them. We assume the adatoms to lie along the (10) direction with $a_{\text{ad}} = a$ and minimize the total energy

$$E_{\text{tot}}(Q) = \tilde{\Omega}(Q) - J_{\text{ex}} \cos Q a_{\text{ad}}, \quad (7.17)$$

where $J_{\text{ex}} > 0$ denotes the strength of the direct exchange interaction and $\tilde{\Omega} = \Omega/N_{\text{ad}}$ is the thermodynamic potential per adatom. In Fig. 7.10 we show how the direct exchange modifies the phase diagram for increasing values of J_{ex} . We find that as J_{ex} is increased the antiferromagnet/spiral phase boundary line shifts to make the antiferromagnetic region smaller, and the ferromagnetic or weak spiral phases larger. At the same time, new regions of strong spiral order with $qa/\pi \sim 0.5$ open near half-filling, previously occupied by the antiferromagnetic phase. This occurs for a moderate exchange coupling $J_{\text{ex}} \sim 5 \cdot 10^{-4}$, which is roughly 1/4 of the scale set by the indirect exchange coupling in that region

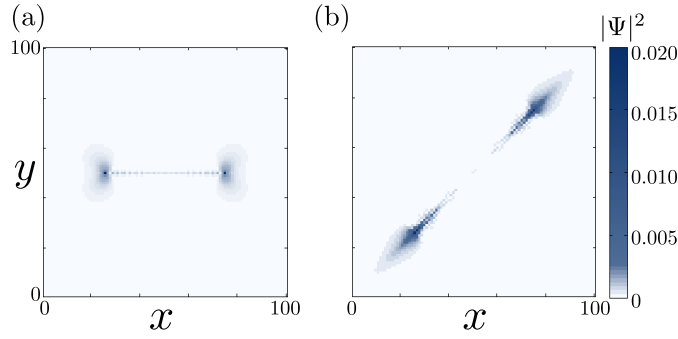


Figure 7.9: (Color online) (a) Majorana end mode for a chain along (10) for $\mu = -2.6$ and $J = 2.1$. (b) Majorana end mode for a chain along (11) for $\mu = -0.65$ and $J = 1.8$. In both cases $\Delta = 0.1$. The localization length along the chain depends sensitively on the chosen parameters.

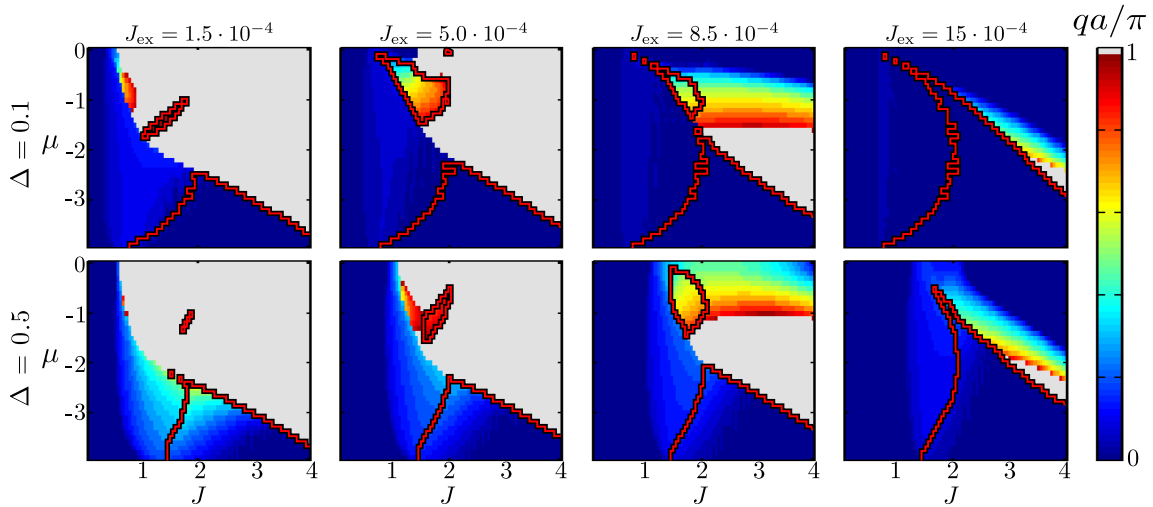


Figure 7.10: (Color online) Phase diagrams illustrating the effect of adding a ferromagnetic direct exchange term between the adatomic impurities. The red outline denotes the boundaries between regions of $\mathcal{M} = 1$ and $\mathcal{M} = -1$.

of parameters. The latter can be estimated, e.g., by calculating the magnetic energy bandwidth near $\mu = -1$, $J = 1.5$ (cf. Fig. 7.10), defined as the difference between the maximum and the minimum of $\tilde{\Omega}(Q)$.

Another interesting feature to observe is that the spiral phase can survive in the presence of rather large J_{ex} . In the case with $\Delta = 0.1$ the spiral phase remains for $J_{\text{ex}} \lesssim 15 \cdot 10^{-4}$ in a narrow vertical region near $J \approx 0.7$ in Fig. 7.10. For $\Delta = 0.5$ the spiral phase can be found for $J_{\text{ex}} \lesssim 8 \cdot 10^{-3}$ in a wider vertical region near $J = 1.5$. For $\Delta = 0.1$, the maximal value of J_{ex} exceeds the indirect exchange coupling (evaluated in the narrow region where the spiral last existed) by a factor of 8-10, while for $\Delta = 0.5$ the maximal value of J_{ex} is 4 times larger than the indirect exchange.

The robustness of spiral order with respect to such large values of the direct exchange interaction can be traced back to the long-range nature of the indirect antiferromagnetic exchange coupling in Eq. 7.9. Adding a direct exchange interaction leads to a total energy

7.5 Effects of selfconsistency

that may be expressed for $\xi^{-1} \ll Q \ll \pi/a_{\text{ad}}$ as

$$E_{\text{tot}}(Q) = \frac{1}{2}(J_{\text{ex}} + J_{\text{RKKY}})(Qa_{\text{ad}})^2 - J_{\text{RKKY}} \frac{a_{\text{ad}}}{\xi} \ln(Qa_{\text{ad}}) \quad (7.18)$$

where for $J \sim 1$ we have $J_{\text{RKKY}} \sim v_F/(k_F a_{\text{ad}}^2)$ (cf. Sec. 7.3). Minimizing E_{tot} leads to

$$qa_{\text{ad}} = \sqrt{\frac{a_{\text{ad}}}{\xi} \frac{J_{\text{RKKY}}}{J_{\text{ex}} + J_{\text{RKKY}}}}. \quad (7.19)$$

The expression in Eq. (7.19) holds only for $q > \xi^{-1}$, or $J_{\text{ex}} < J_{\text{RKKY}}(\xi/a_{\text{ad}} - 1)$, while for larger J_{ex} the true ground state is a ferromagnet. If the chemical potential lies within the YSR band, an exponentially small q , with exponent proportional to J_{ex}/Δ , is expected due to a gain in YSR condensation energy [243]. For the topologically trivial regime we find for $\xi/a_{\text{ad}} \gg 1$ that a spiral phase exists even for parametrically large J_{ex} ,

$$J_{\text{ex}} < J_{\text{RKKY}}(\xi/a_{\text{ad}}) \quad (7.20)$$

implying that a window exists in which the direct exchange interaction exceeds the indirect RKKY exchange interaction but a spiral phase still occurs. The existence of this window ultimately stems from the scaling law $q \propto \sqrt{\Delta}$ discussed in Sec. 7.3. For a 3D substrate one has $q \propto \Delta$ and the window in Eq. (7.20) is absent (i.e. the adatom chain becomes ferromagnetic once $J_{\text{ex}} \gtrsim J_{\text{RKKY}}$). We also note that although the window becomes larger with increasing ξ (decreasing Δ), it also has the adverse effect of decreasing the magnitude of q , see Eq. (7.19). These considerations appear qualitatively consistent with the numerical data shown in Fig. 7.10 and discussed above.

7.5 Effects of selfconsistency

Within selfconsistent mean field theory, the pair-breaking magnetic adatoms will give rise to a local suppression of the superconducting pair potential near the adatom chain [245,266, 279]. This is illustrated in Fig. 7.11, where we plot the spatial profile of the pair potential across the width of the system, with the adatom chain along the (10) direction located on site number 36 along the (01) direction. For fixed chemical potential, the suppression is seen to increase with J , and even lead to an on-chain negative pair potential at $J = 2$. For fixed $J = 2$, on the other hand, the spatial modulation of the pair potential is seen to extend further from the chain when μ is lowered and the Fermi wavelength increases. Both of these trends are consistent with expectations based on results of Refs. [245,266].

To determine to what extent the local suppression affects the magnetic order along the chain we compare the q -vector for selfconsistent and non-selfconsistent evaluations of the thermodynamic potential in Fig. 7.12(a)-(b). The effect of selfconsistency is seen to be minor and dependent on the magnitude of the bulk gap Δ , which is defined here as Δ_i evaluated far from, or in the absence of, the adatom chain. The effect of local suppression of the pairing potential can be understood as follows: The local pairing potential on the chain is suppressed leading to a decrease of the effective chemical potential, $\varepsilon(J)$, for the subgap YSR states [252]. For a single adatom the YSR state crosses zero energy at

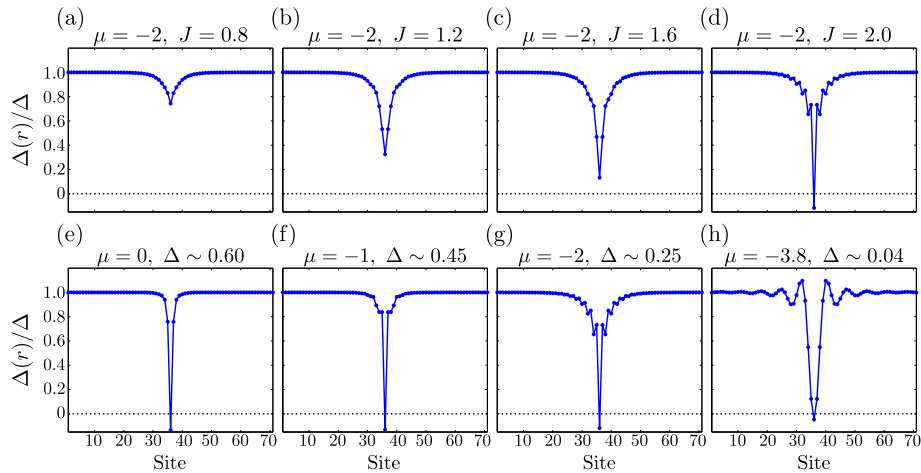


Figure 7.11: (Color online) Effect of self-consistency on the superconducting order parameter for $V = 2.5$ for a chain along (10). (a)–(d) Evolution of the superconducting order parameter as J is increased for a fixed value of the chemical potential. As J is increased above J_c , the order parameter along the chain changes sign. (e)–(h) Superconducting order parameter for different values of μ for fixed $J = 2$. The extent of the suppression is seen to vary with the chemical potential [245].

$J = J_c$. Selfconsistency effectively reduces J_c to \tilde{J}_c , which, for an adatom chain, causes the YSR band to cross the Fermi level at a smaller value of J as depicted in Fig. 7.12(c)–(d). Hence, ferromagnetic double exchange sets in at a lower J , leading to a reduction of q . This behavior is evident in Fig. 7.12. We note that, as before, the appearance of a strictly ferromagnetic state in the selfconsistent calculation is a consequence of finite-size effects and increasing system size reveals a weak spiral state. As Δ is reduced, the renormalization of the effective chemical potential of the YSR band is reduced as well, thus making the effect less prominent. This is indicated in Fig. 7.12 and consistent with Ref. [245].

Selfconsistency does not alter the phase boundary between spiral and antiferromagnetic states within the step-size used for J ($= 0.1$). The onset of antiferromagnetic order occurs even in the absence of superconductivity and can be understood by the higher-order corrections to the exchange interaction, as explained in Sec. 7.4.1. This does not depend on the details of the gap and hence selfconsistency does not significantly shift the onset of antiferromagnetism. This is confirmed by comparing selfconsistent and non-selfconsistent calculations at a higher value of μ (not shown). These observations allow us to disentangle the effects of superconductivity from those arising solely from varying the chemical potential when considering the magnetic order along the chain, as was done in Sec. 7.4.

Due to the reduction of J_c by the local suppression of the pairing potential, selfconsistency also has an effect on the topological gap, as depicted in Fig. 7.13. The topological gap exhibits non-monotonic behavior as a function of J , increasing from zero at the topological phase transition to a maximum at $J \sim J_c$ before decreasing to zero as antiferromagnetic order sets in and the topological phase ceases to exist. As above, the effect of selfconsistency is proportional to the magnitude of Δ , and for $\Delta = 0.1$ (not shown) the two cases are

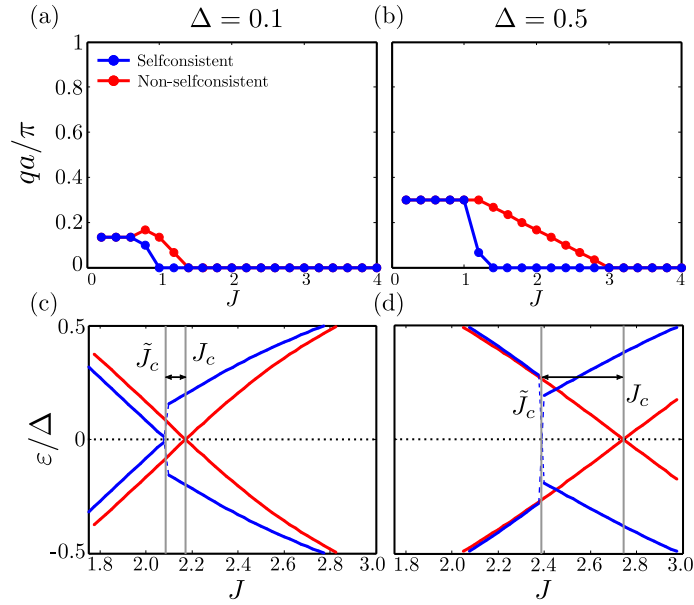


Figure 7.12: (Color online) (a)–(b) Comparison of selfconsistent and non-selfconsistent approaches when evaluating the minimum of the thermodynamic potential for an adatom chain. The selfconsistent approach accounts for the local suppression of the order parameter depicted in Fig. 7.11. Both cases depicted are for $\mu = -3.8$. Here Δ refers to pairing potential far away from the chain, $\Delta = 0.1$ requires $V = 3.09$ while $\Delta = 0.5$ implies $V = 4.80$. The effect depends on the magnitude of Δ as the suppression of the effective chemical potential felt by the subgap YSR states is smaller for smaller Δ . (c)–(d) Illustration of the reduction of J_c for a single adatom by selfconsistency. The dependence on the magnitude of Δ is evident, the reduction in (d) is much more pronounced than in (c).

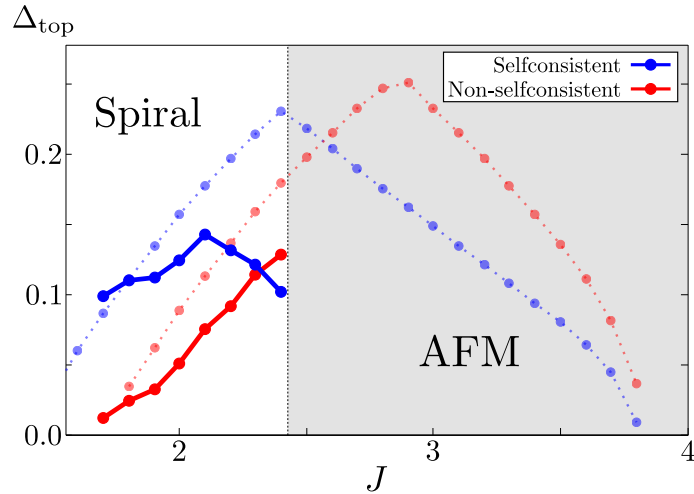


Figure 7.13: (Color online) Illustration of the shift of the maximum of the topological gap towards lower J as the local pairing potential is suppressed by selfconsistency, while the bulk gap is kept fixed at $\Delta = 0.5$. The full curves correspond to the case where the q -vector is determined by minimizing the energy (see Fig. 7.5). To illustrate the entire evolution of the dome, the faded curves were computed for a fixed q -vector ($qa = \frac{14\pi}{30}$). The faded dotted red curve has $\Delta = 0.5$ on all sites while for the faded dotted blue curve, the pairing potential was suppressed locally at the chain sites to $\Delta(r_{i \in \mathcal{I}}) = 0.2$. In these plots $\mu = -2.8$.

barely distinguishable. Together with the Fermi velocity of the YSR band, v_F^* , the topological gap controls the Majorana localization length $\ell \sim v_F^*/\Delta_{\text{top}}$. However, ℓ appears to depend sensitively on parameters despite the fact that the topological gap exhibits the simple shape shown in Fig. 7.13, which could be explained by a sensitivity to parameters in v_F^* .

7.6 Conclusions

In this paper we performed a detailed study of the indirect exchange interactions between impurities deposited on two-dimensional superconducting substrates. We showed that spiral order can form along a chain of adatoms due to such interactions. One component of these is antiferromagnetic and owes its origin to the presence of superconductivity, while the other is the standard oscillating RKKY component. Unless the chain nests the Fermi surface the spiral order does not arise from a $2k_F$ peak in the susceptibility but instead from the competition between the superconducting antiferromagnetic component and the oscillating RKKY component. For a chemical potential near the band bottom we found the dependence $q \propto \sqrt{\Delta}$, implying a pronounced effect of superconductivity on the spiral q -vector. The exchange interactions along (11) for a system close to half filling were shown to exhibit behavior consistent with a chain of adatoms deposited on a 1D conductor; spiral order with $q \propto 2k_F$ forms for $|\mu| < 1$ as seen in Fig. 7.4. This is in stark contrast to the exchange interactions along (10) which display antiferromagnetic behavior close to half filling.

7.6 Conclusions

For a chain of impurities we contrasted selfconsistent and non-selfconsistent approaches and found that the local suppression of the pairing potential induced from the feedback of the impurities on the superconducting order parameter only affects the magnetic order around $J \sim J_c$ where the YSR band crosses the Fermi level. This allows us to study the phase diagram of the chain (in Fig. 7.5) without imposing selfconsistency and thus decoupling the chemical potential from the superconducting order parameter. For $J \lesssim J_c$, when the chemical potential lies outside the YSR band, the magnetic order is described by two-spin exchange interactions. The validity of the weak-coupling description is a consequence of the relatively weak dependence of the magnetic ordering vector q on the YSR energy ε (see Sec. 7.3.1). As the YSR band crosses the Fermi level, the exchange picture breaks down however, and q is reduced by ferromagnetic double exchange. Including a direct exchange coupling between the adatoms allow the formation of spiral phases even for $J_{\text{ex}} > J_{\text{RKKY}}$ due to the strong dependence $q \propto \sqrt{\Delta}$ behavior found for a 2D substrate.

Topologically non-trivial regions of the phase diagrams are found in the spiral phases and exhibit Majorana bound states. The topological transition occurs as the YSR band crosses the Fermi level, at which point double exchange becomes a factor and q is suppressed, see Fig. 7.7. The topological gap in the non-trivial regions were found to exhibit a weak dependence on selfconsistency through the reduction of J_c by the suppression of the local pairing potential.

Appendix

7.A Effect of spin-orbit coupling

The presence of a finite spin-orbit coupling term breaks the spin $SO(3)$ symmetry and introduces a preferred direction in the model. We study a Rashba-type spin-orbit coupling due to its relevance for systems with adatoms deposited on surfaces of bulk systems. The aim is to understand the circumstances under which the spin-orbit coupling can be gauged away and the effect absorbed into the spiral magnetic order. We note that for substrates with dimensionality greater than one such a transformation cannot be achieved exactly due to the presence of multiple non-commuting Pauli matrices in the Hamiltonian Eq. 7.21. The additional SOC-term we consider is

$$\begin{aligned} \mathcal{H}_{\text{SO}} = & t_{\text{so}} \sum_{\substack{i \\ \alpha\beta}} i c_{i\alpha}^\dagger \sigma_{\alpha\beta}^x c_{i+\delta_y\beta} \\ & - i c_{i\alpha}^\dagger \sigma_{\alpha\beta}^y c_{i+\delta_x\beta} + \text{h.c.}, \end{aligned} \quad (7.21)$$

and once again consider two adatoms placed on the substrate a certain distance apart. The spin of one is kept fixed perpendicular to the plane and we use the Ansatz

$$\mathbf{S}_2 = S \begin{pmatrix} \sin \theta \cos \phi \\ \sin \theta \sin \phi \\ \cos \theta \end{pmatrix} \quad (7.22)$$

to describe the other. Here ϕ describes the azimuthal, and θ the polar angle with respect to the first spin. The total energy is evaluated for values of ϕ and θ corresponding to 165 distinct points on a sphere, and the corresponding energy landscape is mapped out in Fig. 7.14(a). At a glance, the energy landscape indicates a non-trivial dependence on the azimuthal angle, ϕ . To understand if this is caused by the choice of rotation plane (and therefore can be gauged away), we consider the simple Hamiltonian

$$\begin{aligned} \mathcal{H} = & - 2(\cos k_x a + \cos k_y a) \\ & + \alpha(\sigma_y \sin k_x a - \sigma_x \sin k_y a) - \mu, \end{aligned} \quad (7.23)$$

and observe that, when the spin-orbit coupling is weak, the modification to the Green function can be approximated as $G(x) \approx G_0(x) e^{-\frac{i}{2} t_{\text{so}} x \sigma_y}$, where $G_0(x)$ is the electron Green function at vanishing SOC [28, 235, 280]. An evaluation of the RKKY exchange interaction reveals that it still contains only a term proportional to the angle between the two spins, $\mathbf{S}_1 \cdot \tilde{\mathbf{S}}_2 = \cos \tilde{\theta}$, where the tilde refers to a new frame, related to the old frame *via*

$$\tilde{\theta} = \arccos(\cos \phi \sin \theta \sin \alpha a_{\text{ad}} + \cos \theta \cos \alpha a_{\text{ad}}), \quad (7.24)$$

$$\tilde{\phi} = \arctan\left(\frac{\sin \theta \sin \phi}{\cos \phi \sin \theta \cos \alpha a_{\text{ad}} - \cos \theta \sin \alpha a_{\text{ad}}}\right). \quad (7.25)$$

Here α can be related to the lattice parameter t_{so} through $\alpha = C t_{\text{so}}$ where C is a constant. For weak spin-orbit coupling, $C \approx 1$. As the spin-orbit coupling t_{so} is increased, C is

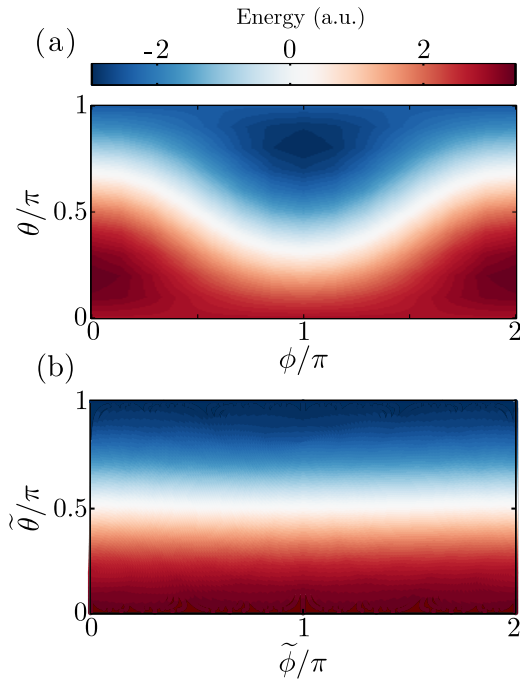


Figure 7.14: (Color online) Energy as function of both polar and azimuthal angles in the presence of spin-orbit coupling with $t_{\text{so}} = 0.1$ and $J = 0.1$ and the distance between the two adatoms $a_{\text{ad}} = 5$. In (a) the energy landscape is depicted prior to the application of the map in Eqs. (7.24) and (7.25) indicating a non-trivial ϕ dependence. In (b) the map has been applied resulting in a manifestly $\tilde{\phi}$ independent energy landscape.

renormalized through higher order contributions to the relation between $G(x)$ and G_0 , until the point where the approximation breaks down, and the effect of spin-orbit coupling can no longer be gauged away. In Fig. 7.14(b) we show the energy landscape in the transformed frame for $t_{\text{so}} = 0.1$ and $J = 0.1$, in which it is clear that the energy does not depend on $\tilde{\phi}$. Thus, as long as spin-orbit coupling is weak, its effect can be included as an additional pitch of the order along the magnetic chain.

Chapter 8

Concluding Remarks and Outlook

In this thesis we considered a number of subjects, some rather distinct while others were more closely linked. Here we summarise some of the key findings and consider possible future directions.

In Sec. 1.1 we saw that the phase diagram obtained from mean-field theory is stable under the renormalisation group flow of the quartic coefficients. We reviewed both commensurate and incommensurate magnetism and saw that the magnetic order is sensitive to the presence of orbitals. In Chapter 2 we used a hybrid model to include the effect of a finite spin-orbit coupling and showed that a phase where the magnetic moments reorient out of the plane is present on the hole doped side, consistent with experimental observations [32–35, 51]. In the experiments however, the reorientation only occurs in the tetragonal phase, unlike the approach presented in Chapter 2 which also exhibits a reoriented stripe phase. Pinpointing the reason for the simultaneous magnetic moment reorientation and appearance of the tetragonal phase presents an interesting problem, which could possibly be addressed using a more realistic model. In Chapter 3 we evaluated the nematic susceptibility within the multi-orbital Hubbard model and demonstrated the existence of a spin-driven nematic instability. While this was done for a specific band structure in a case where a magnetic instability is present, extensions to other band structures and cases where a magnetic instability is absent are possible. For instance, taking a band structure suitable for FeSe and appropriate interaction parameters such that a magnetic transition is absent one could evaluate the nematic susceptibility and check for the presence of a nematic phase.

From the FeSC we proceeded to consider the cuprates in Chapter 4 and Chapter 5. Following Berg. *et al.* [184] we introduced the PDW phase as a possible explanation for the observed resistivity anisotropy in LBCO. Motivated by neutron scattering experiments which indicated the absence of a magnetic resonance we evaluated the dynamic spin susceptibility in the presence of both ordinary d -wave superconductivity and PDW superconductivity and showed that a resonance is absent in the case of a PDW phase. In this context it is interesting to note that a recent experiment on $\text{Bi}_2\text{Sr}_2\text{CaCu}_2\text{O}_{8+x}$ using Josephson STM reported signatures of a PDW phase [186]. However, the interplay between a superconducting tip in the PDW phase and a bulk PDW superconductor is currently not well understood and presents a promising venue for further investigation.

The concept of Majorana modes was introduced in Chapter 6 and a brief overview of possible experimental setups was provided. To improve our understanding of the mechanisms responsible for spiral magnetic order in adatom chains deposited on superconductors we mapped out the phase diagram as a function of chemical potential and adatom strength. Aligning the magnetic chain both along the (10) and the (11) directions we found that the (11) direction displays behaviour reminiscent of magnetic chains on one-dimensional substrates. Contrasting different values of Δ it was seen that the region with spiral magnetic order is rather robust against the addition of superconductivity with only the angle between adjacent adatoms changing. The addition of a direct exchange interaction between the adatoms yielded regions with stable spiral order which were shown to support Majorana end modes. Advances in STM techniques have made it possible to construct arrays of magnetic adatoms and adjust the distance between individual adatoms. The individual control of each adatom also allows for more complicated structures such as T-junctions or magnetic islands to be constructed. The techniques employed in Chapter 7 can be used in the study of such structures as well. In particular, given the importance of the T-junction for braiding of Majorana modes, it would be pertinent to investigate the magnetic order of such a structure and how it changes once a junction is formed. With the discrepancy between (10) and (11) directions highlighted in Chapter 7 one could even consider junctions with legs grown along separate directions. The observation of Majorana modes at the end points of adatom chains was a landmark discovery for the field, and the prospects of using STM tips to control individual adatoms is sure to bring further revelations.

Bibliography

- [1] J. Bardeen, L. N. Cooper, and J. R. Schrieffer, “Theory of Superconductivity,” *Phys. Rev.* **108** (Dec, 1957) 1175–1204.
<http://link.aps.org/doi/10.1103/PhysRev.108.1175>.
- [2] J. G. Bednorz and K. A. Müller, “Possible hightc superconductivity in the ba-la-cu-o system,” *Zeitschrift für Physik B Condensed Matter* **64** no. 2, (1986) 189–193. <http://dx.doi.org/10.1007/BF01303701>.
- [3] J. P. Carbotte, “Properties of boson-exchange superconductors,” *Rev. Mod. Phys.* **62** (Oct, 1990) 1027–1157.
<http://link.aps.org/doi/10.1103/RevModPhys.62.1027>.
- [4] W. Pickett, “The other high-temperature superconductors,” *Physica B: Condensed Matter* **296** (2001) 112–119.
<http://www.sciencedirect.com/science/article/pii/S0921452600007870>.
Proceedings of the Symposium on Wave Propagation and Electronic Structure in Disordered Systems.
- [5] C. M. Varma, P. B. Littlewood, S. Schmitt-Rink, E. Abrahams, and A. E. Ruckenstein, “Phenomenology of the normal state of Cu-O high-temperature superconductors,” *Phys. Rev. Lett.* **63** (Oct, 1989) 1996–1999.
<http://link.aps.org/doi/10.1103/PhysRevLett.63.1996>.
- [6] T. Senthil, S. Sachdev, and M. Vojta, “Fractionalized Fermi Liquids,” *Phys. Rev. Lett.* **90** (May, 2003) 216403.
<http://link.aps.org/doi/10.1103/PhysRevLett.90.216403>.
- [7] P. W. Anderson, “The Resonating Valence Bond State in La_2CuO_4 and Superconductivity,” *Science* **235** no. 4793, (1987) 1196–1198.
<http://science.sciencemag.org/content/235/4793/1196>.
- [8] Y. Kamihara, H. Hiramatsu, M. Hirano, R. Kawamura, H. Yanagi, T. Kamiya, and H. Hosono, “Iron-based layered superconductor: Laofep,” *Journal of the American Chemical Society* **128** no. 31, (2006) 10012–10013.
<http://dx.doi.org/10.1021/ja063355c>. PMID: 16881620.

- [9] P. Dai, “Antiferromagnetic order and spin dynamics in iron-based superconductors,” *Rev. Mod. Phys.* **87** (Aug, 2015) 855–896. <http://link.aps.org/doi/10.1103/RevModPhys.87.855>.
- [10] S. Raghu, X.-L. Qi, C.-X. Liu, D. J. Scalapino, and S.-C. Zhang, “Minimal two-band model of the superconducting iron oxypnictides,” *Phys. Rev. B* **77** (Jun, 2008) 220503. <http://link.aps.org/doi/10.1103/PhysRevB.77.220503>.
- [11] M. Daghofer, A. Nicholson, A. Moreo, and E. Dagotto, “Three orbital model for the iron-based superconductors,” *Phys. Rev. B* **81** (Jan, 2010) 014511. <http://link.aps.org/doi/10.1103/PhysRevB.81.014511>.
- [12] Z. P. Yin, K. Haule, and G. Kotliar, “Kinetic frustration and the nature of the magnetic and paramagnetic states in iron pnictides and iron chalcogenides,” *Nature Materials* **10** (Dec, 2011) 932–935. <http://dx.doi.org/10.1038/nmat3120>.
- [13] L. de’ Medici, S. R. Hassan, M. Capone, and X. Dai, “Orbital-selective mott transition out of band degeneracy lifting,” *Phys. Rev. Lett.* **102** (Mar, 2009) 126401. <http://link.aps.org/doi/10.1103/PhysRevLett.102.126401>.
- [14] L. de’ Medici, G. Giovannetti, and M. Capone, “Selective mott physics as a key to iron superconductors,” *Phys. Rev. Lett.* **112** (Apr, 2014) 177001. <http://link.aps.org/doi/10.1103/PhysRevLett.112.177001>.
- [15] P. O. Sprau, A. Kostin, A. Kreisel, A. E. Böhmer, V. Taufour, P. C. Canfield, S. Mukherjee, P. J. Hirschfeld, B. M. Andersen, and J. C. Séamus Davis, “Discovery of Orbital-Selective Cooper Pairing in FeSe,” *ArXiv e-prints* (Nov., 2016), arXiv:1611.02134 [cond-mat.supr-con].
- [16] J. R. Kirtley, C. C. Tsuei, J. Z. Sun, C. C. Chi, L. S. Yu-Jahnes, A. Gupta, M. Rupp, and M. B. Ketchen, “Symmetry of the order parameter in the high-Tc superconductor YBa₂Cu₃O_{7-δ},” *Nature (London)* **373** (Jan, 1995) 225–228. <http://dx.doi.org/10.1038/373225a0>.
- [17] C. C. Tsuei, J. R. Kirtley, M. Rupp, J. Z. Sun, A. Gupta, M. B. Ketchen, C. A. Wang, Z. F. Ren, J. H. Wang, and M. Bhushan, “Pairing Symmetry in Single-Layer Tetragonal Tl₂Ba₂CuO_{β+δ} Superconductors,” *Science* **271** no. 5247, (1996) 329–332. <http://science.sciencemag.org/content/271/5247/329>.
- [18] P. J. Hirschfeld, M. M. Korshunov, and I. I. Mazin, “Gap symmetry and structure of Fe-based superconductors,” *Reports on Progress in Physics* **74** no. 12, (2011) 124508. <http://stacks.iop.org/0034-4885/74/i=12/a=124508>.
- [19] J. Paglione and R. L. Greene, “High-temperature superconductivity in iron-based materials,” *Nature Physics* **6** (Sep, 2010) 645–658. <http://dx.doi.org/10.1038/nphys1759>.

- [20] D. C. Johnston, “The puzzle of high temperature superconductivity in layered iron pnictides and chalcogenides,” *Advances in Physics* **59** no. 6, (2010) 803–1061.
<http://dx.doi.org/10.1080/00018732.2010.513480>.
- [21] P. C. Canfield and S. L. Bud’ko, “FeAs-Based Superconductivity: A Case Study of the Effects of Transition Metal Doping on BaFe₂As₂,” *Annual Review of Condensed Matter Physics* **1** no. 1, (2010) 27–50.
<http://dx.doi.org/10.1146/annurev-conmatphys-070909-104041>.
- [22] K. Ishida, Y. Nakai, and H. Hosono, “To what extent iron-pnictide new superconductors have been clarified: A progress report,” *Journal of the Physical Society of Japan* **78** no. 6, (2009) 062001,
<http://dx.doi.org/10.1143/JPSJ.78.062001>.
<http://dx.doi.org/10.1143/JPSJ.78.062001>.
- [23] H.-H. Wen and S. Li, “Materials and Novel Superconductivity in Iron Pnictide Superconductors,” *Annual Review of Condensed Matter Physics* **2** no. 1, (2011) 121–140. <http://dx.doi.org/10.1146/annurev-conmatphys-062910-140518>.
- [24] R. M. Fernandes, A. V. Chubukov, and J. Schmalian, “What drives nematic order in iron-based superconductors?,” *Nature Physics* **10** (Feb, 2014) 97–104.
<http://dx.doi.org/10.1038/nphys2877>.
- [25] P. J. Hirschfeld, D. Altenfeld, I. Eremin, and I. I. Mazin, “Robust determination of the superconducting gap sign structure via quasiparticle interference,” *Phys. Rev. B* **92** (Nov, 2015) 184513.
<http://link.aps.org/doi/10.1103/PhysRevB.92.184513>.
- [26] M. Nielsen and I. Chuang, *Quantum Computation and Quantum Information: 10th Anniversary Edition*. Cambridge University Press, 2010.
<https://books.google.dk/books?id=-s4DEy7o-a0C>.
- [27] J. D. Sau, R. M. Lutchyn, S. Tewari, and S. Das Sarma, “Generic new platform for topological quantum computation using semiconductor heterostructures,” *Phys. Rev. Lett.* **104** (Jan, 2010) 040502.
<http://link.aps.org/doi/10.1103/PhysRevLett.104.040502>.
- [28] R. M. Lutchyn, J. D. Sau, and S. Das Sarma, “Majorana fermions and a topological phase transition in semiconductor-superconductor heterostructures,” *Phys. Rev. Lett.* **105** (Aug, 2010) 077001.
<http://link.aps.org/doi/10.1103/PhysRevLett.105.077001>.
- [29] Y. Oreg, G. Refael, and F. von Oppen, “Helical liquids and majorana bound states in quantum wires,” *Phys. Rev. Lett.* **105** (Oct, 2010) 177002.
<http://link.aps.org/doi/10.1103/PhysRevLett.105.177002>.

- [30] M. Kjaergaard, K. Wölms, and K. Flensberg, “Majorana fermions in superconducting nanowires without spin-orbit coupling,” *Phys. Rev. B* **85** (Jan, 2012) 020503. <http://link.aps.org/doi/10.1103/PhysRevB.85.020503>.
- [31] S. Nadj-Perge, I. K. Drozdov, B. A. Bernevig, and A. Yazdani, “Proposal for realizing majorana fermions in chains of magnetic atoms on a superconductor,” *Phys. Rev. B* **88** (Jul, 2013) 020407. <http://link.aps.org/doi/10.1103/PhysRevB.88.020407>.
- [32] F. Waßer, A. Schneidewind, Y. Sidis, S. Wurmehl, S. Aswartham, B. Büchner, and M. Braden, “Spin reorientation in $\text{Ba}_{0.65}\text{Na}_{0.35}\text{Fe}_2\text{As}_2$ studied by single-crystal neutron diffraction,” *Phys. Rev. B* **91** (Feb, 2015) 060505. <http://link.aps.org/doi/10.1103/PhysRevB.91.060505>.
- [33] D. D. Khalyavin, S. W. Lovesey, P. Manuel, F. Krüger, S. Rosenkranz, J. M. Allred, O. Chmaissem, and R. Osborn, “Symmetry of reentrant tetragonal phase in $\text{Ba}_{1-x}\text{Na}_x\text{Fe}_2\text{As}_2$: Magnetic versus orbital ordering mechanism,” *Phys. Rev. B* **90** (Nov, 2014) 174511. <http://link.aps.org/doi/10.1103/PhysRevB.90.174511>.
- [34] J. M. Allred, S. Avci, D. Y. Chung, H. Claus, D. D. Khalyavin, P. Manuel, K. M. Taddei, M. G. Kanatzidis, S. Rosenkranz, R. Osborn, and O. Chmaissem, “Tetragonal magnetic phase in $\text{Ba}_{1-x}\text{K}_x\text{Fe}_2\text{As}_2$ from x-ray and neutron diffraction,” *Phys. Rev. B* **92** (Sep, 2015) 094515. <http://link.aps.org/doi/10.1103/PhysRevB.92.094515>.
- [35] J. M. Allred, K. M. Taddei, D. E. Bugaris, M. J. Krogstad, S. H. Lapidus, D. Y. Chung, H. Claus, M. G. Kanatzidis, D. E. Brown, J. Kang, R. M. Fernandes, I. Eremin, S. Rosenkranz, O. Chmaissem, and R. Osborn, “Double-Q spin-density wave in iron arsenide superconductors,” *Nature Physics* **12** (May, 2016) 493–498. <http://dx.doi.org/10.1038/nphys3629>.
- [36] Z. Xu, C. Stock, S. Chi, A. I. Kolesnikov, G. Xu, G. Gu, and J. M. Tranquada, “Neutron-Scattering Evidence for a Periodically Modulated Superconducting Phase in the Underdoped Cuprate $\text{La}_{1.905}\text{Ba}_{0.095}\text{CuO}_4$,” *Phys. Rev. Lett.* **113** (Oct, 2014) 177002. <http://link.aps.org/doi/10.1103/PhysRevLett.113.177002>.
- [37] R. M. Fernandes and A. V. Chubukov, “Low-energy microscopic models for iron-based superconductors: a review,” *Reports on Progress in Physics* **80** no. 1, (2017) 014503. <http://stacks.iop.org/0034-4885/80/i=1/a=014503>.
- [38] H. Kontani and S. Onari, “Orbital-Fluctuation-Mediated Superconductivity in Iron Pnictides: Analysis of the Five-Orbital Hubbard-Holstein Model,” *Phys. Rev. Lett.* **104** (Apr, 2010) 157001. <http://link.aps.org/doi/10.1103/PhysRevLett.104.157001>.
- [39] E. Abrahams and Q. Si, “Quantum criticality in the iron pnictides and chalcogenides,” *Journal of Physics: Condensed Matter* **23** no. 22, (2011) 223201. <http://stacks.iop.org/0953-8984/23/i=22/a=223201>.

- [40] Q. Si, R. Yu, and E. Abrahams, “High-temperature superconductivity in iron pnictides and chalcogenides,” *Nature Reviews Materials* **1** (Mar, 2016) 16017 EP –. <http://dx.doi.org/10.1038/natrevmats.2016.17>. Review Article.
- [41] L. W. Harriger, H. Q. Luo, M. S. Liu, C. Frost, J. P. Hu, M. R. Norman, and P. Dai, “Nematic spin fluid in the tetragonal phase of BaFe₂As₂,” *Phys. Rev. B* **84** (Aug, 2011) 054544. <http://link.aps.org/doi/10.1103/PhysRevB.84.054544>.
- [42] A. Georges, L. de’ Medici, and J. Mravlje, “Strong Correlations from Hund’s Coupling,” *Annual Review of Condensed Matter Physics* **4** no. 1, (2013) 137–178. <http://dx.doi.org/10.1146/annurev-conmatphys-020911-125045>.
- [43] P. Chandra, P. Coleman, and A. I. Larkin, “Ising transition in frustrated Heisenberg models,” *Phys. Rev. Lett.* **64** (Jan, 1990) 88–91. <http://link.aps.org/doi/10.1103/PhysRevLett.64.88>.
- [44] F. Krüger, S. Kumar, J. Zaanen, and J. van den Brink, “Spin-orbital frustrations and anomalous metallic state in iron-pnictide superconductors,” *Phys. Rev. B* **79** (Feb, 2009) 054504. <http://link.aps.org/doi/10.1103/PhysRevB.79.054504>.
- [45] W. Lv, F. Krüger, and P. Phillips, “Orbital ordering and unfrustrated ($\pi, 0$) magnetism from degenerate double exchange in the iron pnictides,” *Phys. Rev. B* **82** (Jul, 2010) 045125. <http://link.aps.org/doi/10.1103/PhysRevB.82.045125>.
- [46] C. Fang, H. Yao, W.-F. Tsai, J. Hu, and S. A. Kivelson, “Theory of electron nematic order in LaFeAsO,” *Phys. Rev. B* **77** (Jun, 2008) 224509. <http://link.aps.org/doi/10.1103/PhysRevB.77.224509>.
- [47] R. M. Fernandes, A. V. Chubukov, J. Knolle, I. Eremin, and J. Schmalian, “Preemptive nematic order, pseudogap, and orbital order in the iron pnictides,” *Phys. Rev. B* **85** (Jan, 2012) 024534. <http://link.aps.org/doi/10.1103/PhysRevB.85.024534>.
- [48] N. Ni, M. E. Tillman, J.-Q. Yan, A. Kracher, S. T. Hannahs, S. L. Bud’ko, and P. C. Canfield, “Effects of Co substitution on thermodynamic and transport properties and anisotropic H_{c2} in Ba(Fe_{1-x}Co_x)₂As₂ single crystals,” *Phys. Rev. B* **78** (Dec, 2008) 214515. <http://link.aps.org/doi/10.1103/PhysRevB.78.214515>.
- [49] J.-H. Chu, J. G. Analytis, K. De Greve, P. L. McMahon, Z. Islam, Y. Yamamoto, and I. R. Fisher, “In-Plane Resistivity Anisotropy in an Underdoped Iron Arsenide Superconductor,” *Science* **329** no. 5993, (2010) 824–826. <http://science.sciencemag.org/content/329/5993/824>.
- [50] J.-H. Chu, H.-H. Kuo, J. G. Analytis, and I. R. Fisher, “Divergent Nematic Susceptibility in an Iron Arsenide Superconductor,” *Science* **337** no. 6095, (2012) 710–712. <http://science.sciencemag.org/content/337/6095/710>.

- [51] S. Avci, O. Chmaissem, J. Allred, S. Rosenkranz, I. Eremin, A. Chubukov, D. Bugaris, D. Chung, M. Kanatzidis, J.-P. Castellán, J. Schlueter, H. Claus, D. Khalyavin, P. Manuel, A. Daoud-Aladine, and R. Osborn, “Magnetically driven suppression of nematic order in an iron-based superconductor,” *Nature Communications* **5** (May, 2014) . <http://dx.doi.org/10.1038/ncomms4845>.
- [52] A. E. Böhmer, F. Hardy, L. Wang, T. Wolf, P. Schweiss, and C. Meingast, “Superconductivity-induced re-entrance of the orthorhombic distortion in $\text{Ba}_{1-x}\text{K}_x\text{Fe}_2\text{As}_2$,” *Nature Communications* **6** (Jul, 2015) . <http://dx.doi.org/10.1038/ncomms8911>.
- [53] I. I. Mazin and M. D. Johannes, “A key role for unusual spin dynamics in ferropnictides,” *Nature Physics* **5** (Feb, 2009) 141–145. <http://dx.doi.org/10.1038/nphys1160>.
- [54] S.-H. Baek, D. V. Efremov, J. M. Ok, J. S. Kim, J. van den Brink, and B. BÄ¼chner, “Orbital-driven nematicity in FeSe,” *Nature Materials* **14** (Feb, 2015) 210–214. <http://dx.doi.org/10.1038/nmat4138>.
- [55] M. D. Watson, T. K. Kim, L. C. Rhodes, M. Eschrig, M. Hoesch, A. A. Haghighirad, and A. I. Coldea, “Evidence for unidirectional nematic bond ordering in FeSe,” *Phys. Rev. B* **94** (Nov, 2016) 201107. <http://link.aps.org/doi/10.1103/PhysRevB.94.201107>.
- [56] D. D. Scherer, A. Jacko, C. Friedrich, E. Sasioglu, S. Blugel, R. Valenti, and B. M. Andersen, “Interplay of nematic and magnetic orders in FeSe under pressure,” *ArXiv e-prints* (Dec., 2016) , [arXiv:1612.06085](https://arxiv.org/abs/1612.06085) [cond-mat.supr-con].
- [57] A. V. Chubukov, M. Khodas, and R. M. Fernandes, “Magnetism, Superconductivity, and Spontaneous Orbital Order in Iron-Based Superconductors: Which Comes First and Why?,” *Phys. Rev. X* **6** (Dec, 2016) 041045. <http://link.aps.org/doi/10.1103/PhysRevX.6.041045>.
- [58] N. Goldenfeld, *Lectures on Phase Transitions and the Renormalization Group*. Frontiers in physics. Addison-Wesley, Advanced Book Program, 1992. https://books.google.dk/books?id=DdB1__nl7CYC.
- [59] K. G. Wilson and J. Kogut, “The renormalization group and the ϵ expansion,” *Physics Reports* **12** no. 2, (1974) 75 – 199. <http://www.sciencedirect.com/science/article/pii/0370157374900234>.
- [60] J. Wang, G.-Z. Liu, D. V. Efremov, and J. van den Brink, “Order parameter fluctuation and ordering competition in $\text{Ba}_{1-x}\text{K}_x\text{Fe}_2\text{As}_2$,” *ArXiv e-prints* (Aug., 2016) , [arXiv:1608.07935](https://arxiv.org/abs/1608.07935) [cond-mat.str-el].
- [61] H. Ikeda, R. Arita, and J. Kuneš, “Phase diagram and gap anisotropy in iron-pnictide superconductors,” *Phys. Rev. B* **81** (Feb, 2010) 054502. <http://link.aps.org/doi/10.1103/PhysRevB.81.054502>.

- [62] S. Graser, A. F. Kemper, T. A. Maier, H.-P. Cheng, P. J. Hirschfeld, and D. J. Scalapino, “Spin fluctuations and superconductivity in a three-dimensional tight-binding model for BaFe_2As_2 ,” *Phys. Rev. B* **81** (Jun, 2010) 214503. <http://link.aps.org/doi/10.1103/PhysRevB.81.214503>.
- [63] D. Lu, M. Yi, S.-K. Mo, J. Analytis, J.-H. Chu, A. Erickson, D. Singh, Z. Hussain, T. Geballe, I. Fisher, and Z.-X. Shen, “{ARPES} studies of the electronic structure of $\text{LaOFe}(\text{p}, \text{as})$,” *Physica C: Superconductivity* **469** no. 9, (2009) 7. <http://www.sciencedirect.com/science/article/pii/S092145340900080X>. Superconductivity in Iron-Pnictides.
- [64] I. Eremin and A. V. Chubukov, “Magnetic degeneracy and hidden metallicity of the spin-density-wave state in ferropnictides,” *Phys. Rev. B* **81** (Jan, 2010) 024511. <http://link.aps.org/doi/10.1103/PhysRevB.81.024511>.
- [65] V. Cvetkovic and O. Vafek, “Space group symmetry, spin-orbit coupling, and the low-energy effective Hamiltonian for iron-based superconductors,” *Phys. Rev. B* **88** (Oct, 2013) 134510. <http://link.aps.org/doi/10.1103/PhysRevB.88.134510>.
- [66] S. Graser, T. A. Maier, P. J. Hirschfeld, and D. J. Scalapino, “Near-degeneracy of several pairing channels in multiorbital models for the Fe pnictides,” *New Journal of Physics* **11** no. 2, (2009) 025016. <http://stacks.iop.org/1367-2630/11/i=2/a=025016>.
- [67] M. J. Calderón, B. Valenzuela, and E. Bascones, “Tight-binding model for iron pnictides,” *Phys. Rev. B* **80** (Sep, 2009) 094531. <http://link.aps.org/doi/10.1103/PhysRevB.80.094531>.
- [68] L. Ortenzi, E. Cappelluti, L. Benfatto, and L. Pietronero, “Fermi-Surface Shrinking and Interband Coupling in Iron-Based Pnictides,” *Phys. Rev. Lett.* **103** (Jul, 2009) 046404. <http://link.aps.org/doi/10.1103/PhysRevLett.103.046404>.
- [69] E. M. Nica, R. Yu, and Q. Si, “Glide reflection symmetry, Brillouin zone folding, and superconducting pairing for the $P4/nmm$ space group,” *Phys. Rev. B* **92** (Nov, 2015) 174520. <http://link.aps.org/doi/10.1103/PhysRevB.92.174520>.
- [70] A. V. Chubukov, D. V. Efremov, and I. Eremin, “Magnetism, superconductivity, and pairing symmetry in iron-based superconductors,” *Phys. Rev. B* **78** (Oct, 2008) 134512. <http://link.aps.org/doi/10.1103/PhysRevB.78.134512>.
- [71] A. B. Vorontsov, M. G. Vavilov, and A. V. Chubukov, “Superconductivity and spin-density waves in multiband metals,” *Phys. Rev. B* **81** (May, 2010) 174538. <http://link.aps.org/doi/10.1103/PhysRevB.81.174538>.
- [72] M. N. Gastiasoro and B. M. Andersen, “Competing magnetic double- Q phases and superconductivity-induced reentrance of C_2 magnetic stripe order in iron pnictides,” *Phys. Rev. B* **92** (Oct, 2015) 140506. <http://link.aps.org/doi/10.1103/PhysRevB.92.140506>.

- [73] M. Hoyer, R. M. Fernandes, A. Levchenko, and J. Schmalian, “Disorder-promoted C_4 -symmetric magnetic order in iron-based superconductors,” *Phys. Rev. B* **93** (Apr, 2016) 144414. <http://link.aps.org/doi/10.1103/PhysRevB.93.144414>.
- [74] R. M. Fernandes, L. H. VanBebber, S. Bhattacharya, P. Chandra, V. Keppens, D. Mandrus, M. A. McGuire, B. C. Sales, A. S. Sefat, and J. Schmalian, “Effects of Nematic Fluctuations on the Elastic Properties of Iron Arsenide Superconductors,” *Phys. Rev. Lett.* **105** (Oct, 2010) 157003. <http://link.aps.org/doi/10.1103/PhysRevLett.105.157003>.
- [75] A. I. Larkin and A. A. Varlamov, “Fluctuation Phenomena in Superconductors,” *arXiv:cond-mat/0109177* (Sept., 2001) , [cond-mat/0109177](http://arxiv.org/abs/cond-mat/0109177).
- [76] V. Cvetkovic and Z. Tesanovic, “Multiband magnetism and superconductivity in Fe-based compounds,” *EPL (Europhysics Letters)* **85** no. 3, (2009) 37002. <http://stacks.iop.org/0295-5075/85/i=3/a=37002>.
- [77] P. A. Lee and X.-G. Wen, “Spin-triplet p -wave pairing in a three-orbital model for iron pnictide superconductors,” *Phys. Rev. B* **78** (Oct, 2008) 144517. <http://link.aps.org/doi/10.1103/PhysRevB.78.144517>.
- [78] S. Mukherjee, A. Kreisel, P. J. Hirschfeld, and B. M. Andersen, “Model of Electronic Structure and Superconductivity in Orbitaly Ordered FeSe,” *Phys. Rev. Lett.* **115** (Jul, 2015) 026402. <http://link.aps.org/doi/10.1103/PhysRevLett.115.026402>.
- [79] X. Wang, J. Kang, and R. M. Fernandes, “Magnetic order without tetragonal-symmetry-breaking in iron arsenides: Microscopic mechanism and spin-wave spectrum,” *Phys. Rev. B* **91** (Jan, 2015) 024401. <http://link.aps.org/doi/10.1103/PhysRevB.91.024401>.
- [80] M. Wang, C. Zhang, X. Lu, G. Tan, H. Luo, Y. Song, M. Wang, X. Zhang, E. Goremychkin, T. Perring, T. Maier, Z. Yin, K. Haule, G. Kotliar, and P. Dai, “Doping dependence of spin excitations and its correlations with high-temperature superconductivity in iron pnictides,” *Nature Communications* **4** (Dec, 2013) . <http://dx.doi.org/10.1038/ncomms3874>.
- [81] A. B. Vorontsov, M. G. Vavilov, and A. V. Chubukov, “Interplay between magnetism and superconductivity in the iron pnictides,” *Phys. Rev. B* **79** (Feb, 2009) 060508. <http://link.aps.org/doi/10.1103/PhysRevB.79.060508>.
- [82] D. K. Pratt, M. G. Kim, A. Kreyssig, Y. B. Lee, G. S. Tucker, A. Thaler, W. Tian, J. L. Zarestky, S. L. Bud’ko, P. C. Canfield, B. N. Harmon, A. I. Goldman, and R. J. McQueeney, “Incommensurate Spin-Density Wave Order in Electron-Doped BaFe₂As₂ Superconductors,” *Phys. Rev. Lett.* **106** (Jun, 2011) 257001. <http://link.aps.org/doi/10.1103/PhysRevLett.106.257001>.

- [83] H. Luo, R. Zhang, M. Laver, Z. Yamani, M. Wang, X. Lu, M. Wang, Y. Chen, S. Li, S. Chang, J. W. Lynn, and P. Dai, “Coexistence and Competition of the Short-Range Incommensurate Antiferromagnetic Order with the Superconducting State of $\text{BaFe}_{2-x}\text{Ni}_x\text{As}_2$,” *Phys. Rev. Lett.* **108** (Jun, 2012) 247002.
<http://link.aps.org/doi/10.1103/PhysRevLett.108.247002>.
- [84] N. Qureshi, P. Steffens, Y. Drees, A. C. Komarek, D. Lamago, Y. Sidis, L. Harnagea, H.-J. Grafe, S. Wurmehl, B. Büchner, and M. Braden, “Inelastic Neutron-Scattering Measurements of Incommensurate Magnetic Excitations on Superconducting LiFeAs Single Crystals,” *Phys. Rev. Lett.* **108** (Mar, 2012) 117001. <http://link.aps.org/doi/10.1103/PhysRevLett.108.117001>.
- [85] H. J. Schulz, “Incommensurate antiferromagnetism in the two-dimensional Hubbard model,” *Phys. Rev. Lett.* **64** (Mar, 1990) 1445–1448.
<http://link.aps.org/doi/10.1103/PhysRevLett.64.1445>.
- [86] Y. Ando and L. Fu, “Topological Crystalline Insulators and Topological Superconductors: From Concepts to Materials,” *Annual Review of Condensed Matter Physics* **6** no. 1, (2015) 361–381.
<http://dx.doi.org/10.1146/annurev-conmatphys-031214-014501>.
- [87] H. Nielsen and M. Ninomiya, “A no-go theorem for regularizing chiral fermions,” *Physics Letters B* **105** no. 2, (1981) 219 – 223.
<http://www.sciencedirect.com/science/article/pii/0370269381910261>.
- [88] A. Chubukov, “Pairing mechanism in fe-based superconductors,” *Annual Review of Condensed Matter Physics* **3** no. 1, (2012) 57–92,
<http://dx.doi.org/10.1146/annurev-conmatphys-020911-125055>.
<http://dx.doi.org/10.1146/annurev-conmatphys-020911-125055>.
- [89] P. Dai, J. Hu, and E. Dagotto, “Magnetism and its microscopic origin in iron-based high-temperature superconductors,” *Nature Physics* **8** (Oct, 2012) 709–718.
<http://dx.doi.org/10.1038/nphys2438>.
- [90] D. S. Inosov, “Spin fluctuations in iron pnictides and chalcogenides: From antiferromagnetism to superconductivity,” *Comptes Rendus Physique* **17** no. 1–2, (2016) 60–89.
<http://www.sciencedirect.com/science/article/pii/S1631070515000523>.
Iron-based superconductors / Supraconducteurs À base de fer.
- [91] C. Xu, M. Müller, and S. Sachdev, “Ising and spin orders in the iron-based superconductors,” *Phys. Rev. B* **78** (Jul, 2008) 020501.
<http://link.aps.org/doi/10.1103/PhysRevB.78.020501>.
- [92] Y. Kamiya, N. Kawashima, and C. D. Batista, “Dimensional crossover in the quasi-two-dimensional Ising- $\text{O}(3)$ model,” *Phys. Rev. B* **84** (Dec, 2011) 214429.
<http://link.aps.org/doi/10.1103/PhysRevB.84.214429>.

- [93] V. Cvetkovic and Z. Tesanovic, “Valley density-wave and multiband superconductivity in iron-based pnictide superconductors,” *Phys. Rev. B* **80** (Jul, 2009) 024512. <http://link.aps.org/doi/10.1103/PhysRevB.80.024512>.
- [94] P. M. R. Brydon and C. Timm, “Theory of the excitonic spin-density-wave state in iron pnictides,” *Phys. Rev. B* **79** (May, 2009) 180504. <http://link.aps.org/doi/10.1103/PhysRevB.79.180504>.
- [95] J. Lorenzana, G. Seibold, C. Ortix, and M. Grilli, “Competing Orders in FeAs Layers,” *Phys. Rev. Lett.* **101** (Oct, 2008) 186402. <http://link.aps.org/doi/10.1103/PhysRevLett.101.186402>.
- [96] M. Kovacic, M. H. Christensen, M. N. Gastiasoro, and B. M. Andersen, “Spin excitations in the nematic phase and the metallic stripe spin-density wave phase of iron pnictides,” *Phys. Rev. B* **91** (Feb, 2015) 064424. <http://link.aps.org/doi/10.1103/PhysRevB.91.064424>.
- [97] H.-H. Klauss, H. Luetkens, R. Klingeler, C. Hess, F. J. Litterst, M. Kraken, M. M. Korshunov, I. Eremin, S.-L. Drechsler, R. Khasanov, A. Amato, J. Hamann-Borrero, N. Leps, A. Kondrat, G. Behr, J. Werner, and B. Büchner, “Commensurate Spin Density Wave in LaFeAsO: A Local Probe Study,” *Phys. Rev. Lett.* **101** (Aug, 2008) 077005. <http://link.aps.org/doi/10.1103/PhysRevLett.101.077005>.
- [98] M. M. Korshunov and I. Eremin, “Doping evolution of itinerant magnetic fluctuations in Fe-based pnictides,” *EPL (Europhysics Letters)* **83** no. 6, (2008) 67003. <http://stacks.iop.org/0295-5075/83/i=6/a=67003>.
- [99] J. Knolle, I. Eremin, A. V. Chubukov, and R. Moessner, “Theory of itinerant magnetic excitations in the spin-density-wave phase of iron-based superconductors,” *Phys. Rev. B* **81** (Apr, 2010) 140506. <http://link.aps.org/doi/10.1103/PhysRevB.81.140506>.
- [100] W.-G. Yin, C.-C. Lee, and W. Ku, “Unified Picture for Magnetic Correlations in Iron-Based Superconductors,” *Phys. Rev. Lett.* **105** (Sep, 2010) 107004. <http://link.aps.org/doi/10.1103/PhysRevLett.105.107004>.
- [101] S. Ducatman, R. M. Fernandes, and N. B. Perkins, “Theory of the evolution of magnetic order in Fe_{1+y}Te compounds with increasing interstitial iron,” *Phys. Rev. B* **90** (Oct, 2014) 165123. <http://link.aps.org/doi/10.1103/PhysRevB.90.165123>.
- [102] M. D. Johannes and I. I. Mazin, “Microscopic origin of magnetism and magnetic interactions in ferropnictides,” *Phys. Rev. B* **79** (Jun, 2009) 220510. <http://link.aps.org/doi/10.1103/PhysRevB.79.220510>.
- [103] S. Liang, A. Moreo, and E. Dagotto, “Nematic State of Pnictides Stabilized by Interplay between Spin, Orbital, and Lattice Degrees of Freedom,” *Phys. Rev. Lett.*

- 111 (Jul, 2013) 047004.
<http://link.aps.org/doi/10.1103/PhysRevLett.111.047004>.
- [104] L. Fanfarillo, A. Cortijo, and B. Valenzuela, “Spin-orbital interplay and topology in the nematic phase of iron pnictides,” *Phys. Rev. B* **91** (Jun, 2015) 214515.
<http://link.aps.org/doi/10.1103/PhysRevB.91.214515>.
- [105] R. Applegate, R. R. P. Singh, C.-C. Chen, and T. P. Devereaux, “Phase transitions in spin-orbital models with spin-space anisotropies for iron pnictides: Monte Carlo simulations,” *Phys. Rev. B* **85** (Feb, 2012) 054411.
<http://link.aps.org/doi/10.1103/PhysRevB.85.054411>.
- [106] J. T. Park, G. Friemel, T. Loew, V. Hinkov, Y. Li, B. H. Min, D. L. Sun, A. Ivanov, A. Piovano, C. T. Lin, B. Keimer, Y. S. Kwon, and D. S. Inosov, “Similar zone-center gaps in the low-energy spin-wave spectra of $\text{Na}_{1-\delta}\text{FeAs}$ and BaFe_2As_2 ,” *Phys. Rev. B* **86** (Jul, 2012) 024437.
<http://link.aps.org/doi/10.1103/PhysRevB.86.024437>.
- [107] G. S. Tucker, R. M. Fernandes, D. K. Pratt, A. Thaler, N. Ni, K. Marty, A. D. Christianson, M. D. Lumsden, B. C. Sales, A. S. Sefat, S. L. Bud’ko, P. C. Canfield, A. Kreyssig, A. I. Goldman, and R. J. McQueeney, “Crossover from spin waves to diffusive spin excitations in underdoped $\text{Ba}(\text{Fe}_{1-x}\text{Co}_x)_2\text{As}_2$,” *Phys. Rev. B* **89** (May, 2014) 180503. <http://link.aps.org/doi/10.1103/PhysRevB.89.180503>.
- [108] Y. Song, L.-P. Regnault, C. Zhang, G. Tan, S. V. Carr, S. Chi, A. D. Christianson, T. Xiang, and P. Dai, “In-plane spin excitation anisotropy in the paramagnetic state of NaFeAs ,” *Phys. Rev. B* **88** (Oct, 2013) 134512.
<http://link.aps.org/doi/10.1103/PhysRevB.88.134512>.
- [109] H. Luo, M. Wang, C. Zhang, X. Lu, L.-P. Regnault, R. Zhang, S. Li, J. Hu, and P. Dai, “Spin Excitation Anisotropy as a Probe of Orbital Ordering in the Paramagnetic Tetragonal Phase of Superconducting $\text{BaFe}_{1.904}\text{Ni}_{0.096}\text{As}_2$,” *Phys. Rev. Lett.* **111** (Sep, 2013) 107006.
<http://link.aps.org/doi/10.1103/PhysRevLett.111.107006>.
- [110] R. M. Fernandes and O. Vafek, “Distinguishing spin-orbit coupling and nematic order in the electronic spectrum of iron-based superconductors,” *Phys. Rev. B* **90** (Dec, 2014) 214514. <http://link.aps.org/doi/10.1103/PhysRevB.90.214514>.
- [111] M. M. Korshunov, Y. N. Togushova, I. Eremin, and P. J. Hirschfeld, “Spin-Orbit Coupling in Fe-Based Superconductors,” *Journal of Superconductivity and Novel Magnetism* **26** no. 9, (2013) 2873–2874.
<http://dx.doi.org/10.1007/s10948-013-2212-6>.
- [112] S. V. Borisenko, D. V. Evtushinsky, Z.-H. Liu, I. Morozov, R. Kappenberger, S. Wurmehl, B. Buchner, A. N. Yaresko, T. K. Kim, M. Hoesch, T. Wolf, and N. D. Zhigadlo, “Direct observation of spin-orbit coupling in iron-based

- superconductors,” *Nature Physics* **12** (Apr, 2016) 311–317.
<http://dx.doi.org/10.1038/nphys3594>.
- [113] M. Nakajima, S. Ishida, K. Kihou, Y. Tomioka, T. Ito, Y. Yoshida, C. H. Lee, H. Kito, A. Iyo, H. Eisaki, K. M. Kojima, and S. Uchida, “Evolution of the optical spectrum with doping in $\text{Ba}(\text{Fe}_{1-x}\text{Co}_x)_2\text{As}_2$,” *Phys. Rev. B* **81** (Mar, 2010) 104528. <http://link.aps.org/doi/10.1103/PhysRevB.81.104528>.
- [114] A. Lucarelli, A. Dusza, F. Pfuner, P. Lerch, J. G. Analytis, J.-H. Chu, I. R. Fisher, and L. Degiorgi, “Charge dynamics of Co-doped BaFe_2As_2 ,” *New Journal of Physics* **12** no. 7, (2010) 073036.
<http://stacks.iop.org/1367-2630/12/i=7/a=073036>.
- [115] M. Daghofer, A. Nicholson, A. Moreo, and E. Dagotto, “Three orbital model for the iron-based superconductors,” *Phys. Rev. B* **81** (Jan, 2010) 014511.
<http://link.aps.org/doi/10.1103/PhysRevB.81.014511>.
- [116] F. Ahn.
- [117] R. M. Fernandes, S. A. Kivelson, and E. Berg, “Vestigial chiral and charge orders from bidirectional spin-density waves: Application to the iron-based superconductors,” *Phys. Rev. B* **93** (Jan, 2016) 014511.
<http://link.aps.org/doi/10.1103/PhysRevB.93.014511>.
- [118] G. Giovannetti, C. Ortix, M. Marsman, M. Capone, J. van den Brink, and J. Lorenzana, “Proximity of iron pnictide superconductors to a quantum tricritical point,” *Nature Communications* **2** (Jul, 2011) .
<http://dx.doi.org/10.1038/ncomms1407>.
- [119] J. Kang, X. Wang, A. V. Chubukov, and R. M. Fernandes, “Interplay between tetragonal magnetic order, stripe magnetism, and superconductivity in iron-based materials,” *Phys. Rev. B* **91** (Mar, 2015) 121104.
<http://link.aps.org/doi/10.1103/PhysRevB.91.121104>.
- [120] I. Paul, “Magnetoelastic Quantum Fluctuations and Phase Transitions in the Iron Superconductors,” *Phys. Rev. Lett.* **107** (Jul, 2011) 047004.
<http://link.aps.org/doi/10.1103/PhysRevLett.107.047004>.
- [121] B. P. P. Mallett, P. Marsik, M. Yazdi-Rizi, T. Wolf, A. E. Böhmer, F. Hardy, C. Meingast, D. Munzar, and C. Bernhard, “Infrared Study of the Spin Reorientation Transition and Its Reversal in the Superconducting State in Underdoped $\text{Ba}_{1-x}\text{K}_x\text{Fe}_2\text{As}_2$,” *Phys. Rev. Lett.* **115** (Jul, 2015) 027003.
<http://link.aps.org/doi/10.1103/PhysRevLett.115.027003>.
- [122] M. G. Kim, A. Kreyssig, A. Thaler, D. K. Pratt, W. Tian, J. L. Zarestky, M. A. Green, S. L. Bud’ko, P. C. Canfield, R. J. McQueeney, and A. I. Goldman, “Antiferromagnetic ordering in the absence of structural distortion in

- $\text{Ba}(\text{Fe}_{1-x}\text{Mn}_x)_2\text{As}_2$,” *Phys. Rev. B* **82** (Dec, 2010) 220503.
<http://link.aps.org/doi/10.1103/PhysRevB.82.220503>.
- [123] B. P. P. Mallett, Y. G. Pashkevich, A. Gusev, T. Wolf, and C. Bernhard, “Muon spin rotation study of the magnetic structure in the tetragonal antiferromagnetic state of weakly underdoped $\text{Ba}_{1-x}\text{K}_x\text{Fe}_2\text{As}_2$,” *EPL (Europhysics Letters)* **111** no. 5, (2015) 57001. <http://stacks.iop.org/0295-5075/111/i=5/a=57001>.
- [124] M. Capati, M. Grilli, and J. Lorenzana, “Nematic phase without Heisenberg physics in FeAs planes,” *Phys. Rev. B* **84** (Dec, 2011) 214520.
<http://link.aps.org/doi/10.1103/PhysRevB.84.214520>.
- [125] K. K. Ng and M. Sigrist, “The role of spin-orbit coupling for the superconducting state in Sr_2RuO_4 ,” *EPL (Europhysics Letters)* **49** no. 4, (2000) 473.
<http://stacks.iop.org/0295-5075/49/i=4/a=473>.
- [126] S. A. Kivelson, I. P. Bindloss, E. Fradkin, V. Oganesyan, J. M. Tranquada, A. Kapitulnik, and C. Howald, “How to detect fluctuating stripes in the high-temperature superconductors,” *Rev. Mod. Phys.* **75** (Oct, 2003) 1201–1241.
<http://link.aps.org/doi/10.1103/RevModPhys.75.1201>.
- [127] T.-M. Chuang, M. P. Allan, J. Lee, Y. Xie, N. Ni, S. L. Bud’ko, G. S. Boebinger, P. C. Canfield, and J. C. Davis, “Nematic Electronic Structure in the “Parent” State of the Iron-Based Superconductor $\text{Ca}(\text{Fe}_{1-x}\text{Co}_x)_2\text{As}_2$,” *Science* **327** no. 5962, (2010) 181–184. <http://science.sciencemag.org/content/327/5962/181>.
- [128] M. Yi, D. Lu, J.-H. Chu, J. G. Analytis, A. P. Sorini, A. F. Kemper, B. Moritz, S.-K. Mo, R. G. Moore, M. Hashimoto, W.-S. Lee, Z. Hussain, T. P. Devereaux, I. R. Fisher, and Z.-X. Shen, “Symmetry-breaking orbital anisotropy observed for detwinned $\text{Ba}(\text{Fe}_{1-x}\text{Co}_x)_2\text{As}_2$ above the spin density wave transition,” *Proceedings of the National Academy of Sciences* **108** no. 17, (2011) 6878–6883.
<http://www.pnas.org/content/108/17/6878.abstract>.
- [129] S. Kasahara, H. J. Shi, K. Hashimoto, S. Tonegawa, Y. Mizukami, T. Shibauchi, K. Sugimoto, T. Fukuda, T. Terashima, A. H. Nevidomskyy, and Y. Matsuda, “Electronic nematicity above the structural and superconducting transition in $\text{BaFe}_2(\text{As}_{1-x}\text{P}_x)_2$,” *Nature* **486** (Jun, 2012) 382–385.
<http://dx.doi.org/10.1038/nature11178>.
- [130] C. Mirri, A. Dusza, S. Bastelberger, M. Chinotti, L. Degiorgi, J.-H. Chu, H.-H. Kuo, and I. R. Fisher, “Origin of the Resistive Anisotropy in the Electronic Nematic Phase of BaFe_2As_2 Revealed by Optical Spectroscopy,” *Phys. Rev. Lett.* **115** (Sep, 2015) 107001.
<http://link.aps.org/doi/10.1103/PhysRevLett.115.107001>.
- [131] V. Hinkov, D. Haug, B. Fauqué, P. Bourges, Y. Sidis, A. Ivanov, C. Bernhard, C. T. Lin, and B. Keimer, “Electronic Liquid Crystal State in the

- High-Temperature Superconductor $\text{YBa}_2\text{Cu}_3\text{O}_{6.45}$,” *Science* **319** no. 5863, (2008) 597–600. <http://science.sciencemag.org/content/319/5863/597>.
- [132] R. Daou, J. Chang, D. LeBoeuf, O. Cyr-Choiniere, F. Laliberte, N. Doiron-Leyraud, B. J. Ramshaw, R. Liang, D. A. Bonn, W. N. Hardy, and L. Taillefer, “Broken rotational symmetry in the pseudogap phase of a high-Tc superconductor,” *Nature* **463** (Jan, 2010) 519–522. <http://dx.doi.org/10.1038/nature08716>.
- [133] M. J. Lawler, K. Fujita, J. Lee, A. R. Schmidt, Y. Kohsaka, C. K. Kim, H. Eisaki, S. Uchida, J. C. Davis, J. P. Sethna, and E.-A. Kim, “Intra-unit-cell electronic nematicity of the high-Tc copper-oxide pseudogap states,” *Nature* **466** (Jun, 2010) 347–351. <http://dx.doi.org/10.1038/nature09169>.
- [134] S. A. Kivelson, E. Fradkin, and V. J. Emery, “Electronic liquid-crystal phases of a doped Mott insulator,” *Nature (London)* **393** (Jun, 1998) 550–553. <http://dx.doi.org/10.1038/31177>.
- [135] L. Nie, G. Tarjus, and S. A. Kivelson, “Quenched disorder and vestigial nematicity in the pseudogap regime of the cuprates,” *Proceedings of the National Academy of Sciences* **111** no. 22, (2014) 7980–7985.
- [136] Y. Wang and A. Chubukov, “Charge-density-wave order with momentum $(2Q, 0)$ and $(0, 2Q)$ within the spin-fermion model: Continuous and discrete symmetry breaking, preemptive composite order, and relation to pseudogap in hole-doped cuprates,” *Phys. Rev. B* **90** (Jul, 2014) 035149. <http://link.aps.org/doi/10.1103/PhysRevB.90.035149>.
- [137] S. Okamoto, D. Sénéchal, M. Civelli, and A.-M. S. Tremblay, “Dynamical electronic nematicity from Mott physics,” *Phys. Rev. B* **82** (Nov, 2010) 180511. <http://link.aps.org/doi/10.1103/PhysRevB.82.180511>.
- [138] S.-Q. Su and T. A. Maier, “Coexistence of strong nematic and superconducting correlations in a two-dimensional Hubbard model,” *Phys. Rev. B* **84** (Dec, 2011) 220506. <http://link.aps.org/doi/10.1103/PhysRevB.84.220506>.
- [139] K. Kuroki, S. Onari, R. Arita, H. Usui, Y. Tanaka, H. Kontani, and H. Aoki, “Unconventional Pairing Originating from the Disconnected Fermi Surfaces of Superconducting $\text{LaFeAsO}_{1-x}\text{F}_x$,” *Phys. Rev. Lett.* **101** (Aug, 2008) 087004. <http://link.aps.org/doi/10.1103/PhysRevLett.101.087004>.
- [140] A. F. Kemper, T. A. Maier, S. Graser, H.-P. Cheng, P. J. Hirschfeld, and D. J. Scalapino, “Sensitivity of the superconducting state and magnetic susceptibility to key aspects of electronic structure in ferropnictides,” *New Journal of Physics* **12** no. 7, (2010) 073030. <http://stacks.iop.org/1367-2630/12/i=7/a=073030>.

- [141] A. V. Chubukov, R. M. Fernandes, and J. Schmalian, “Origin of nematic order in FeSe,” *Phys. Rev. B* **91** (May, 2015) 201105.
<http://link.aps.org/doi/10.1103/PhysRevB.91.201105>.
- [142] J. K. Glasbrenner, I. I. Mazin, H. O. Jeschke, P. J. Hirschfeld, R. M. Fernandes, and R. Valenti, “Effect of magnetic frustration on nematicity and superconductivity in iron chalcogenides,” *Nature Physics* **11** (Nov, 2015) 953–958.
<http://dx.doi.org/10.1038/nphys3434>.
- [143] F. Wang, S. A. Kivelson, and D.-H. Lee, “Nematicity and quantum paramagnetism in FeSe,” *Nature Physics* **11** (Nov, 2015) 959–963.
<http://dx.doi.org/10.1038/nphys3456>.
- [144] R. Yu and Q. Si, “Antiferroquadrupolar and Ising-Nematic Orders of a Frustrated Bilinear-Biquadratic Heisenberg Model and Implications for the Magnetism of FeSe,” *Phys. Rev. Lett.* **115** (Sep, 2015) 116401.
<http://link.aps.org/doi/10.1103/PhysRevLett.115.116401>.
- [145] Y. Yamakawa, S. Onari, and H. Kontani, “Nematicity and Magnetism in FeSe and Other Families of Fe-Based Superconductors,” *Phys. Rev. X* **6** (Jun, 2016) 021032.
<http://link.aps.org/doi/10.1103/PhysRevX.6.021032>.
- [146] H. Park, K. Haule, and G. Kotliar, “Magnetic Excitation Spectra in BaFe₂As₂: A Two-Particle Approach within a Combination of the Density Functional Theory and the Dynamical Mean-Field Theory Method,” *Phys. Rev. Lett.* **107** (Sep, 2011) 137007. <http://link.aps.org/doi/10.1103/PhysRevLett.107.137007>.
- [147] S. Onari and H. Kontani, “Self-consistent Vertex Correction Analysis for Iron-based Superconductors: Mechanism of Coulomb Interaction-Driven Orbital Fluctuations,” *Phys. Rev. Lett.* **109** (Sep, 2012) 137001.
<http://link.aps.org/doi/10.1103/PhysRevLett.109.137001>.
- [148] M. Khodas and A. Levchenko, “Raman scattering as a probe of nematic correlations,” *Phys. Rev. B* **91** (Jun, 2015) 235119.
<http://link.aps.org/doi/10.1103/PhysRevB.91.235119>.
- [149] H. Yamase and R. Zeyher, “Spin nematic fluctuations near a spin-density-wave phase,” *New Journal of Physics* **17** no. 7, (2015) 073030.
<http://stacks.iop.org/1367-2630/17/i=7/a=073030>.
- [150] Y. Gallais and I. Paul, “Charge nematicity and electronic Raman scattering in iron-based superconductors,” *Comptes Rendus Physique* **17** no. 1–2, (2016) 113–139.
<http://www.sciencedirect.com/science/article/pii/S1631070515001681>.
Iron-based superconductors / Supraconducteurs À base de fer.
- [151] V. Vildosola, L. Pourovskii, R. Arita, S. Biermann, and A. Georges, “Bandwidth and Fermi surface of iron oxypnictides: Covalency and sensitivity to structural

- changes,” *Phys. Rev. B* **78** (Aug, 2008) 064518.
<http://link.aps.org/doi/10.1103/PhysRevB.78.064518>.
- [152] R. M. Fernandes, M. G. Vavilov, and A. V. Chubukov, “Enhancement of T_c by disorder in underdoped iron pnictide superconductors,” *Phys. Rev. B* **85** (Apr, 2012) 140512. <http://link.aps.org/doi/10.1103/PhysRevB.85.140512>.
- [153] S. Liang, C. B. Bishop, A. Moreo, and E. Dagotto, “Isotropic in-plane quenched disorder and dilution induce a robust nematic state in electron-doped pnictides,” *Phys. Rev. B* **92** (Sep, 2015) 104512.
<http://link.aps.org/doi/10.1103/PhysRevB.92.104512>.
- [154] A. E. Böhrer, T. Arai, F. Hardy, T. Hattori, T. Iye, T. Wolf, H. v. Löhneysen, K. Ishida, and C. Meingast, “Origin of the Tetragonal-to-Orthorhombic Phase Transition in FeSe: A Combined Thermodynamic and NMR Study of Nematicity,” *Phys. Rev. Lett.* **114** (Jan, 2015) 027001.
<http://link.aps.org/doi/10.1103/PhysRevLett.114.027001>.
- [155] M. C. Rahn, R. A. Ewings, S. J. Sedlmaier, S. J. Clarke, and A. T. Boothroyd, “Strong $(\pi, 0)$ spin fluctuations in β – FeSe observed by neutron spectroscopy,” *Phys. Rev. B* **91** (May, 2015) 180501.
<http://link.aps.org/doi/10.1103/PhysRevB.91.180501>.
- [156] Q. Wang, Y. Shen, B. Pan, Y. Hao, M. Ma, F. Zhou, P. Steffens, K. Schmalzl, T. R. Forrest, M. Abdel-Hafiez, X. Chen, D. A. Chareev, A. N. Vasiliev, P. Bourges, Y. Sidis, H. Cao, and J. Zhao, “Strong interplay between stripe spin fluctuations, nematicity and superconductivity in FeSe,” *Nature Materials* **15** (Feb, 2016) 159–163. <http://dx.doi.org/10.1038/nmat4492>.
- [157] C.-C. Chen, B. Moritz, J. van den Brink, T. P. Devereaux, and R. R. P. Singh, “Finite-temperature spin dynamics and phase transitions in spin-orbital models,” *Phys. Rev. B* **80** (Nov, 2009) 180418.
<http://link.aps.org/doi/10.1103/PhysRevB.80.180418>.
- [158] W. Lv, J. Wu, and P. Phillips, “Orbital ordering induces structural phase transition and the resistivity anomaly in iron pnictides,” *Phys. Rev. B* **80** (Dec, 2009) 224506. <http://link.aps.org/doi/10.1103/PhysRevB.80.224506>.
- [159] C.-C. Lee, W.-G. Yin, and W. Ku, “Ferro-Orbital Order and Strong Magnetic Anisotropy in the Parent Compounds of Iron-Pnictide Superconductors,” *Phys. Rev. Lett.* **103** (Dec, 2009) 267001.
<http://link.aps.org/doi/10.1103/PhysRevLett.103.267001>.
- [160] Z. Wang and A. H. Nevidomskyy, “Orbital nematic order and interplay with magnetism in the two-orbital Hubbard model,” *Journal of Physics: Condensed Matter* **27** no. 22, (2015) 225602.
<http://stacks.iop.org/0953-8984/27/i=22/a=225602>.

- [161] H.-H. Wu, M. Buchholz, C. Trabant, C. Chang, A. Komarek, F. Heigl, M. Zimmermann, M. Cwik, F. Nakamura, M. Braden, and C. Schüßler-Langeheine, “Charge stripe order near the surface of 12-percent doped $\text{La}_{2-x}\text{Sr}_x\text{CuO}_4$,” *Nature Communications* **3** (Aug, 2012) . <http://dx.doi.org/10.1038/ncomms2019>.
- [162] E. Fradkin, S. A. Kivelson, and J. M. Tranquada, “*Colloquium* : Theory of intertwined orders in high temperature superconductors,” *Rev. Mod. Phys.* **87** (May, 2015) 457–482. <http://link.aps.org/doi/10.1103/RevModPhys.87.457>.
- [163] C. M. Varma, “Non-Fermi-liquid states and pairing instability of a general model of copper oxide metals,” *Phys. Rev. B* **55** (Jun, 1997) 14554–14580. <http://link.aps.org/doi/10.1103/PhysRevB.55.14554>.
- [164] Y. Li, V. Baledent, G. Yu, N. Barisic, K. Hradil, R. A. Mole, Y. Sidis, P. Steffens, X. Zhao, P. Bourges, and M. Greven, “Hidden magnetic excitation in the pseudogap phase of a high- T_c superconductor,” *Nature* **468** no. 7321, (Nov, 2010) 283–285. <http://dx.doi.org/10.1038/nature09477>.
- [165] C. Nayak, “Density-wave states of nonzero angular momentum,” *Phys. Rev. B* **62** (Aug, 2000) 4880–4889. <http://link.aps.org/doi/10.1103/PhysRevB.62.4880>.
- [166] S. Chakravarty, H.-Y. Kee, and K. Völker, “An explanation for a universality of transition temperatures in families of copper oxide superconductors,” *Nature* **428** (Mar, 2004) 53–55. <http://dx.doi.org/10.1038/nature02348>.
- [167] V. J. Emery, “Theory of high- t_c superconductivity in oxides,” *Phys. Rev. Lett.* **58** (Jun, 1987) 2794–2797. <http://link.aps.org/doi/10.1103/PhysRevLett.58.2794>.
- [168] C. Varma, S. Schmitt-Rink, and E. Abrahams, “Charge transfer excitations and superconductivity in “ionic” metals,” *Solid State Communications* **62** no. 10, (1987) 681 – 685. <http://www.sciencedirect.com/science/article/pii/0038109887904078>.
- [169] F. C. Zhang and T. M. Rice, “Effective hamiltonian for the superconducting cu oxides,” *Phys. Rev. B* **37** (Mar, 1988) 3759–3761. <http://link.aps.org/doi/10.1103/PhysRevB.37.3759>.
- [170] H. Eskes and G. A. Sawatzky, “Tendency towards local spin compensation of holes in the high- T_c copper compounds,” *Phys. Rev. Lett.* **61** (Sep, 1988) 1415–1418. <http://link.aps.org/doi/10.1103/PhysRevLett.61.1415>.
- [171] V. J. Emery and G. Reiter, “Quasiparticles in the copper-oxygen planes of high- T_c superconductors: An exact solution for a ferromagnetic background,” *Phys. Rev. B* **38** (Dec, 1988) 11938–11941. <http://link.aps.org/doi/10.1103/PhysRevB.38.11938>.

- [172] F. C. Zhang and T. M. Rice, “Validity of the $t - J$ model,” *Phys. Rev. B* **41** (Apr, 1990) 7243–7246. <http://link.aps.org/doi/10.1103/PhysRevB.41.7243>.
- [173] V. J. Emery and G. Reiter, “Reply to “validity of the $t - J$ model”,” *Phys. Rev. B* **41** (Apr, 1990) 7247–7249. <http://link.aps.org/doi/10.1103/PhysRevB.41.7247>.
- [174] G. Yu, Y. Li, E. M. Motoyama, and M. Greven, “A universal relationship between magnetic resonance and superconducting gap in unconventional superconductors,” *Nature Physics* **5** no. 12, (2009) 873–875.
- [175] S. Onari and H. Kontani, “Neutron inelastic scattering peak by dissipationless mechanism in the s_{++} -wave state in iron-based superconductors,” *Phys. Rev. B* **84** (Oct, 2011) 144518. <http://link.aps.org/doi/10.1103/PhysRevB.84.144518>.
- [176] J. M. Tranquada, B. J. Sternlieb, J. D. Axe, Y. Nakamura, and S. Uchida, “Evidence for stripe correlations of spins and holes in copper oxide superconductors,” *Nature (London)* **375** (Jun, 1995) 561–563. <http://dx.doi.org/10.1038/375561a0>.
- [177] J. M. Tranquada, J. D. Axe, N. Ichikawa, Y. Nakamura, S. Uchida, and B. Nachumi, “Neutron-scattering study of stripe-phase order of holes and spins in $\text{La}_{1.48}\text{Nd}_{0.4}\text{Sr}_{0.12}\text{CuO}_4$,” *Phys. Rev. B* **54** (Sep, 1996) 7489–7499. <http://link.aps.org/doi/10.1103/PhysRevB.54.7489>.
- [178] M. Fujita, H. Goka, K. Yamada, J. M. Tranquada, and L. P. Regnault, “Stripe order, depinning, and fluctuations in $\text{La}_{1.875}\text{Ba}_{0.125}\text{CuO}_4$ and $\text{La}_{1.875}\text{Ba}_{0.075}\text{Sr}_{0.050}\text{CuO}_4$,” *Phys. Rev. B* **70** (Sep, 2004) 104517. <http://link.aps.org/doi/10.1103/PhysRevB.70.104517>.
- [179] P. Abbamonte, A. Ruydi, S. Smadici, G. D. Gu, G. A. Sawatzky, and D. L. Feng, “Spatially modulated ‘Mottness’ in $\text{La}_{2-x}\text{Ba}_x\text{CuO}_4$,” *Nature Physics* **1** (Dec, 2005) 155–158. <http://dx.doi.org/10.1038/nphys178>.
- [180] K. Yamada, C. H. Lee, K. Kurahashi, J. Wada, S. Wakimoto, S. Ueki, H. Kimura, Y. Endoh, S. Hosoya, G. Shirane, R. J. Birgeneau, M. Greven, M. A. Kastner, and Y. J. Kim, “Doping dependence of the spatially modulated dynamical spin correlations and the superconducting-transition temperature in $\text{La}_{2-x}\text{Sr}_x\text{CuO}_4$,” *Phys. Rev. B* **57** (Mar, 1998) 6165–6172. <http://link.aps.org/doi/10.1103/PhysRevB.57.6165>.
- [181] A. R. Moodenbaugh, Y. Xu, M. Suenaga, T. J. Folkerts, and R. N. Shelton, “Superconducting properties of $\text{La}_{2-x}\text{Ba}_x\text{CuO}_4$,” *Phys. Rev. B* **38** (Sep, 1988) 4596–4600. <http://link.aps.org/doi/10.1103/PhysRevB.38.4596>.
- [182] M. Hücker, M. v. Zimmermann, G. D. Gu, Z. J. Xu, J. S. Wen, G. Xu, H. J. Kang, A. Zheludev, and J. M. Tranquada, “Stripe order in superconducting

- $\text{La}_{2-x}\text{Ba}_x\text{CuO}_4$ ($0.095 \leq x \leq 0.155$),” *Phys. Rev. B* **83** (Mar, 2011) 104506.
<http://link.aps.org/doi/10.1103/PhysRevB.83.104506>.
- [183] Q. Li, M. Hücker, G. D. Gu, A. M. Tsvelik, and J. M. Tranquada, “Two-Dimensional Superconducting Fluctuations in Stripe-Ordered $\text{La}_{1.875}\text{Ba}_{0.125}\text{CuO}_4$,” *Phys. Rev. Lett.* **99** (Aug, 2007) 067001.
<http://link.aps.org/doi/10.1103/PhysRevLett.99.067001>.
- [184] E. Berg, E. Fradkin, E.-A. Kim, S. A. Kivelson, V. Oganesyan, J. M. Tranquada, and S. C. Zhang, “Dynamical Layer Decoupling in a Stripe-Ordered High- T_c Superconductor,” *Phys. Rev. Lett.* **99** (Sep, 2007) 127003.
<http://link.aps.org/doi/10.1103/PhysRevLett.99.127003>.
- [185] E. Berg, E. Fradkin, and S. A. Kivelson, “Theory of the striped superconductor,” *Phys. Rev. B* **79** (Feb, 2009) 064515.
<http://link.aps.org/doi/10.1103/PhysRevB.79.064515>.
- [186] M. H. Hamidian, S. D. Edkins, S. H. Joo, A. Kostin, H. Eisaki, S. Uchida, M. J. Lawler, E.-A. Kim, A. P. Mackenzie, K. Fujita, J. Lee, and J. C. S. Davis, “Detection of a Cooper-pair density wave in $\text{Bi}_2\text{Sr}_2\text{CaCu}_2\text{O}_{8+x}$,” *Nature* **532** no. 7599, (Apr, 2016) 343–347. <http://dx.doi.org/10.1038/nature17411>. Letter.
- [187] D. J. Scalapino, “A common thread: The pairing interaction for unconventional superconductors,” *Rev. Mod. Phys.* **84** (Oct, 2012) 1383–1417.
<http://link.aps.org/doi/10.1103/RevModPhys.84.1383>.
- [188] N. F. Berk and J. R. Schrieffer, “Effect of Ferromagnetic Spin Correlations on Superconductivity,” *Phys. Rev. Lett.* **17** (Aug, 1966) 433–435.
<http://link.aps.org/doi/10.1103/PhysRevLett.17.433>.
- [189] H.-H. Klauss, W. Wagener, M. Hillberg, W. Kopmann, H. Walf, F. J. Litterst, M. Hücker, and B. Büchner, “From Antiferromagnetic Order to Static Magnetic Stripes: The Phase Diagram of $(\text{La}, \text{Eu})_{2-x}\text{Sr}_x\text{CuO}_4$,” *Phys. Rev. Lett.* **85** (Nov, 2000) 4590–4593. <http://link.aps.org/doi/10.1103/PhysRevLett.85.4590>.
- [190] J. Fink, E. Schierle, E. Weschke, J. Geck, D. Hawthorn, V. Soltwisch, H. Wadati, H.-H. Wu, H. A. Dürr, N. Wizen, B. Büchner, and G. A. Sawatzky, “Charge ordering in $\text{La}_{1.8-x}\text{Eu}_{0.2}\text{Sr}_x\text{CuO}_4$ studied by resonant soft x-ray diffraction,” *Phys. Rev. B* **79** (Mar, 2009) 100502.
<http://link.aps.org/doi/10.1103/PhysRevB.79.100502>.
- [191] J. Brooks and J. Schrieffer, *Handbook of High-Temperature Superconductivity: Theory and Experiment*. Springer New York, 2007.
https://books.google.dk/books?id=nLJFc_gDexcC.

- [192] M. Vojta, “Lattice symmetry breaking in cuprate superconductors: stripes, nematics, and superconductivity,” *Advances in Physics* **58** no. 6, (2009) 699–820. <http://dx.doi.org/10.1080/00018730903122242>.
- [193] M. Eschrig, “The effect of collective spin-1 excitations on electronic spectra in high-Tc superconductors,” *Advances in Physics* **55** no. 1-2, (2006) 47–183. <http://dx.doi.org/10.1080/00018730600645636>.
- [194] D. F. Agterberg and H. Tsunetsugu, “Dislocations and vortices in pair-density-wave superconductors,” *Nature Physics* **4** (Aug, 2008) 639–642. <http://dx.doi.org/10.1038/nphys999>.
- [195] S. Baruch and D. Orgad, “Spectral signatures of modulated d -wave superconducting phases,” *Phys. Rev. B* **77** (May, 2008) 174502. <http://link.aps.org/doi/10.1103/PhysRevB.77.174502>.
- [196] A. Himeda, T. Kato, and M. Ogata, “Stripe States with Spatially Oscillating d -Wave Superconductivity in the Two-Dimensional t - t' - J Model,” *Phys. Rev. Lett.* **88** (Feb, 2002) 117001. <http://link.aps.org/doi/10.1103/PhysRevLett.88.117001>.
- [197] M. Raczkowski, M. Capello, D. Poilblanc, R. Frésard, and A. M. Oleś, “Unidirectional d -wave superconducting domains in the two-dimensional t - j model,” *Phys. Rev. B* **76** (Oct, 2007) 140505. <http://link.aps.org/doi/10.1103/PhysRevB.76.140505>.
- [198] K.-Y. Yang, W. Q. Chen, T. M. Rice, M. Sigrist, and F.-C. Zhang, “Nature of stripes in the generalized t - j model applied to the cuprate superconductors,” *New Journal of Physics* **11** no. 5, (2009) 055053. <http://stacks.iop.org/1367-2630/11/i=5/a=055053>.
- [199] P. Corboz, T. M. Rice, and M. Troyer, “Competing States in the t - J Model: Uniform d -Wave State versus Stripe State,” *Phys. Rev. Lett.* **113** (Jul, 2014) 046402. <http://link.aps.org/doi/10.1103/PhysRevLett.113.046402>.
- [200] F. Loder, A. P. Kampf, and T. Kopp, “Superconducting state with a finite-momentum pairing mechanism in zero external magnetic field,” *Phys. Rev. B* **81** (Jan, 2010) 020511. <http://link.aps.org/doi/10.1103/PhysRevB.81.020511>.
- [201] F. Loder, S. Graser, A. P. Kampf, and T. Kopp, “Mean-Field Pairing Theory for the Charge-Stripe Phase of High-Temperature Cuprate Superconductors,” *Phys. Rev. Lett.* **107** (Oct, 2011) 187001. <http://link.aps.org/doi/10.1103/PhysRevLett.107.187001>.
- [202] F. Loder, S. Graser, M. Schmid, A. P. Kampf, and T. Kopp, “Modeling of superconducting stripe phases in high-Tc cuprates,” *New Journal of Physics* **13** no. 11, (2011) 113037. <http://stacks.iop.org/1367-2630/13/i=11/a=113037>.

- [203] P. A. Lee, “Amperean Pairing and the Pseudogap Phase of Cuprate Superconductors,” *Phys. Rev. X* **4** (Jul, 2014) 031017.
<http://link.aps.org/doi/10.1103/PhysRevX.4.031017>.
- [204] C. Pépin, V. S. de Carvalho, T. Kloss, and X. Montiel, “Pseudogap, charge order, and pairing density wave at the hot spots in cuprate superconductors,” *Phys. Rev. B* **90** (Nov, 2014) 195207.
<http://link.aps.org/doi/10.1103/PhysRevB.90.195207>.
- [205] H. Freire, V. S. de Carvalho, and C. Pépin, “Renormalization group analysis of the pair-density-wave and charge order within the fermionic hot-spot model for cuprate superconductors,” *Phys. Rev. B* **92** (Jul, 2015) 045132.
<http://link.aps.org/doi/10.1103/PhysRevB.92.045132>.
- [206] Y. Wang, D. F. Agterberg, and A. Chubukov, “Coexistence of Charge-Density-Wave and Pair-Density-Wave Orders in Underdoped Cuprates,” *Phys. Rev. Lett.* **114** (May, 2015) 197001.
<http://link.aps.org/doi/10.1103/PhysRevLett.114.197001>.
- [207] Y. Wang, D. F. Agterberg, and A. Chubukov, “Interplay between pair- and charge-density-wave orders in underdoped cuprates,” *Phys. Rev. B* **91** (Mar, 2015) 115103. <http://link.aps.org/doi/10.1103/PhysRevB.91.115103>.
- [208] J.-X. Zhu, I. Martin, and A. R. Bishop, “Spin and Charge Order around Vortices and Impurities in High- T_c Superconductors,” *Phys. Rev. Lett.* **89** (Jul, 2002) 067003. <http://link.aps.org/doi/10.1103/PhysRevLett.89.067003>.
- [209] Y. Chen and C. S. Ting, “States of Local Moment Induced by Nonmagnetic Impurities in Cuprate Superconductors,” *Phys. Rev. Lett.* **92** (Feb, 2004) 077203. <http://link.aps.org/doi/10.1103/PhysRevLett.92.077203>.
- [210] B. M. Andersen and P. Hedegård, “Spin Dynamics in the Stripe Phase of the Cuprate Superconductors,” *Phys. Rev. Lett.* **95** (Jul, 2005) 037002. <http://link.aps.org/doi/10.1103/PhysRevLett.95.037002>.
- [211] B. M. Andersen, S. Graser, and P. J. Hirschfeld, “Disorder-Induced Freezing of Dynamical Spin Fluctuations in Underdoped Cuprate Superconductors,” *Phys. Rev. Lett.* **105** (Sep, 2010) 147002. <http://link.aps.org/doi/10.1103/PhysRevLett.105.147002>.
- [212] B. Dalla Piazza, M. Mourigal, N. B. Christensen, G. J. Nilsen, P. Tregenna-Piggott, T. G. Perring, M. Enderle, D. F. McMorrow, D. A. Ivanov, and H. M. Rønnow, “Fractional excitations in the square-lattice quantum antiferromagnet,” *Nature Physics* **11** (Jan, 2015) 62–68. <http://dx.doi.org/10.1038/nphys3172>.
- [213] B. M. Andersen, A. Melikyan, T. S. Nunner, and P. J. Hirschfeld, “Andreev States near Short-Ranged Pairing Potential Impurities,” *Phys. Rev. Lett.* **96** (Mar, 2006) 097004. <http://link.aps.org/doi/10.1103/PhysRevLett.96.097004>.

- [214] F. Krüger and S. Scheidl, “Spin dynamics of stripes,” *Phys. Rev. B* **67** (Apr, 2003) 134512. <http://link.aps.org/doi/10.1103/PhysRevB.67.134512>.
- [215] G. Seibold and J. Lorenzana, “Doping dependence of spin excitations in the stripe phase of high- T_c superconductors,” *Phys. Rev. B* **73** (Apr, 2006) 144515. <http://link.aps.org/doi/10.1103/PhysRevB.73.144515>.
- [216] D. X. Yao, E. W. Carlson, and D. K. Campbell, “Magnetic excitations of stripes and checkerboards in the cuprates,” *Phys. Rev. B* **73** (Jun, 2006) 224525. <http://link.aps.org/doi/10.1103/PhysRevB.73.224525>.
- [217] A. W. Harrow, A. Hassidim, and S. Lloyd, “Quantum Algorithm for Linear Systems of Equations,” *Phys. Rev. Lett.* **103** (Oct, 2009) 150502. <http://link.aps.org/doi/10.1103/PhysRevLett.103.150502>.
- [218] C. Nayak, S. H. Simon, A. Stern, M. Freedman, and S. Das Sarma, “Non-Abelian anyons and topological quantum computation,” *Rev. Mod. Phys.* **80** (Sep, 2008) 1083–1159. <http://link.aps.org/doi/10.1103/RevModPhys.80.1083>.
- [219] E. Majorana, “Teoria simmetrica dell’elettrone e del positrone,” *Il Nuovo Cimento* **14** no. 4, (1937) 171. <http://dx.doi.org/10.1007/BF02961314>.
- [220] S. R. Elliott and M. Franz, “*Colloquium* : Majorana fermions in nuclear, particle, and solid-state physics,” *Rev. Mod. Phys.* **87** (Feb, 2015) 137–163. <http://link.aps.org/doi/10.1103/RevModPhys.87.137>.
- [221] F. Wilczek, “Majorana returns,” *Nature Physics* **5** (Sep, 2009) 614–618. <http://dx.doi.org/10.1038/nphys1380>.
- [222] G. Moore and N. Read, “Nonabelions in the fractional quantum hall effect,” *Nuclear Physics B* **360** no. 2, (1991) 362 – 396. <http://www.sciencedirect.com/science/article/pii/0550321391904070>.
- [223] N. Read and D. Green, “Paired states of fermions in two dimensions with breaking of parity and time-reversal symmetries and the fractional quantum Hall effect,” *Phys. Rev. B* **61** (Apr, 2000) 10267–10297. <http://link.aps.org/doi/10.1103/PhysRevB.61.10267>.
- [224] A. Y. Kitaev, “Unpaired majorana fermions in quantum wires,” *Physics-Uspekhi* **44** no. 10S, (2001) 131. <http://stacks.iop.org/1063-7869/44/i=10S/a=S29>.
- [225] C. L. Kane and E. J. Mele, “Quantum Spin Hall Effect in Graphene,” *Phys. Rev. Lett.* **95** (Nov, 2005) 226801. <http://link.aps.org/doi/10.1103/PhysRevLett.95.226801>.
- [226] C. L. Kane and E. J. Mele, “ Z_2 Topological Order and the Quantum Spin Hall Effect,” *Phys. Rev. Lett.* **95** (Sep, 2005) 146802. <http://link.aps.org/doi/10.1103/PhysRevLett.95.146802>.

- [227] B. A. Bernevig, T. L. Hughes, and S.-C. Zhang, “Quantum Spin Hall Effect and Topological Phase Transition in HgTe Quantum Wells,” *Science* **314** no. 5806, (2006) 1757–1761. <http://science.sciencemag.org/content/314/5806/1757>.
- [228] L. Fu and C. L. Kane, “Superconducting Proximity Effect and Majorana Fermions at the Surface of a Topological Insulator,” *Phys. Rev. Lett.* **100** (Mar, 2008) 096407. <http://link.aps.org/doi/10.1103/PhysRevLett.100.096407>.
- [229] M. Z. Hasan and C. L. Kane, “*Colloquium* : Topological insulators,” *Rev. Mod. Phys.* **82** (Nov, 2010) 3045–3067. <http://link.aps.org/doi/10.1103/RevModPhys.82.3045>.
- [230] M. Leijnse and K. Flensberg, “Introduction to topological superconductivity and Majorana fermions,” *Semiconductor Science and Technology* **27** no. 12, (2012) 124003. <http://stacks.iop.org/0268-1242/27/i=12/a=124003>.
- [231] A. Altland and M. R. Zirnbauer, “Nonstandard symmetry classes in mesoscopic normal-superconducting hybrid structures,” *Phys. Rev. B* **55** (Jan, 1997) 1142–1161. <http://link.aps.org/doi/10.1103/PhysRevB.55.1142>.
- [232] A. P. Schnyder, S. Ryu, A. Furusaki, and A. W. W. Ludwig, “Classification of topological insulators and superconductors in three spatial dimensions,” *Phys. Rev. B* **78** (Nov, 2008) 195125. <http://link.aps.org/doi/10.1103/PhysRevB.78.195125>.
- [233] S. Tewari and J. D. Sau, “Topological invariants for spin-orbit coupled superconductor nanowires,” *Phys. Rev. Lett.* **109** (Oct, 2012) 150408. <http://link.aps.org/doi/10.1103/PhysRevLett.109.150408>.
- [234] A. Heimes, P. Kotetes, and G. Schön, “Majorana fermions from shiba states in an antiferromagnetic chain on top of a superconductor,” *Phys. Rev. B* **90** (Aug, 2014) 060507. <http://link.aps.org/doi/10.1103/PhysRevB.90.060507>.
- [235] A. Heimes, D. Mandler, and P. Kotetes, “Interplay of topological phases in magnetic adatom-chains on top of a rashba superconducting surface,” *New Journal of Physics* **17** no. 2, (2015) 023051. <http://stacks.iop.org/1367-2630/17/i=2/a=023051>.
- [236] V. Mourik, K. Zuo, S. M. Frolov, S. R. Plissard, E. P. A. M. Bakkers, and L. P. Kouwenhoven, “Signatures of majorana fermions in hybrid superconductor-semiconductor nanowire devices,” *Science* **336** no. 6084, (2012) 1003–1007. <http://science.sciencemag.org/content/336/6084/1003>.
- [237] S. M. Albrecht, A. P. Higginbotham, M. Madsen, F. Kuemmeth, T. S. Jespersen, J. NygÅrdd, P. Krogstrup, and C. M. Marcus, “Exponential protection of zero modes in majorana islands,” *Nature* **531** (Mar, 2016) 206–209. <http://dx.doi.org/10.1038/nature17162>.

- [238] H. Shiba, “Classical Spins in Superconductors,” *Progress of Theoretical Physics* **40** no. 3, (1968) 435–451.
<http://ptp.oxfordjournals.org/content/40/3/435.abstract>.
- [239] S. Nadj-Perge, I. K. Drozdov, J. Li, H. Chen, S. Jeon, J. Seo, A. H. MacDonald, B. A. Bernevig, and A. Yazdani, “Observation of majorana fermions in ferromagnetic atomic chains on a superconductor,” *Science* **346** no. 6209, (2014) 602–607. <http://science.sciencemag.org/content/346/6209/602>.
- [240] M. A. Ruderman and C. Kittel, “Indirect exchange coupling of nuclear magnetic moments by conduction electrons,” *Phys. Rev.* **96** (Oct, 1954) 99–102.
<http://link.aps.org/doi/10.1103/PhysRev.96.99>.
- [241] T. Kasuya, “A theory of metallic ferro- and antiferromagnetism on zener’s model,” *Progress of Theoretical Physics* **16** no. 1, (1956) 45–57.
<http://ptp.oxfordjournals.org/content/16/1/45.abstract>.
- [242] K. Yosida, “Magnetic properties of cu-mn alloys,” *Phys. Rev.* **106** (Jun, 1957) 893–898. <http://link.aps.org/doi/10.1103/PhysRev.106.893>.
- [243] M. Schecter, K. Flensberg, M. H. Christensen, B. M. Andersen, and J. Paaske, “Self-organized topological superconductivity in a yu-shiba-rusinov chain,” *Phys. Rev. B* **93** (Apr, 2016) 140503.
<http://link.aps.org/doi/10.1103/PhysRevB.93.140503>.
- [244] H. Bruus and K. Flensberg, *Many-Body Quantum Theory in Condensed Matter Physics: An Introduction*. Oxford Graduate Texts. OUP Oxford, 2004.
<https://books.google.dk/books?id=v5vhg1tYLC8C>.
- [245] M. E. Flatté and J. M. Byers, “Local electronic structure of defects in superconductors,” *Phys. Rev. B* **56** (Nov, 1997) 11213–11231.
<http://link.aps.org/doi/10.1103/PhysRevB.56.11213>.
- [246] M. E. Flatté and J. M. Byers, “Local electronic structure of a single magnetic impurity in a superconductor,” *Phys. Rev. Lett.* **78** (May, 1997) 3761–3764.
<http://link.aps.org/doi/10.1103/PhysRevLett.78.3761>.
- [247] M. I. Salkola, A. V. Balatsky, and J. R. Schrieffer, “Spectral properties of quasiparticle excitations induced by magnetic moments in superconductors,” *Phys. Rev. B* **55** (May, 1997) 12648–12661.
<http://link.aps.org/doi/10.1103/PhysRevB.55.12648>.
- [248] A. Sakurai, “Comments on superconductors with magnetic impurities,” *Progress of Theoretical Physics* **44** no. 6, (1970) 1472–1476.
<http://ptp.oxfordjournals.org/content/44/6/1472.abstract>.
- [249] J. Li, H. Chen, I. K. Drozdov, A. Yazdani, B. A. Bernevig, and A. H. MacDonald, “Topological superconductivity induced by ferromagnetic metal chains,” *Phys. Rev.*

- B* **90** (Dec, 2014) 235433.
<http://link.aps.org/doi/10.1103/PhysRevB.90.235433>.
- [250] M. Ruby, F. Pientka, Y. Peng, F. von Oppen, B. W. Heinrich, and K. J. Franke, “End States and Subgap Structure in Proximity-Coupled Chains of Magnetic Adatoms,” *Phys. Rev. Lett.* **115** (Nov, 2015) 197204.
<http://link.aps.org/doi/10.1103/PhysRevLett.115.197204>.
- [251] R. Pawlak, M. Kisiel, J. Klinovaja, T. Meier, S. Kawai, T. Glatzel, D. Loss, and E. Meyer, “Probing atomic structure and Majorana wavefunctions in mono-atomic Fe chains on superconducting Pb surface,” *Npj Quantum Information* **2** (Nov, 2016) . <http://dx.doi.org/10.1038/npjqi.2016.35>.
- [252] F. Pientka, L. I. Glazman, and F. von Oppen, “Topological superconducting phase in helical Shiba chains,” *Phys. Rev. B* **88** (Oct, 2013) 155420.
<http://link.aps.org/doi/10.1103/PhysRevB.88.155420>.
- [253] F. Pientka, L. I. Glazman, and F. von Oppen, “Unconventional topological phase transitions in helical Shiba chains,” *Phys. Rev. B* **89** (May, 2014) 180505.
<http://link.aps.org/doi/10.1103/PhysRevB.89.180505>.
- [254] Y. Peng, F. Pientka, L. I. Glazman, and F. von Oppen, “Strong Localization of Majorana End States in Chains of Magnetic Adatoms,” *Phys. Rev. Lett.* **114** (Mar, 2015) 106801. <http://link.aps.org/doi/10.1103/PhysRevLett.114.106801>.
- [255] J. Klinovaja, P. Stano, A. Yazdani, and D. Loss, “Topological Superconductivity and Majorana Fermions in RKKY Systems,” *Phys. Rev. Lett.* **111** (Nov, 2013) 186805. <http://link.aps.org/doi/10.1103/PhysRevLett.111.186805>.
- [256] B. Braunecker and P. Simon, “Interplay between Classical Magnetic Moments and Superconductivity in Quantum One-Dimensional Conductors: Toward a Self-Sustained Topological Majorana Phase,” *Phys. Rev. Lett.* **111** (Oct, 2013) 147202. <http://link.aps.org/doi/10.1103/PhysRevLett.111.147202>.
- [257] M. M. Vazifeh and M. Franz, “Self-Organized Topological State with Majorana Fermions,” *Phys. Rev. Lett.* **111** (Nov, 2013) 206802.
<http://link.aps.org/doi/10.1103/PhysRevLett.111.206802>.
- [258] Y. Kim, M. Cheng, B. Bauer, R. M. Lutchyn, and S. Das Sarma, “Helical order in one-dimensional magnetic atom chains and possible emergence of Majorana bound states,” *Phys. Rev. B* **90** (Aug, 2014) 060401.
<http://link.aps.org/doi/10.1103/PhysRevB.90.060401>.
- [259] P. M. R. Brydon, S. Das Sarma, H.-Y. Hui, and J. D. Sau, “Topological Yu-Shiba-Rusinov chain from spin-orbit coupling,” *Phys. Rev. B* **91** (Feb, 2015) 064505. <http://link.aps.org/doi/10.1103/PhysRevB.91.064505>.

- [260] I. Reis, D. J. J. Marchand, and M. Franz, “Self-organized topological state in a magnetic chain on the surface of a superconductor,” *Phys. Rev. B* **90** (Aug, 2014) 085124. <http://link.aps.org/doi/10.1103/PhysRevB.90.085124>.
- [261] K. Pöyhönen, A. Westström, J. Röntynen, and T. Ojanen, “Majorana states in helical Shiba chains and ladders,” *Phys. Rev. B* **89** (Mar, 2014) 115109. <http://link.aps.org/doi/10.1103/PhysRevB.89.115109>.
- [262] W. Hu, R. T. Scalettar, and R. R. P. Singh, “Interplay of magnetic order, pairing, and phase separation in a one-dimensional spin-fermion model,” *Phys. Rev. B* **92** (Sep, 2015) 115133. <http://link.aps.org/doi/10.1103/PhysRevB.92.115133>.
- [263] B. Braunecker and P. Simon, “Self-stabilizing temperature-driven crossover between topological and nontopological ordered phases in one-dimensional conductors,” *Phys. Rev. B* **92** (Dec, 2015) 241410. <http://link.aps.org/doi/10.1103/PhysRevB.92.241410>.
- [264] L. Yu, “Bound state in superconductors with paramagnetic impurities,” *Acta Physica Sinica* **21** no. 1, (1965) 75. http://wulixb.iphy.ac.cn/EN/abstract/article_851.shtml.
- [265] A. I. Rusinov, “On the theory of gapless superconductivity in alloys containing paramagnetic impurities,” *Soviet Physics JETP* **29** no. 6, (1969) .
- [266] A. V. Balatsky, I. Vekhter, and J.-X. Zhu, “Impurity-induced states in conventional and unconventional superconductors,” *Rev. Mod. Phys.* **78** (May, 2006) 373–433. <http://link.aps.org/doi/10.1103/RevModPhys.78.373>.
- [267] A. Yazdani, B. A. Jones, C. P. Lutz, M. F. Crommie, and D. M. Eigler, “Probing the Local Effects of Magnetic Impurities on Superconductivity,” *Science* **275** no. 5307, (1997) 1767–1770. <http://science.sciencemag.org/content/275/5307/1767>.
- [268] A. Yazdani, C. M. Howald, C. P. Lutz, A. Kapitulnik, and D. M. Eigler, “Impurity-Induced Bound Excitations on the Surface of $\text{Bi}_2\text{Sr}_2\text{CaCu}_2\text{O}_8$,” *Phys. Rev. Lett.* **83** (Jul, 1999) 176–179. <http://link.aps.org/doi/10.1103/PhysRevLett.83.176>.
- [269] T.-P. Choy, J. M. Edge, A. R. Akhmerov, and C. W. J. Beenakker, “Majorana fermions emerging from magnetic nanoparticles on a superconductor without spin-orbit coupling,” *Phys. Rev. B* **84** (Nov, 2011) 195442. <http://link.aps.org/doi/10.1103/PhysRevB.84.195442>.
- [270] I. Martin and A. F. Morpurgo, “Majorana fermions in superconducting helical magnets,” *Phys. Rev. B* **85** (Apr, 2012) 144505. <http://link.aps.org/doi/10.1103/PhysRevB.85.144505>.

- [271] B. Braunecker, G. I. Japaridze, J. Klinovaja, and D. Loss, “Spin-selective Peierls transition in interacting one-dimensional conductors with spin-orbit interaction,” *Phys. Rev. B* **82** (Jul, 2010) 045127.
<http://link.aps.org/doi/10.1103/PhysRevB.82.045127>.
- [272] M. Schecter, M. S. Rudner, and K. Flensberg, “Spin-Lattice Order in One-Dimensional Conductors: Beyond the RKKY Effect,” *Phys. Rev. Lett.* **114** (Jun, 2015) 247205.
<http://link.aps.org/doi/10.1103/PhysRevLett.114.247205>.
- [273] G. C. Menard, S. Guissart, C. Brun, S. Pons, V. S. Stolyarov, F. Debontridder, M. V. Leclerc, E. Janod, L. Cario, D. Roditchev, P. Simon, and T. Cren, “Coherent long-range magnetic bound states in a superconductor,” *Nature Physics* **11** (Dec, 2015) 1013–1016. <http://dx.doi.org/10.1038/nphys3508>.
- [274] D. N. Aristov and S. V. Maleyev, “RKKY interaction in the nearly nested Fermi liquid,” *Phys. Rev. B* **56** (Oct, 1997) 8841–8848.
<http://link.aps.org/doi/10.1103/PhysRevB.56.8841>.
- [275] D. N. Aristov, S. V. Maleyev, and A. G. Yashenkin, “RKKY interaction in layered superconductors with anisotropic pairing,” *Zeitschrift für Physik B Condensed Matter* **102** no. 4, (1997) 467–471. <http://dx.doi.org/10.1007/s002570050313>.
- [276] A. Abrikosov, *Fundamentals of the Theory of Metals*. Fundamentals of the Theory of Metals. North-Holland, 1988.
<https://books.google.ch/books?id=mKHvAAAAAAAJ>.
- [277] N. Y. Yao, L. I. Glazman, E. A. Demler, M. D. Lukin, and J. D. Sau, “Enhanced Antiferromagnetic Exchange between Magnetic Impurities in a Superconducting Host,” *Phys. Rev. Lett.* **113** (Aug, 2014) 087202.
<http://link.aps.org/doi/10.1103/PhysRevLett.113.087202>.
- [278] “Spin Alignment in the Superconducting State, author = Anderson, P. W. and Suhl, H., journal = Phys. Rev., volume = 116, issue = 4, pages = 898–900, numpages = 0, year = 1959, month = Nov, publisher = American Physical Society, doi = 10.1103/PhysRev.116.898, url = <http://link.aps.org/doi/10.1103/PhysRev.116.898>,”
- [279] T. Meng, J. Klinovaja, S. Hoffman, P. Simon, and D. Loss, “Superconducting gap renormalization around two magnetic impurities: From Shiba to Andreev bound states,” *Phys. Rev. B* **92** (Aug, 2015) 064503.
<http://link.aps.org/doi/10.1103/PhysRevB.92.064503>.
- [280] H. Imamura, P. Bruno, and Y. Utsumi, “Twisted exchange interaction between localized spins embedded in a one- or two-dimensional electron gas with Rashba spin-orbit coupling,” *Phys. Rev. B* **69** (Mar, 2004) 121303.
<http://link.aps.org/doi/10.1103/PhysRevB.69.121303>.